Design of Models for the Planning of Indoor Multi-technology Wireless Networks

Marc Emmanuel Vivien-Marie Wozan Kacou

THESE DE DOCTORAT DE

L'INSTITUT NATIONAL DES SCIENCES APPLIQUEES RENNES

COMUE UNIVERSITE BRETAGNE LOIRE

ECOLE DOCTORALE N° 601
Mathématiques et Sciences et Technologies de l'Information et de la Communication
Spécialité : *Télécommunications*

Par

Marc KACOU

Design of Models for the Planning of Indoor Multi-technology Wireless Networks

Thèse présentée et soutenue à Rennes, le 12/12/2019
Unité de recherche : IETR INSA de Rennes
Thèse N° : D19 – 32/19 ISAR 32

Rapporteurs avant soutenance :

Martine Liénard	Professeur des Universités – Université de Lille 1
Jean-Marie Gorce	Professeur des Universités – INSA de Lyon

Composition du Jury :

Président :	Xavier Lagrange	Professeur des Universités – IMT Atlantique Rennes
Examinateurs :	Jean-Marie Gorce	Professeur des Universités – INSA de Lyon
	Martine Liénard	Professeur des Universités – Université de Lille 1
	Florence Sagnard	Chargée de Recherche HDR – IFSTTAR
	Ali Louzir	Principal Scientist – Interdigital R&D Cesson-Sévigné
Encadrant :	Valéry Guillet	Ingénieur de Recherche - Orange Labs Belfort
Dir. de thèse :	Ghaïs El Zein	Professeur des Universités - INSA de Rennes
Co-Encadrant:	Gheorghe Zaharia	Maître de Conférences - INSA de Rennes

Invité(s)

Sylvie Le Dall	R&D software manager - MVG Industries Plouzané

Intitulé de la thèse :

Design of Models for the Planning of Indoor Multi-technology Wireless Networks

Marc KACOU

En partenariat avec :

Acknowledgements

At the end of this 3 year-long journey, I would like to my express thanks and gratitude to the persons that helped all along this challenging adventure.

First and foremost, I would like to thank my supervisors for their availability, support and guidance throughout this thesis; To Dr Valéry Guillet, with whom I worked on a daily basis at Orange Labs Belfort, for its thoughtfulness and from whom I have learned so much; To Dr Ghaïs El Zein, my main academic supervisor, who has been of great help from the first day of this thesis to the last one and who greatly facilitated the achievement of all the formalities related to this thesis; To Dr Gheorghe Zaharia, my second academic supervisor, for its foolproof enthusiasm and its wonderful critical mind.

I am also grateful to the committee members of this thesis, Martine Liénard, Jean-Marie Gorce, Xavier Lagrange, Ali Louzir and Sylvie Le Dall, for accepting to review and discuss this work.

I would like to express my sincere thanks to Daniel Milli, manager at Orange Labs Belfort, for welcoming me in the team WEP (Wireless Engineering and Propagation) as well as for its comprehensiveness; To the team members: Brieuc Berruet, Mounir Boti, Patrice Galleau, Claude Moroni, ..., that provided me with a pleasant working environment.

My final words are addressed to my family and friends who encouraged me and helped me to persevere till this final accomplishment, Thank you!

Marc KACOU

Table of contents

Résumé étendu en français

1. Introduction

1.1. Contexte

L'évolution constante des technologies sans fil telles que le Wi-Fi (802.11n/ac/ad/ax/ ay), les réseaux mobiles (2G/3G/4G et la 5G à venir) ou les réseaux d'objets connectés (Z-wave, ZigBee, etc) a permis aux utilisateurs finaux d'accéder à de nombreux types de services tels que la téléphonie, l'accès Internet ou la connectivité ambiante (maison connectée, ville intelligente, …). Ces technologies qui, historiquement, formaient des réseaux distincts ayant des infrastructures dédiées peuvent aujourd'hui être combinées au sein d'un même réseau qualifié d'hétérogène. Dans cette thèse, le terme de réseau sans fil **multi-technologies** fait référence à un réseau sans fil hétérogène mutualisant sur de mêmes équipements (par exemple des points d'accès) différentes technologies radio.

Pour un opérateur de réseau, les réseaux sans fil multi-technologies permettent de proposer à un coût réduit différents types de services (avec un nombre limité d'appareils à déployer). De plus, ce type de réseau améliore la fiabilité de la couverture, car en cas de défaillance d'une technologie, il est toujours possible de se replier sur une autre. Enfin, en ce qui concerne les utilisateurs, ces derniers bénéficient de la complémentarité des services de façon complètement transparente.

Cependant, pour bénéficier pleinement des avantages susmentionnés, plusieurs défis techniques sont à relever. L'un d'eux concerne le **déploiement** de ces réseaux hétérogènes. En effet, si le déploiement se fait, par exemple, par rapport à la technologie offrant le meilleur débit utilisateur (et ayant le plus souvent la portée de couverture la plus réduite), on peut facilement se retrouver en situation de surdimensionnement pour les autres technologies. Il en résulte une dégradation des performances pour ces dernières à cause des interférences générées et une augmentation du coût de déploiement, ce qui est contraire à l'objectif de départ.

C'est donc cette problématique de déploiement de réseaux multi-technologies que s'inscrit cette thèse dont les objectifs sont en lien étroit avec un projet collaboratif FUI appelé OptimiSME[1]. Ce projet auquel ont contribué 6 acteurs, dont Orange et l'INSA de Rennes, avait pour objectif de proposer des solutions de **réseau local** par le biais d'extendeur de couverture radio (voir Figure 1) mutualisant des technologies sans fil opérant sur des bandes de fréquence allant de 800 MHz à 60 GHz.

1.2. Objectifs de la thèse

L'un des principaux enjeux de ce projet a été l'**optimisation** du déploiement de ces extendeurs dans des **environnements résidentiels**. En pratique, cette tâche d'optimisation est réalisée par des outils d'ingénierie radio qui se basent notamment sur des modèles de propagation et de débit. Dans ce contexte, les objectifs de cette thèse peuvent être regroupés en deux grands axes.

[1] https://vimeo.com/278629814

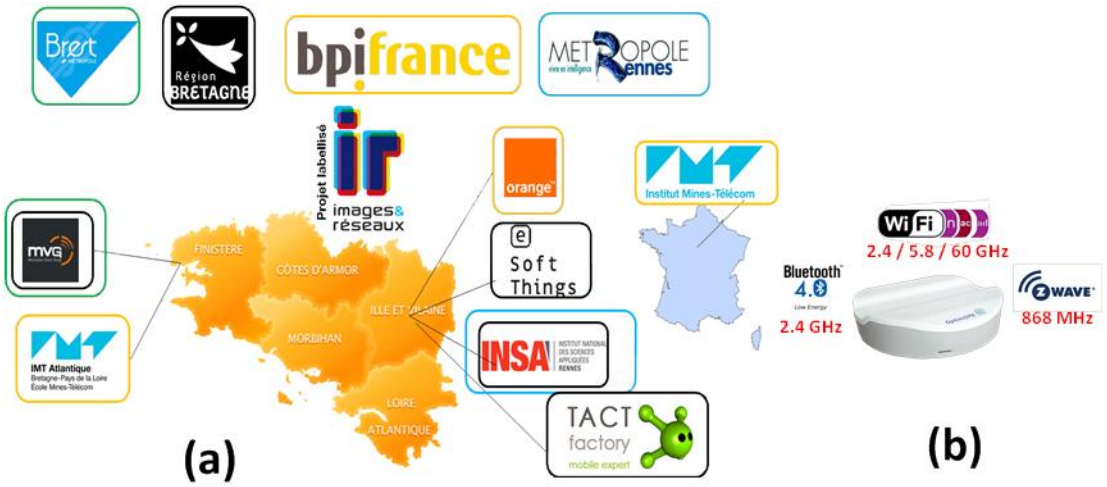

Figure 1. (a) Contributeurs et financeurs du projet, (b) Extendeur OptimiSME

Le premier a été de **fournir des modèles** sur lesquels pourraient se baser des outils d'ingénierie radio afin d'optimiser le déploiement de réseaux locaux sans fil multi-technologies. Il s'agit principalement de modèles de propagation multifréquences (pour l'estimation de couverture), d'un modèle de débit (pour l'estimation de capacité) et d'un modèle de résolution multi-objectifs (pour optimiser le positionnement des points d'accès dans un contexte multi-technologies).

Le second axe a été de **fournir des recommandations** visant à placer au mieux les points d'accès lorsque certaines situations sont rencontrées en phase de déploiement (en aval de l'étape précédente). Cela s'est fait par le biais d'étude de sensibilité de couverture.

2. Modèles de path loss indoor

Toutes les technologies d'accès radio ont un point commun : elles servent à transmettre des informations par le biais d'un canal de propagation dont le comportement varie dans le temps. Il est donc vital, pour tout système, de pouvoir caractériser ce medium de transmission. Pour cela, différents types de modèles de propagation existent ; les modèles statistiques de path loss (affaiblissement de trajet) en sont un exemple. Ces derniers sont utilisés pour estimer le niveau moyen du signal côté récepteur pour une distance de séparation donnée avec l'émetteur, comme illustré par la Figure 2.

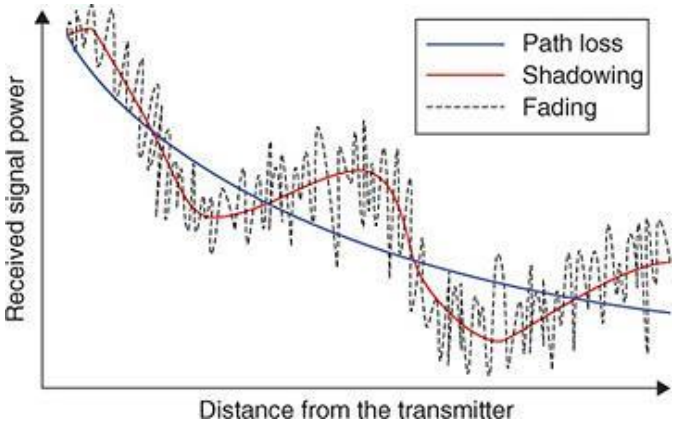

Figure 2. Affaiblissement du signal reçu avec la distance

Parmi les modèles de path loss indoor existants, deux ont été choisis pour les travaux de cette thèse, principalement en raison de leur simplicité. Il s'agit du modèle **log-distance** qui représente le path loss comme étant une fonction linéaire croissante selon le logarithmique de la distance, et du modèle de **Motley-Keenan** [1] qui, en plus de la distance, tient compte du nombre de murs/étages traversés par le trajet direct reliant l'émetteur et le récepteur. Pour être utilisables, ces modèles ont besoin d'être calibrés par le biais de mesures du canal de propagation dans l'environnement considéré.

2.1. Environnement de mesure

Les mesures de canal ont été réalisées dans un environnement résidentiel constitué d'un appartement meublé (fond gris sur la Figure 3) et de son voisinage. Les différentes pièces sont séparées par deux catégories de murs : des **cloisons** (DW), en rouge ayant une épaisseur inférieure à 10 cm et des **murs porteurs** (BW) en bleu, ayant une épaisseur supérieure à 10 cm. Des illustrations de l'environnement de mesure sont disponibles en annexe A. Deux campagnes de mesures ont été réalisées dans cet environnement indoor résidentiel. La première a été réalisée de 800 MHz à 6 GHz tandis que la seconde a été réalisée dans les bandes millimétriques autour de 60 GHz.

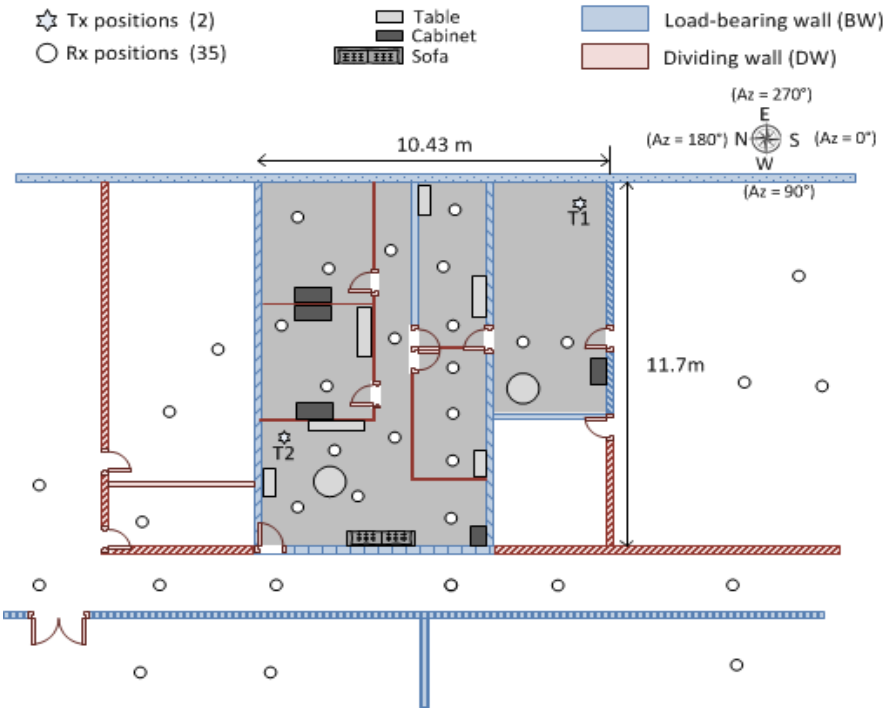

Figure 3. Plan de l'environnement de mesure

2.2. Modèles de path loss en dessous de 6 GHz

Le dispositif de mesure, illustré par la Figure 4, est constitué d'une **antenne d'émission** omnidirectionnelle, polarisée verticalement et se trouvant à une hauteur de 2,3 m. L'**antenne de réception**, du même type que celle d'émission, se trouve à une hauteur de 1,19 m. Ces deux antennes sont reliées à un **analyseur de réseau vectoriel** (VNA) qui permet de mesurer le path loss sur 7 sous-bandes de fréquences entre 868 MHz et 6 GHz. La campagne de mesure a été réalisée pour 2 positions d'émissions (T1 et T2) et au total 70 positions de

réception. Après analyse des résultats obtenus pour toutes les sous-bandes de fréquences, deux modèles de path loss multifréquences ont été calibrés.

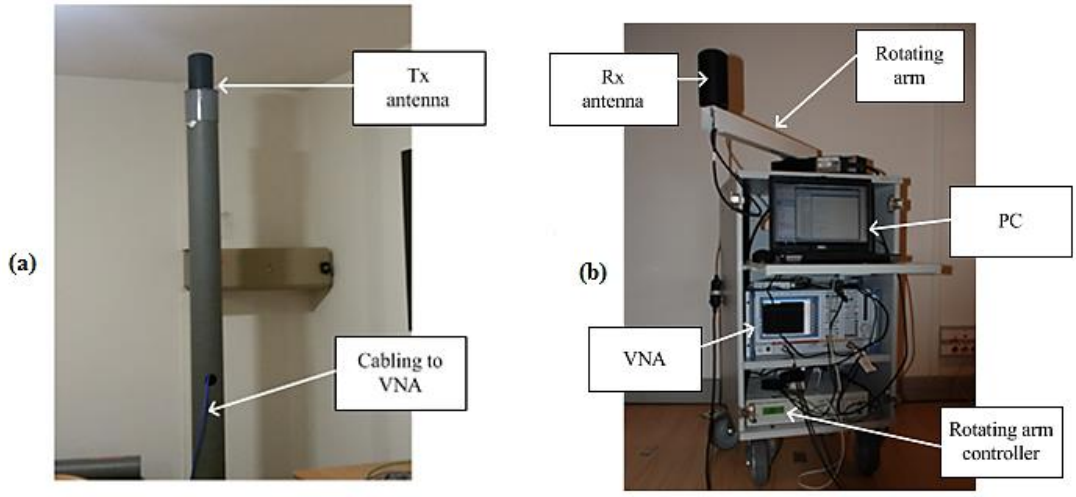

Figure 4. Dispositif de mesure en dessous de 6 GHz

Le premier est un modèle log-distance défini par la relation :

$$PL(d,f)[\text{dB}] = PL_0 + 10n\log_{10}\left(\frac{d}{d_0}\right) + 10n_f \log_{10}(f) + X_\sigma \quad (1)$$

avec : PL_0[dB] le path loss mesuré à une distance de référence d_0= 1 m, d[m] la distance entre l'émetteur et le récepteur, n l'exposant d'affaiblissement avec la distance, f[GHz] la fréquence du signal émis, n_f l'exposant d'affaiblissement avec la fréquence et X_σ une variable aléatoire gaussienne centrée, d'écart type σ[dB] modélisant la variation du path loss autour de sa valeur moyenne, notamment due aux effets de trajets multiples.

Le second est le modèle multi-murs simplifié (G-MWM). Ce modèle basé sur celui de Motley-Keenan distingue deux types de murs : cloisons et murs porteurs et modélise le path loss selon la relation :

$$PL(d,f)[\text{dB}] = PL_0 + 20\log_{10}\left(\frac{d}{d_0}\right) + 10n_f \log_{10}(f) + k_{DW}L_{DW} + k_{BW}L_{BW} + X_\sigma \quad (2)$$

avec k_{DW} et k_{BW} étant respectivement le nombre de cloisons et murs porteurs traversés par le trajet direct reliant l'émetteur et le récepteur, L_{DW} et L_{BW} représentant les pertes de transmission associées à la traversée respectivement d'une cloison et d'un mur porteur.

L'étude régressive réalisée pour déterminer la valeur des paramètres de ces modèles montre qu'ils traduisent la même dépendance en fréquence n_f = 3,2 (voir Tableau 1). En revanche, une étude comparative entre ces deux modèles suggère que le modèle G-MWM est plus précis pour estimer le path loss.

Tableau 1. Paramètres des modèles log-distance et G-MWM en dessous de 6 GHz

Model	PL_0[dB]	n	n_f	L_{DW}[dB]	L_{BW}[dB]	σ [dB]
Log-distance model	20.36	4.0	3.2	-	-	6.07
G-MWM	28.59	2.0	3.2	1.27	6.07	4.66

2.3. Modèles de path loss à 60 GHz

Le dispositif de mesure utilisé est présenté dans la Figure 5. Il est constitué d'une **antenne d'émission** directionnelle**,** polarisée verticalement, se trouvant à une hauteur de 1,97 m. Cette antenne qui a une ouverture de 120° (à 6 dB) et un gain de 7,9 dBi, est reliée à un **analyseur de réseau vectoriel** par le biais d'un **module de transposition** à 60 GHz. L'**antenne de réception,** plus directionnelle, a une ouverture de 20° (à 3dB) et un gain de 19,5 dBi. Cette campagne de mesure a été réalisée pour 2 positions d'émission (T1 et T2) et au total 43 positions de réception.

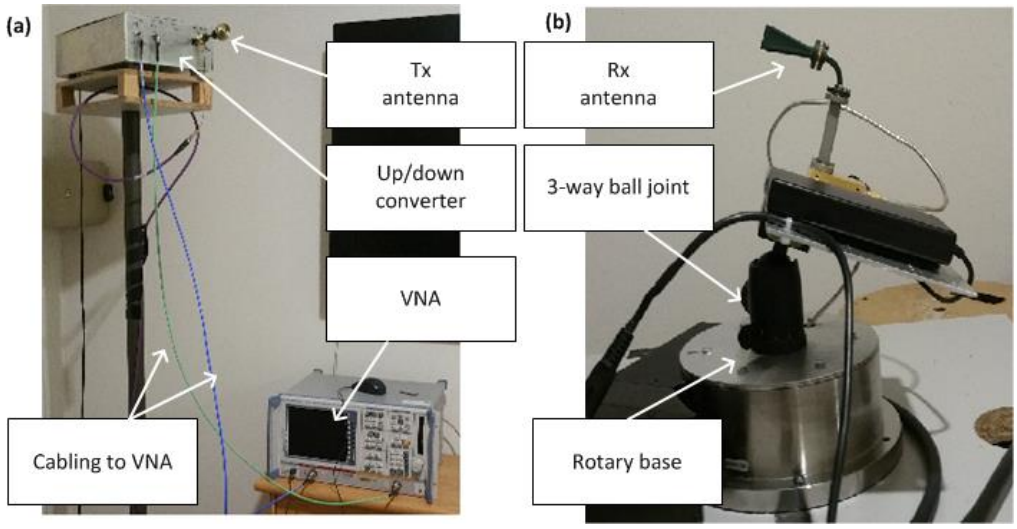

Figure 5. Dispositif de mesure à 60 GHz

Afin de simuler le beamforming, plusieurs orientations de l'antenne de réception sont testées pendant les mesures. Pour cela, une **rotule avec joint tournant** a été utilisée pour modifier l'angle d'élévation de l'antenne aux valeurs : 0°, 10°, 20°, 30° et 40° (du plan horizontal vers le haut) ; et pour chaque angle d'élévation, le **socle rotatif** sur lequel est posée l'antenne fait une rotation complète en azimut avec un pas de 6°. En conséquence, à chaque position de réception, le path loss a été mesuré dans 300 directions (5x60) en termes d'azimut et d'élévation.

Le traitement des données de mesure s'est focalisé sur 2 directions particulières : celles correspondant au **trajet direct** et au **meilleur trajet indirect**. Une analyse régressive a par la suite permis de calibrer un modèle log-distance pour ces deux directions (voir Tableau 2).

Tableau 2. Paramètres du modèle log-distance à 60 GHz

Model	PL_0[dB]	n	σ [dB]
LOS direct path	43.26	1.59	3.30
LOS best indirect path	64.74	-0.57	3.02
NLOS direct path	69.89	1.82	14.92
NLOS best indirect path	64.24	2.32	9.58

La Figure 6 met en relation le modèle et les données de mesures ayant servi à l'établir. On constate qu'en visibilité directe (LOS), le path loss est bien plus important sur le meilleur trajet indirect comparativement au trajet direct. Cet écart décroit cependant avec la distance, on passe ainsi d'un différentiel d'environs 26 dB à moins de 5 dB. La tendance inverse est observée en non-visibilité directe (NLOS). Le path loss est cette fois plus important sur le

trajet direct comparativement au meilleur trajet indirect. Cependant l'écart est moins important et reste globalement inférieur à 5 dB.

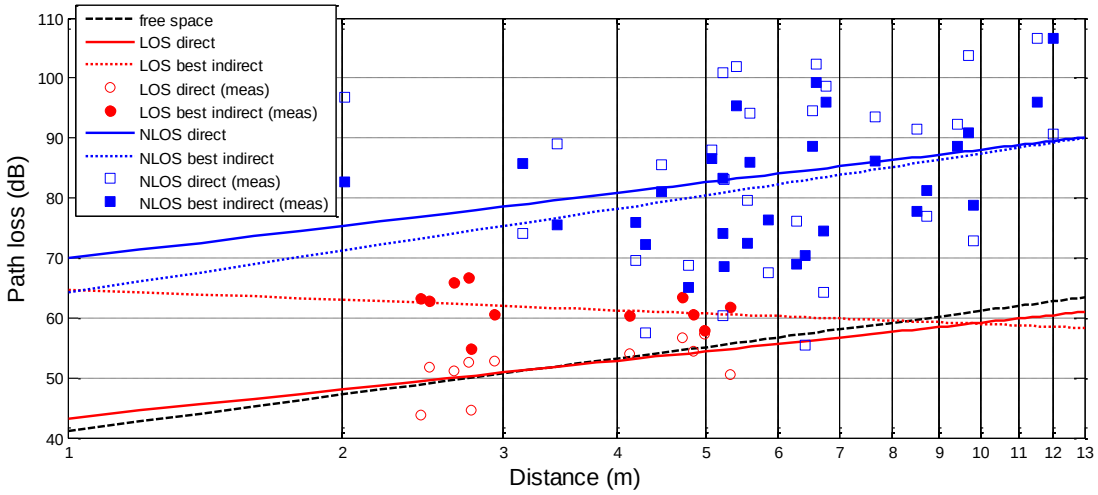

Figure 6. Modèle de path loss à 60 GHz et valeurs mesurées

3. Etudes de sensibilité de couverture

D'autres mesures de canal ont été réalisées dans l'optique d'étudier la sensibilité de couverture de l'émetteur à deux facteurs : son environnement immédiat et la présence de personnes dans le canal de propagation.

3.1. Sensibilité à l'environnement immédiat

L'impact de l'environnement immédiat de l'émetteur sur la couverture a été investigué dans 4 situations. Dans le premier cas, l'émetteur a été placé près **d'une arête de mur**. En dessous de 6 GHz, plusieurs positions d'émission rapprochées d'environ 5 cm ont été testées de part et d'autre du mur. Les résultats obtenus n'ont montré aucune différence significative aux positions de réception considérées. A 60 GHz, l'étude s'est plutôt focalisée sur la possibilité d'exploiter les phénomènes de diffraction se produisant au contact de l'arête du mur. Il a été constaté que la diffraction était la moins intéressante à exploiter avec une atténuation supplémentaire par rapport à la réflexion allant de 2 à 18 dB.

La deuxième situation a concerné la présence de **portes en bois** faisant potentiellement obstruction entre l'émetteur et le récepteur. Les résultats les plus significatifs ont été obtenus à 60 GHz où il a été possible d'améliorer le bilan de liaison de 9 dB en ouvrant simplement les portes. Dans le troisième cas, l'émetteur a été placé au **milieu d'une pièce** sans obstacle dans son environnement immédiat, à plusieurs positions d'émission rapprochées de 5 cm en moyenne. Les résultats obtenus à 6 GHz aux positions de réception sélectionnées ont montré une faible sensibilité des puissances reçues dans ce cas de figure. La dernière situation a étudié l'impact du positionnement de l'émetteur à plusieurs niveaux d'une armoire. Les meilleurs résultats ont été obtenus lorsque l'émetteur se trouvait en dehors de dudit mobilier avec un gain allant jusqu'à 10 dB.

3.2. Sensibilité à la présence de personnes

Tous les résultats de mesures présentés jusqu'ici ont été obtenus dans un environnement statique, sans présence humaine. De façon générale, introduire des personnes dans l'environnement de mesure a pour effet de potentiellement rajouter des obstacles supplémentaires entre l'émetteur et le récepteur. Dans une telle situation, des pertes additionnelles peuvent être observées par rapport au cas où il n'y a personne. Des mesures ont donc été réalisées afin de pouvoir caractériser ces pertes en dessous de 6 GHz et à 60 GHz.

3.2.1. Mesures en dessous de 6 GHz

Deux cas de figure impliquant un émetteur et un récepteur dont la communication pourrait être entravée par la présence de personnes ont été étudiés. Dans le premier cas, il s'agit d'une communication en LOS (Figure 7.a) tandis que le second cas étudié est relatif à une communication en NLOS (Figure 7.b). Dans les deux cas, les mesures ont été réalisées pour 4 hauteurs d'émission (23 cm, 1,05 m, 1,67 m et 2,30 m). Pour chacune de ces hauteurs, le path loss a été mesuré au cours de 32 scénarios faisant intervenir entre 1 et 4 personnes dans l'environnement de mesure. Les positions de personne p_i sur la Figure 7 représentent des positions potentielles. Un scénario est donc une combinaison d'un sous ensemble de ces positions.

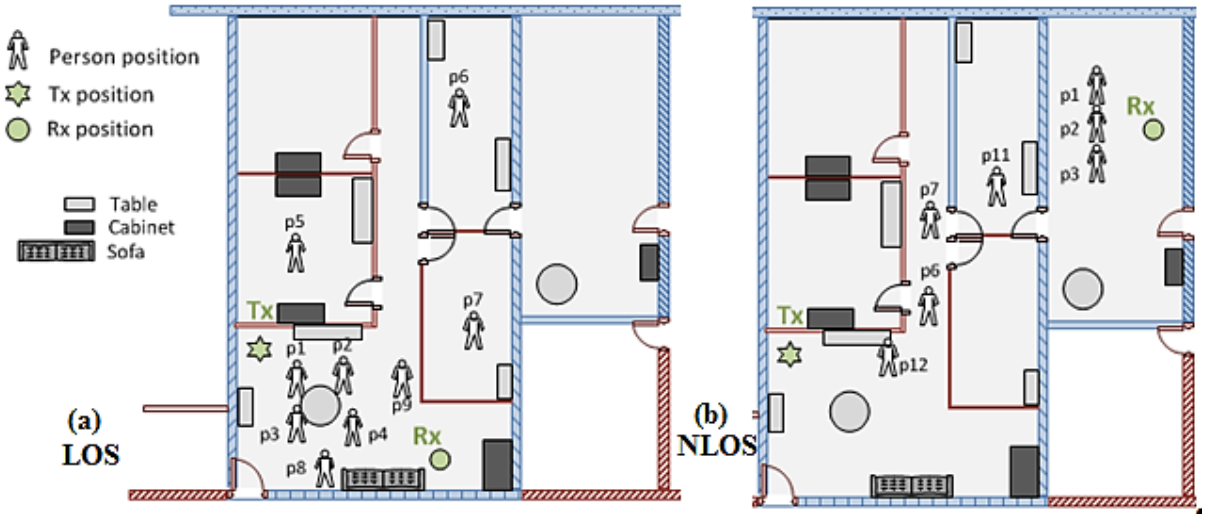

Figure 7. Etude de l'effet du blocage humain sous 6 GHz en LOS (a) et NLOS (b)

Les résultats obtenus ont montré que pour chaque hauteur, la perte supplémentaire reste globalement inférieure à 2 dB mais peut excéder cette valeur quand l'obstruction a lieu proche de l'émetteur (cas de *p1* en LOS) ou du récepteur (cas de *p3* en NLOS). La Figure 8 indiquant l'atténuation supplémentaire moyenne en fonction de la hauteur à différentes bandes de fréquences[2], laisse suggérer qu'augmenter le dénivelé entre l'émetteur et le récepteur permet de réduire ces pertes.

3.2.2. Mesures à 60 GHz

Les mesures réalisées à 60 GHz sont similaires sur le principe avec celles réalisées en dessous de 6 GHz, avec un cas de figure LOS (Rx1) et un cas de figure NLOS (Rx2) étudiés (voir Figure 9).

[2] SB2 va de 968 à 1028 MHz, SB4 va de 2,4 à 2,5 GHz, SB6 va de 5,25 à 5,35 GHz

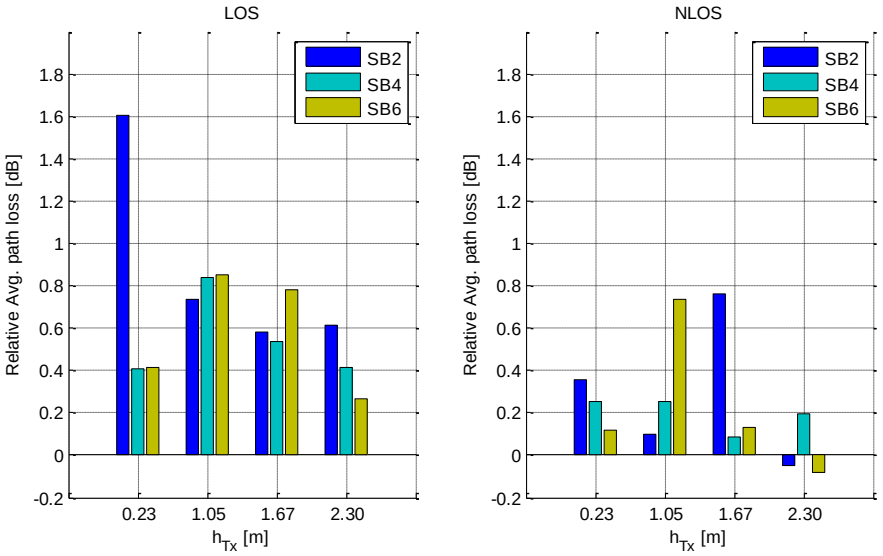

Figure 8. Pertes supplémentaires moyennes en fonction de la hauteur d'émission

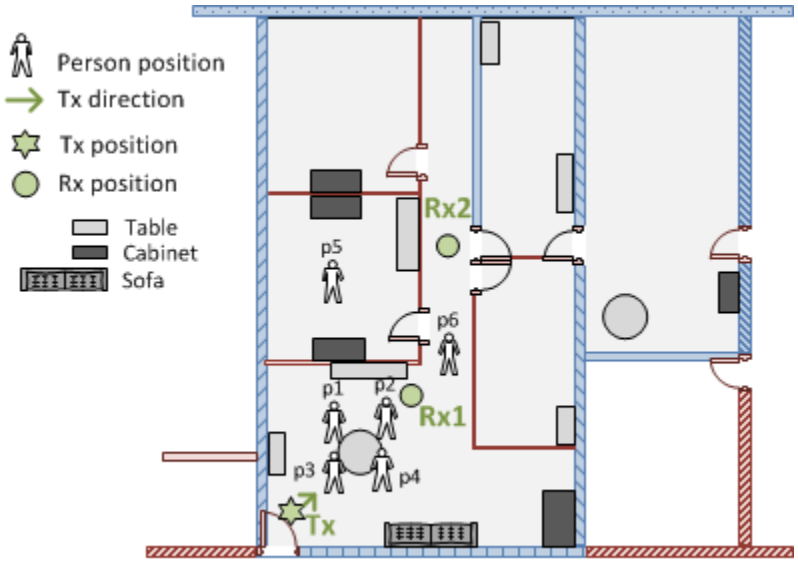

Figure 9. Etude de l'effet du blocage humain à 60 GHz en LOS (Rx1) et NLOS (Rx2)

Le path loss a été calculé au cours de 28 scénarios faisant intervenir de 1 à 4 personnes dans l'environnement de mesure. La Figure 10 donne, pour chaque scénario, la variation relative du path loss par rapport au cas de référence (0 personne). Dans la nomenclature des scénarios, les chiffres indiquent les positions concernées (ex : 123 fait référence aux positions *p1*, *p2* et *p3*) et la lettre de l'état dans lequel se trouvent les personnes (A pour *assis* et D pour *debout*). En LOS et NLOS, les pires cas se produisent lorsque le trajet dominant est obstrué (par *p2* en LOS et par *p6* en NLOS). Ainsi, des pertes supplémentaires pouvant aller jusqu'à 15 dB sont observées en LOS contre 3 dB en NLOS. Il convient, cependant, de rappeler que le modèle de path loss établi à 60 GHz a montré un écart d'environ 30 dB entre les niveaux de puissance reçus en LOS et NLOS. En conséquence, une perte de 3 dB en NLOS peut avoir un effet plus nocif qu'une perte de 15 dB en LOS. Cela est mis en lumière dans la section suivante.

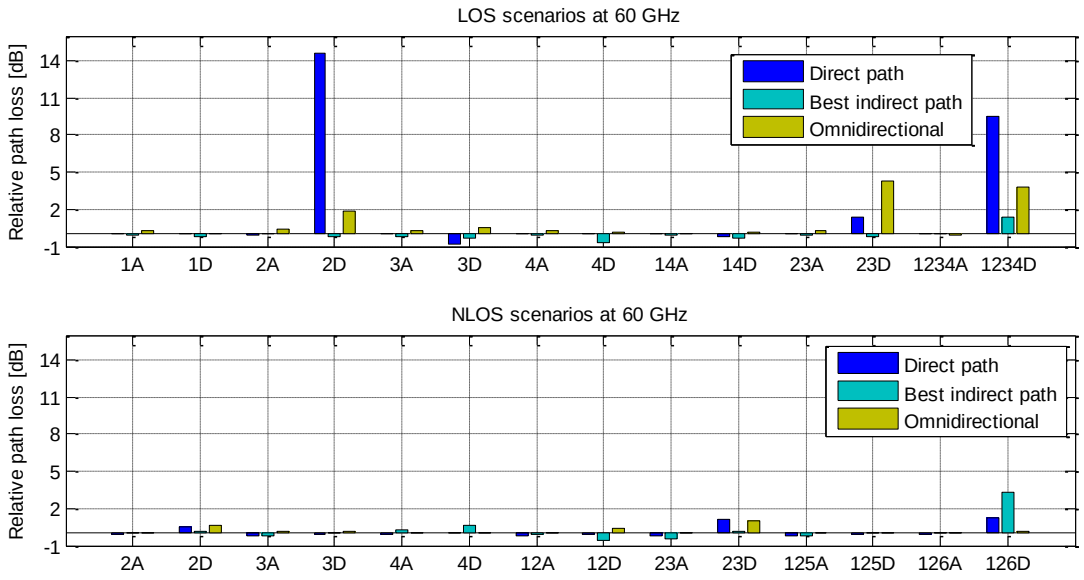

Figure 10. Variation du path loss pour chaque scenario par rapport au cas de référence

3.3. Impact des conditions de visibilité à 60 GHz

L'objectif de cette étude a été de déterminer s'il était possible de garantir une qualité de service pour des communications à 60 GHz en non visibilité. Cela peut paraître contradictoire car les bandes millimétriques sont réputées pour avoir une courte portée et une très faible capacité de pénétration à travers les obstacles. Mais des mesures de débit réalisées au cours de cette thèse avec des équipements 802.11ad (Wi-Fi à 60 GHz) ont conduit à des résultats intéressants indiqués par la Figure 11. En effet, en LOS, il a été observé en moyenne un débit de 1.6 Gbps pouvant aller jusqu'à 2.5 Gbps.

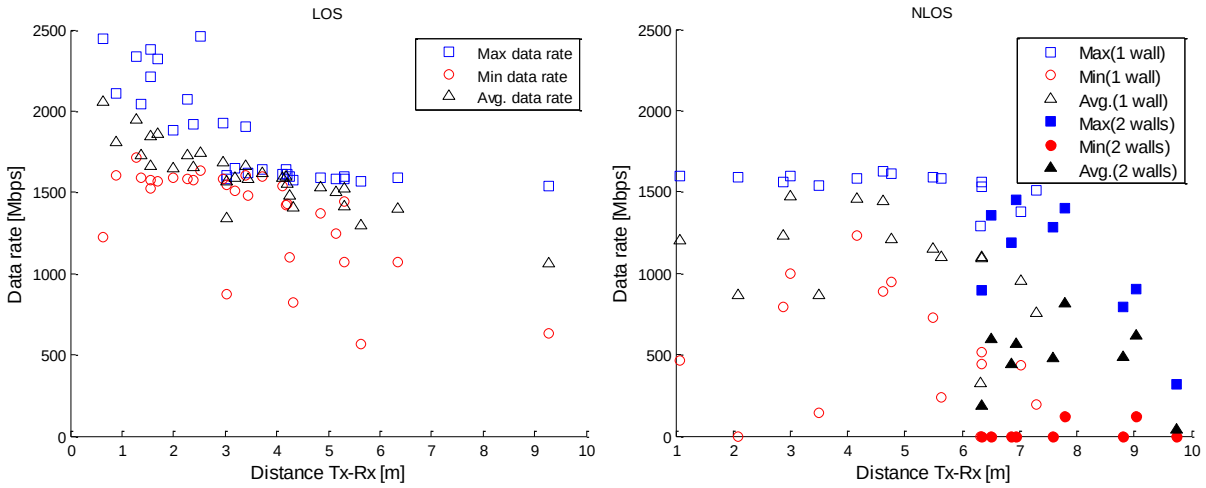

Figure 11. Débit 802.11ad en fonction de la distance en LOS (gauche) et NLOS (droite)

En NLOS, les débits sont comme attendus moins importants qu'en LOS, mais peuvent aller jusqu'à 1.6 Gbps, avec une valeur moyenne de 800 Mbps, même en présence de deux cloisons placoplatre faisant obstruction. Ces débits restent supérieurs à ceux d'autres versions du Wi-Fi couramment utilisées, comme le 802.11n (Wi-Fi 4) allant jusqu'à 600 Mbps. De ces observations, ont découlé d'autres études pour déterminer dans quelle mesure il serait possible de garantir une qualité de service pour les communications en NLOS.

La première étape a consisté à analyser, à partir des mesures de path loss réalisées à 60 GHz, l'écart-type des retards (RMS delay spread) en LOS et NLOS. Les valeurs de RMS delay spread obtenues restent globalement inférieures à 4 ns en LOS contre 15.8 ns en NLOS (voir Figure 12). Ces résultats suggèrent de fortes probabilités d'interférence inter-symboles en NLOS car la durée d'égalisation du 802.11ad en mono-porteuse est trop courte (36 ns) et devrait être au moins 4 fois plus grande.

Des mesures de débit ont également été réalisées en présence de personnes statiques ou en mouvement pouvant agir comme obstacles. Dans le cas des mesures statiques, jusqu'à 4 personnes ont été positionnées entre le point d'accès et des stations pouvant être en LOS ou NLOS. En guise de résultat, la Figure 13 donne les pertes relatives de débit observées par rapport au cas de référence (0 personne). En LOS, ces pertes restent globalement inférieures à 20% et sont maximales lorsqu'une personne fait obstruction au trajet direct. En revanche, en NLOS, les pertes relatives observées dans la moitié des scenarios sont d'au moins 50%, allant pour la plupart à 100% (rupture de liaison). Cela montre la forte sensibilité des communications en non visibilité à la présence de personnes.

Cette tendance se confirme avec d'autres mesures réalisées avec 4 personnes se déplaçant aléatoirement dans l'environnement de mesure. En LOS, le débit reste globalement supérieur à 1 Gbps pendant 2 minutes, tandis qu'en NLOS, il y a rupture de liaison radio au bout de 20 secondes (voir Figure 14). En conclusion, les communications en LOS sont assez robustes, même en présence de personnes faisant obstacles. En revanche, en NLOS, la trop grande sensibilité de la liaison radio ne permet pas de garantir une qualité de service dans ces conditions.

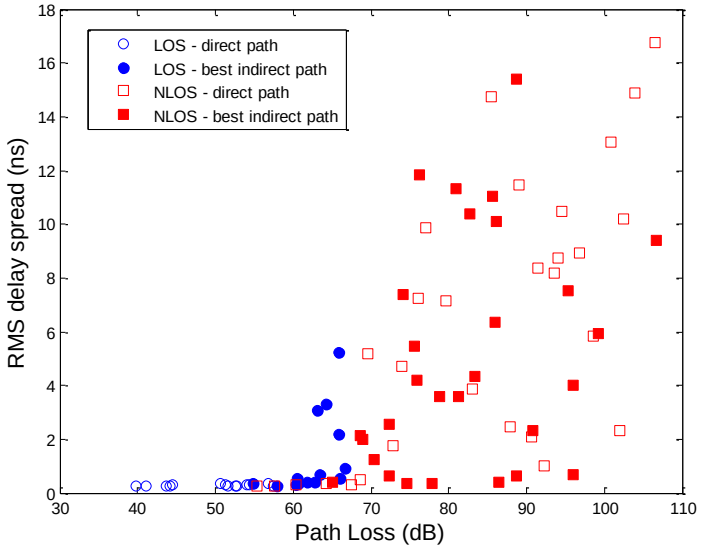

Figure 12. RMS delay spread à 60 GHz en LOS et NLOS

4. Planification de réseaux multi-technologies

La planification des réseaux sans fil est une tâche difficile qui est réalisée par le biais d'outils d'ingénierie radio. La plupart de ces outils disposent de modules dédiés dits ACP (*Automatic Cell Planning*) ayant, entre autre pour mission, de trouver les meilleurs emplacements des sites (AP dans ce contexte). Ces modules s'aident pour cela de divers modèles pour faire notamment des estimations de couverture (modèles de propagation) et de capacité (modèles de débit).

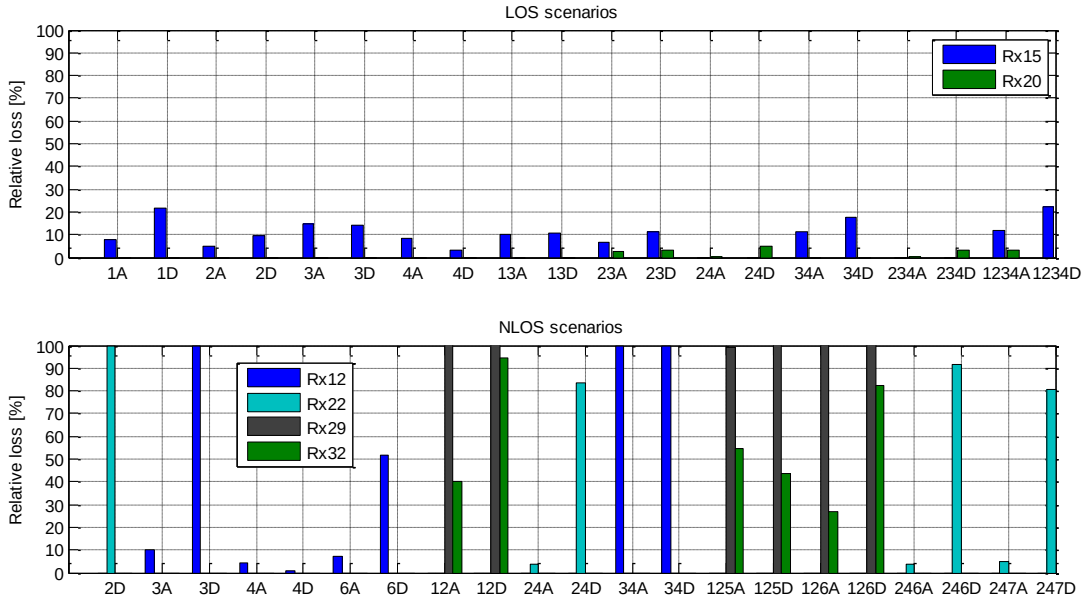

Figure 13. Pertes relatives de débit en LOS et NLOS

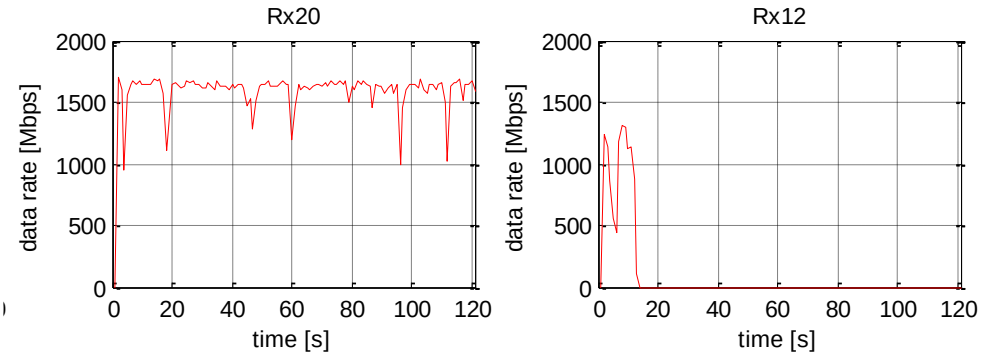

Figure 14. Variation du débit instantané en LOS (Rx20) et NLOS (Rx12)

Dans ce contexte et sur la base de l'outil XANDA développé par Orange Labs Belfort, deux modèles analytiques ont été établis dans le cadre de cette thèse pour la planification de réseaux Wi-Fi : d'une part un modèle considérant la capacité en uplink et downlink et d'autre part un modèle considérant des AP opérant à 5 et 60 GHz.

4.1. Modèle de débit pour réseau Wi-Fi

Avec l'apparition des services cloud, des réseaux sociaux ou des plateformes de direct streaming, l'utilisateur ordinaire d'Internet s'est mué en créateur de contenu pour qui le débit montant (UL) est devenu tout aussi important que le descendant (DL). C'est fort de ce constat qu'un modèle de débit pour réseau Wi-Fi a été établi durant cette thèse. Ce modèle simplifié permet d'estimer la capacité totale d'une cellule Wi-Fi à partir d'un rapport souhaité entre le débit montant et le débit descendant.

Considérons la cellule Wi-Fi illustrée dans la Figure 15. Elle est constituée d'un point d'accès (AP) et de N stations (STA) parmi lesquelles N_1 ne font que recevoir des paquets de l'AP (DL), N_2 ne font que transmettre des paquets vers l'AP (UL) et N_3 transmettent et reçoivent des paquets de l'AP (UL et DL).

Figure 15. Cellule Wi-Fi avec 3 groupes de stations

Le rapport de débit α, souhaité pour la cellule, est défini comme étant le rapport entre le débit total sur le sens montant et le débit total sur le sens descendant. Si les paquets échangés sont supposés de taille fixe L, α correspond, sur une durée d'observation du canal T_{obs}, au nombre total de paquets reçus par l'AP divisé par le nombre total de paquets reçus par l'ensemble des stations.

$$\alpha = \frac{\text{Débit montant total}}{\text{Débit déscendant total}} \tag{3}$$

Le débit cellule S est modélisé en considérant les événements se produisant lorsqu'un paquet est transmis avec succès. Sous l'hypothèse que toutes les stations ont le même type de trafic, S est obtenu par la relation :

$$S = \frac{(1+\alpha)L}{\frac{1}{N_1+N_3}\left(\sum_{i=1}^{N_1} T_{i,1} + \sum_{j=1}^{N_3} T_{j,3}\right) + \frac{\alpha}{N_2+N_3}\left(\sum_{k=1}^{N_2} t_{k,2} + \sum_{m=1}^{N_3} t_{m,3}\right)} \tag{4}$$

avec :

- L la taille du paquet transmis avec succès,
- $T_{i,j}$ la durée de transmission du paquet de l'AP vers STA_i de type j (DL),
- $t_{k,m}$ la durée à transmission du paquet de STA_k de type m vers l'AP (UL).

Ce modèle simplifié a été comparé avec un autre modèle de débit [2] basé sur une chaîne de Markov à deux dimensions et à une simulation écrite sur MATLAB pour un réseau 802.11a. Les résultats obtenus montrent que le modèle de débit établi durant cette thèse permet d'estimer la capacité maximale (en vert sur la Figure 16) d'une cellule pour un rapport de débit α souhaité.

Une application de ce modèle à un outil d'ingénierie radio, développé sur le site d'Orange Labs Belfort, permet de déterminer S_p, la capacité garantie par une cellule avec une probabilité p, selon la relation :

$$p = P(S \geq S_p) = \frac{1}{2}\left(1 + \text{erf}\left[\frac{\frac{1+\alpha}{S_p} - \mu_{DL} - \alpha\mu_{UL}}{\sqrt{2\left(\frac{{\sigma_{DL}}^2}{N_1+N_3} + \frac{\alpha^2{\sigma_{UL}}^2}{N_2+N_3}\right)}}\right]\right) \tag{5}$$

avec :

- μ_{DL} et μ_{UL} étant respectivement la moyenne de la somme des variables aléatoires $T_{i,j}/L$ et $t_{k,m}/L$.
- σ_{DL} et σ_{UL} étant respectivement l'écart-type de la somme des variables aléatoires $T_{i,j}/L$ et $t_{k,m}/L$.

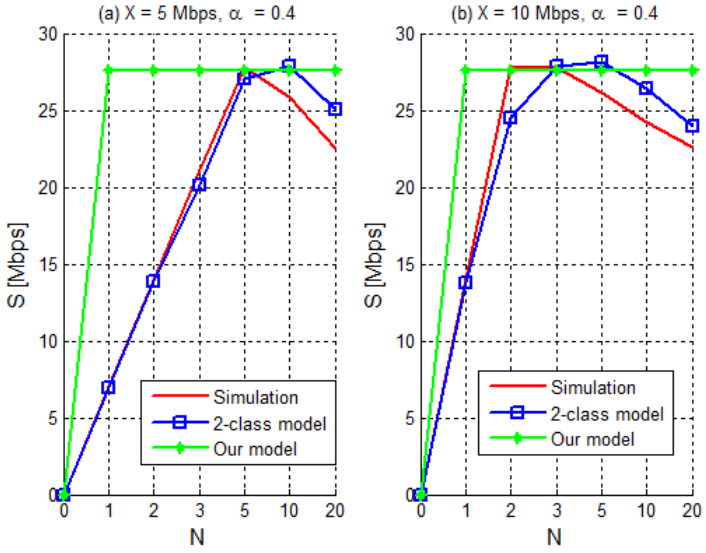

Figure 16. Débit cellule estimé en fonction du nombre d'utilisateurs

La valeur de S_p se déduit de (5) par relation réciproque.

Cette application du modèle a été un élément fondamental sur lequel s'est basé le modèle de résolution multi-objectif, présenté dans la prochaine section.

4.2. Modèle de résolution multi-objectif

La planification d'un réseau local sans fil (multi-technologies ou non) sur un site donné peut être vue comme un problème d'optimisation combinatoire consistant à trouver la combinaison optimale de positions (d'AP) solutions parmi un ensemble de positions candidates (voir Figure 17). Afin de résoudre ce problème dans le cas de réseaux locaux sans fil multi-technologies opérant à 5 et 60 GHz, un modèle de multi-objectif a été établi afin de proposer une méthode d'évaluation des solutions.

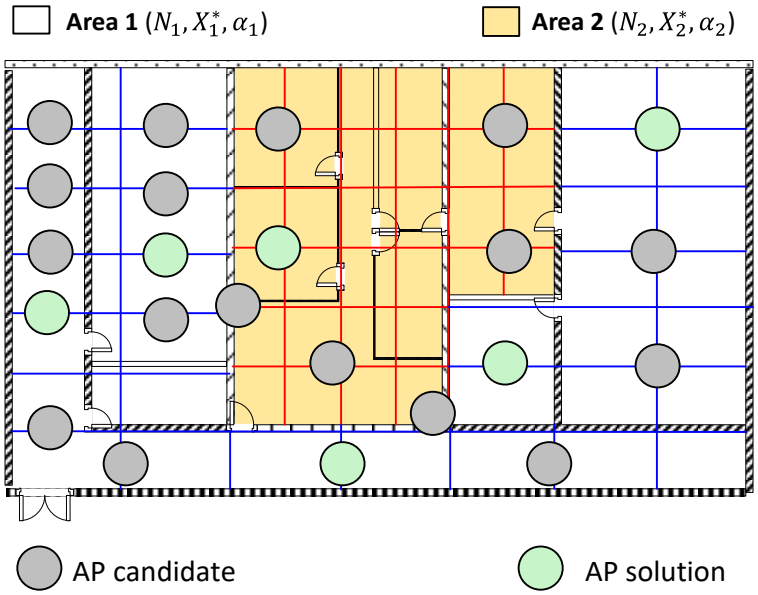

Figure 17. Combinaison d'AP solutions (vert) parmi positions candidates (gris)

Considérons un site à couvrir divisé en N_z zones de services (la Figure 17 donne un exemple de site à 2 zones de service) contenant chacune N_k utilisateurs ($1 \leq k \leq N_Z$). Le débit descendant par utilisateur souhaité pour chaque zone de service est représenté par le vecteur X^*= (X_1^*,…,$X_{N_z}^*$) et le rapport de débit UL/DL souhaité par zone est α = (α_1,…,α_{N_z}).

Soit une solution ω_s définie comme étant une combinaison de N_{AP} AP solutions parmi un ensemble de positions de candidates : ω_s = (AP_1^s,…,$AP_{N_{AP}}^s$). Le débit par utilisateur garanti (avec une probabilité p) par la solution ω_s dans chaque zone de service est représenté par le vecteur X = (X_1,...,X_{N_z}). Chaque composante de ce vecteur est déterminée en résolvant l'équation donnant la probabilité p qu'un débit par utilisateur X_k soit atteignable dans la zone de service k ($1 \leq k \leq N_z$):

$$\sum_{i=1}^{N_{AP}} \sum_{b=1}^{N_{technos}^i} U_k^{i,b} P\left(\frac{S^{i,b}}{N^{i,b}} \geq (1+\alpha_k)X_k\right) = p \qquad (6)$$

sachant que :

- $N_{technos}^i$ est le nombre de technologies mutualisées sur AP_i^s, vaut 2 si l'AP opère à 5 GHz (b = 1) et 60 GHz (b = 2).
- $U_k^{i,b}$ est la probabilité qu'un utilisateur dans la zone de service k échange des paquets avec AP_i^s par le biais de la technologie b.
- $N^{i,b}$ représente le nombre total d'utilisateurs échangeant des paquets avec AP_i^s par le biais de la technologie b ; ces utilisateurs peuvent se trouver dans différentes zones de service.
- $S^{i,b}$ correspond au débit total de la cellule opéré par AP_i^spar le biais de la technologie b (déduit du modèle de débit simplifié présenté plus tôt).

De plus, les liaisons radio à 60 GHz étant particulièrement sensibles aux obstacles, il est nécessaire de prévoir une **couverture de repli** à 5 GHz. Cette couverture de repli est construite en remplaçant tous les liens à 60 GHz par des liens à 5 GHz. Le débit par utilisateur garanti par la couverture résultante est alors donné par le vecteur X'= (X_1',…,X_{N_z}'). Chaque composante de ce vecteur est déterminée en résolvant l'équation :

$$\sum_{i=1}^{N_{AP}} U_k^{i,1}\ P\left(\frac{S^{i,1}}{N^{i,1}} \geq (1+\alpha_k)X_k'\right) = p, \qquad 1 \leq k \leq N_z \qquad (7)$$

Sachant déterminer les valeurs de X = (X_1,...,X_{N_z}) et X'= (X_1',…,X_{N_z}') pour chaque solution, la comparaison des différentes solutions entre elles, se fait selon 2 critères : f_1 et f_2 définis de la manière suivante.

Le critère f_1 est mathématiquement défini par :

$$f_1 = \min_{1 \leq k \leq N_z} \frac{X_k}{X_k^*} \qquad (8)$$

Il indique le gain de débit minimum, par rapport à la demande de chaque zone de service, garanti par la **couverture initiale** (à 5 et 60 GHz). Si $f_1 < 1$, cela signifie que la solution évaluée ne garantit pas la demande d'au moins une zone de service ; dans ce cas, cette solution est considérée comme non éligible.

Le critère f_2 est défini par la relation :

$$f_2 = \min_{1 \le k \le N_z} \frac{X'_k}{X^*_k} \quad (9)$$

Il indique le gain de débit minimum, par rapport à la demande de chaque zone de service, garanti par la **couverture de repli**. Si $f_2 \geq 1$, cela signifie que la couverture de repli permet de combler la demande de chaque zone de service.

Ainsi, les solutions optimales au problème de planification multi-technologies sont celles qui ont les valeurs f_1 et f_2 les plus grandes possibles (on parle de maximisation des critères).

Cette méthode a été testée pour la résolution de 3 problèmes de planification de réseau local sans fil sur un même site:

- Dans le 1er, tous les AP candidats opèrent à 5 et 60 GHz, il s'agit du cas F-MT (pour *full multi-technology*).
- Dans le 2e cas, tous les AP candidats opèrent à 5 GHz, il s'agit du cas ST (pour *single-technology*).
- Enfin, le 3e cas fait intervenir un mix aléatoire entre candidats opérant uniquement à 5 GHz et candidats opérant à 5 et 60 GHz ; il s'agit du cas P-MT (pour *partial multi-technology*).

L'algorithme NSGA-II [3] a été utilisé pour rechercher les solutions de chaque problème. Les résultats obtenus après 100 itérations montrent que les solutions optimales trouvées dans un contexte multi-technologies sont les meilleures (voir Figure 18). Le choix de la solution à retenir dépendra des préférences du décideur final.

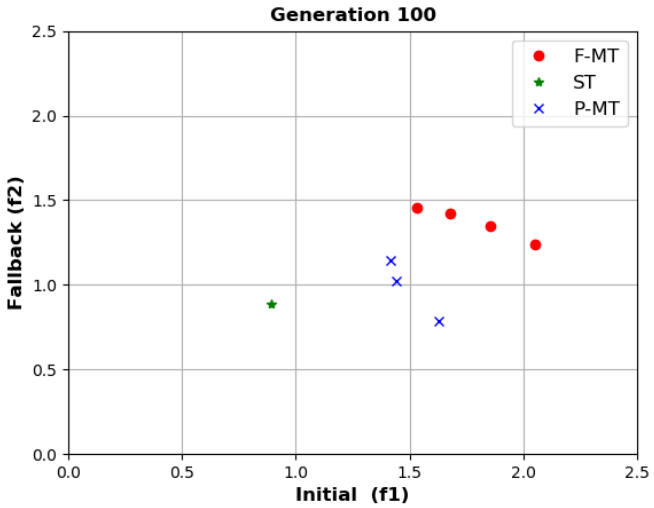

Figure 18. Solutions optimales obtenues pour chaque problème après 100 itérations

5. Conclusion et perspectives

Les réseaux hétérogènes de par les avantages qu'ils confèrent sont le futur des communications sans fil; en témoigne la prochaine génération de réseau mobile (5G) qui prévoit de combiner plusieurs technologies d'accès radio (multi-RAT). Les réseaux Wi-Fi avec les versions Wi-Fi 6 et 802.11ay à venir ne sont pas en reste. A cet égard, les modèles développés au cours de cette thèse devront être adaptés pour les usages futurs introduits par ces nouvelles technologies. Parmi les pistes envisagées, il y a la prise en compte des transmissions multi-utilisateurs (MU-MIMO et OFDMA) par le modèle de débit Wi-Fi. Le modèle de résolution multi-objectif peut également être amélioré par l'ajout d'autres critères

d'évaluation et contraintes comme, par exemple, le partage équitable de l'utilisation du canal entre les stations, et la réduction du niveau global d'exposition aux ondes des différentes technologies.

Acronyms

ACP	Automatic Cell Planning
AP	Access Point
BS	Base Station
BSS	Basic Service Set
BW	Load bearing wall
CSMA/CA	Carrier Sense Multiple Access with Collision Avoidance
DCF	Distributed Coordination Function
DL	Downlink
D-MWM	Detailed Multi-Wall Model
DW	Diving wall
EIRP	Effective isotropic radiated power
EM	Electromagnetic
G-MWM	Generalized Multi-Wall Model
GPS	Global Positioning System
IoT	Internet of Things
ISI	Intersymbol Interference
LNA	Low Noise Amplifier
LOS	Line-Of-Sight
MAC	Medium Access Control
MCS	Modulation and coding scheme
MIMO	Multiple Input Multiple Output
MU-MIMO	Multi-User MIMO
MWM	Multi-Wall Model
NLOS	Non-Line-Of-Sight
OFDM	Orthogonal Frequency-Division Multiplexing
OFDMA	Orthogonal Frequency Division Multiple Access
PDP	Power Delay Profile
QoS	Quality of Service
RMS	Root Mean Square
Rx	Receiver
SB	(Frequency) Sub-band
SC-PHY	Single Carrier Physical Layer
SINR	Signal-to-Interference-plus-Noise-Ratio

STA	Station
TV	Television
Tx	Transmitter
UL	Uplink
VNA	Vector Network Analyzer
Wi-Fi	Wireless Fidelity
WLAN	Wireless Local Area Network
WPAN	Wireless Personal Area Network

List of figures

List of tables

Chapter 1

Introduction

1.1 Context

Over the past few decades, wireless communications have become an essential component of digital information exchange. Indeed the constant evolution of wireless systems such as Wi-Fi (802.11n/ac/ad/ax/ay), mobile technologies (2G/3G/4G and the incoming 5G) or IoT (Z-wave, ZigBee, …) provides the end-users with numerous types of services like TV, telephony, Internet access, GPS or Smart connectivity (Smart home, Smart city, …). These wireless technologies had historically been designed with a dedicated set of interconnected devices (network nodes) referred to as network infrastructure. However, it has now become possible to pool over the same network nodes (e.g. access points) different radio technologies having distinct applications. In this document, such heterogeneous wireless networks will be referred to as **multi-technology** wireless networks.

For a network operator, multi-technology networks, firstly, allow to propose various types of services at a reduced cost (with a limited number of devices to deploy). Moreover, this type of wireless network improves the coverage reliability: if one technology fails, it's still possible to fall back to another one. Also, multi-technology networks, featuring non-interfering technologies, improve the spectrum efficiency through a load balancing between technologies. Concerning the end-users, they benefits of a seamless experience from the complementariness between the technologies applications.

However, multi-technology wireless networks rise many technical issues. One of them revolves around **the deployment** of such heterogeneous networks. In fact, they combine distinct wireless systems which may operate at different frequency bands. It results in dimensioning issues because there is an antagonist relationship between the radio coverage and the frequency band: the higher the frequency is the lower is the coverage radius. Thus, dimensioning the network according to the technology having the lowest coverage area (and also providing the highest bandwidth) may lead to an over-dimensioning for less restrictive technologies. As a result, the deployment cost may increase and the network performances may be negatively impacted because of the potential interferences generated.

This initial planning problematic is the main subject of this thesis which has primarily been motivated by a French collaborative project called **OptimiSME**.

1.2 Motivations and objectives

OptimiSME[3] is a collaborative project in which took part *Orange* and five partners (including the *INSA de Rennes*, Figure 1.1.a). Its final goal is to provide Wireless Local Area Network (WLAN) solutions for office and residential environments. This project involved the design of multi-technology wireless extenders (Figure 1.1.b) featuring radio technologies

[3] https://vimeo.com/278629814

operating from 800 MHz to 60 GHz. This thesis has been focused on an important issue related to this project which is the **optimal positioning** of these extenders in **indoor residential environments**. For this purpose, three major axes have been covered: propagation modeling, coverage sensitivity study and multi-technology wireless networks planning.

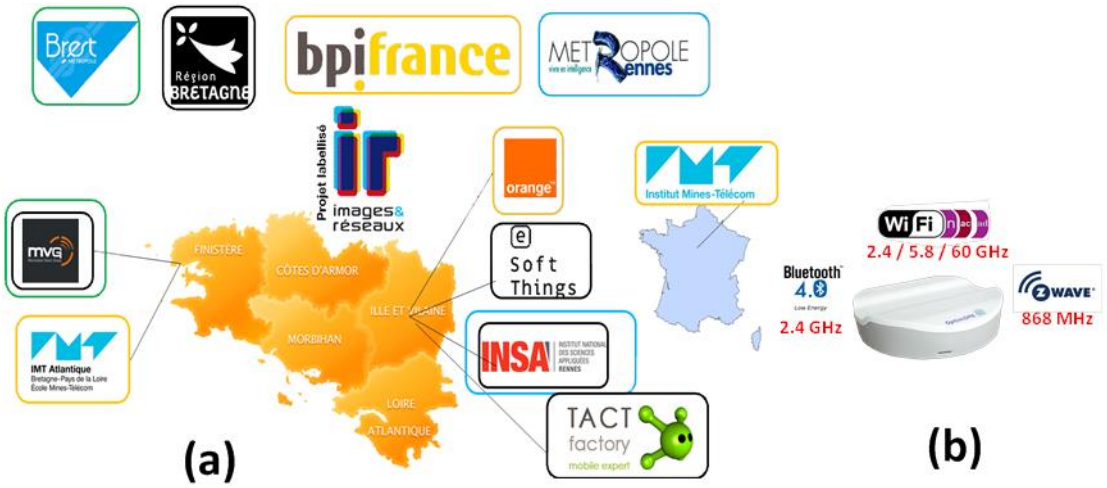

Figure 1.1. (a) OptimiSME project contributors and financers, (b) OptimiSME extender

1.2.1 Multi-frequency propagation modeling

In practice, the choice of the optimal locations of the extenders is achieved by using radio network design software. These planning tools are able to compute coverage areas based on specified propagation models. One of these tools, developed during the OptimiSME project, is called *MyWiFiPlanner* (see Figure 1.2) and is meant to be used by devices potentially having limited computing capabilities such as smartphones. The first goal of this thesis has been to provide simplified yet relatively accurate multi-frequency propagation models that could be used by *light* software planning tools such as the one aforementioned.

1.2.2 Coverage sensitivity study

When using a radio network design tool, it may happen that an optimal location chosen by the software appears to be unavailable in practice due, for instance, to the lack of electrical outlet, or present some specificity (e.g. located near a well edge). In this regard, the radio coverage sensitivity to the transmitter location has been studied, during this thesis, in some particular use case by the means of propagation measurements. The goal of this investigation has been to produce positioning recommendations for the wireless extenders when specific locations are encountered.

1.2.3 Analytical models for multi-technology WLANs planning

Most of the existing radio network planning tools approach the design of WLANs as a combinatorial optimization problem. This problem is solved by optimization algorithms relying on various complementary types of models (propagation models, capacity models …). The final goal of this thesis is to propose analytical models applicable to these optimization algorithms, in order to design multi-technology WLANs.

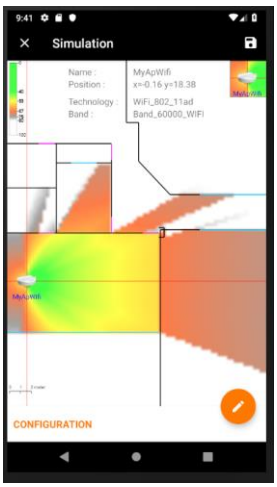

Figure 1.2. MyWifiPlanner user interface

1.3 Report outline

The remainder of this document is organized as follows. Chapter 2 gives a brief overview of the different wireless systems (co)existing in indoor environments. All of these technologies involve information exchange over a propagation channel which essential to know. In this regard, this chapter also presents some important characteristics of radio channels, as well as a state of the art of existing indoor propagation models and channel sounding techniques.

Chapter 3 is dedicated to the first goal of this thesis. It describes two measurement campaigns carried out, during this thesis, with a frequency domain channel sounder in an indoor residential environment. The first campaign has been performed over 7 frequency bands in order to establish multi-frequency path loss models available from 800 MHz to 6 GHz. The second campaign, conducted at 60 GHz, has led to path loss models in line-of-sight (LOS) and non-line-of-sight (NLOS) conditions for directional and omnidirectional transmissions.

Chapter 4 focuses on the second goal of this thesis. It presents a study, realized below 6 GHz and at 60 GHz, of the sensitivity of the transmitter's radio coverage to two factors. The first one is related to the transmitter surroundings where four situations have been evaluated: the transmitter is near a well-edge, close to a wooden door, in the middle of room and inside a piece of furniture. The second factor concerned the characterization of the additional loss induced by the presence of people in the propagation channel.

Chapter 5 treats of the last goal of this thesis. It establishes two analytical models available for radio planning tools in order to design of multi-technology WLANs. The first one is a throughput model which features a fairness parameter enabling the accounting of uplink traffic during WLANs planning. The second model, which reuses the previous throughput model, proposes a multi-objective resolution of the combinatorial problem induced by the planning of multi-technology WLANs.

Finally, Chapter 6 draws a general conclusion that sums up the key results of this thesis and indicates some potential further research topics.

1.4 Contributions and publications

In this section are listed the contributions and publications related to this thesis.

1.4.1 Journal papers

- M. Kacou, V. Guillet, G. El Zein, G. Zaharia, J. Y. Thiriet, "An uplink and downlink-oriented approach in Automatic Cell Planning for IEEE 802.11 Networks", *Lecture Notes in Electrical Engineering, Proceedings of the Conference on Smart Information & Communication Technologies (SmartICT 2019)*, Springer 2019.

1.4.2 International conferences

- M. Kacou, V. Guillet, G. El Zein, and G. Zaharia, "A Multi-wall and Multi-frequency Home Environment Path Loss Characterization and Modeling," in *12th European Conference on Antennas and Propagation (EUCAP 2018)*, London, United Kingdom, 2018.
- M. Kacou, V. Guillet, G. El. Zein, and G. Zaharia, "Coverage and Throughput Analysis at 60 GHz for Indoor WLAN with Indirect Paths," in *29th IEEE International Symposium on Personal, Indoor and Mobile Radio Communications (PIMRC 2018)*, Bologna, Italy, 2018.
- M. Kacou, V. Guillet, G. El Zein, G. Zaharia, J. Y. Thiriet, "An uplink and downlink-oriented approach in Automatic Cell Planning for IEEE 802.11 Networks", in *1st Conference on Smart Information & Communication Technologies (SmartICT 2019)*, Saïdia, Morocco, 2019.

1.4.3 National workshop

- M. Kacou, V. Guillet, G. El Zein, G. Zahara, "Mesures et caractérisation de la propagation à 60 GHz en non visibilité en environnement indoor résidentiel", *Actes des Journées d'études SEE-DGA "Propagation radioélectrique - Caractérisation de l'environnement"*, IMT Atlantique, Rennes, 28-29 November, 2018.

1.4.4 OptimiSME project

- M. Kacou, "Report 2.1.1. Characterization of electrical properties of different indoor materials from 900 MHz to 60 GHz", February, 2017.
- M. Kacou, V. Guillet, S. Kaddouri, G. El Zein, G. Zaharia, "Report 2.1.2. Extenders positioning recommendations", February, 2018.

Chapter 2

Indoor radio waves propagation overview

An indoor environment is defined as a closed area delimited by walls of any form. Homes, buildings or airports are common example of indoor environments. In such places, a variety of wireless technologies may (co)exist. Some of them are non-exhaustively presented in the first section of this chapter. The other sections will introduce the main characteristics of radio wave propagation and some well-known indoor propagation models.

2.1 Wireless technologies for indoor environments

2.1.1 Wireless Local Area Network

A Wireless Local Area Network (WLAN) interconnects devices through radio links within a maximum range around 100 m. The IEEE 802.11 standard [4], also known by the name of Wi-Fi (Wireless Fidelity), is the most common WLAN. It allows high-speed communications and has several versions operating in different frequency bands.

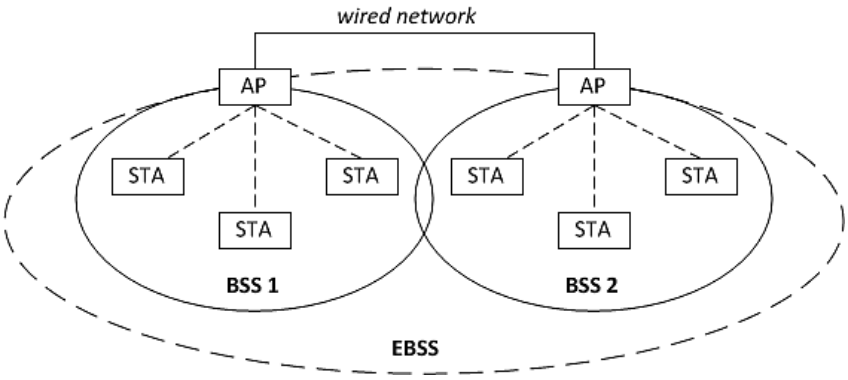

Figure 2.1. Basic architecture of an 802.11 network (infrastructure mode)

2.1.1.1 802.11n

Confirmed in 2009, this amendment [5], concerning networks operating at 2.4 and 5 GHz, was the first version to introduce Multiple Input Multiple Output (MIMO) transmission allowing data rates up to 600 Mbps (for 4 spatial streams).

2.1.1.2 802.11ac

Approved in 2013, this version [6] is an evolution of the 802.11n. It features more spatial streams (up to 8), new channel bandwidths (80 MHz and 160 MHz) and introduces the Multi-User MIMO (MU-MIMO) for downlink (DL) transmissions allowing the Access Point (AP) to communicate simultaneously with at most 4 stations. This standard allows, theoretically, up to 6 Gbps and is restricted to the 5 GHz band.

2.1.1.3 802.11ad

The IEEE 802.11ad standard [7] is not an evolution of the 802.11ac standard (it was ratified one year before, in 2012). This is the first ever 802.11 version to provide networking in the millimeter bands. This standard allows high speed directional communication at 60 GHz over a large channel bandwidth (2160 MHz). The achievable data rate is theoretically 4.6 Gbps for the Single Carrier Physical Layer (SC-PHY) and 6.8 Gbps for the Orthogonal Frequency-Division Multiplexing (OFDM) Physical Layer.

In Chapter 4, results of a measurement campaign performed in a typical home environment at 60 GHz using 802.11ad equipment which implement the SC-PHY are discussed.

2.1.1.4 802.11ax/802.11ay

In 2020[4], two versions are meant to receive final approval. The first one is the 802.11ax operating at both 2.4 and 5 GHz. It's the successor of the 802.11ac and is designed to provide a better traffic (up to 10 Gbps) and more efficient management. This standard features multi-user transmission in uplink (UL) as well as in DL thanks to MU-MIMO and Orthogonal Frequency Division Multiple Access (OFDMA).

The second one is the 802.11ay which enhanced the 802.11ad by adding MIMO (up to 4 streams) and combining channels bandwidths (up to 8640 MHz) in order to achieve a transmission rate around 44 Gbps per stream.

2.1.2 Wireless Personal Area Network

A Wireless Personal Area Network (WPAN) is a short-distance network for interconnecting devices over radio links. There exist different wireless technologies such as Bluetooth, Z-Wave or ZigBee.

2.1.2.1 Bluetooth

Bluetooth is a short-range wireless technology for data exchange between devices in a master-slave architecture (see Figure 2.2). The achievable data rate is 2 Mbps between 2.4 and 2.483 GHz. Its latest version, Bluetooth 5.1, introduced in 2019, provides low energy consumption options that enable this technology for Internet of Things (IoT).

2.1.2.2 Z-Wave

Z-Wave is a wireless technology used primarily for domotics. It is a mesh of IoT devices communicating with low-energy consumption (see Figure 2.3). The achievable data rate is 100 kbps in the 868 MHz band in Europe. Z-Wave systems can be controlled (or monitored) from computers, tablets or smartphones connected to Internet.

[4] http://www.ieee802.org/11/Reports/802.11_Timelines.htm

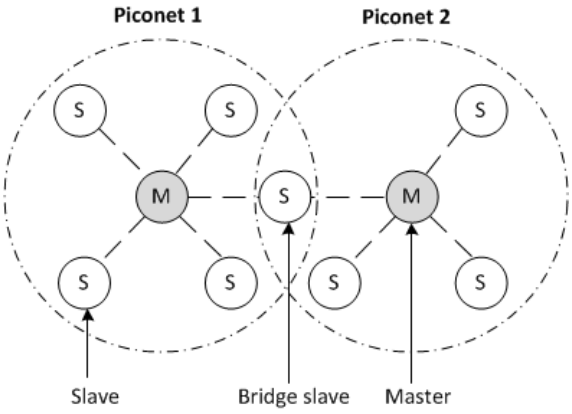

Figure 2.2. Architecture of a Bluetooth network

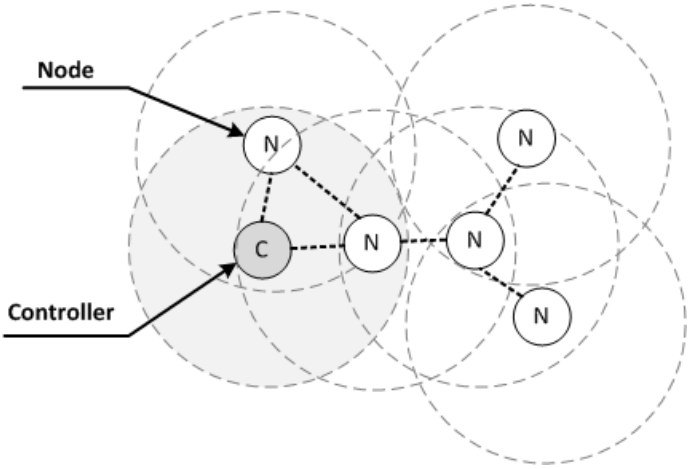

Figure 2.3. Architecture of a Z-Wave network

2.1.2.3 ZigBee

Based on IEEE 802.15.4, ZigBee is a wireless technology that enables low-power and low data rate communications between appliances (up to 250 kbps). It can be used for domotics, medical data collection, etc., and may operate in the 2.4 GHz band (worldwide) or in the 868 MHz band (only in Europe).

2.1.3 Cellular networks

A cellular network (or mobile network) is a radio network which consists of a set of base station (BS) covering large areas called macrocells and connected to a core network. For very crowded buildings (malls, train-stations, etc.) or facilities located at cell edges, macrocells may not be able to provide enough capacity to sustain the end-users demand. The small cells are then used to address this issue by extending radio coverage to indoor environments where the outdoor signal is poor or to improve the network capacity in places with dense phone usage.

There exist different types of small cells of various sizes: microcells (less than 2 km), picocells (up to 200 m) and femtocells (around 10 m). They are available for most cellular technologies such as GSM (2G), UMTS (3G) and LTE-Advanced (4G) and are a very important component of the future generation of cellular networks (5G) which is meant to provide numerous indoor services (Massive IoT).

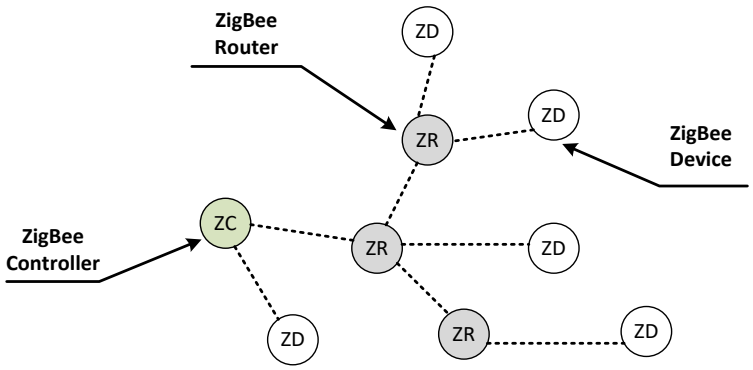

Figure 2.4. Architecture of a ZigBee network

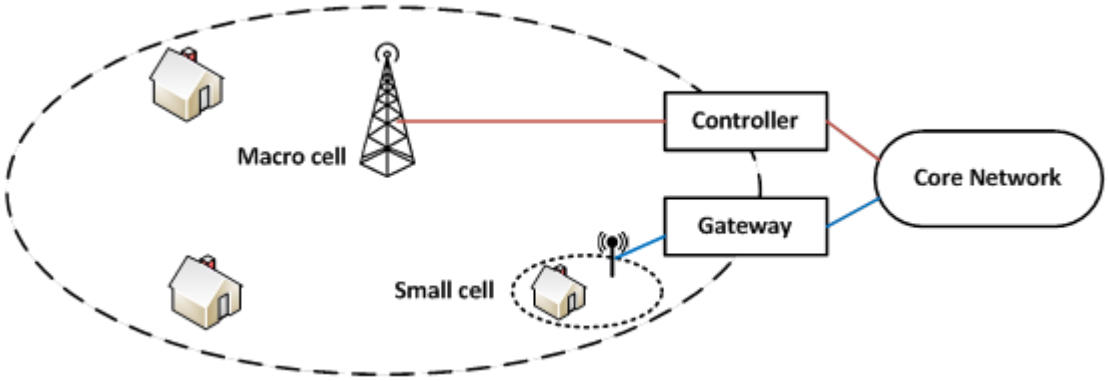

Figure 2.5. Basic cellular network architecture with both macro and small cells

2.2 Propagation channel characterization

For any of the above wireless technologies, a basic communication may be defined as follows: a transmitter (Tx) sends an encoded radio signal to a receiver (Rx) through a propagation channel. This mechanism is illustrated in Figure 2.6.

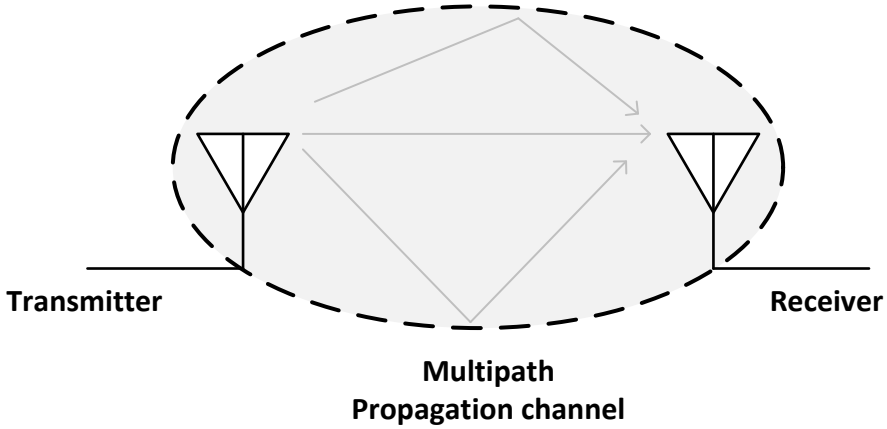

Figure 2.6. Basic wireless communication

The knowledge of the propagation channel is important for any wireless system because it has a great impact on the quality of the received signal.

Table 2.1. Example of coexisting wireless technologies in indoor environments

Technology	Type	Frequency band (GHz)	Peak Throughput
Bluetooth	WPAN	2.400 – 2.483	2 Mbps
Z-Wave		0.868 – 0.869	100 kbps
ZigBee		0.868 – 0.869, 2.405 – 2.480	250 kbps
802.11n	WLAN	2.412 – 2.472 5.150 – 5.835	600 Mbps
802.11ac		5.150 – 5.835	6 Gbps
802.11ad		57.24 – 65.88	6.8 Gbps
2G (GSM to EDGE)	Cellular Network	0.880 – 0.960 1.710 – 1.879	384 kbps
3G (UTMS to LTE)		0.880 – 0.960 1.920 – 2.170	150 Mbps
4G (LTE-Advanced)		0.791 – 0.862 1.710 – 1.880 1.920 – 2.170 2.500 – 2.690	1 Gbps
5G (N/C)		0.694 – 0.790 3.400 – 3.800 24.25 – 27.50	10 Gbps

In practice, this difficult task is achieved by the means of two types of propagation models. Firstly, we have propagation models that estimate the mean signal strength for a given distance between the transmitter and the receiver. Such models are called *large-scale* propagation models. They will be discussed in Section 2.3.

This section will be focused on the second type of models called *small-scale* or *fading* models. They are used to characterize the variations of the received signal strength over small distances (order of wavelengths) or short duration (order of seconds) [8]. These fluctuations are due to the multipath propagation which is the direct consequence of different propagation mechanisms.

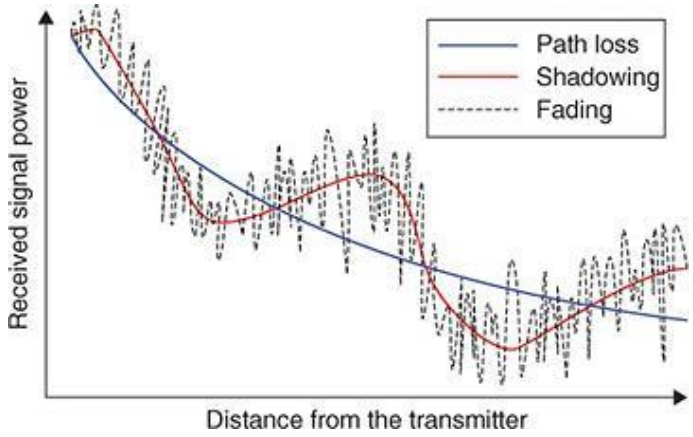

Figure 2.7. Large-scale (red, blue) and small-scale (black) fading [9]

2.2.1 Basic propagation mechanisms

There are four basic propagation mechanisms: reflection, transmission, diffraction and scattering (see Figure 2.8).

2.2.1.1 Reflection and transmission

When a propagating electromagnetic (EM) wave collides with an object or flat surfaces having a dimension far greater than the wavelength, a part of the energy is *reflected* back (specular reflection) while the other one is *transmitted* through the object (transmission). In indoor environments, this phenomenon is caused by the presence of obstacles such as floors, walls or furniture.

Moreover, depending on the obstacle electrical properties, the reflected and transmitted energy may be strongly attenuated (see Section 2.3.2.3).

2.2.1.2 Diffraction

Diffraction happens when a propagating EM wave meets the edge of an obstacle having a large dimension when compared to the wavelength. From the collision, secondary EM waves are created with some of them propagating in the shadowed region behind the obstacle.

In indoor environments, the diffraction phenomenon happens for example around wall-edges as investigated later in this document (see Chapter 4).

2.2.1.3 Scattering

Scattering occurs when an EM wave propagates through mediums which consist of objects of small dimensions (order of the wavelength), and where the number of obstacles per unit of volume is large. In practice, this phenomenon is caused by rough surfaces (diffuse reflection) or small objects.

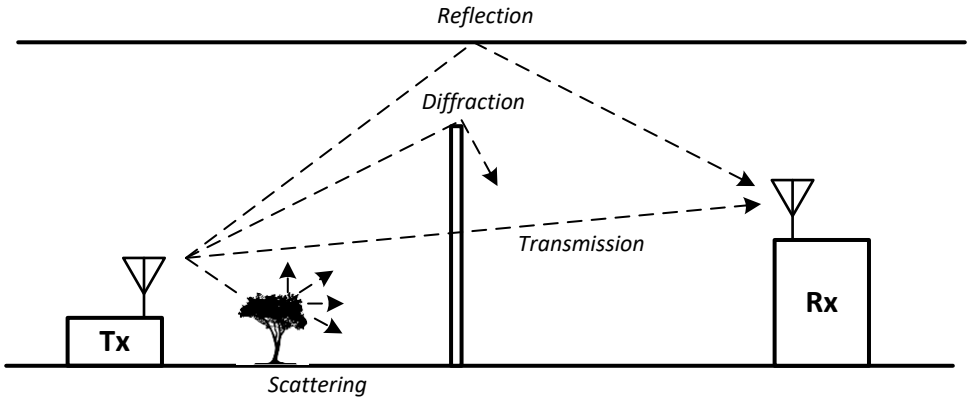

Figure 2.8. Basic propagation mechanisms

2.2.2 Factors inducing fading

As aforementioned, fading describes the variation of the attenuation of a received signal over a short distance or period of time. It may sometimes be so destructive that large-scale path loss effects may be overlooked. There exist different factors inducing fading.

2.2.2.1 The multipath propagation

The multipath in a radio channel is the direct consequence of basic propagation mechanisms such as reflection and scattering. The receiver antenna collects from diverse directions different versions of the transmitted signal having randomly distributed delays, angles of arrival, amplitudes and phases (see Figure 2.8). The combination of these multipath components leads to constructive or destructive effects. The multipath propagation is the main source of intersymbol interference (ISI) because it induces time dispersion at the receiver which may not be negligible depending on the transmitted symbols period.

As shown in Figure 2.6, the Tx and Rx antennas have been included in the propagation channel because they have an influence on how the channel is perceived. For instance the number of multipath components collected by an Rx antenna depends on its aperture.

2.2.2.2 The Doppler Effect

The Doppler Effect is observed when there is mobility in the propagation channel. This mobility happens when there is a relative motion between the transmitter and the receiver, or when surrounding objects in the channel are in motion. As a result, each propagation path undergoes a shift in frequency.

Let consider a receiver in motion at a constant velocity v; this shift in frequency, called Doppler shift, is expressed as follows

$$f_d = f_0 \frac{v}{c} \cos(\alpha), \tag{2.1}$$

where:

- f_d is the Doppler shift,
- c is the speed of light,
- f_0 is the transmitted signal frequency,
- α is the direction of arrival of the propagation path.

This means that the Doppler shift of a given propagation path lies within $[-f_d^m, f_d^m]$ where f_d^m is the maximum Doppler shift corresponding to the corner case $|\cos(\alpha)| = 1$ (see Figure 2.9).

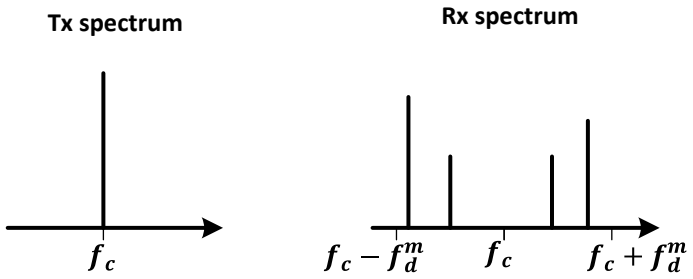

Figure 2.9. Doppler Effect

During this thesis, the channel measurements were performed in static environments. As a consequence, Doppler effects did not happen. In such cases, fading effects are mostly related to the spatial positions of the receiver.

2.2.3 Multipath propagation channel characterization

2.2.3.1 The channel impulse response

Because of phenomena such as multipath effects, the propagation channel has a selective nature. For this reason, it can be modeled as a linear filter having a time-varying impulse response. At a given time *t*, the received signal *y*(*t*) for a single-input single-output transmission can be expressed as:

$$y(t) = x(t) * h(t,\tau) + n(t) = \int_{-\infty}^{+\infty} x(t-\tau)h(t,\tau)\,d\tau + n(t) \tag{2.2}$$

where $x(t)$ is the transmitted signal, $h(t,\tau)$ the channel impulse response, $n(t)$ is the additive noise, and $*$ represents the convolution operator.

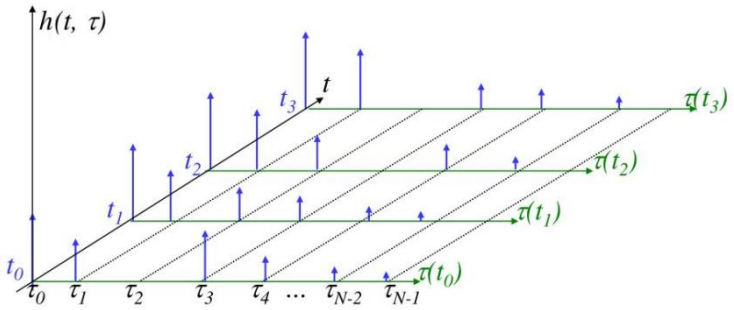

Figure 2.10. Time varying baseband impulse response for a multipath radio channel

The impulse response is a valuable characterization of the channel because it helps predicting the transmission performance for a particular channel condition. It may be related to small-scale variations of the channel via the following baseband expression:

$$h(t,\tau) = \sum_{i=0}^{M(t)-1} a_i(t,\tau)\exp[j\theta_i(t,\tau)]\delta(\tau-\tau_i(t)) \tag{2.3}$$

where $M(t)$ is the number of propagation paths at time *t*, $a_i(t,\tau)$, $\tau_i(t)$ and $\theta_i(t,\tau)$ are respectively the real amplitude, excess delay and phase shift of the *i*-th propagation path at time *t* (see Figure 2.10).

Assuming that the channel impulse response is time invariant (or wide-sense stationary) over a short period of time or distance, Eq.(2.3) can be simplified as follows:

$$h(\tau) = \sum_{i=0}^{M-1} a_i\exp[j\theta_i]\delta(\tau-\tau_i) \tag{2.4}$$

Finally, the representation of the propagation channel is not limited to the time-delay domain. It can also be characterized in the frequency domain using the channel frequency response $H(f,t)$ which is mathematically expressed as the Fourier transform of the channel impulse response:

$$H(f,t) = \int_{-\infty}^{+\infty} h(t,\tau)\exp[-j2\pi f\tau]d\tau \tag{2.5}$$

where f is the frequency, t the time and τ the excess delay.

2.2.3.2 Parameters of multipath channels

In order to characterize a multipath propagation channel, other parameters are derived from the impulse response.

a) The Power Delay Profile

For multipath channels, the Power Delay Profile (PDP) gives the distribution of the received signal power as a function of propagation delays [10]. The PDP is obtained by computing the time average or the spatial average of the channel impulse response over a local area:

$$PDP(\tau) = \frac{1}{N}\sum_{i=1}^{N}|h(t_i,\tau)|^2 \tag{2.6}$$

where N is the number of samples of the channel impulse response and τ is the propagation delay.

b) The excess delay

The excess delay is defined as the relative delay measured with respect to the first arrival delay (τ_0) as illustrated in Figure 2.11.

c) The mean excess delay

The mean excess delay represents the statistical mean delay of a propagation path in a multipath propagation channel. It is computed as the first moment of the PDP:

$$\bar{\tau} = \frac{\int_0^\infty \tau PDP(\tau)d\tau}{\int_0^\infty PDP(\tau)d\tau} \tag{2.7}$$

d) The RMS delay spread

The Root Mean Square (RMS) delay spread is the square root of the second central moment of the PDP [11]:

$$\tau_{RMS} = \sqrt{\frac{\int_0^\infty (\tau - \bar{\tau})^2 PDP(\tau)d\tau}{\int_0^\infty PDP(\tau)d\tau}} = \sqrt{\overline{\tau^2} - (\bar{\tau})^2} \tag{2.8}$$

As shown above, the RMS delay spread is the standard deviation of the excess delay. This parameter is important because it has a great impact on intersymbol interference (ISI). If the transmission duration of a symbol over a multipath propagation channel is large when compared to the RMS delay spread (typically at least 10 times greater), the channel is supposed to be ISI-free. The order of magnitude of the RMS delay spread is microseconds in outdoor conditions and nanoseconds in indoor environments [8].

e) The maximum excess delay (X dB)

The maximum excess delay (X dB) is the excess delay corresponding to the last multipath component having a power at most X dB lower than the strongest propagation path. It's defined as $\tau_X - \tau_0$, where τ_0 is the first arrival delay and τ_X is the maximum delay at which a multipath component is within X dB of the strongest propagation path.

When processing the PDP, the choice of the noise threshold has an impact on the values of $\bar{\tau}$ and τ_{RMS}. The noise threshold is used to distinguish multipath components from thermal noise. If it's too low, then noise will be processed as multipath resulting in an artificial increase of $\bar{\tau}$ and τ_{RMS} [8].

The PDP and the time dispersion parameters are represented in Figure 2.11.

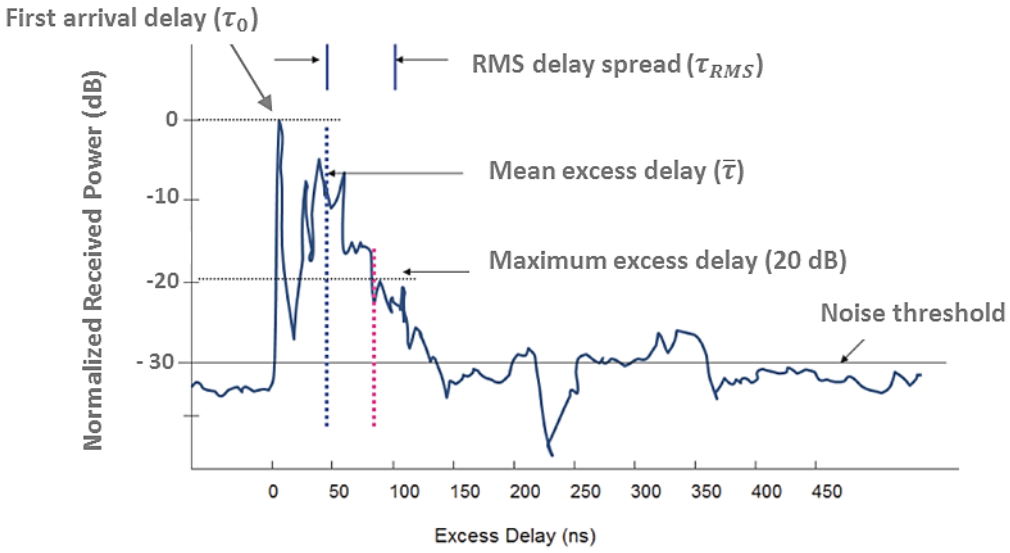

Figure 2.11. PDP and time dispersion parameters of a multipath channel [12]

f) The coherence bandwidth

The coherence bandwidth, B_c, is a frequency characterization parameter of the channel. It corresponds to the frequency range over which the channel alters transmitted frequency components with approximately equal gain and linear phase. The channel is said to be "flat" in such conditions.

Mathematically, the coherence bandwidth is defined as the frequency range over which the autocorrelation of the Fourier transform of the PDP is greater than a threshold a. It is approximated to be inversely proportional to the RMS delay spread as follows [13]:

$$B_c \approx \frac{1}{50\,\tau_{RMS}}, \qquad \text{if } \alpha = 90\% \tag{2.9}$$

$$B_c \approx \frac{1}{5\,\tau_{RMS}}, \qquad \text{if } \alpha = 50\% \tag{2.10}$$

Delay spread and coherence bandwidth are important parameters that characterize the channel over a small-scale area. However, other parameters are needed to typify the time varying nature of the channel induced by the presence of moving entities. Doppler spread and coherence time are used to describe this time varying nature over local areas.

g) The Doppler spread

The Doppler spread, B_D, is the frequency range over which the multipath components are spread due to Doppler effect. Its value equals to two times the maximum Doppler shift. For instance, in Figure 2.9, $B_D = 2f_d^m$.

When the transmitted symbol bandwidth, B_{sym}, is far greater than the Doppler spread, the Doppler effect is negligible at the receiver. This is called *slow* fading.

h) The coherence time

The coherence time, T_c, is the duration over which the channel impulse response is considered to be invariant. If the transmitted symbol duration, T_{sym}, is greater than the coherence time of the channel, then the received signal will be distorted due to the time varying nature of the channel. The coherence time is approximated to be inversely proportional to the Doppler spread, B_D, as follows:

$$T_c \approx \frac{2}{\alpha B_D} \tag{2.11}$$

where α is a coefficient depending on the time correlation function [8].

2.2.4 Classification of multipath channels

Two transmitted signals at a given time interval may not be altered by the channel in the same way. Indeed, the fading experienced by a transmitting signal depends not only on its own characteristics (symbol duration, bandwidth), but on the channel parameters presented in section 2.2.3.1 as well. As shown in Table 2.2, a transmitted signal may suffer from four different types of fading induced by two factors independent of one another: multipath which generates delay dispersion and Doppler spread which causes frequency dispersion.

Table 2.2. Types of small-scale fading

Inducing factor	Type of fading	Time domain	Frequency domain
Multipath delay spread	Flat Fading	$T_{sym} \gg \tau_{RMS}$	$B_{sym} \ll B_c$
	Frequency Selective Fading	T_{sym} not sufficiently greater than τ_{RMS}	$B_{sym} > B_c$
Doppler spread	Fast Fading	$T_{sym} > T_c$	B_{sym} not sufficiently greater than B_D
	Slow Fading	$T_{sym} < T_c$	$B_{sym} \gg B_D$

2.2.4.1 Flat fading

In flat fading, the channel conserves the spectral characteristics of the transmitted signal at the receiver. However the strength of the received signal changes over time due to the effects of the multipath propagation [8]. Flat fading channels are also called narrowband channels because the transmitted signal bandwidth is much narrower than the channel bandwidth ($B_{sym} \ll B_c$).

2.2.4.2 Frequency selective fading

In frequency selective fading, some frequency components are much more attenuated than others resulting in a distorted received signal. Such channels are also referred to as wideband channels because the transmitted signal bandwidth is wider than the channel coherence bandwidth. The delay dispersion in this type of channel induces ISI and it is commonly admitted that a channel is frequency selective if the transmitted symbol duration is not sufficiently greater than the RMS delay spread.

2.2.4.3 Fast fading

Fast fading occurs when the channel impulse response varies within the transmitted symbol duration ($T_{sym} > T_c$). The received signal is then distorted due to the frequency dispersion induced by the Doppler spreading. In practice, fast fading happens for very low data rates.

2.2.4.4 Slow fading

During slow fading, the channel is supposed to be static when a symbol is transmitted ($T_{sym} < T_c$). As a consequence, the Doppler spread has little effect on the frequency spectrum of the received signal.

Since multipath delay spread and Doppler spread are separate mechanisms, a flat fading channel may be a fast or slow fading channel as well. Same goes for a frequency selective fading channel.

2.3 Indoor propagation models

Large-scale propagation models are used to estimate the mean signal level at the receiver side for a given separation distance with the transmitter. They are useful in predicting the coverage area of a transmitter and are the basis of all radio planning tools to perform design and further network optimization like frequency assignment, dimensioning, site selection, etc.

2.3.1 Path loss models

For a radio transmission, the path loss is defined as the difference (in dB) between the effective transmitted and received powers. Path loss is estimated with large-scale models (path loss models) which express the attenuation for a given type of environment and frequency range.

Like the definition of propagation channel, path loss models may or may not include Tx and Rx antennas gain. There exist 3 types of path loss models, mainly differentiated by how they are established:

2.3.1.1 Empirical path loss models

Empirical path loss models (also called statistical models) are based on actual propagation measurements. They have the advantage to be simple to establish (when compared to deterministic models) but are not very accurate if used outside of the environment where they have been established[5]. Log-distance models are an example of empirical path loss models (see Section 2.3.2.1).

2.3.1.2 Deterministic path loss models

Deterministic models estimate analytically the path loss based on the theory around propagation mechanisms. They are expected to be more accurate than empirical path loss models but require a very detailed description of the environment and have high computational cost. This analytical approach may be carried out by solving Maxwell's

[5] Their validity in a new environment has to be established by additional measurements in this new environment.

equations or using ray tracing. During this thesis, these models have been overlooked because they cannot be used on devices having limited computing capabilities such as smartphones (see Chapter 1).

2.3.1.3 Semi-deterministic path loss models

Semi-deterministic models are basically empirical models taking into account some deterministic aspects such as the direct propagation path between the transmitter and the receiver. The Motley-Keenan model is an example of semi-deterministic path loss model (see Section 2.3.2.5).

During this thesis, several path loss models have been established following measurement campaigns conducted in a typical home environment (see Chapter 3). They are based on classical existing approaches for modeling path loss in indoor environments.

2.3.2 Path loss models for indoor environments

Outdoor and indoor propagations are governed by similar mechanisms such as reflection, scattering or diffraction. However due to the difference in the propagation conditions, their radio channels differ greatly. As an example, in indoor environments, the presence of walls, floors, furniture or people may have a strong impact on the radio waves propagation. For this reason, specific path loss models are required for indoor scenarios.

The following indoor path loss models are only applicable when the receiver is located in the far-field of the transmitting antenna. The far-field is defined as the region where, d, the separation distance between the transmitter and the receiver is greater than d_f, the far-field distance, given by:

$$d_f = \frac{2D^2}{\lambda} \tag{2.12}$$

where *D* is the largest dimension of the transmitting antenna and λ the wavelength.

2.3.2.1 Log-distance path loss model

Log-distance path loss models represent the path loss as a logarithmically increasing linear function with distance:

$$PL(d)\ [\text{dB}] = PL_0 + 10n\log_{10}\left(\frac{d}{d_0}\right) + X_\sigma \tag{2.13}$$

where:

- PL_0 is the average path loss measured at a reference distance d_0.
- d_0 is the reference distance chosen such that $d \geq d_0 \geq d_f$. In indoor environments, d_0 is often equal to 1 m [8].
- *n* is the path loss exponent. Its value depends on the measurement environment and describes the increase rate of the path loss with distance. In free space, *n* is equal to 2.
- X_σ is a zero-mean Gaussian random variable with a standard deviation σ (in dB) modeling the shadowing effects. The shadowing is caused by the presence of obstacles between the transmitter and the receiver resulting in a fluctuation of the received power (see Figure 2.7).

A Log-distance path loss model for an arbitrary frequency range and indoor environment is fully characterized by 2 parameters: n and σ. In practice, these parameters can be computed by applying linear regressions to a set of measured data (see Chapter 3).

In free space propagation conditions (clear and unobstructed line-of-sight (LOS) between the transmitter and the receiver), Eq. (2.13) becomes:

$$PL(d,f)\ [\text{dB}] = 20\log_{10}\left(\frac{4\pi f d_0}{c}\right) + 20\log_{10}\left(\frac{d}{d_0}\right) \qquad (2.14)$$

where c is the speed of light and f the transmitted signal frequency.

Since only satellite and microwave line-of-sight transmissions experience free space propagation, the free space model is not applicable in indoor environments. However, it remains useful and can be used to compute the value of PL_0 in Eq. (2.13).

Log-distance models are relatively simple to establish and can be used for both indoor and outdoor large-scale propagation modeling. As a consequence, they do not explicitly account for indoor environment specificities such as the presence of walls or floors made of various construction materials. This issue is addressed by other models derived from the Log-distance model.

2.3.2.2 ITU-R model (Rec. P.1238-4)

The model recommended by ITU-R P.1238-4 [14] is a site-general path loss model for indoor transmissions which accounts for attenuators such as walls and floors. The average path loss (L_{total}) is given by:

$$L_{total}\ [dB] = 20\log_{10} f + N\log_{10} d + L_f(n)\ [\text{dB}] - 28 + X_\sigma \qquad (2.15)$$

where :

- N is the distance power loss coefficient,
- f is the frequency expressed in MHz,
- d is the separation distance between the transmitter and receiver (in meter),
- L_f is the floor penetration loss factor, and
- n is the number of floors between the transmitter and the receiver.

The parameters value of this model is given in Table 2.3 for 3 frequency bands and 3 types of indoor environment.

Table 2.3. ITU-R P.1238-4 model parameters value [14]

	N			L_f[dB]			σ[dB]		
	900 MHz	**1.8 – 2GHz**	**5.2 GHz**	**900 MHz**	**1.8 - 2GHz**	**5.2 GHz**	**900 MHz**	**1.8 – 2GHz**	**5.2 GHz**
Residential	-	28	-	-	4n	-	-	8	-
Office	33	30	31	9 (1 floor)	15 + 4(n-1)	16 (1 floor)	-	10	12
Commercial	20	22	-	-	6 + 3(n-1)	-	-	10	-

This multi-frequency model is theoretically valid from 900 MHz to 100 GHz but remains too site-generic. It's also lacking in reference values for indoor residential environments which are the main target of this thesis.

2.3.2.3 Linear attenuation model (LAM)

The linear attenuation model (LAM) [15] represents the indoor path loss as the free space loss added with a loss factor increasing exponentially with distance. The path loss is given by:

$$PL(d)[\text{dB}] = PL_0 + 20\log_{10}\left(\frac{d}{d_0}\right) + \alpha d + X_\sigma \qquad (2.16)$$

where α is an attenuation constant expressed in dB/m.

Table 2.4. Model parameters in building OFC/NCO [15]

Frequency	**α [dB/m]**	**σ [dB]**
850 MHz	0.62	8.4
1.7 GHz	0.57	8.5
4.0 GHz	0.47	8.6

2.3.2.4 Attenuation factor model

This model [16] accounts for additional attenuation factors in multi-floor environments when transmitter and receiver are not on the same floor and estimates the path loss as follows:

$$PL(d)[\text{dB}] = PL_0 + 10n_{SF}\log_{10}\left(\frac{d}{d_0}\right) + FAF\ [dB] + X_\sigma \qquad (2.17)$$

where :

- n_{SF} is the path loss exponent when transmitter and receiver are on the same floor,
- FAF is the floor attenuation factor which depends on the number of floors crossed by the direct line between the transmitter and the receiver.

These parameters are estimated from measurements data (see Table 2.5).

Table 2.5. Floor Attenuation Factor for up to four floors in Building 1 [16]

Building 1	**n_{SF}**	**FAF [dB]**	**σ [dB]**
Same Floor	3.27	-	11.2
Through one Floor	-	12.9	7.0
Through Two Floors	-	18.7	2.8
Through Three Floors	-	24.4	1.7
Through Four Floors	-	27.0	1.5

The LAM model can be extended by using the floor attenuation factor. The combination of Eq.(2.17) and (2.18) results in:

$$PL(d)[\text{dB}] = PL_0 + 20\log_{10}\left(\frac{d}{d_0}\right) + \alpha d + FAF\ [dB] + X_\sigma \qquad (2.18)$$

2.3.2.5 Motley-Keenan model (MK)

The Motley-Keenan model [1] is similar to the LAM model [15] except that the exponentially-increasing loss factor is replaced by the attenuation induced by the number of walls and floors crossed by the direct path between the transmitter and the receiver. The path loss is given by:

$$PL(d)[\text{dB}] = PL_0 + 20\log_{10}\left(\frac{d}{d_0}\right) + \sum k_{wi}L_{wi} + \sum k_{fi}L_{fi} \qquad (2.19)$$

where:

- k_{wi} is the number of walls of type *i*,
- L_{wi} is the penetration loss (in dB) of the walls of type *i*,
- k_{fj} is the number of floors of type *j*,
- L_{fj} is the penetration loss (in dB) of the floors of type *j*.

This model has received a significant attention because of its simplicity (reflection and obstacles thickness are overlooked). However, it requires determining the transmission losses of different building materials at the frequency band of interest. In the literature, some approximated values may be found for typical penetration losses of indoor building materials (see Table 2.6).

Table 2.6. Transmission loss of 3 building materials (1-2 GHz) [17]

Material	Loss [dB]	Typical thickness
Glass	1.4	2 x 0.3 cm
Wood	1.5	5 cm
Plasterboard	2.5	2 x 1.3 cm
Concrete	6	25 cm

An extension of the Motley-Keenan model is proposed in [18] to account for the thickness of walls as follows:

$$PL(d)[\text{dB}] = PL_0 + 10n\log_{10}\left(\frac{d}{d_0}\right) + \sum k_i L_{0i} 2^{\log_3\left(\frac{e_i}{e_{0i}}\right)} \qquad (2.20)$$

where:

- e_i is the thickness of the type *i* wall,
- e_{0i} is the thickness of the type *i* reference wall,
- L_{0i} is the penetration of loss of type *i* reference wall.

Another model similar to the Motley-Keenan model is presented in [19]. Instead of considering only the direct path like the MK model does, this model looks upon the dominant propagation path which results in:

$$PL(d)[\text{dB}] = PL_0 + 10n\log_{10}\left(\frac{d}{d_0}\right) + \sum_{i=1}^{N_T} L_i + \frac{1}{\alpha_L}\sum_{j=1}^{N_I} \alpha_j \qquad (2.21)$$

where :

- N_T is the number of wall crossed by the dominant propagation path,
- L_i is the penetration loss of the i^{th} wall crossed by the dominant path,
- N_I is the number of change of direction of the dominant path,
- α_j is the angle variation after j^{th} change of direction,
- α_L is a normalization factor.

During this thesis, two MK-based models have been established and presented in Chapter 3. The penetration loss parameters were determined using a software planning tool developed at Orange Labs Belfort.

2.3.2.6 COST 231 Multi-Wall model (MWM)

In the Motley-Keenan model, the loss induced by walls/floors is proportional to the number of walls penetrated by the direct path between the transmitter and the receiver. In practice, it has been observed that this is not the case: the total floor loss is not a linear function of the number of penetrated floors. The COST 231 Multi-wall model [17] account for this as follows:

$$PL(d)[\text{dB}] = PL_0 + 20\log_{10}\left(\frac{d}{d_0}\right) + L_c + \sum k_{wi}L_{wi} + k_f^{\left[\frac{k_f+2}{k_f+1}-b\right]}L_f \qquad (2.22)$$

where:

- L_c is a constant loss resulting when wall losses are determined with linear multiple regression from measurements results,
- k_f is the number of penetrated floors,
- L_f is the loss between adjacent floors,
- b is an empirical parameter.

This model recommends keeping low the number of different type of walls for practical reasons. A division into two types of walls has been proposed in Table 2.7.

Table 2.7. Wall types for the COST 231 MWM model [17]

Wall type	Description
Light wall (L_{w_1})	A wall that is not bearing load: e.g. plasterboard, particle board, thin wall (<10 cm), light concrete wall.
Heavy wall (L_{w_2})	A load-bearing wall, thick wall (>10 cm) made of concrete or brick.

This recommendation has been taken into consideration when modeling the *generalized* multi-wall model introduced later in this document (see Chapter 3).

The COST 259 MWM model [9] is an extension of the COST 231 model which accounts for the nonlinearity of the total penetration loss with the number of walls. This model is valid when the transmitter and the receiver are on the same floor and the path loss is given by:

$$PL(d)[\text{dB}] = PL_0 + 20\log_{10}\left(\frac{d}{d_0}\right) + \sum k_{wi}^{\left[\frac{k_{wi}+1.5}{k_{wi}+1} - b_{w_i}\right]} L_{wi} \quad (2.23)$$

where:

- k_{wi} is the number of walls of type *i*,
- L_{wi} is the penetration loss (in dB) of the walls of type *i*,
- b_{wi} is an empirical parameter given by

$$b_{wi} = -0.064 + 0.0705\, L_{wi} - 0.0018\, L_{wi}^2 \quad (2.24)$$

The indoor propagation models discussed in this section gave a parameterized approach of the path loss modeling. The value of the parameters depends generally on the frequency and the specificities of the measurement environment (residential, office, mall, etc.). The parameters value may obtained by referring to the literature (see Table 2.3 or Table 2.6) or be computed from measurement data.

The latter approach requires channel measurements in the radio environment of interest. The following section will take a look at existing channel sounding techniques.

2.4 Channel sounding techniques

Channel sounding is a method used to assess all the properties of a multipath propagation channel (see Section 2.2.3.2). The wideband channel sounding[6] techniques can be divided into two categories: time-domain sounding and frequency-domain sounding.

2.4.1 Time-domain channel sounding

Time-domain channel sounders determine the channel impulse response by transmitting series of pulses as follows [20]:

$$s(t) = \sum_{i=0}^{N-1} a_i p(t - iT_{Rep}) \quad (2.25)$$

where:

- $s(t)$ is the transmitted signal,
- N is the number of pulses,
- a_i is the amplitude of the i^{th} pulse,
- $p(t)$ is the pulse which is repeated each T_{Rep}.

Based on $p(t)$ waveform, two types of time-domain sounding techniques can be identified.

2.4.1.1 Direct pulse system

This technique consists in transmitting periodically a pulse of width T_w. Before being displayed, the received signal is processed by a bandpass filter ($Bw = 2/T_w$), amplified and detected by an envelope detector. This process is illustrated in Figure 2.12.

This technique is easy to implement and allows determining rapidly the power delay profile when the oscilloscope is set on average mode [8]. However, its main drawback is that

[6] MIMO channel sounding is not discussed in this document.

it's prone to interference and noise due to the wide bandpass filter needed for multipath resolution.

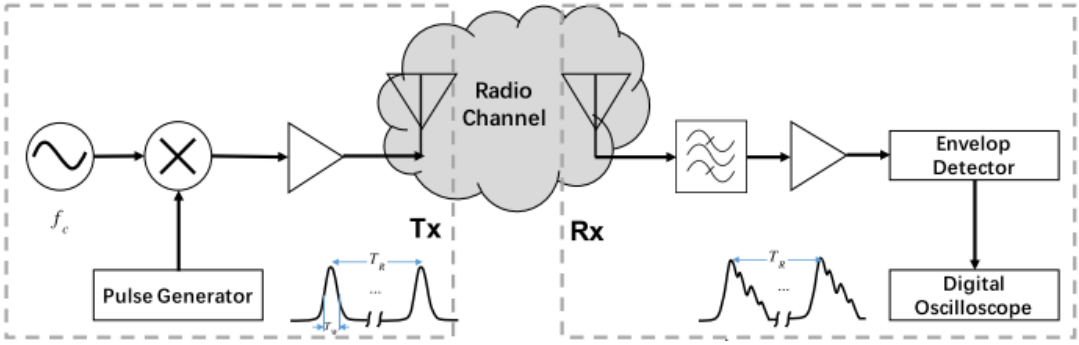

Figure 2.12. Direct pulse channel measurement system [20]

2.4.1.2 Spread spectrum sliding correlator channel sounding

This correlative channel sounding technique achieves pulse compression by mixing the transmitted signal with a pseudo-noise (PN) sequence. This results in a spreading of the transmitted signal over a large bandwidth. The spread spectrum signal is then received and *despread* using a PN sequence identical to the one used at the transmitter (see Figure 2.13).

Aside the lower power consumption inherent to spread spectrum systems, the main advantage of this system is its capacity to improve its dynamic range [21]. However, the measurements are not made in real time. This means that the channel measurements processed at an instant *t* by the system corresponds to a previous state of the channel (*t* – *dt*), and depending on the settings, this delay (*dt*) may be too long when compared to the channel coherence time. This technique remains faster than the one presented in the next section.

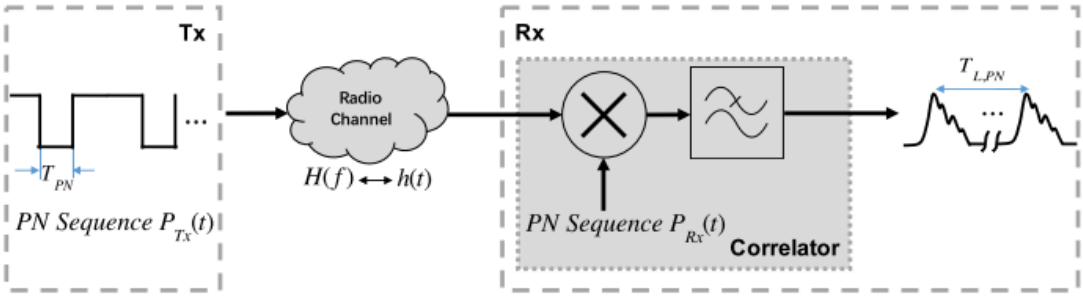

Figure 2.13. A correlative channel sounder [20]

2.4.2 Frequency-domain channel sounding

As mentioned in Section 2.2.3.1, a multipath propagation channel can be characterized in the frequency domain by its channel frequency response which has a dual relationship with the channel impulse response (Fourier transform). The frequency-domain channel sounding takes advantage of this connection.

First, this technique determines the channel frequency response by using an S-parameter test set and a Vector Network Analyzer (VNA) controlling a frequency sweeper which scans a chosen frequency range with a specified frequency step. At each frequency step, the VNA determines the channel frequency response (S_{21} parameter) by comparing the signals level at port 1 (transmitted signal which is known) and port 2 (received signal

distorted by the channel) of the S-parameter test set. The obtained frequency response is then converted back to the time domain by applying an inverse discrete Fourier transform. As result, a band-limited version of the impulse response is obtained. This process is summarized in Figure 2.14.

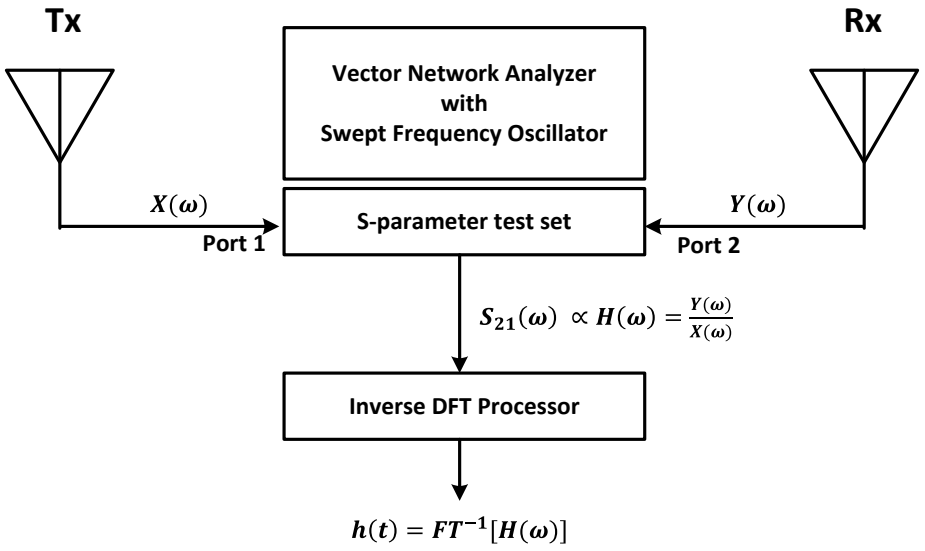

Figure 2.14. Frequency-domain channel sounding technique [8]

This system provides useful amplitude and phase information in the time domain. However, the measurements are not performed in real-time and this technique is slower than the previous one because of the sweep time duration. Also, this type of channel sounding is mostly used for close-range measurements because a wired synchronization is required between the transmitter and the receiver. Because of this constraint this technique is mostly practical for indoor measurements.

The measurement campaigns described in the next chapter are an example of successful use of this procedure in an indoor environment.

2.5 Chapter summary

Nowadays, there exist a lot of wireless technologies available in indoor environments. Even though they have different applications, they share in common the fact that they exchange information through a propagation channel varying over time. The knowledge of the propagation channel is a critical task which is undertaken via two types of propagation models.

The first ones are called *small-scale* or *fading* models. They are used to characterize the variations of the received signal strength over a short distance or period of time. Here, the propagation channel is modeled as a linear filter having a time varying channel impulse response. From this impulse response are derived several parameters which are useful in predicting the type of distortion a transmitted signal will experience over a propagation channel.

The second ones are called *large-scale* propagation models. They are used to estimate the mean signal level at the receiver side for a given distance with the transmitter. A path loss model is a *large-scale* propagation model which expresses the attenuation of the transmitted signal as a positive value. There exist a lot of indoor path loss models and most of them

account for the specificities of indoor environments by adding loss factors to represent the attenuation induced by walls and/or floors. These models are generally parameterized and require to be fitted to a given environment by performing channel sounding measurements.

There exist different channel sounding techniques. One of them is the frequency-domain channel sounding which uses a Vector Network Analyzer (VNA) to determine the channel frequency response. This frequency response is then related to the channel impulse response by applying an inverse discrete Fourier transform. This technique has been used to establish the path loss models presented in the next chapter.

Chapter 3

Path loss characterization in indoor home environments from 800 MHz to 60 GHz

The cornerstone of any radio design software is its ability to accurately predict the coverage area, in a specified environment, of a given transmitter at an arbitrary location. For such prediction task, path loss models can be used as reference. However, as explained in Chapter 2 there exist different categories and types of indoor path loss models, each of them having its own singularities (strength and drawback).

The choice of a propagation model is most of the time influenced by its intrinsic properties combined to extern and practical constraints. In the context of this thesis, the constraint is to provide a *simplified* path loss model for *multi-room residential environments*, relatively *accurate* and that can be used by radio design software on devices having potentially *limited computing* capabilities such as smartphones.

In this chapter, two types of indoor path loss models have been selected: Log-distance path loss models and Motley-Keenan path loss models (see Chapter 2). Due to different antennas and transmission characteristics, the calibration of these models has been carried out separately below 6 GHz and at 60 GHz.

3.1 Path loss modeling below 6 GHz

It's relevant to mention that, by referring to literature, it's possible to find different path loss models which, when put together, allow covering the 0.8-6 GHz band. For instance, [22] and [23] introduce log-distance path loss models that have been calibrated at 2.4 and 5 GHz for residential environments in LOS (Line-Of-Sight) and NLOS (Non-Line-Of-Sight). Other models such as [14] cover a wider frequency range below 6 GHz but are not very accurate for residential environments, etc. The main problem with such approach is the coherence of the results between measurements that have been carried out at different places with different antennas characteristics.

To address this issue, the path loss models presented in this section have been obtained by performing measurements from 800 MHz to 6 GHz with the same wideband antennas in the residential environment which is now described.

3.1.1 Measurement environment

The measurement campaigns described in this chapter have been performed in a multi-room residential environment which is a typical apartment fully provided with furniture such

as wooden tables, closets, chairs, sofa and domestic equipment. Some pictures of this home environment are available in Appendix A.

This residence, having a gray background in Figure 3.1, has a dimension of 10.43 x 11.7 x 2.6 m^3 and consists of a suite of rooms separated by different kinds of walls of various thicknesses (from 7 to 56 cm). Nine different kinds of walls have been identified and categorized into two groups: *dividing walls* (represented in red) having a thickness smaller than 8 cm and *load-bearing walls* (in blue) having a thickness greater than 10 cm. A detailed description is given in Table 3.1.

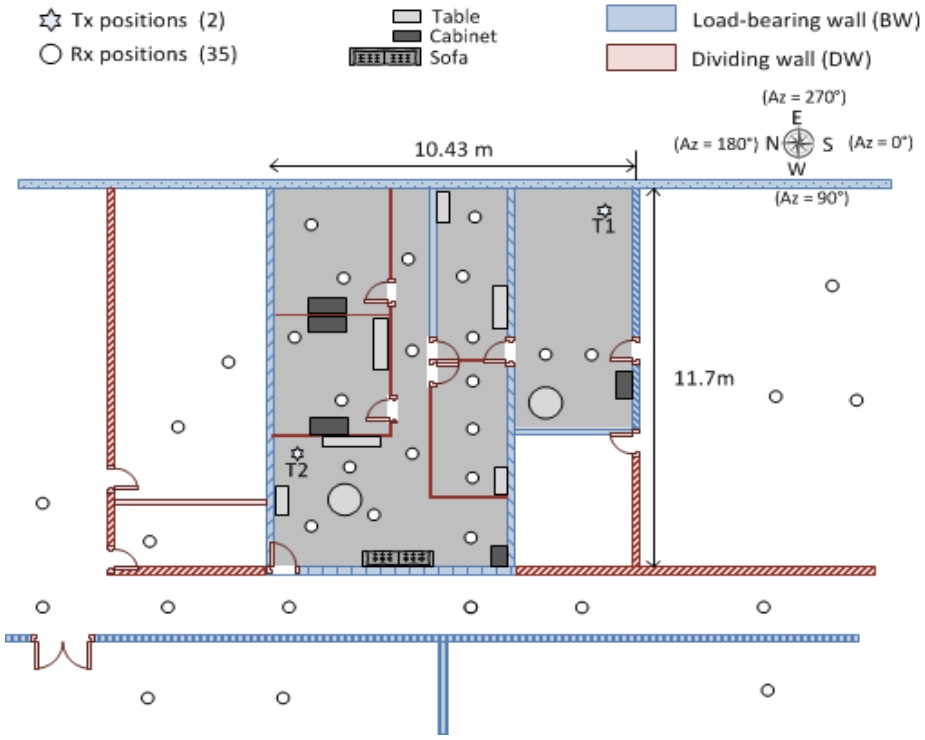

Figure 3.1. Plan of the measurement environment below 6 GHz

Table 3.1. Different kinds of walls

Legend	Label	Description	Thickness (cm)
	Mat0	Wall with windows	7.5
	Mat1	Wooden door	4
	Mat2	Load-bearing wall 1	28
	Mat3	Load-bearing wall 2	24
	Mat4	Plasterboard	7
	Mat5	Concrete wall 3	14
	Mat6	Load-bearing wall 4	56
	Mat7	Load-bearing wall 5	23
	Mat8	Load-bearing wall 6	52

3.1.2 Measurement system

The measurement system is presented in Figure 3.2. It consists of the **transmitting** (Tx) and **receiving** (Rx) **antennas** that are both omnidirectional and vertically polarized.

They have a peak gain increasing from 0 to 3.1 dBi, between 800 MHz and 6 GHz, and an elevation beamwidth around 40 – 70 degrees (see Appendix B for more details). These antennas are both connected to the same **vector network analyzer** (VNA) as follows:

- the Tx antenna is connected to the VNA's output through a 25-meter **coaxial cable** which indicates how far the transmitter may be located from the receiver,
- the Rx antenna is connected to the VNA's other port via a 25-dB **low noise amplifier** (LNA) which is not visible in Figure 3.2.b because located behind the PC.

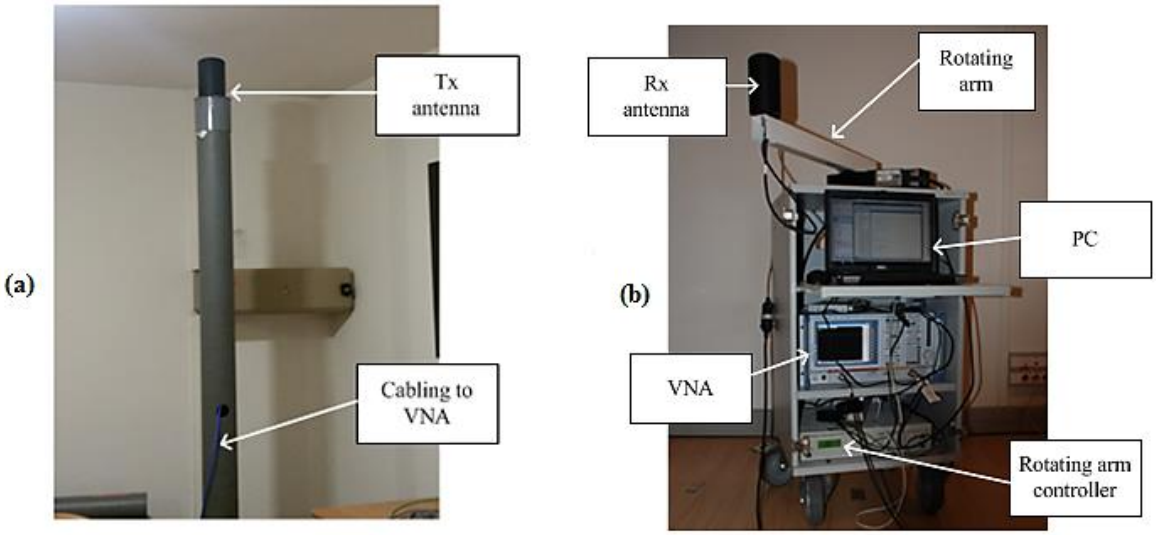

Figure 3.2. Measurement system, (a) Tx side for h_{Tx}= 2.3 m, (b) Rx side

The **VNA** determines the channel frequency response for 7 frequency sub-bands (SBs) within the 0.8 – 6 GHz band. In each band, the number of frequency sweeping points is 512. These sub-bands (labeled SB1 to SB7) have intentionally been chosen in the operating frequency range of different radio technologies as indicated in Table 3.2. Due to the lack of interference-free radio channels, only SB1 and SB2 have a bandwidth inferior to 100 MHz (respectively 20 MHz and 60 MHz).

Table 3.2. Target frequency bands

Sub-band	Frequency range (MHz)	Bandwidth (MHz)	Radio technology
SB1	864 – 884	20	IoT
SB2	968 – 1028	60	2G
SB3	1980 – 2080	100	DECT
SB4	2400 – 2500	100	Wi-Fi
SB5	3600 – 3700	100	5G
SB6	5250 – 5350	100	Wi-Fi
SB7	5500 – 5600	100	Wi-Fi

A **laptop** (PC) commands the VNA and a **rotating arm controller**. It is also used to store the measured data containing the channel frequency responses. Moreover, two back to

back measurements have been performed per measurement day[7] in order to remove, during the measured data processing, the effects of intermediary components such as cables and LNA, from the collected frequency responses. The **Tx power** is 13 dBm at the VNA's output.

3.1.3 Measurement procedure

As shown in Figure 3.1, two transmitting positions, T1 and T2, have been considered. T1 is placed in furthest room while T2 is located in the living room of the apartment. In both cases, 4 transmit antenna heights, denoted h_{Tx}, have been chosen. Each height is meant to represent a particular use case:

- For h_{Tx}= 0.23 m, the Tx antenna is supposed to be near an electrical outlet,
- For h_{Tx}= 1.03 m, the Tx antenna is assumed to be on a desk,
- For h_{Tx}= 1.67 m, the Tx antenna is expected to be on a closet,
- For h_{Tx}= 2.30 m, the Tx antenna is near the ceiling (see Figure 3.2.a).

For each Tx position, and at each Tx height, have sequentially been tested 35 Rx positions, represented by the circles in Figure 3.1. Among these Rx positions, 19 have been chosen inside the apartment versus 16 outside. For all of them, the Rx antenna is placed at height of 1.19 m on a **rotating arm** having a radius of 56 cm.

During measurements, at any Rx position, the rotating arm, triggered by its controller, does a full rotation in azimuth with a step size of 6°. The reference azimuth angle (0°) corresponds to the South direction, as indicated in Figure 3.1. At each of the 60 angular steps, the VNA determines the channel frequency response for each frequency sub-band. These measurements have been performed in a static environment without human presence. The specifications are summarized in Table 3.3.

3.1.4 Indoor path loss modeling

For each Rx position, the relative received power at the i-th azimuth step is given, for each frequency sub-band, by:

$$P_r'(\theta_i)[dB] = 10\log_{10}\left(\frac{1}{N_p}\sum_{k=1}^{N_p}|H(\theta_i, f_k)|^2\right) \quad (3.1)$$

where:

- θ_i is i-th angular step which corresponds to an azimuth angle of $\theta_i[°] = 6i$,
- N_p is the number of frequency sweeping points (= 512 here),
- f_k is the frequency corresponding to the k-th frequency point,
- H is the measured discrete channel frequency response by the VNA for θ_i at f_k.

This relative power (P_r') is related to the path loss (PL) by the following equation:

$$PL(\theta_i)[dB] = -P_r'(\theta_i) \quad (3.2)$$

Finally, the path loss, at each Rx position, is estimated by computing its average over the 60 angular steps. In fact, since the distance, δ, covered by the Rx antenna during a full rotation is ten times greater than the greatest wavelength (λ_{SB1}= 34.7 cm and $\delta \approx$ 352 cm), it's possible to get an average path loss estimation because the small-scale fading effects are minimized [8] [24].

[7] The first one is performed in the morning before any channel measurement and the other one at the end of the afternoon, after the last channel measurement.

Table 3.3. Specifications of the measurement campaign below 6 GHz

Antennas							
	Tx side	**Rx side**					
Type	Omnidirectional in azimuth						
Polarization	V						
Beamwidth	75°(El)						
Gain	0 – 3.1 dBi						
Tx-Rx configurations							
Antenna height	0.23 m, 1.03 m, 1.67 m, 2.30 m	1.19 m					
Number of positions	2	35					
Number of azimuths	1	60					
Elevation angle	0°						
Measurement setup							
Central frequency [MHz]	874	998	2030	2450	3650	5300	5550
RF bandwidth [MHz]	20	60	100	100	100	100	100
Max multipath delay	25 µs	8 µs	5 µs	5 µs	5 µs	5 µs	5 µs
Tx power	13 dBm						
Number of path loss measurements							
Per Rx position	60 (1 on average)						
Per sub-band	4,200 (70 on average)						
Per Tx Height	29,400 (490 on average)						
Total	117,600 (1960 on average)						

The average path loss is then given by:

$$\overline{PL}[dB] = 10\log_{10}\left(\frac{1}{60}\sum_{i=0}^{59} 10^{\frac{PL[\theta_i]}{10}}\right) \quad (3.3)$$

Based on the average path loss computed at different Rx locations and frequency sub-bands, three indoor path loss models have been established. The first one is a log-distance model and the other ones are based on the Motley-Keenan model [1]. These models did not remove the Tx and Rx antennas gain and are available for h_{Tx} = 2.30 m.

3.1.4.1 Log-distance model

Log-distance path loss models represent the path loss as a logarithmically increasing linear function with distance:

$$PL(d)\ [\text{dB}] = PL_0 + 10n\log_{10}\left(\frac{d}{d_0}\right) + X_\sigma \qquad (3.4)$$

where:

- PL_0 is the path loss at a reference distance d_0 = 1 m,
- n is the path loss exponent which characterizes the loss increase with distance,
- X_σ is a zero-mean Gaussian random variable with a standard deviation σ (in dB) modeling the shadowing effects.

For each frequency sub-band, the parameters of this model, given in Table 3.4, have been determined by the means of a linear regression between:

- Y = the average path loss measured at a given Rx position resulting from (3.3),
- X = the corresponding Tx-Rx separation distance ($\log_{10}[d_{Tx-Rx}]$).

The results in Figure 3.3 show a global increase of the parameters value from 800 MHz to 6 GHz. The reference path loss rises of about 12 dB while the loss exponent varies from 3.1 to 4.4. The growth of σ suggests that the effect of indirect paths (caused by reflection and scattering) becomes stronger when increasing the carrier frequency. The model and the measured average path loss are plotted together for SB2, SB4 and SB6 in Figure 3.4.

Table 3.4. Parameters of the log-distance model per frequency sub-band

Sub-band	PL_0 [dB]	n	σ [dB]
SB1	26.81	3.1	3.56
SB2	25.84	3.4	4.14
SB3	27.14	4.0	5.52
SB4	27.75	4.2	5.94
SB5	29.69	4.4	7.30
SB6	34.79	4.4	7.38
SB7	38.66	4.2	6.87

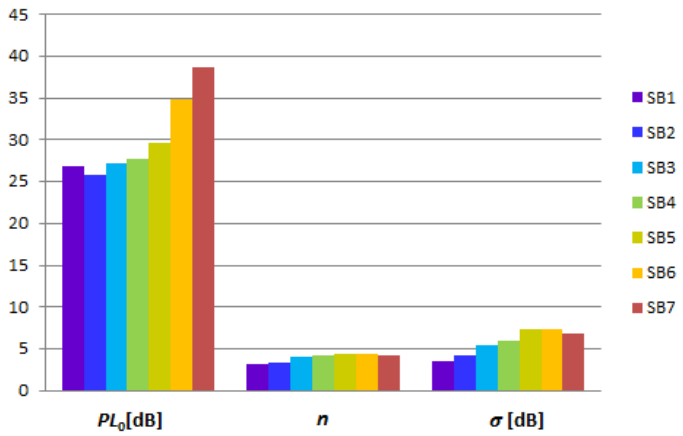

Figure 3.3. Parameters of the log-distance model

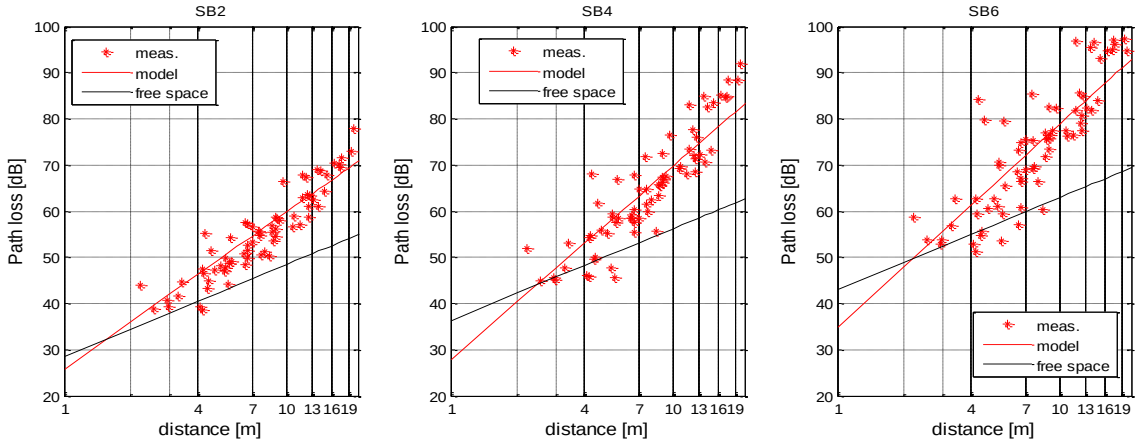

Figure 3.4. Path loss model versus measurements for SB2, SB4 and SB6

3.1.4.2 Multi-wall model

The multi-wall models presented in this section are based on the Motley-Keenan model which estimates the path loss by taking into account the number of walls crossed by the direct path between the transmitter and the receiver. The path loss is given by:

$$PL(d)[\text{dB}] = PL_0 + 20\log_{10}\left(\frac{d}{d_0}\right) + \sum k_{wi}L_{wi} + X_\sigma \qquad (3.5)$$

where:

- PL_0 is the path loss at a reference distance d_0 = 1 m,
- k_{wi} is the number of walls of type i,
- L_{wi} is the penetration loss (in dB) of the walls of type i,
- X_σ is a zero-mean Gaussian random variable with a standard deviation σ (in dB) modeling the shadowing effects.

For each sub-band, two multi-wall path loss models have been established. The main difference between them lies in the level of details when representing the building. The first one is the *generalized* multi-wall model (G-MWM) and the second is the *detailed* multi-wall model (D-MWM).

a) Generalized multi-wall model (G-MWM)

Following the COST 231 recommendation presented in Chapter 2 , the different types of walls listed in Table 3.1 have been divided into two groups. The first group, called *dividing wall* (DW) group, encompasses light walls having a thickness smaller than 10 cm (Mat0, Mat1 and Mat4). The second group is the *load-bearing wall* (BW) group, which consists of load-bearing walls having a thickness greater than 10 cm (Mat2, Mat3, Mat5, Mat6, Mat7 and Mat8).

For the G-MWM, the path loss is then given by:

$$PL(d)[\text{dB}] = PL_0 + 20\log_{10}\left(\frac{d}{d_0}\right) + k_{DW}L_{DW} + k_{BW}L_{BW} + X_\sigma \qquad (3.6)$$

The parameters of this model, given in Table 3.5, have been computed for each sub-band as explained now. Firstly, for each Tx-Rx configuration, the values k_{DW} and k_{BW} have been deduced after importing in a radio design software, developed at Orange Labs Belfort, the measurement plan, displayed in Figure 3.1, as well as the Tx and Rx locations. This software,

named XANDA (see Chapter 5), has determined the number and type of the walls crossed by the direct line between the transmitter and the receiver. Secondly, the separation distance d being known for each Tx-Rx configuration, the following multivariate linear regression has been applied based on all the configurations:

$$\overline{PL} - 20\log_{10}(d) = \boldsymbol{PL_0} + k_{DW}\boldsymbol{L_{DW}} + k_{BW}\boldsymbol{L_{BW}} \quad (3.7)$$

where $\overline{PL}$ is the average path loss computed as indicated in (3.3). The obtained results lead finally to Table 3.5.

Table 3.5. Parameters of the G-MWM per frequency sub-band

Sub-band	PL_0 [dB]	L_{DW} [dB]	L_{BW} [dB]	σ [dB]
SB1	31.42	1.03	3.07	2.99
SB2	31.36	0.99	4.14	3.10
SB3	35.84	1.49	6.01	4.08
SB4	36.98	1.83	6.51	4.21
SB5	39.62	1.72	7.59	5.21
SB6	45.12	0.89	8.05	5.24
SB7	47.97	0.95	7.14	5.12

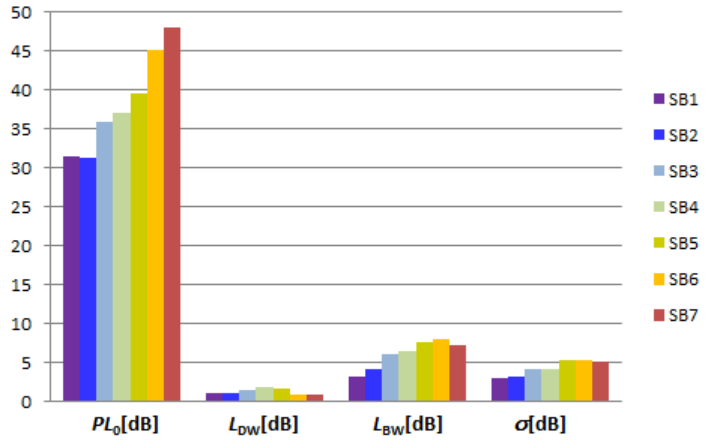

Figure 3.5. Parameters of the G-MWM

The results in Figure 3.5 show a rise of the transmission losses with the frequency. The losses through load-bearing walls are, as expected, more important than the losses due to dividing walls with a factor globally near four (corresponding to a 6 dB-difference) especially at high frequencies (SB5 to SB7). Also, like the log-distance model, an increase of the shadow factor σ with the frequency is observed.

b) Detailed multi-wall model (D-MWM)

As its denomination implies, this model is more detailed than the G-MWM. Indeed, the nine kinds of walls identified in Table 3.1 (Mat0 to Mat8) have been considered during its calibration. In practice, it's not always possible to exhaustively and accurately determine the building materials involved in a construction (which is neither the case here). However, this model is relevant to investigate the impact having a more detailed description of the measurement environment on the accuracy of the path loss estimation.

For each sub-band, the parameters of this model, given in Table 3.6 and illustrated in Figure 3.6, have been determined using the same method than the G-MWM. The results show similar trends with the G-MWM: an increase of the penetration loss along the carrier frequency with load-bearing walls attenuation globally dominant when compared to dividing walls. However, it's observed that the dividing walls having glass windows (Mat0) have penetration losses (L_0) that may be similar to load-bearing walls. This observation shows a weakness in grouping walls only by thickness as does the G-MWM.

Table 3.6. Parameters of the D-MWM per frequency sub-band

Sub-band	***SB1***	***SB2***	***SB3***	***SB4***	***SB5***	***SB6***	***SB7***
PL_0 [dB]	31.61	31.6	36.05	37.15	40.27	45.33	48.23
L_0 [dB]	3.59	3.31	5.44	4.80	4.21	3.09	3.09
L_1 [dB]	0.84	0.72	0.98	0.92	1.85	0.52	0.77
L_2 [dB]	2.91	3.07	5.56	6.12	6.97	7.98	6.90
L_3 [dB]	2.24	4.06	6.31	6.16	6.43	9.43	8.81
L_4 [dB]	1.04	0.86	1.58	2.21	1.49	0.94	0.93
L_5 [dB]	1.28	1.88	2.80	3.12	3.57	3.40	3.17
L_6 [dB]	4.84	5.68	8.94	9.98	13.40	13.30	11.91
L_7 [dB]	1.86	3.79	4.67	5.26	5.19	7.43	6.18
L_8 [dB]	5.74	6.49	8.61	9.74	11.96	8.83	7.92
σ [dB]	2.24	2.60	2.97	3.26	3.64	4.59	4.58

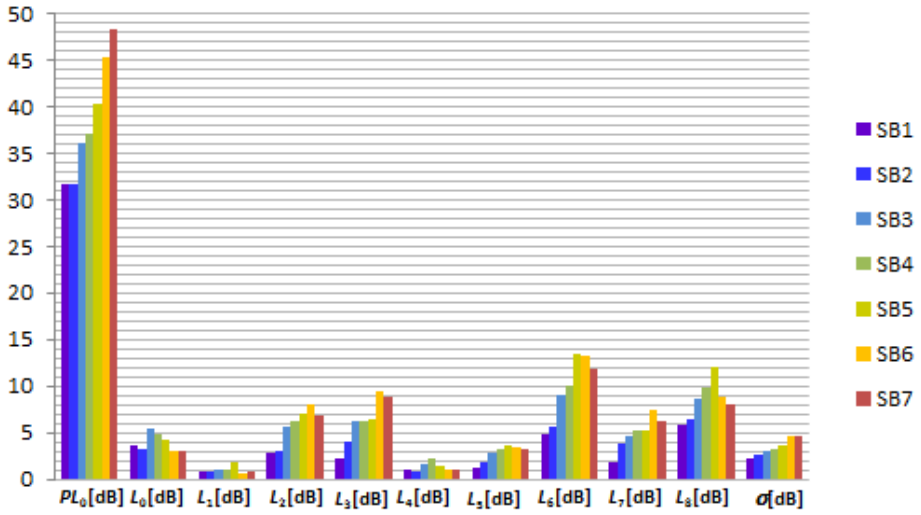

Figure 3.6. Parameters of the D-MWM

3.1.4.3 Comparative analysis

If only one of the three models presented in this section has to be recommended, which one would it be? To give an answer, a comparative study between their prediction errors has been conducted. For each frequency band, the standard deviation of the prediction error is given in Table 3.7 and illustrated in Figure 3.7.

Table 3.7. Prediction error of the three path loss models

Sub-band	Log-distance model		G-MWM		D-MWM
	σ_1 [dB]	$\sigma_1 - \sigma_3$ [dB]	σ_2 [dB]	$\sigma_2 - \sigma_3$ [dB]	σ_3 [dB]
SB1	3.56	1.32	2.99	0.75	2.24
SB2	4.14	1.54	3.10	0.50	2.60
SB3	5.52	2.55	4.08	1.11	2.97
SB4	5.94	2.68	4.21	0.95	3.26
SB5	7.30	3.66	5.21	1.57	3.64
SB6	7.38	2.79	5.24	0.65	4.59
SB7	6.87	2.29	5.12	0.54	4.58

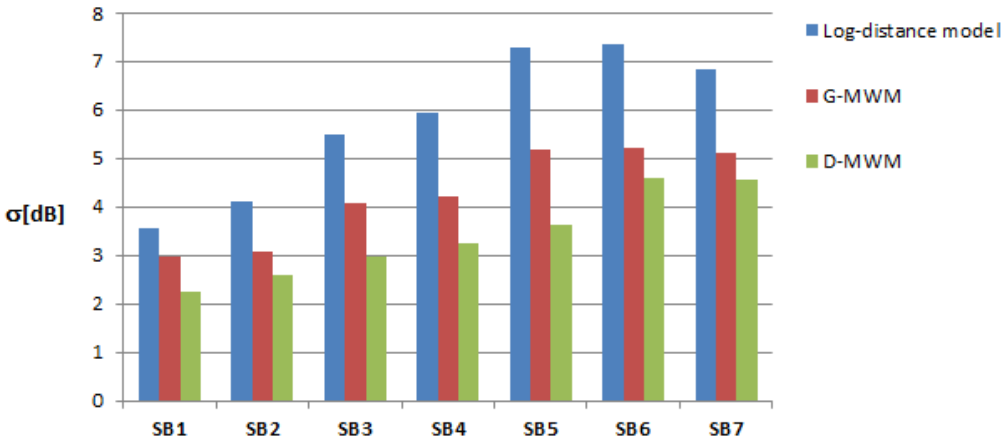

Figure 3.7. Prediction error of the three models per frequency band

The results show that from the three models, the detailed multi-wall model is the most accurate in the estimation of the path loss (less than 5 dB RMS error at high frequency). It's followed by the generalized multi-wall model which is less accurate of about 1 dB but offers a simpler building representation. Finally, the log-distance model which is the most simplified is also the least accurate ($\sigma_1 - \sigma_3$ is greater than 2.5 dB above SB3).

As a conclusion, the G-MWM model seems to be the *best* because it achieves a great trade-off between accuracy and simplicity of the building's representation.

3.1.5 Multi-frequency path loss models

The integration complexity of the models presented in the previous section within a network design tools grows with N_{SB}, the number of considered frequency sub-bands, and is at least $O(N_{SB})$. One solution to reduce this complexity to $O(1)$ is to cover all the frequency sub-bands with the same model. This task is achieved by generalizing the frequency-dependent parameter n_f (which is equal to 2 in the free space model). Thus the log-distance model in (3.4) and the generalized multi-wall model in (3.6) become respectively in this multi-frequency context:

$$PL(d,f)[\text{dB}] = PL_0 + 10n\log_{10}\left(\frac{d}{d_0}\right) + 10n_f \log_{10}(f) + X_\sigma \text{ , and} \quad (3.8)$$

$$PL(d,f)[\text{dB}] = PL_0 + 20\log_{10}\left(\frac{d}{d_0}\right) + 10n_f \log_{10}(f) + k_{DW}L_{DW} + k_{BW}L_{DW} + X_\sigma \quad (3.9)$$

where:

- f is the operating frequency expressed in GHz,
- n_f is the frequency exponent which characterizes the increase of the path loss with the frequency.

In order to calibrate these models, all of the 490 path loss measurement (35 Rx positions, 2 Tx positions, 7 SBs) have been considered. The value of f is chosen to be equal to the central frequency of the corresponding sub-band as indicated in Table 3.8.

Table 3.8. Measured path loss for one Tx-Rx configuration from SB1 to SB7

x_{Tx}	y_{Tx}	h_{Tx}	x_{Rx}	y_{Rx}	h_{Rx}	k_{DW}	k_{BW}	$PL\ [dB]$	SB	f [GHz]
105.41	-14.65	2.3	105.01	-2.4	1.19	1	1	65.45	SB1	0.874
105.41	-14.65	2.3	105.01	-2.4	1.19	1	1	67.26	SB2	0.998
105.41	-14.65	2.3	105.01	-2.4	1.19	1	1	75.48	SB3	2.030
105.41	-14.65	2.3	105.01	-2.4	1.19	1	1	77.71	SB4	2.450
105.41	-14.65	2.3	105.01	-2.4	1.19	1	1	81.77	SB5	3.650
105.41	-14.65	2.3	105.01	-2.4	1.19	1	1	85.70	SB6	5.300
105.41	-14.65	2.3	105.01	-2.4	1.19	1	1	86.58	SB7	5.550

The parameters have been determined by the means of a multivariate linear regression between:

- Y, the average path loss measured at a given Rx position,
- X_1, the corresponding Tx-Rx separation distance,
- X_2, the corresponding operating frequency ($\log_{10} f$),
- k_{DW} and k_{BW}, respectively the number of dividing walls and load-bearing walls crossed by the Tx-Rx direct path determined with XANDA as previously explained (for the G-MWM only).

The results, presented in Table 3.9, show that both models express the same dependency in frequency with an exponent of 2.5. However this frequency exponent is actually around 3.2 when the Tx-Rx antennas effects are removed, since their combined peak gain increase can be approximated as $7.4 \log_{10}(f)$ (see Appendix B.1.b).

Table 3.9. Parameters of the multi-frequency models

Model	PL_0[dB]	n	n_f	L_{DW}[dB]	L_{BW}[dB]	σ [dB]
Log-distance model	20.36	4.0	2.5	-	-	6.07
G-MWM	28.59	2.0	2.5	1.27	6.07	4.66

The observations are similar to the previous ones: the path loss exponent of the log-distance model is still between 3.1 and 4.4, the penetration losses due to load-bearing walls (L_{BW}) are more significant than the losses due to dividing walls (L_{DW}). Also, the generalized multi-wall model is still the *best* model because of its accuracy and low complexity in the building's representation.

3.1.6 Effect of the Tx antenna height

As aforementioned, the measurements have been performed for four Tx heights (h_{Tx} = 0.23, 1.03, 1.67 and 2.3 m) but only the results obtained for the highest Tx height have been considered when calibrating the models previously detailed.

In order to have a brief insight of the impact of the Tx height on the path loss, the average of the 70 measured path loss has been computed for each Tx height, at each sub-band, as follows:

$$\overline{PL}[dB](h_{Tx}) = 10\log_{10}\left(\frac{1}{70}\sum_{tx=1}^{2}\sum_{rx=1}^{35}10^{\frac{PL[tx,rx,h_{Tx}]}{10}}\right) \quad (3.10)$$

Considering as reference the smallest Tx height (h_{ref} = 0.23 m), is derived from (3.10) the relative average path loss given by:

$$PL_r[dB](h_{Tx}) = \overline{PL}[dB](h_{Tx}) - \overline{PL}[dB](h_{ref}) \quad (3.11)$$

The results in Figure 3.8, plotting the relative average path loss versus the Tx height, show that at each sub-band, the height gain (corresponding to a negative relative average path loss) describes a relatively convex curve. A similar trend is observed (at a different scale) in Figure 3.9, taken from [25] which proposes indoor path loss prediction for different floors based on outdoor estimations at ground-level added with height gain model.

The curve in Figure 3.8 indicates that the height gain decreases when the height difference increases (going upward or downward). Conversely this gain increases when the height difference decreases; in [26], this gain is maximum when the Tx and Rx antennas are of the same height. Here, Figure 3.8 shows that, at each sub-band, the gain is globally better for h_{Tx}= 1.67 m (Δ_h= 48 cm) and varies from 1.2 dB to 3.6 dB.

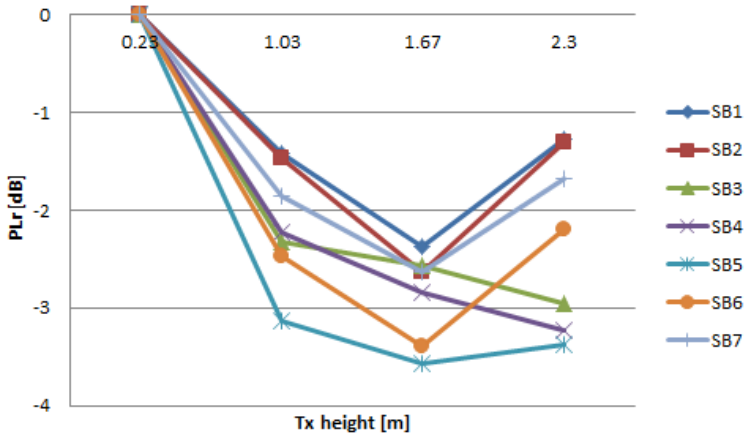

Figure 3.8. Relative average path loss versus Tx height

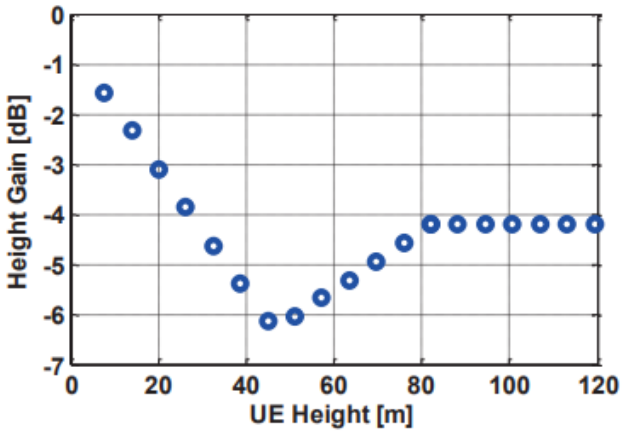

Figure 3.9. Height gain curve (UE: User Equipment)[25]

3.2 Path loss modeling at 60 GHz

The path loss characterization in the mm-waves band is essentially achieved by the means of experimental measurements [27]–[32] and extensive ray-tracing simulations [33]–[36]. As explained in Chapter 2 , deterministic approaches such as ray-tracing have not been considered because they have a high computational cost and require a precise environment description. Thus, the path loss modeling at 60 GHz presented in this section has been focused on the calibration of log-distance models.

In [27] is presented the IEEE 802.11ad log-distance path loss model for Single-Input and Single-Output (SISO) transmissions in three indoor scenarios (see Table 3.10). Since the transmissions are directional, this model accounts for beamforming by pointing the Tx and Rx antennas towards the direction having the maximum ray power. During this thesis, a similar approach has been used by focusing the path loss analysis on the *best* directions in terms of received power (see Section 3.2.3).

Table 3.10. Parameters of the 802.11ad path loss model [27]

Scenario	Configuration	PL_0[dB]	n	σ[dB]
Living room	LOS	32.4	2.0	0
	NLOS	44.7	1.5	3.4
Conference room	LOS	32.5	2.0	0
	NLOS	45.5	1.4	3.0
Cubicle environment	LOS	32.5	2.0	0
	NLOS	44.2	1.8	1.5

However, the 802.11ad path loss model is restricted to single-room environments where the NLOS configuration is actually an *obstructed* visibility condition. That is not the case in [28] which proposes directional and omnidirectional path loss models based on propagation measurements performed in a modern office building (65.5 x 35 x 2.7 m^3) at 28 GHz and 73 GHz.

The study presented in this section, is in some aspects similar to [28], and has been conducted at 60 GHz in the same residential environment described previously in Section 3.1.1.

3.2.1 Measurement system

The measurement system, presented in Figure 3.10, comprises the **Tx and Rx antennas** which are both sectoral and vertically polarized horn antennas. The Tx antenna, manufactured at Orange Labs Belfort, has a 120° 6 dB-beamwidth in both E and H planes with a gain of 7.3 dBi (see Appendix B.2). The Rx antenna is more directional with a half power beamwidth of 20° and a gain around 19.5 dBi (see Appendix B.3). These antennas are both connected to the same VNA as follows:

- The Tx antenna is linked to an external **up converter** (to 60 GHz) that is connected via a 2-meter cable to the VNA which operates at an intermediate frequency around 15 GHz,
- The Rx antenna is connected to the VNA trough major components which are respectively a 20 dB **low noise amplifier**, a 25-meter low loss (12 dB) **coaxial cable** and an external **down converter** (back to 15 GHz).

For practical reasons, the roles of Tx and Rx antennas have been functionally reversed during measurements. This means that the 20° directional antenna is actually the one transmitting while the 120°-directional antenna is the receiving end. But, thanks to the channel reciprocity, the radio channel characteristics remain unaffected by this switching.

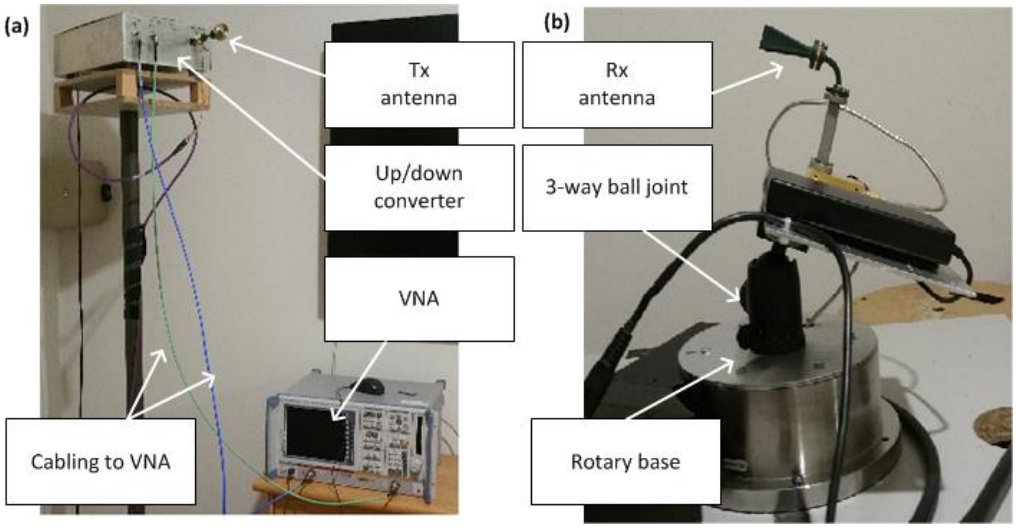

Figure 3.10. Measurement system at 60 GHz, (a) Tx side, (b) Rx side

The **VNA** measures the S_{21} parameters in the 60 – 62.047 GHz band by sweeping over 2048 frequency points with a frequency step of 1 MHz. This large transmission bandwidth (2.047 GHz) guarantees a high multipath diversity resulting in a more accurate estimation of the average path loss thanks to reduced small-scale fading [37]. Also, the maximum measurable delay (1 µs) of the channel impulse response is long enough to differentiate multipath components (having delay smaller than 100 ns) from the noise or measurement impairments (above 100 ns).

The **3-way ball joint** is used to manually adjust the elevation angle of the Rx antenna to five angles successively: 0° (horizontal plane), 10°, 20° 30° and 40° (towards the ceiling). For each of these elevation angles, the **rotary base** does a full rotation in azimuth with a step

size of 6°, so that at each Rx position, the path loss is measured in 5x60 = 300 directions in terms of azimuth and elevation. A value of 0° in azimuth corresponds to the West direction as indicated Figure 3.12.

It's worth to mention that two times per measurement day have been performed back to back measurements in order to **remove from**[8] the measured frequency responses the effect of intermediary components such as cables, and correct the temperature effects causing a drift of the received power level between the morning and the afternoon. The transmit power is 13 dBm at the Tx antenna input.

3.2.2 Measurement scenario

As shown in Figure 3.11, two transmitting positions, T1 and T2, have been considered. These positions are located at opposite corners in the living room. In both cases the Tx antenna height is h_{Tx} = 1.97 m (near the ceiling), its azimuth is directed towards the main diagonal of the room without tilt (elevation angle of 0°).

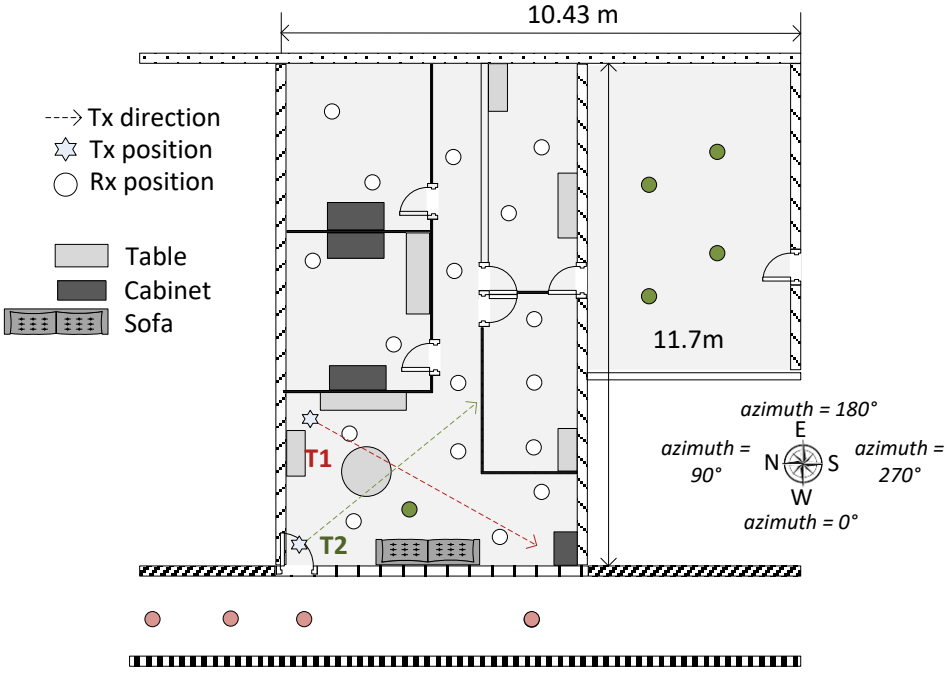

Figure 3.11. Plan of the measurement environment at 60 GHz

On the receiving side, 43 Rx positions have been chosen. With respect to the Tx position, 31 positions are in NLOS versus 12 in LOS. This disparity is explained by the fact that during this thesis, a particular emphasis has been put on communications at 60 GHz in NLOS (this part will be developed later, in Chapter 4). In Figure 3.11, the Rx positions filled in red, green and white have respectively been tested for T1 only, T2 only, and both positions. The Rx antenna height is equal to 1.31 m.

The measurements have been performed in a static environment without human presence (walls and furniture are the only obstacles). The study of the effect of human body shadowing is conducted in Chapter 4. The specifications of this campaign are summarized in Table 3.11.

[8] During the processing the measured data.

Table 3.11. Specifications of the campaign at 60 GHz with directional antennas

Antennas		
	Tx side	**Rx side**
Type	Directional	
Polarization	V	
Beamwidth	120° (6 dB)	20° (3 dB)
Gain	7.3 dBi	19.5 dBi
Tx-Rx configurations		
Antenna height	1.97 m	1.3 m
Number of positions	2	43 (LOS:12, NLOS:31)
Number of azimuths	1	60
Elevation angle	0°	0°, 10°, 20°, 30°, 40°
Measurement setup		
Central frequency	61.0235 GHz	
RF bandwidth	2.047 GHz	
Max multipath delay	1 μs	
Tx power	13 dBm	
Number of path loss measurements		
Per Rx position	300	
Total	12,900	

3.2.3 Measurement data processing

At each Rx position, the path loss has been measured in 300 directions in terms of azimuth and elevation. However, between all of these directions, only two have been of interest: the one in direct line with the transmitter and the best path resulting from multipath propagation. The latter propagation path will be called **best indirect path** in the remainder of this document.

The process leading to the identification of the path loss on these two directions is illustrated in Figure 3.12:

- First, at each azimuth step, the relative received powers corresponding to the 5 elevation angles are compared with each other so that only the maximum value is considered;
- From the previous step are then identified the local maxima of the received power; they coincide with minimal values of the path loss as shown by (3.2);
- Since the Tx and Rx positions are known, the actual azimuth between them is also known (the reference being the West direction). Thus, the path loss on the **direct path** is approximated to be the opposite of the local maximum having its azimuth closest to the actual one;
- At last, the path loss on the **best indirect path** corresponds to the opposite of the highest local maximum which does not meet the condition stated in the previous step.

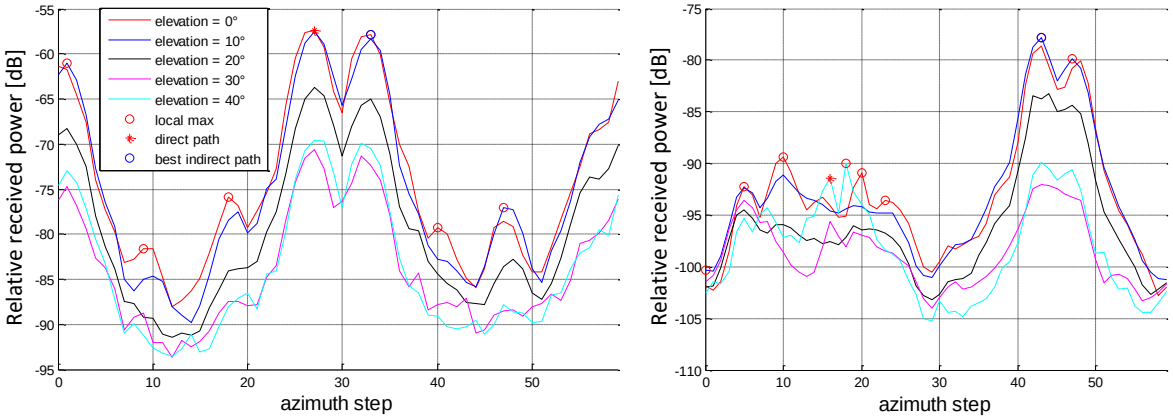

Figure 3.12. Direct and best indirect paths identification in LOS (left) and NLOS (right)

This algorithm based on power level comparison and local optima research has been adjusted and validated by comparing its results with more detailed information such as propagation delays allowing an easy differentiation between the direct path and the multipath components as shown in Figure 3.13.

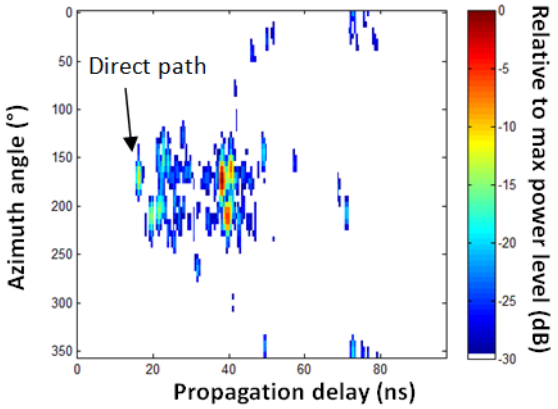

Figure 3.13. Example of spatio-temporal data

Finally, for each Rx position, the path loss values, identified by the algorithm, have been stored in the format presented in Table 3.12. This data formatting have enabled an easy calibration of the path loss model presented in the next section and from which have not been removed the Tx and Rx antennas gain.

Table 3.12. Example of measurement data formatting after the processing

$d_{Tx\text{-}Rx}$ [m]	LOS/NLOS	PL direct path [dB]	PL best indirect path [dB]	Azimuth [°]
2.49	LOS	51.68	62.73	90
2.65	LOS	51.22	65.98	72
4.78	NLOS	68.67	65.01	84
4.47	NLOS	85.49	80.95	36

3.2.4 Measurement results

From the previous results, a directional path loss model has been calibrated. It is based on the log-distance model given by Eq.(3.4). Its parameters have been determined by applying a linear regression between:

- Y = the path loss measured in the direction of interest,
- X = the corresponding Tx-Rx separation distance ($\log_{10}[d_{Tx-Rx}]$).

This model, whose parameters are given in Table 3.13, is illustrated in Figure 3.14.

Table 3.13. Parameters of the 60 GHz directional path loss model

Model	PL_0(dB)	n	σ(dB)
LOS direct path	43.26	1.59	3.30
LOS best indirect path	64.74	-0.57	3.02
NLOS direct path	69.89	1.82	14.92
NLOS best indirect path	64.24	2.32	9.58

In LOS, this model shows that the path loss is greater on the best indirect path when compared to the direct path. However, this additional path loss decreases as the Tx-Rx distance increases (from 26 dB to less than 5dB here).

In NLOS, a reverse observation is done. The path loss is greater on the direct path when compared to the best indirect. However, the additional path loss is not as significant as in the LOS scenario and stay around 5 dB or less. Also, the prediction error (due to shadowing) has significantly increased in NLOS; a similar trend is observed in [28].

In both LOS and NLOS cases, the path loss exponent on the direct path is smaller than 2. This improvement when compared to the free space may indicate that the direct path benefits from the constructive effects of multipath propagation.

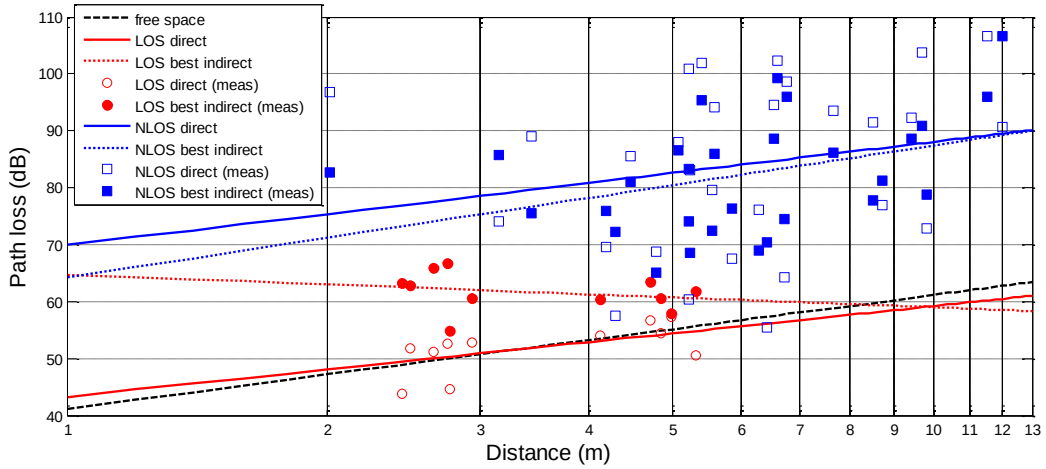

Figure 3.14. 60 GHz directional path loss model versus measurements

3.2.5 Omnidirectional path loss model

Since the signal attenuation over distance is severe at 60 GHz, high-speed communications require mostly directional antennas to compensate for the path loss. However, in some cases, omnidirectional antennas may be useful. For instance, in IEEE

802.11ad [7], quasi-omnidirectional patterns at the receiver side are needed prior to beamforming training, when the peer best direction (sector) is still unknown [38]. The omnidirectional path loss model presented in this section has then been established for addressing low data rate applications such as beamforming training or node discovery.

3.2.5.1 Measurement system and procedure

The measurement environment remains unchanged (see Section 3.1.1). Same goes for the measurement system which is the same as the one used for the 60 GHz directional path loss model except that the directional Rx antenna has been replaced by an omnidirectional antenna vertically polarized having a gain a of 2 dBi with an elevation angle of 0° (see Appendix B.4).

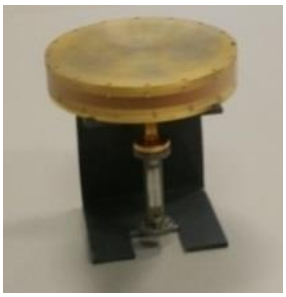

Figure 3.15. 60 GHz omnidirectional Rx antenna

The measurement plan is identical to the one illustrated in Figure 3.11 except that the Rx positions in red have not been taken into account. The specifications of this measurement campaign are summarized in Table 3.14.

3.2.5.2 Measurement data processing

At each Rx position, has been computed the average path loss over the 60 angular steps in azimuth as follows:

$$\overline{PL}[dB] = 10\log_{10}\left(\frac{1}{60}\sum_{i=0}^{59} 10^{\frac{PL[\theta_i]}{10}}\right) \tag{3.12}$$

where $PL[\theta_i]$ is the path loss measured in dB by the means of the VNA at the i-th angular step which corresponds to an azimuth angle of $\theta_i[°] = 6i$.

The average path loss is then stored in a table format similar to Table 3.12 for an easy calibration of the log-distance model presented in the next section.

3.2.5.3 Measurement results

From the previous results have been deduced an omnidirectional path loss model based on the log-distance model given by (3.4). Its parameters, indicated in Table 3.15, have been determined by applying a linear regression between:

- Y = the average path loss at each Rx position resulting from (3.12),
- X = the corresponding Tx-Rx separation distance ($\log_{10}[d_{Tx-Rx}]$).

Table 3.14. Specifications of the 60 GHz-measurements with an omnidirectional antenna

Antennas		
	Tx side	**Rx side**
Type	Directional	Omnidirectional in azimuth
Polarization	V	
Beamwidth	120° (6 dB)	30° (3 dB in elevation)
Gain	7.3 dBi	2 dBi
Antenna height	1.97 m	1.31 m
Number of positions	2	39 (LOS:12, NLOS:27)
Number of azimuths	1	60
Number of elevations	1	
Measurement setup		
Central frequency	61.0235 GHz	
RF bandwidth	2.047 GHz	
Max multipath delay	1 μs	
Tx power	13 dBm	
Number of path loss measurements		
Per Rx position	60	
Total	2,340	

Table 3.15. Parameters of the 60 GHz omnidirectional path loss model

Model	**PL_0(dB)**	**n**	**σ (dB)**
LOS Omni	64.43	0.84	1.80
NLOS Omni	61.68	3.37	8.76

In LOS, this model shows a slight improvement in the received signal power when compared to the free space (see Figure 3.16) as a result of constructive effects of multipath propagation. In NLOS, the path loss exponent of 3.37 indicates significant signal attenuation over distance due to obstructions.

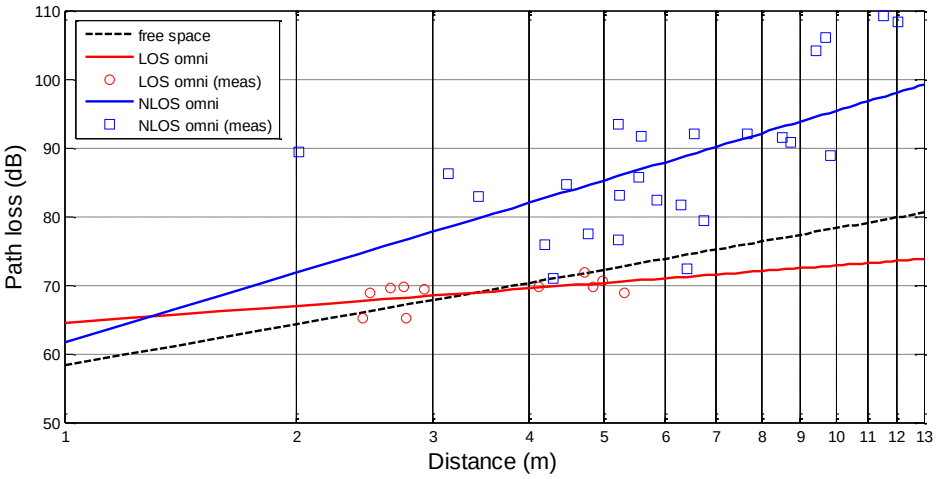

Figure 3.16. 60 GHz omnidirectional path loss model versus measurements

3.3 Chapter summary

Propagation models are required by radio-design tools in order to predict the coverage areas based on transmitters location. In order to run such design tools on devices with limited computing capabilities, path loss models with low computational cost are required. This requirement is met by (semi-)empirical propagation models such as log-distance and multi-wall models. However these models have, first, to be parameterized for specific environments and frequency bands by the means of actual measurements.

In this chapter, three path loss models have been calibrated, based on a measurement campaign carried out in an indoor residential environment from 800 MHz to 6 GHz. The first one is a log-distance model which estimates the path loss based on the Tx-Rx separation distance. The second one is the *generalized* multi-wall model which, in addition to the Tx-Rx distance, takes into account two types of obstacles met by the direct path between the transmitter and the receiver: *dividing walls* having a thickness smaller than 10 cm and *load-bearing* walls having a thickness greater than 10 cm. The last one is the *detailed* multi-wall model which describes more precisely the obstacles met by the direct path between the transmitter and the receiver. A comparative study has proved the *generalized* multi-wall model to be the best because of its balance between accuracy and building's map representation simplicity.

Other measurement campaigns have also been carried out at 60 GHz leading to directional and omnidirectional path loss models. The directional path loss model which accounts for Rx beamforming shows that in LOS, the received signal level is better on direct path when compared to the best indirect path. However as the distance increases between the transmitter and the receiver, the difference in path loss tends to be less significant. Conversely, in NLOS, the received signal level is higher on the best indirect path. The omnidirectional model which has been established for low-data rate application such as node discovery in IEEE 802.11ad shows that LOS communications benefits from multipath propagation while NLOS transmissions are strongly hindered by obstacles and surrounding objects.

Chapter 4

Study of the radio coverage sensitivity in a residential environment

The previous chapter has presented simple path loss models that can be used by radio-design software in order to find, for a particular building, optimal access points locations in terms of throughput and radio coverage. However, in practice, a given optimal location may not be available due to practical limitations like, for instance, the lack of electrical outlets. In such cases, a backup position has sometimes to be manually, yet optimally, chosen.

In this chapter, the sensitivity of the radio coverage is studied in a residential environment below 6 GHz and at 60 GHz. The first section (Section 4.1) is focused on the impact of the transmitter surroundings. The goal is to come up with recommendations to be followed when one of the four studied situations is encountered. The second section (Section 4.2) examines the impact on the coverage of the presence of people in the measurement environment. In the last section (see Section 4.3) is carried out an investigation whose final objective is to determine whether it's possible to ensure a quality of service at 60 GHz in non-visibility condition.

4.1 Impact of the transmitter surroundings

The sensitivity of the coverage area to the transmitter surroundings has been studied by performing radio measurements in four situations:

- when the transmitter is near a wall edge,
- when there are wooden doors between the transmitter and the receiver,
- when the transmitter is in the middle of a room,
- when the transmitter is located inside a piece of furniture (cabinet).

The measurements have been conducted in the home environment presented in Chapter 3.The results are intended to provide useful information when such situations are met in practice for wireless systems operating below 6 GHz or at 60 GHz.

4.1.1 Presence of a wall edge

Two measurement campaigns have been carried out with the transmitting position near a **wall edge**. The first one has been conducted with omnidirectional antennas below 6 GHz, while the other one, performed at 60 GHz, has involved directional Tx and Rx antennas.

4.1.1.1 Measurements below 6 GHz

a) Measurement procedure

The measurement system is identical to the one used for the calibration of the path loss models below 6 GHz presented in Chapter 3 except that only 3 frequency sub-bands have been selected (SB2, SB4 and SB6) to reduce the measurements time, and the Tx antenna is at the same height than the Rx antenna (around 1.2 m).

As shown in Figure 4.1, two **Tx locations** (T3 and T4 represented by the stars) have been sequentially considered on either side of a wall made of plasterboard and pictured on Figure 4.3.a.

At each location, several **Tx positions** distant from 5 cm on average have been chosen for the Tx antenna (highlighted as the blue circles on the right side of Figure 4.1). These positions have been selected so that they describe two types of motion:

- movement alongside the wall (parallel to the wall, 9 positions),
- movement away from the wall (perpendicular to the wall, 9 positions)

Note that four Tx positions have not been of used for this scenario. They will be considered later on (see Section 4.1.3).

For each Tx position, 6 Rx positions have been considered. During measurements, at each Rx position, the rotating arm does a full rotation in azimuth with a step size of 6° so that at each of the 60 angular steps, the VNA determines the channel frequency response of each of the 3 frequency sub-bands by sweeping over 512 frequency points. The average path loss is then computed over the 60 azimuth steps as explained in Chapter 3. The specifications of this campaign are summarized in Table 4.1.

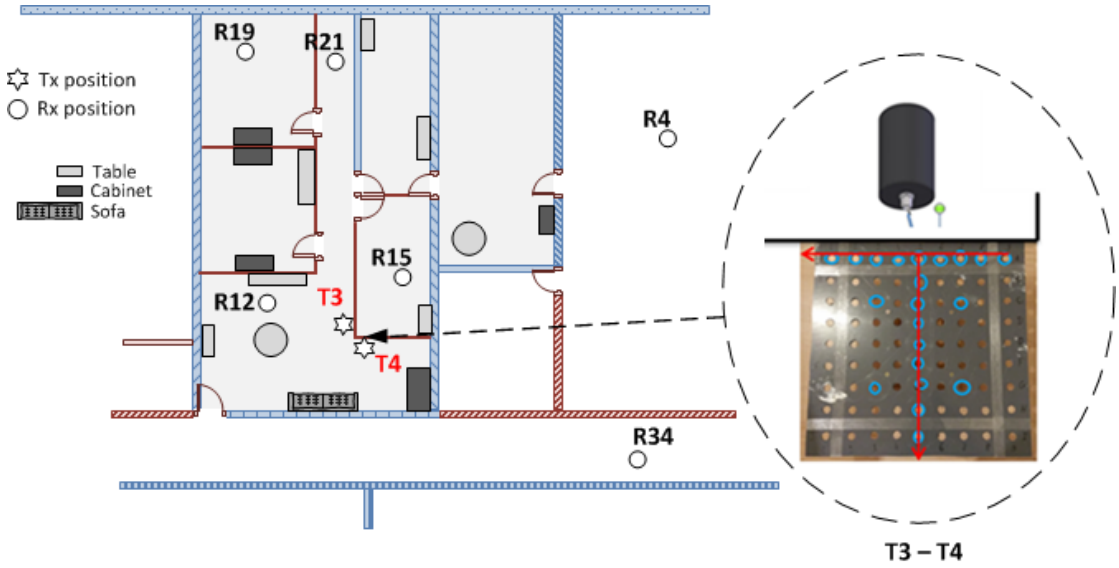

Figure 4.1.Tx locations grid near a wall edge below 6 GHz

a) Measurement results

The variation of the path loss, at each Rx position, has been characterized by its standard deviation when considering all Tx positions. The results in Figure 4.2 show that, for each type of motion, the path loss variation exhibits the same behavior on either side of the wall. The Tx positioning has more impact on closer Rx positions (at least 1 dB) than on farther ones (globally less than 1 dB).

Table 4.1. Specifications of the wall edge scenario below 6 GHz

Antennas			
	Tx side	**Rx side**	
Type of wall	Plasterboard		
Type / Polarization	Omnidirectional in azimuth / V		
Beamwidth / Gain	75°(El) / 0 – 3.1 dBi		
Tx-Rx configurations			
Antenna height	1.19 m	1.19 m	
Number of positions	17x2	6	
Number of azimuths	1	60	
Elevation angle	0°		
Total	102x2		
Measurement setup			
Central frequency [MHz]	998	2450	5300
RF bandwidth [MHz]	60	100	
Max multipath delay	8 µs	5 µs	
Tx power	13 dBm		

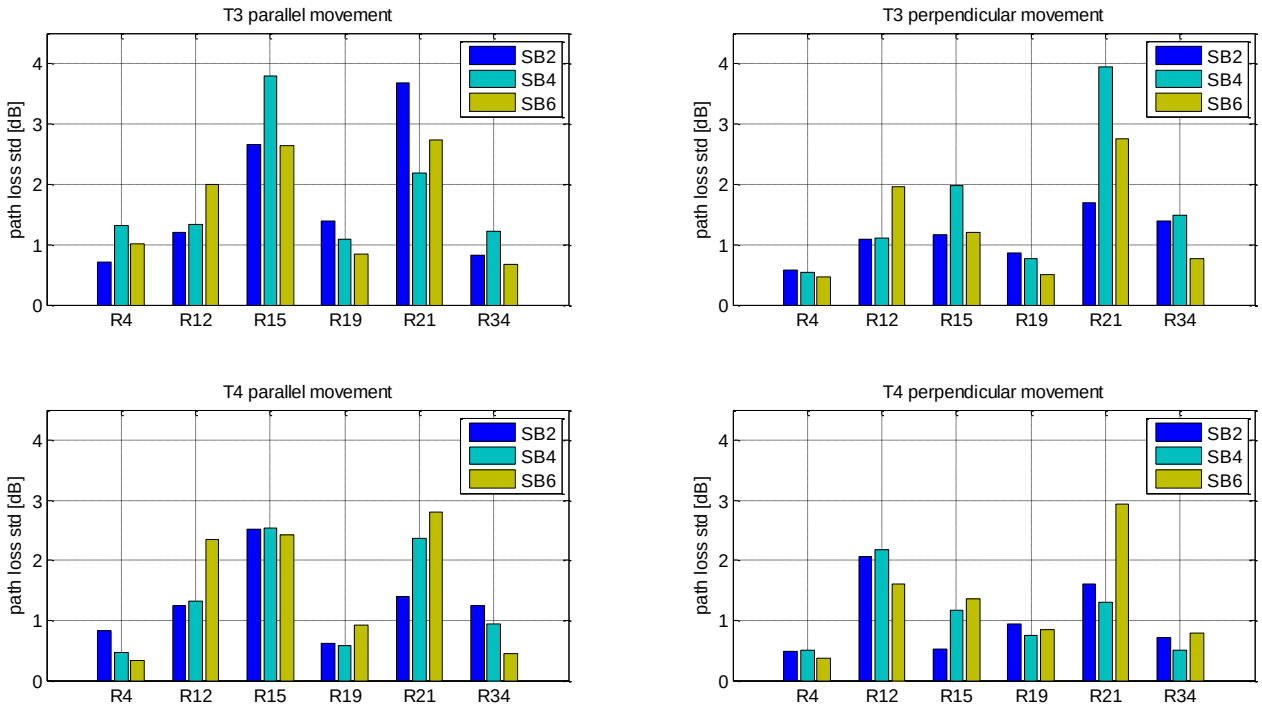

Figure 4.2. Path loss variation in the wall edge scenario below 6 GHz

Also, the results do not indicate a dependency between the path loss variation and the operating frequency band. As to know which side of the wall is generally the *best*, the results show that the received power is generally better when the transmitter is closer to the receiver. Thus, the best side is the one meeting the previous requirement in most cases. More details about the results of this campaign are given in Appendix C.1.

4.1.1.2 Measurements at 60 GHz

The measurements at 60 GHz have been carried out with a different goal than the campaign below 6 GHz. In fact, the objective has been to determine the importance of diffraction (on the wall edge) when compared to transmission (through the wall) and reflection.

a) Measurement procedure

The path loss is intended to be analyzed on the diffracted, direct and the best indirect paths for two kinds of wall. The first one is made of plasterboard (Figure 4.3.a) and is the same wall considered during the campaign below 6 GHz. The second one is made of concrete (Figure 4.3.b) and cannot be penetrated at 60 GHz (i.e. no transmission phenomenon in NLOS). This wall is located outside the apartment and has not been represented in Figure 4.1.

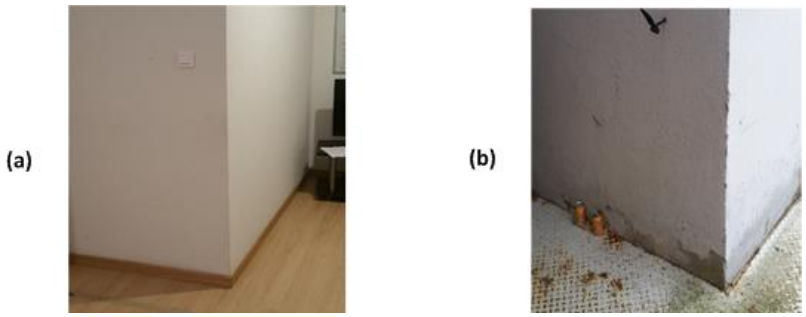

Figure 4.3.Wall made of (a) plasterboard, (b) concrete

In both cases only the Tx-Rx configuration, illustrated in Figure 4.4, has been considered. The Tx and Rx antennas are at the same height (1.31 m) on either side of the wall. On the Tx side, the antenna is 92 cm-far from the wall edge pointing towards the North direction. On the Rx side, the antenna is moved over 110 cm alongside the wall, with a step size of 5 cm, from a visibility condition (the first 25 cm) to a non-visibility condition (the remaining 85 cm).

The measurements have been performed at each Rx step alongside the wall, with the same system than the one used to calibrate the directional path loss model at 60 GHz in Chapter 3. However, in this case, there are two major differences: only the elevation of 0° has been considered and, in the case of the wall made of plasterboard, the 20° horn antenna used at for Rx has been replaced by a 8.5° horn antenna for a better differentiation between the direct path and the diffracted path. The specifications of this campaign are summarized in Table 4.2.

b) Measurement results

The path loss on the direct, best indirect and diffracted paths have been identified for each Tx-Rx configuration based on the direction of arrival (DoA), as illustrated in Figure 4.5. In ambiguous cases, the propagation delays have also been taken into account for a better differentiation. As an example, the reflected path received at 96° is not considered to be the

best indirect path because, by referring to the delay propagation, it's identified as a consequence of the irregular structure of the wall made of plasterboard.

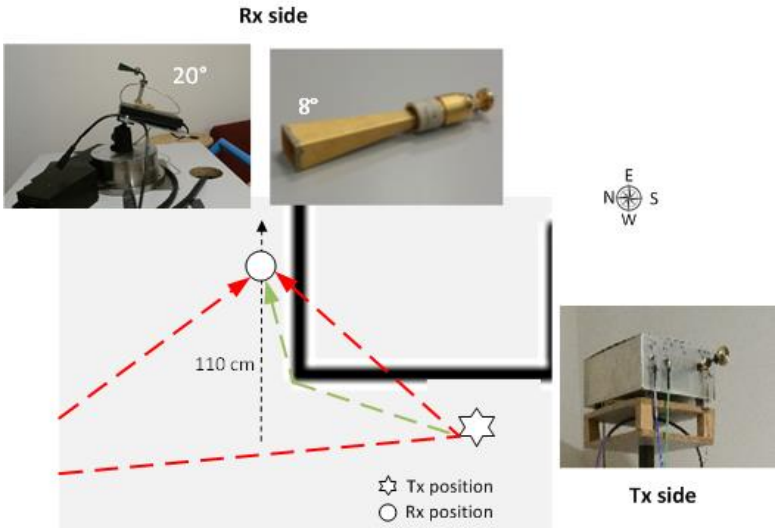

Figure 4.4. Transmitter near a wall edge at 60 GHz

Table 4.2. Specifications of the wall edge scenario at 60 GHz

Antennas			
	Tx side	**Rx side**	
Type of wall	Plasterboard + concrete	Plasterboard	concrete
Type	Directional		
Polarization	V		
Beamwidth	120° (6 dB)	8.5° (Az), 5° (El)	20°
Gain	7.3 dBi	23 dBi	19.5 dBi
Tx-Rx configurations			
Antenna height	1.31 m		
Number of positions	1	21	
Number of azimuths	1	60	
Elevation angle	0°		
Measurement setup			
Central frequency	61.0235 GHz		
RF bandwidth	2.047 GHz		
Max multipath delay	1 µs		
Tx power	13 dBm		

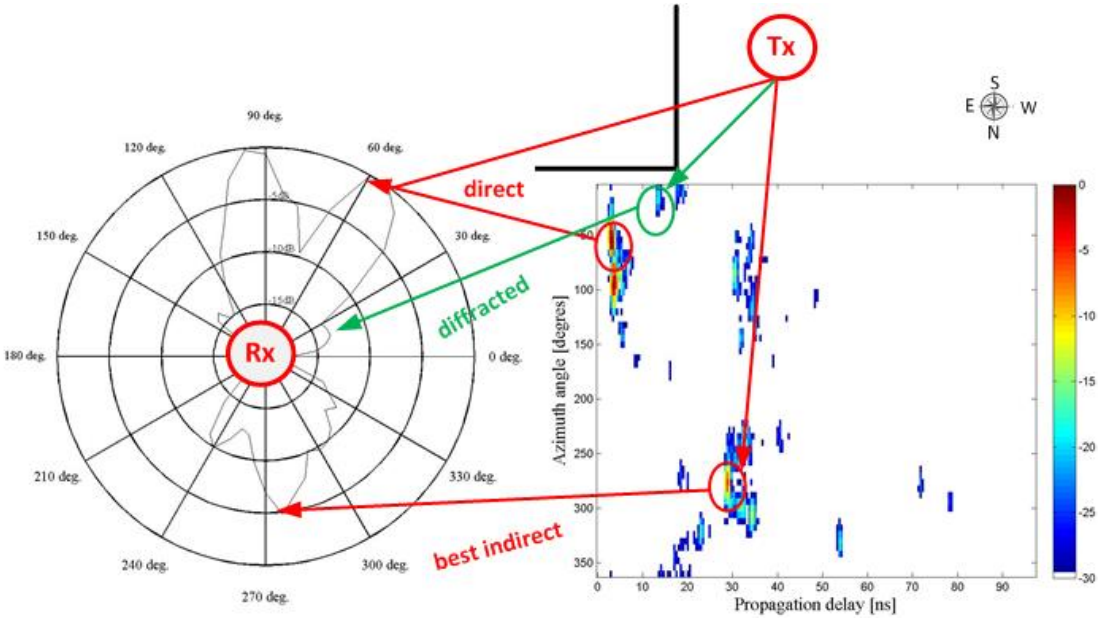

Figure 4.5.Identification of the propagation paths based on DoA and excess delay

In Figure 4.6, the results show that, for the two types of wall, the path loss is the highest on the diffracted path than on any other path. In the case of the wall made of concrete, a loss of around 25 dB on the diffracted path is observed during the transition over a small distance (5 to 10 cm) between visibility and non-visibility conditions. Also for this study, the difference between the diffracted path and the best indirect path, in NLOS, varies from 2 to 18 dB, especially in the case of the concrete wall where there is a reflector (window glass) close to the receiver of about 2 m.

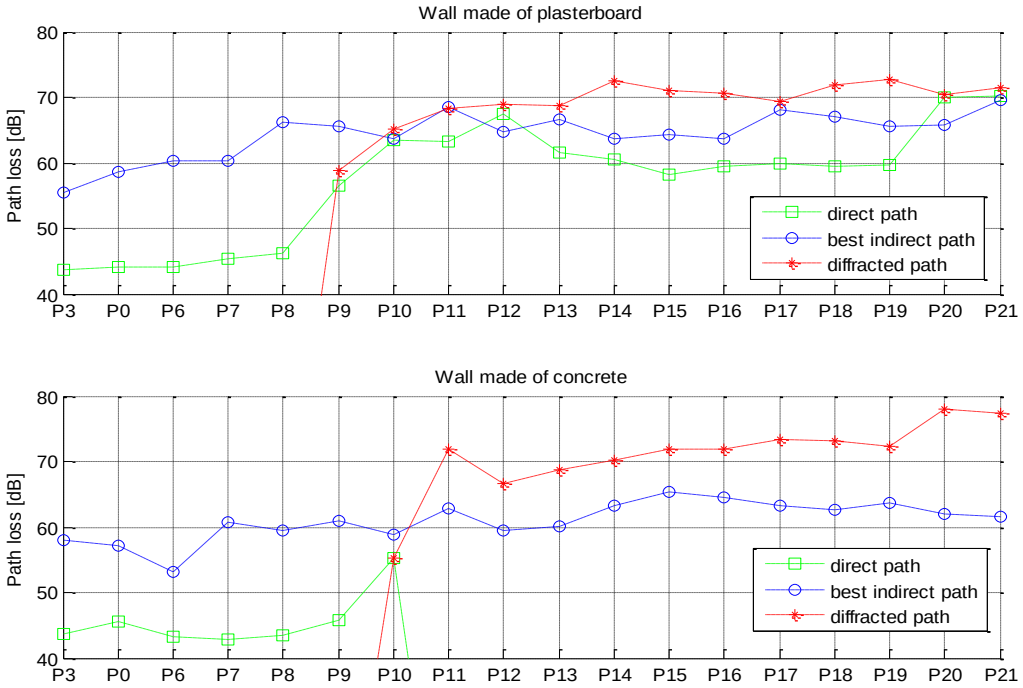

Figure 4.6. Path loss at the receiver side along the two walls

In the case of the wall made of plasterboard, the peaks of the path loss observed on the direct path at P12 or P20 are due to the irregular structure of the plasterboard wall containing metallic bars as well (see Figure 4.7).

Figure 4.7. Irregular structure of the plasterboard wall

4.1.2 Presence of obstructing doors

As for the previous case, the study of the sensitivity of the radio coverage to the presence of obstructing doors has been conducted through radio measurements below 6 GHz and at 60 GHz.

4.1.2.1 Measurements below 6 GHz

a) Measurement procedure

As illustrated in Figure 4.8, the Tx location (T6) has been chosen near a wooden door. At that location, different Tx positions, labeled *p1* to *p8*, close from each other consecutively of about 25 cm have been considered in order to match the following situations:

- the Tx position is above a door (*p1* to *p5*),
- the Tx position is on the other side of a door (*p6* and *p7*),
- the Tx position faces a door (*p8*).

For each Tx position, 6 Rx positions have been investigated with a measurement system identical to the one used for the calibration of the path loss models below 6 GHz (see Chapter 3). However, there are 2 differences: the VNA determines the channel frequency response in only three frequency sub-bands (SB2, SB4 and SB6) and the Tx antenna remains at a height of 2.3 m. The specifications of this campaign are summarized in Table 4.3.

b) Measurement results

The standard deviation of the path loss has been computed at each Rx position in the three considered scenarios; the results are available in Figure 4.9. When the Tx position moves above the door, a global variation of the path loss between 0.6 and 2 dB is noted. No major difference is observed when the position facing the door (*p8*) is tested with the positions above the door.

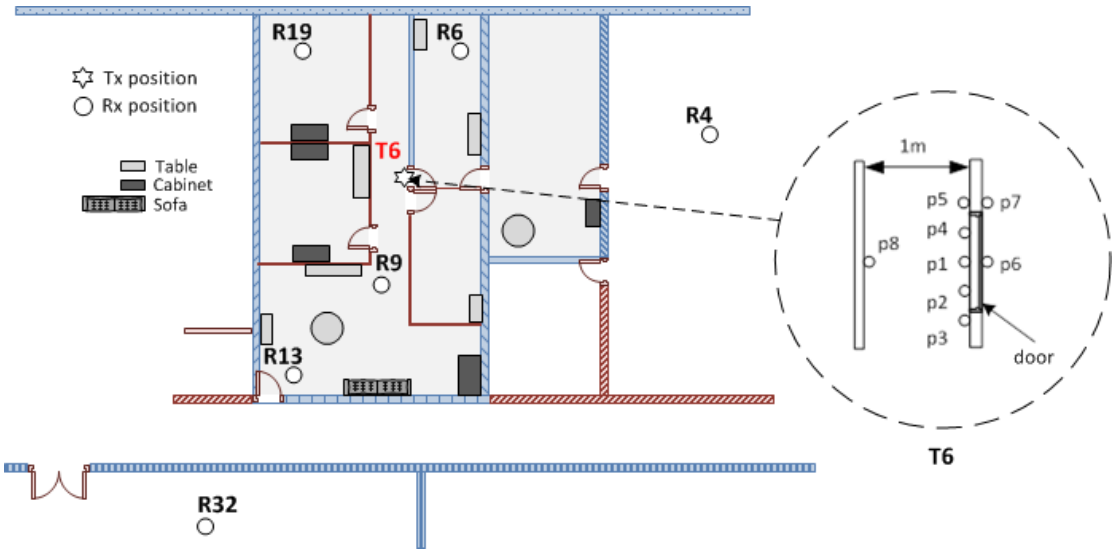

Figure 4.8. Tx location near a wooden door below 6 GHz

Table 4.3. Specifications of the campaign below 6 GHz with the Tx near a door

Antennas			
	Tx side	**Rx side**	
Type / Polarization	Omnidirectional in azimuth / V		
Beamwidth / Gain	75°(El) / 0 – 3.1 dBi		
Tx-Rx configurations			
Antenna height	2.3 m	1.19 m	
Number of positions	8	6	
Number of azimuths	1	60	
Elevation angle	0°		
Total	48		
Measurement setup			
Central frequency [MHz]	998	2450	5300
RF bandwidth [MHz]	60	100	
Max multipath delay	8 µs	5 µs	
Tx power	13 dBm		

However, when compared to the other side of the door, the variation becomes noticeable with at least 2 dB at R6, R9 and R19. These 3 positions have the particularity to be the closest to the door. By observing their localization and analyzing the information given by Table 4.4, the following conclusion can be drawn: the best side of the door is the one having the most Rx positions on its side. In such case, the gain, when compared to the other side, mostly depends on the constitution of the wall separating them (here a load bearing wall).

More details about the results of this campaign are available in Appendix C.2.

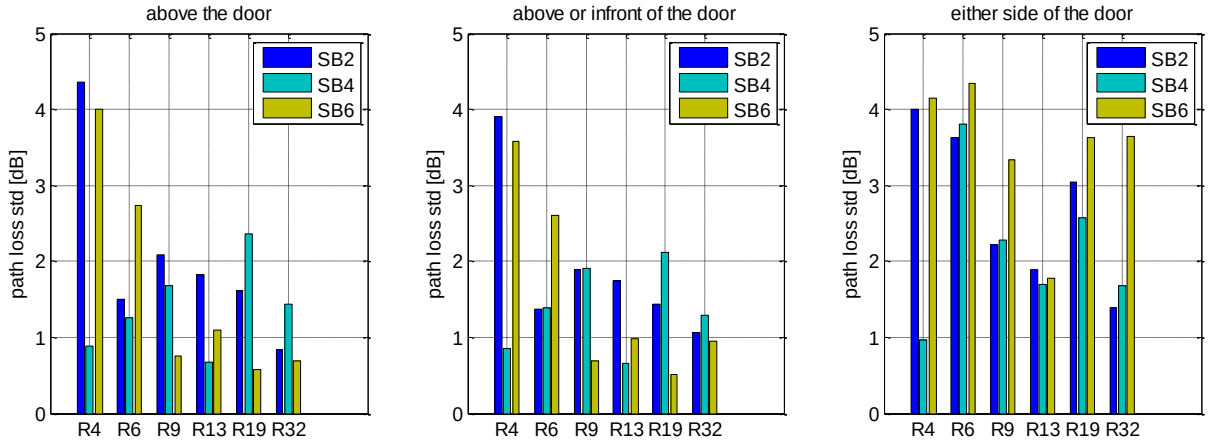

Figure 4.9. Path loss variation when the Tx is near a door below 6 GHz

Table 4.4. Best Tx position per Rx position

	R4	**R6**	**R9**	**R13**	**R19**	**R32**
SB2	*p4*	*p6*	*p3*	*p3*	*p5*	*p3*
SB4	*p6*	*p6*	*p2*	*p4*	*p5*	*p3*
SB6	*p7*	*p6*	*p5*	*p3*	*p3*	*p1*
Total	(p1 to p5) = 13, (p6 to p7) = 5					

4.1.2.2 Measurements at 60 GHz

The study realized at 60 GHz has consisted in determining the path loss variation at different positions in NLOS when the potentially obstructing doors switch from a closed state to an open one.

a) Measurement procedure

The measurement system is the same system than the one used to calibrate the directional and omnidirectional path loss models at 60 GHz (see Chapter 3). However, as shown in Figure 4.10, only one Tx position (T2) and 6 Rx positions in NLOS have been selected. Also the doors (highlighted in yellow) which were initially closed during the path loss models calibration have been opened for this study. The specifications of this campaign are summarized in Table 4.5.

b) Measurement results

During the closed-doors measurements presented in Section 3.2.3, the directions corresponding to the direct and best indirect paths have been identified at each Rx position. For this open-doors campaign, the previously identified directions have been conserved at each Rx position having a directional antenna in order to compute the path loss variation between the open and closed states. In the case of omnidirectional Rx positions, the average path loss is computed over the 60 angular steps in azimuth, as explained in Chapter 3.

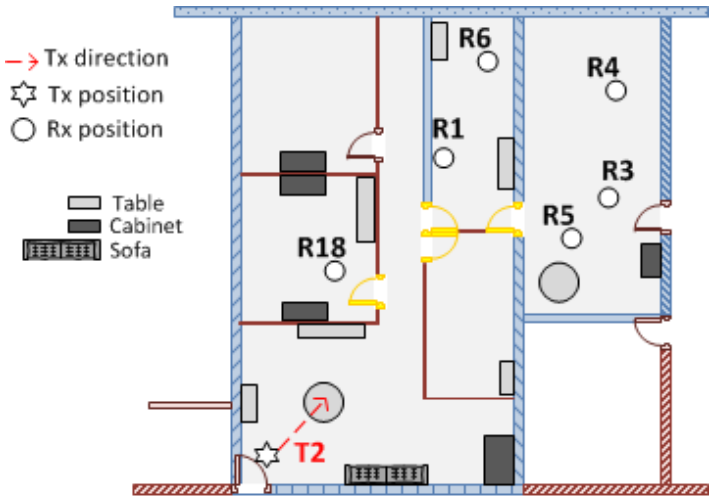

Figure 4.10. Presence of obstructing doors between Tx and Rx antennas at 60 GHz

Table 4.5. Setup of the campaign at 60 GHz with open doors

Antennas			
	Tx side	**Rx side**	
Type	Directional	Directional	Omnidirectional in azimuth
Polarization	V		
Beamwidth	120° (6 dB)	20°	30° (El)
Gain	7.3 dBi	19.5 dBi	2 dBi
Tx-Rx configurations			
Tx height	1.97 m	1.31 m	
Number of positions	1	R1, R3, R4, R5, R6, R18	R3, R4, R6
Number of azimuths	1	60	
Elevation angle	0°	0°, 10°, 20°, 30°, 40°	0°
Measurement setup			
Central frequency	61.0235 GHz		
RF bandwidth	2.047 GHz		
Max multipath delay	1 µs		
Tx power	13 dBm		

Based on the aforementioned process, the path loss variation corresponding to the difference between the open and closed states can then be determined at each Rx position. The results in Figure 4.11 show a decrease of the path loss due to having the doors open. The gain here goes up to 9 dB on the direct path. In [39], a gain varying from 7 to 15 dB was observed when opening the doors.

However, at R18, an increase of the path loss of about 6 dB is observed on the best indirect path. In fact, since the same direction has been processed when opening the doors, this additional loss is due to a door obstructing the direction (which is no more the actual best indirect path of the open-doors measurements, but of the closed-doors ones used as reference).

This study shows that the link budget in NLOS at 60 GHz may be significantly improved by simply opening the doors in a residential environment.

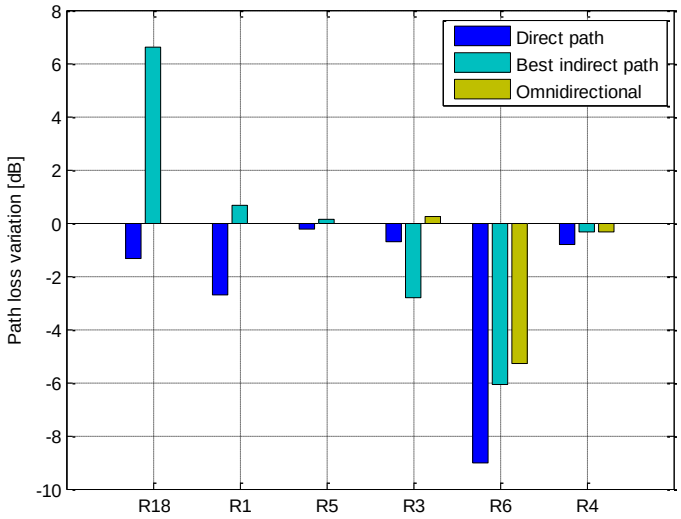

Figure 4.11. Path loss variation due to doors opening at 60 GHz

4.1.3 Transmitter in the middle of a room

In this scenario, the transmitter has been placed in the middle of a room without obstacles in its nearby environment. Unlike the two previous use cases, the measurements have only been performed below 6 GHz and not at 60 GHz. This is explained by the fact that for such scenario to be meaningful at 60 GHz, the directional Tx antenna should be near the ceiling, with its radiation pattern pointing downwards[9]. However, due to practical limitations (measurement system at disposal) this configuration has not been explored.

4.1.3.1 Measurement procedure

As shown in Figure 4.12, the transmitter (T5) is located on a table in the middle of the living room. At this location, several Tx positions distant from each other by 5 cm on average have been chosen so that they describe three types of motion:

- an horizontal movement (in red, 9 positions),
- a vertical movement (in green, 9 positions),
- a square movement (in yellow, 4 positions).

Also, for each Tx position, 5 Rx positions have been investigated with the same measurement system than the one used in the wall edge scenario (see Section 4.1.1.1). The specifications of this campaign are summarized in Table 4.6.

[9] A better positioning could be in the corner of a room.

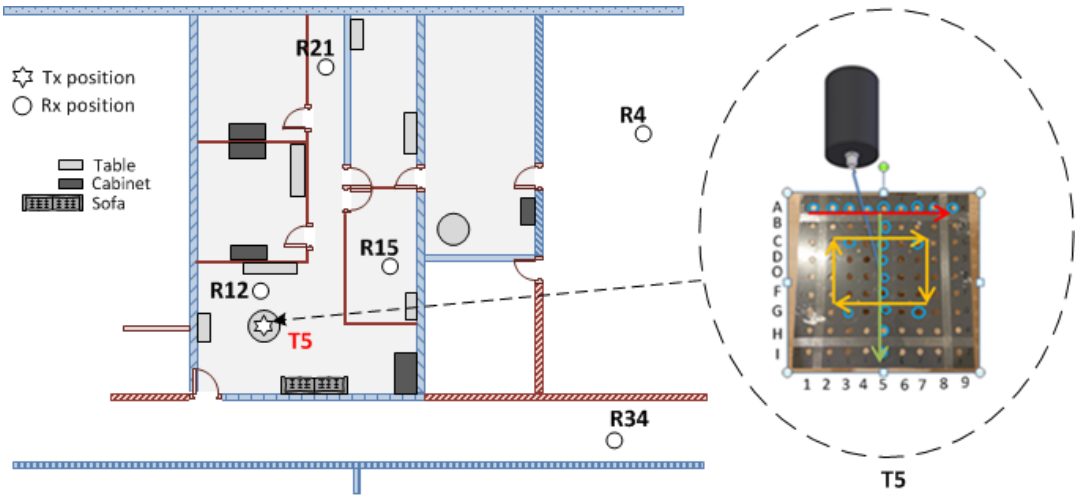

Figure 4.12.Tx position in the middle of a room

Table 4.6. Setup of the "middle-room" campaign below 6 GHz

Antennas			
	Tx side	**Rx side**	
Type / Polarization	Omnidirectional in azimuth / V		
Beamwidth / Gain	75°(El) / 0 – 3.1 dBi		
Tx-Rx configurations			
Antenna height	1.19 m		
Number of positions	21	5	
Number of azimuths	1	60	
Elevation angle	0°		
Total	110		
Measurement setup			
Central frequency [MHz]	998	2450	5300
RF bandwidth [MHz]	60	100	
Max multipath delay	8 µs	5 µs	
Tx power	13 dBm		

4.1.3.2 Measurement results

At each Rx position, the path loss variation has been characterized by its standard deviation when considering all Tx positions. The results in Figure 4.13 display a variation globally around 0.5 dB. This indicates a weak sensitivity to the Tx position at the receivers side, except for R21.

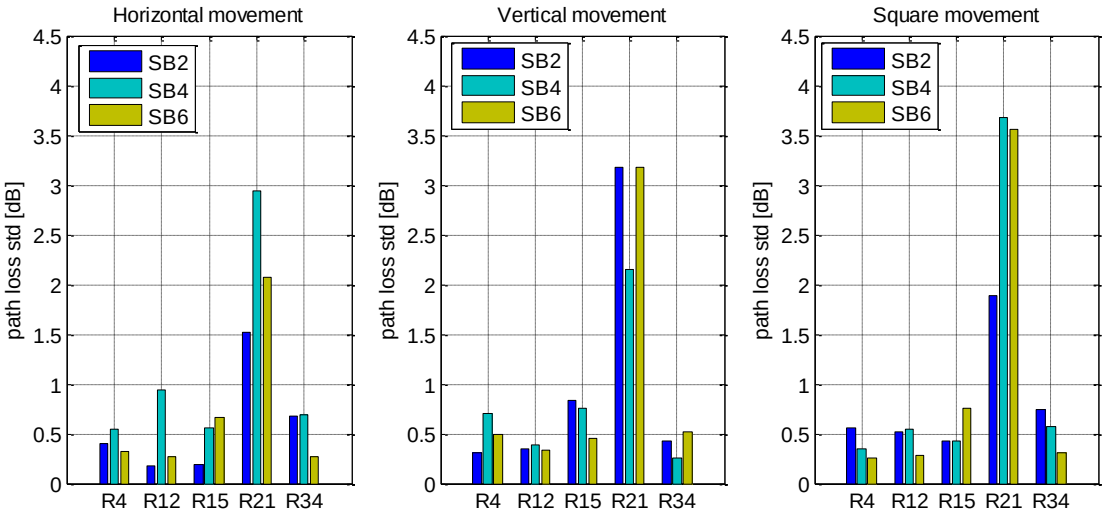

Figure 4.13. Path loss standard deviation when the Tx is in the middle of a room

The explanation of this difference lies in the estimation of the average path loss at R21. Since that position was located in a 1 meter-width corridor, the rotating having a radius of 56 cm could not rotate in azimuth over the 60 angular steps. Instead, 60 snapshots of the channel have been taken for the same azimuth (0°) resulting in a less accurate estimation of the path loss. More details about the results of this campaign are available in Appendix C.3.

4.1.4 Transmitter inside a piece of furniture

In this scenario, the transmitter has been placed inside a cabinet. As for the previous use case, the measurements have only been performed below 6 GHz and not at 60 GHz due to some practical limitations: the Tx module, being too large, could not fit inside the cabinet.

4.1.4.1 Measurement procedure

As shown in Figure 4.14, five Tx positions have been considered at various heights inside a cabinet. The highest position, *n5*, is the only one located outside the cabinet, on its top. For each Tx height, the measurements have been performed at 6 Rx positions with the same measurement system than the one used during the wall edge scenario (see Section 4.1.1.1). The specifications of this campaign are summarized in Table 4.7.

4.1.4.2 Measurement results

At each Rx position, the path loss variation has been investigated by computing its standard deviation when considering all Tx positions. The results in Figure 4.15 exhibit in most cases a variation of at least 2 dB, which can exceed 3 dB especially for SB6. It's globally observed that the higher is the frequency, the higher is the variation. This is probably due to the frequency dependent electrical properties of the materials constituting the cabinet (wood and glass). As a matter of fact, the only Tx position having no obstructing material (*n5*) is actually the best one in most cases as indicated in Table 4.8. More details about the results of this campaign are available in Appendix C.4.

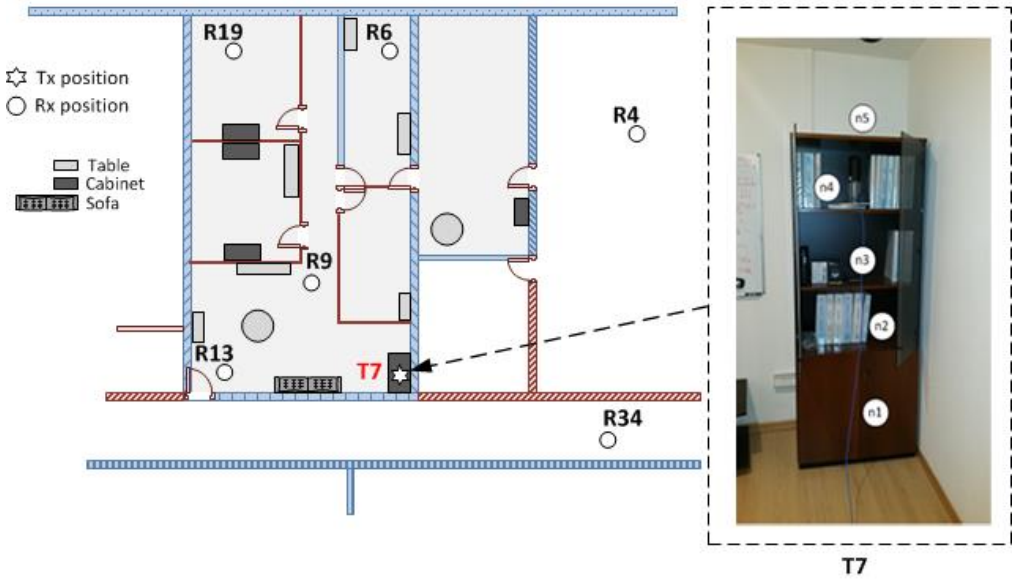

Figure 4.14. Tx position inside a cabinet at different heights

Table 4.7. Setup of the campaign with the Tx inside a cabinet

Antennas			
	Tx side	**Rx side**	
Type / Polarization	Omnidirectional in azimuth / V		
Beamwidth / Gain	75°(El) / 0 – 3.1 dBi 0		
Tx-Rx configurations			
Antenna height	0.21 m, 0.91 m, 1.30 m 1.73 m, 2.10 m	1.19 m	
Number of positions	1	6	
Number of azimuths	1	60	
Elevation angle	0°		
Total	30		
Measurement setup			
Central frequency [MHz]	998	2450	5300
RF bandwidth [MHz]	60	100	
Max multipath delay	8 µs	5 µs	
Tx power	13 dBm		

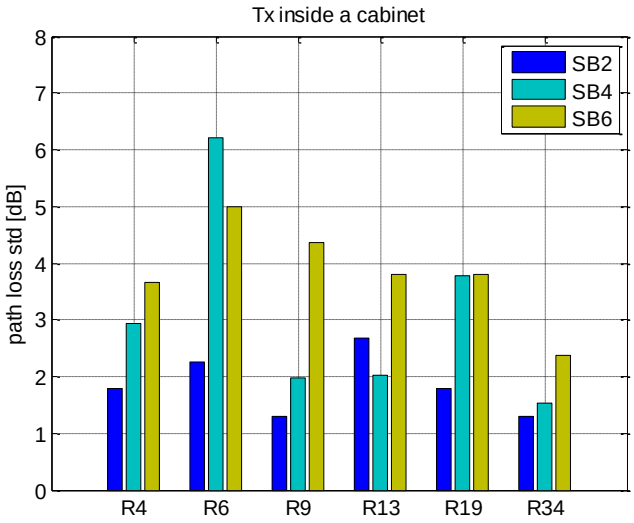

Figure 4.15. Path loss standard deviation when the Tx is inside a cabinet

Table 4.8. Best Tx position per Rx position

	R4	**R6**	**R9**	**R13**	**R19**	**R34**
SB2	*n5*	*n4*	*n5*	*n3*	*n5*	*n2*
SB4	*n5*	*n5*	*n5*	*n4*	*n5*	*n5*
SB6	*n5*	*n5*	*n5*	*n5*	*n5*	*n5*

4.2 Impact of the presence of people

The measurements that have been described in Chapter 3 and in the first sections of this chapter have been performed in a static environment, without people inside. In fact, when there are people in the transmission channel between a transmitter and a receiver, they act as supplementary obstacles. As a result, an additional attenuation of the signal may be observed at the receiver side depending on the people locations; this effect is called human-body shadowing [40]. In order to characterize this extra loss, two measurement campaigns have been carried out respectively below 6 GHz and at 60 GHz. The measurements have been conducted in the same home environment described in Chapter 3.

4.2.1 Human body shadowing below 6 GHz

4.2.1.1 Measurement procedure

Two scenarios have been considered. Both of them involve one transmitter and one receiver whose communication might be hindered by the presence of people. The first one, depicted in Figure 4.16, is a LOS transmission while the other one, illustrated in Figure 4.17, is a non-visibility scenario. In both cases:

- 4 Tx heights have been considered,
- up to 4 persons may be simultaneously present in the measurement environment because of various configurations (19 in LOS and 13 in NLOS),

- each person present in the measurement environment may be located at one of the p_i positions (see Figure 4.16, Figure 4.17 and Table 4.9),
- all the persons present in the measurement environment are in the same static state which is either the *state A* (meaning "*Assis*" in French) in which everyone is seated, or the *state D* (meaning "*Debout*" in French) in which everyone is standing.

The measurement system is the same than the one used during the wall edge scenario (see Section 4.1.1.1). The specifications of this campaign are summarized in Table 4.9. Note that the scenario labeled "*1234D*" involving 4 persons in LOS means that only the people at locations *p1*, *p2*, *p3* and *p4* are present inside the measurement environment, and are in the *state D*. The same logic is applied to the other notations.

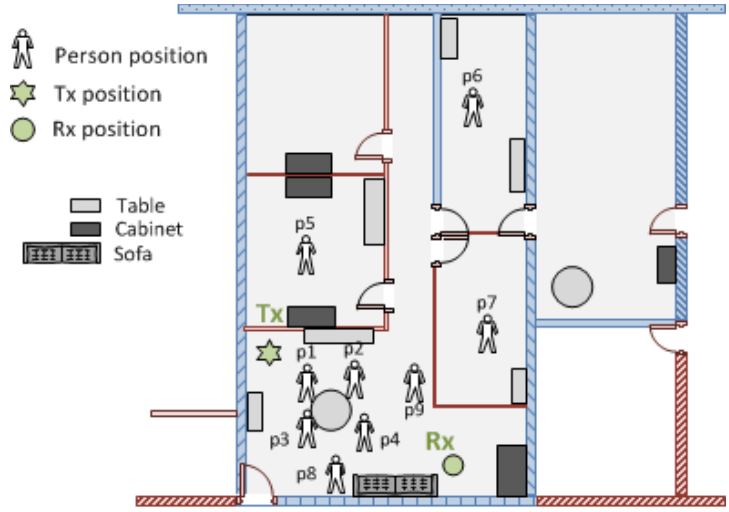

Figure 4.16. Study of the effect of human blockage in LOS below 6 GHz

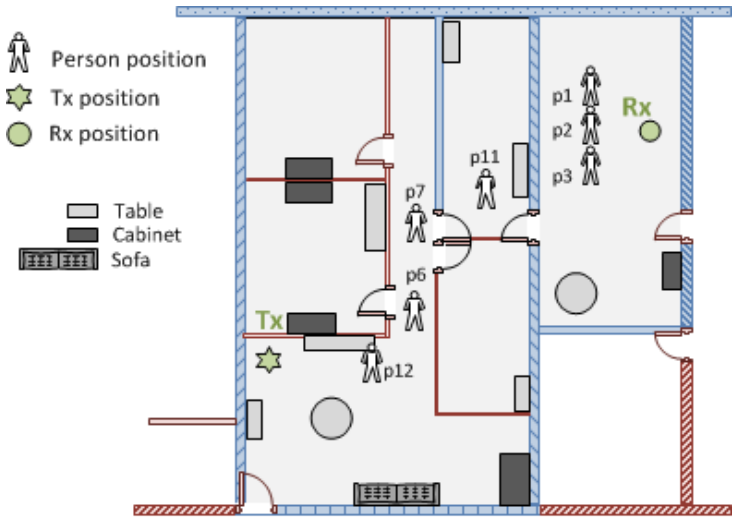

Figure 4.17. Study of the effect of human blockage in NLOS below 6 GHz

Table 4.9. Parameters of the study of the effect of human blockage below 6 GHz

Antennas				
	Tx side		**Rx side**	
Type / Polarization	Omnidirectional in azimuth / V			
Beamwidth / Gain	75°(El) / 0 – 3.1 dBi			
Tx-Rx configurations				
Antenna height	0.23 m, 1.05 m, 1.67 m, 2.30 m		1.19 m	
Number of positions	1		2 (LOS:1, NLOS:1)	
Number of azimuths	1		60	
Elevation angle	0°			
Scenarios per Rx position				
	1 person	**2 persons**	**3 persons**	**4 persons**
Rx LOS (19)	1A, 1D, 2A, 2D, 3A, 3D, 4A, 4D	14A, 14D, 24A, 24D, 34A, 34D	489A, 489D	1234A, 1234D, 4567D
Rx NLOS (13)	2A, 2D, 6D, 7D, 8D, 11D, 12D	6_12D, 7_11D	123A, 124D	6_7_11_12D, 2_7_8_11D
Measurement setup				
Central frequency [MHz]	998		2450	5300
RF bandwidth [MHz]	60		100	
Max multipath delay	8 µs		5 µs	
Tx power	13 dBm			

4.2.1.2 Measurement results

For each scenario, the average path loss, $\overline{PL_s}$ is computed over the 60 angular steps in azimuth as explained in Chapter 3. From this mean value is derived the relative loss given by:

$$PL_R(s)[dB] = \overline{PL_S} - \overline{PL_E} \quad (4.1)$$

where:

- PL_R is the relative path loss for scenario s,
- $\overline{PL_E}$ is the average path loss determined at the chosen Rx position when there is no one inside the measurement environment (see Chapter 3).

Figure 4.18 and Figure 4.19 illustrate the path loss variation in LOS and NLOS for h_{Tx} = 1.05 m. In this case, the Tx and Rx antennas are nearly of the same height. It is observed that the relative loss stays globally below 2 dB. However, it may exceed 2 dB when the blockage occurs near the transmitter (see *p1* in LOS) or the receiver (see *p3* in NLOS).

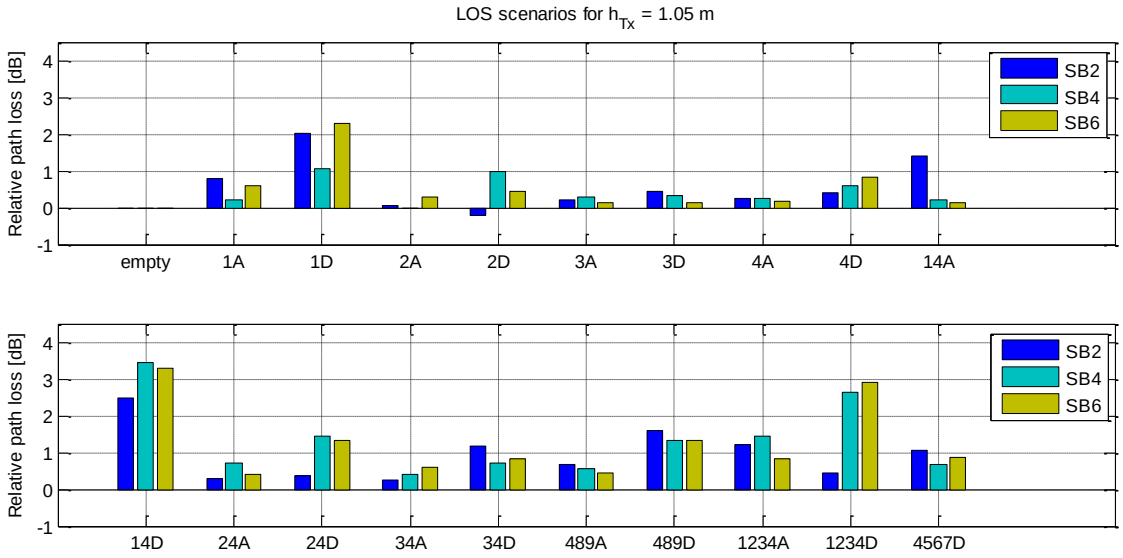

Figure 4.18. Path loss variation with respect to the empty rooms scenario in LOS

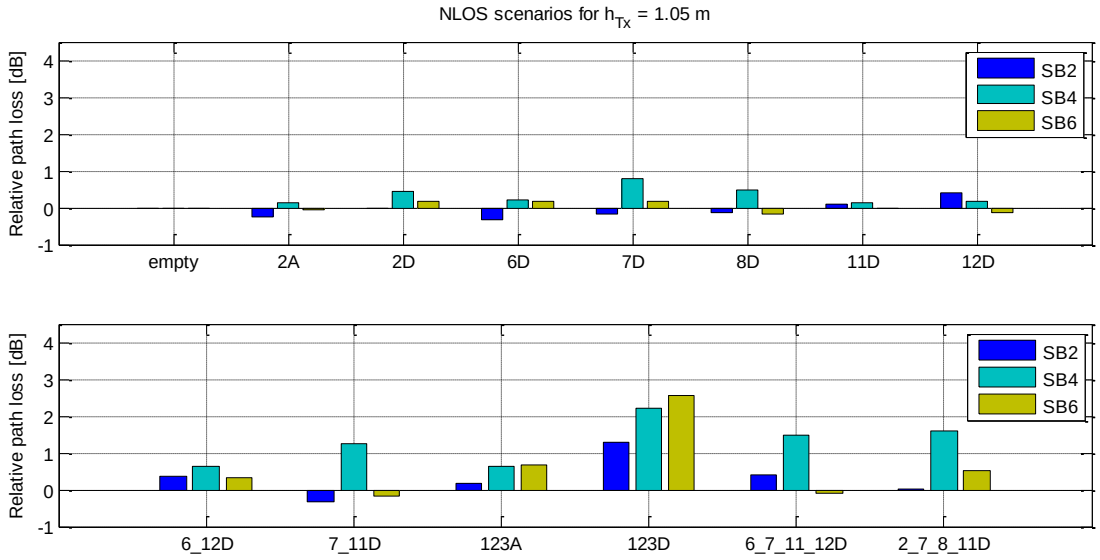

Figure 4.19. Path loss variation with respect to the empty rooms scenario in NLOS

Even if similar observations can be made for the other Tx heights (see Appendix C.5), an explicit study of the effect of the Tx antenna height has been carried out by computing the relative average path loss given by:

$$\overline{PL_R}(h_{Tx})[dB] = 10\log_{10}\left(\frac{1}{N_s} * \sum_{i=1}^{N_s} 10^{\left[\frac{PL_{S_i}(h_{Tx})}{10}\right]}\right) - \overline{PL_E}(h_{Tx}) \qquad (4.2)$$

where :

- $\overline{PL_R}$ is the relative average path loss,
- $\overline{PL_E}$ is the average path loss determined at Rx when there is no people inside the measurement environment,
- N_s is the total number of scenarios at Rx,

- PL_{S_i} is the average path loss computed over the 60 azimuth steps for the i-th scenario.

The results presented in Figure 4.20 indicate that the effect of human body shadowing is maximal when the transmitter and the receiver are relatively at the same height. However, it's possible to decrease its influence by increasing the Tx antenna height.

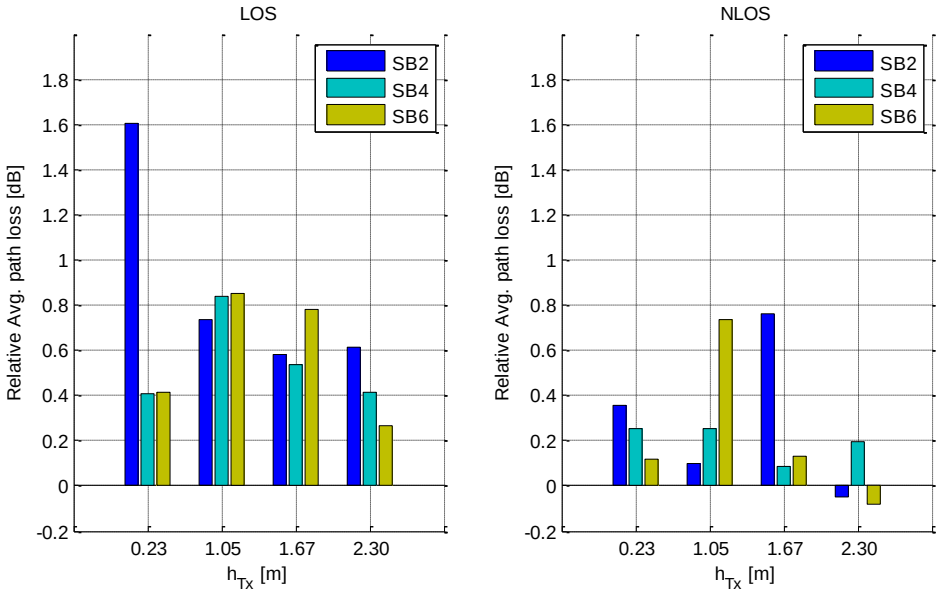

Figure 4.20. Effect of the Tx antenna height on the path loss variation

4.2.2 Human body shadowing at 60 GHz

The effect of human body shadowing in the mm-waves has been the subject of several works in the literature, especially in LOS conditions. In [41]–[45], the attenuation is found to be between 10 and 25 dB and can even exceed 40 dB when the direct path is blocked [46] [47]. The study conducted in [48] has shown that there is no obvious relationship between the increase of the frequency and the losses in mm-wave bands.

The measurements presented in this section have been conducted at 60 GHz in both LOS and NLOS conditions.

4.2.2.1 Measurement procedure

As shown in Figure 4.21, two configurations involving human blockage have been studied at 60 GHz. The first one is about a LOS transmission (Rx1) while the other one relates to a transmission in NLOS (Rx2). Both of them features 14 scenarios involving up to 4 people who are either in the state A or state D, as previously explained in Section 4.2.2.a. In each scenario, the measurements have been performed with the same system than the one used to calibrate the path loss models at 60 GHz except that:

- the measurements have sequentially been achieved with a directional (20°) and an omnidirectional antenna at the receiver side,
- the elevation angle of the directional antenna has been steered to 10°, while that of the omnidirectional antenna remains at 0°.

The specifications of this campaign are summarized in Table 4.10.

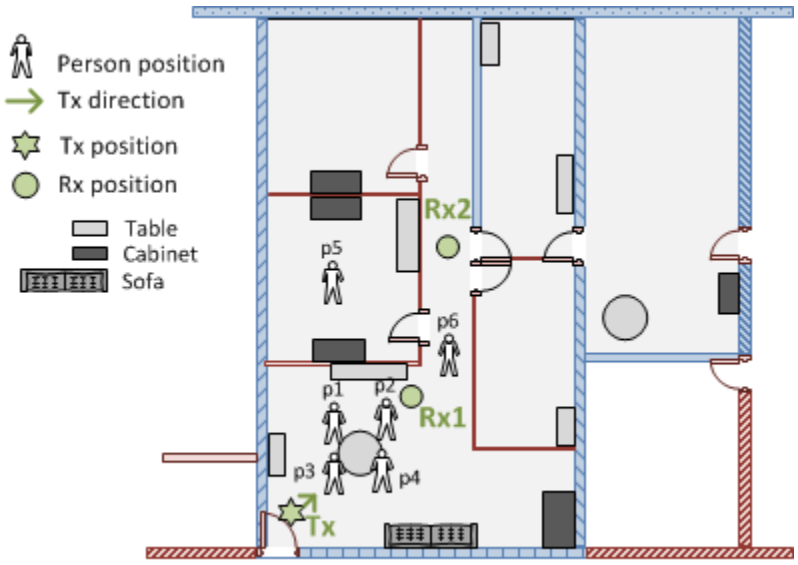

Figure 4.21. Study of the effect of human blockage at 60 GHz

Table 4.10. Parameters of the study of the effect of human blockage at 60 GHz

Antennas				
	Tx side	**Rx side**		
Type /Polarization	Directional/V	Directional/V	Omnidirectional/V	
Beamwidth/Gain	120°/7.3 dBi	20°/19.5 dBi	30° (El)/ 2 dBi	
Tx-Rx configurations				
Antenna height	1.97 m	1.31 m		
Number of positions	1	2		
Number of azimuths	1	60		
Elevation angle	0°	10°	0°	
Scenarios per Rx position				
	1 person	**2 persons**	**3 persons**	**4 persons**
Rx LOS (14)	1A, 1D; 2A; 2D; 3A; 3D; 4A; 4D	14A, 14D, 23A, 23D	-	1234A, 1234D
Rx NLOS (14)	2A, 2D, 3A, 3D, 4A, 4D	12A, 12D, 23A, 23D	125A, 125D, 126A, 126D	-
Measurement setup				
Central frequency	61.0235 GHz			
RF bandwidth	2.047 GHz			
Max multipath delay	1 μs			
Tx power	13 dBm			

4.2.2.2 Measurement results

In each scenario involving a directional Rx antenna, the path loss on the direct and best indirect paths has been determined as explained in Section 3.2.3. In the case of omnidirectional Rx antenna, the average path loss is computed over the 60 angular steps in azimuth, as described in Section 3.2.5. The results are then compared to the empty-rooms scenario, addressed in Chapter 3, by applying a difference similar to (4.1).

In Figure 4.22 is given, for each scenario, the path loss variation induced by the presence of people when compared to the empty-rooms scenario in LOS and NLOS. In both configurations, the worst cases occur when there is someone obstructing the dominant propagation path (*p2* in LOS and *p6* in NLOS). It's observed up to 15 dB of supplementary loss in LOS versus 3 dB in NLOS. However, it's important to remember that the gap between the received power levels in LOS and NLOS are most of the time important (around 30 dB for the model presented in 3.2.4). Thus, a loss of 3 dB in NLOS may be more harmful to a data transmission at this frequency band than a loss of 15 dB in LOS. This is demonstrated in the next section.

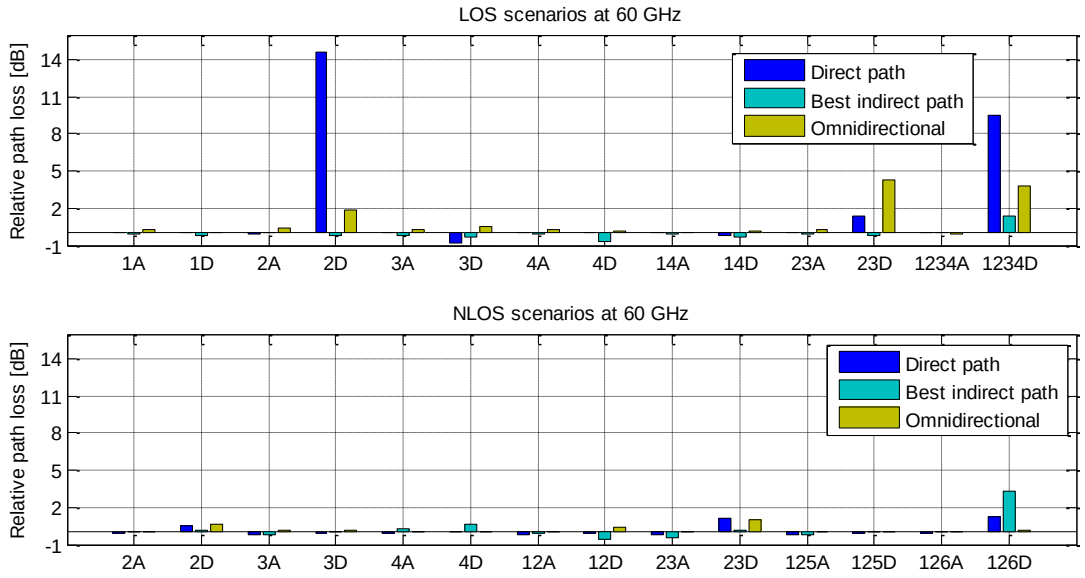

Figure 4.22. Path loss variation with respect to the empty rooms scenario at 60 GHz

4.3 Impact of the visibility condition at 60 GHz

Radio links at 60 GHz are known to be strongly attenuated over distance due to factors like oxygen attenuation (can be overlooked in indoor), coupled to a low penetration through obstacles [49]. This suggests that mm-waves communications are particularly inefficient in non-visibility conditions. In fact, most use cases involving communication at 60 GHz revolve primarily around LOS scenarios [50].

In this section is conducted a more practical study of the impact of the visibility condition on indoor communications at 60 GHz. The first step consisted in determining the achievable throughput by the means of IEEE 802.11ad equipment. The following step explores the possibility to ensure a quality of service at 60 GHz with a particular focus on NLOS communications.

The measurements described in this section have been conducted in the same residential environment depicted in Chapter 3.

4.3.1 Throughput measurements

4.3.1.1 Measurement system

The measurement system, illustrated in Figure 4.23, consists of one **access point** (AP) and one **laptop** which acts as the station (STA). Both devices are equipped with a 12 elements rectangular **antenna array** of dimension 17 mm x 7 mm, and a Qualcomm 802.11ad **mini PCIe card** based on the Sparrow chipset. This commercial solution of the IEEE 802.11ad standard implements the single carrier physical layer (SC-PHY), as well as the Tx and Rx beamforming mechanisms mainly in the azimuth plane.

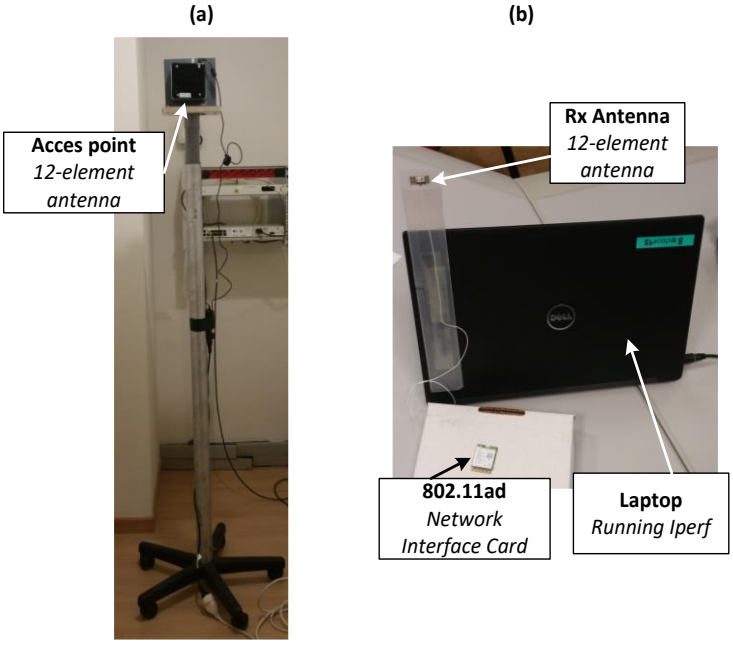

Figure 4.23. 802.11ad access point (a) and station (b)

4.3.1.2 Measurement procedure

As shown in Figure 4.24, the 802.11ad throughput has been measured for 5 Tx positions at 51 locations inside the measurement environment. Among these locations, 31 Tx-Rx configurations are in LOS versus 23 in NLOS. Concerning the non-visibility scenarios, they have involved up to 2 obstructing dividing walls made of plasterboard (see T5). However, it was generally not possible to maintain the 802.11ad radio link through load-bearing walls (see T1 and T2).

During measurements, the laptop has been rotated in azimuth with a step size of 45° for each Tx-Rx configuration. At each of the 8 angular steps, the laptop, by the means of the iperf software, measures each second the Transmission Control Protocol (TCP) throughput for a total duration of 40 seconds. The output is then stored in order to be processed as explained in the next section.

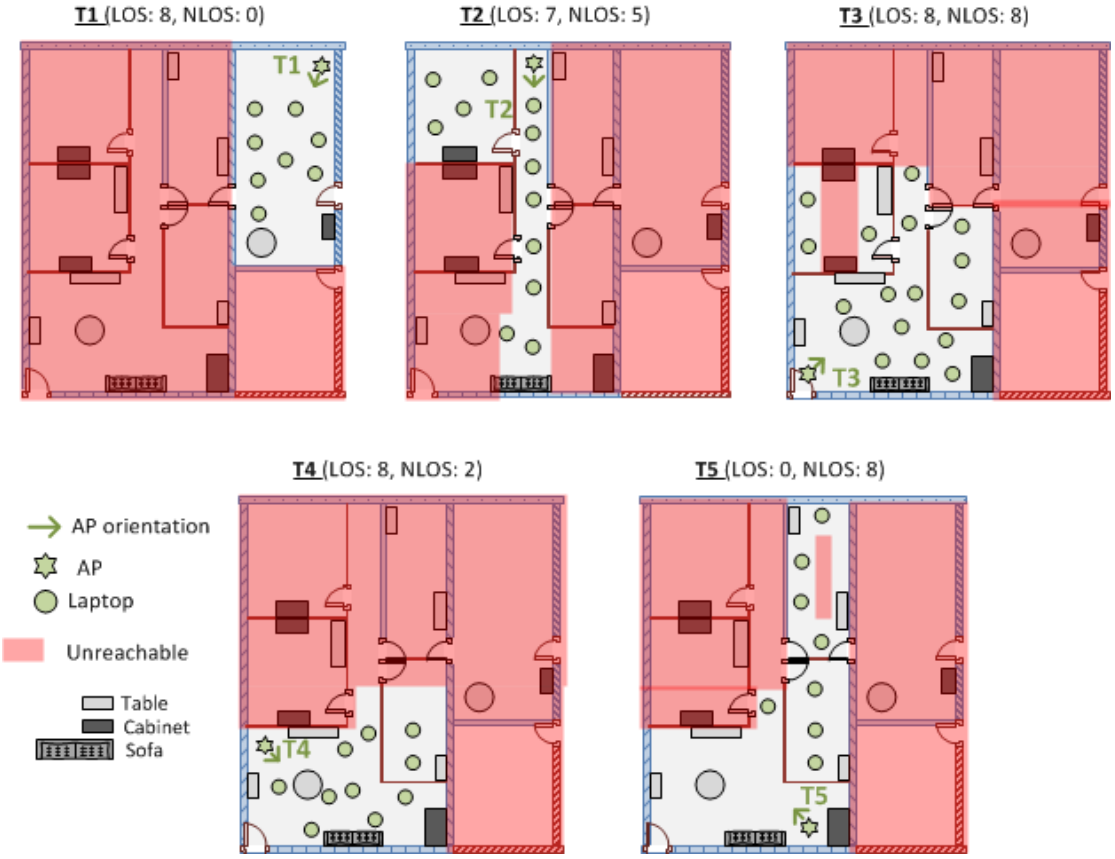

Figure 4.24. 802.11ad throughput measurement plan for various Tx locations

4.3.1.3 Measurement results

For each Tx-Rx configuration, the angular average throughput at a given azimuth step is computed as follows:

$$D(T_i, R_{ji}, \theta_k) = \frac{1}{30} \sum_{t=11}^{40} d(T_i, R_{ji}, \theta_k, t) \qquad (4.3)$$

where :

- T_i is the i-th Tx position and R_{ji} is the j-th Rx position associated to T_i,
- θ_k is the azimuth angle corresponding to the k-th step at the R_{ji} position,
- d is the instantaneous TCP throughput measured after t seconds,
- D is the angular average throughput at θ_k.

From (4.3), it's observed that the average throughput has been deduced from the last 30 seconds because of the throughput fluctuation during the first seconds of the test. Three data rate metrics are derived from the 8 angular average throughputs determined for each Tx-Rx configuration:

- D_{min}, the minimum data rate of the Tx-Rx configuration, which corresponds to the smallest angular average throughput,
- D_{max}, the maximum data rate of the Tx-Rx configuration, which corresponds to the greatest angular average throughput,
- D_{avg}, the average data rate of the Tx-Rx configuration, which corresponds to the average value of the 8 angular average throughputs.

Thus, knowing for each Tx-Rx configuration the values of D_{min}, D_{max}, D_{avg} as well as the Tx-Rx separation distance, the obtained 802.11ad data rates can be expressed as a function of distance in LOS and NLOS as shown in Figure 4.25 and Figure 4.26.

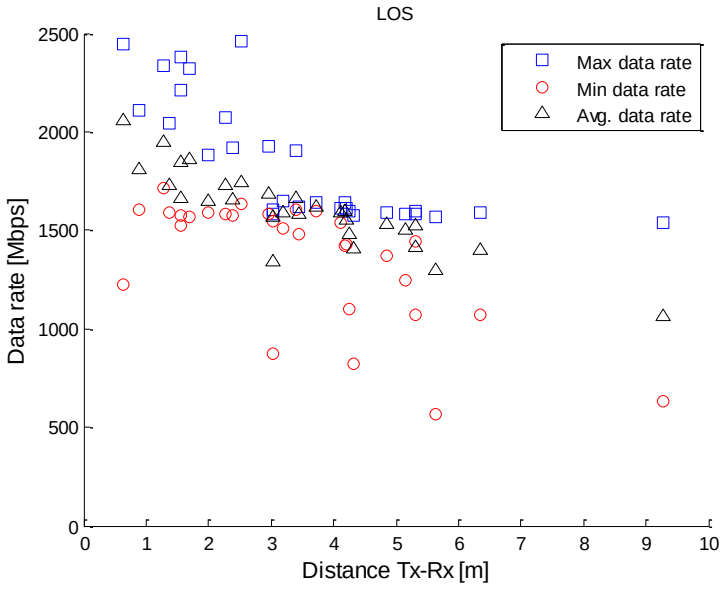

Figure 4.25. 802.11ad TCP throughput in LOS

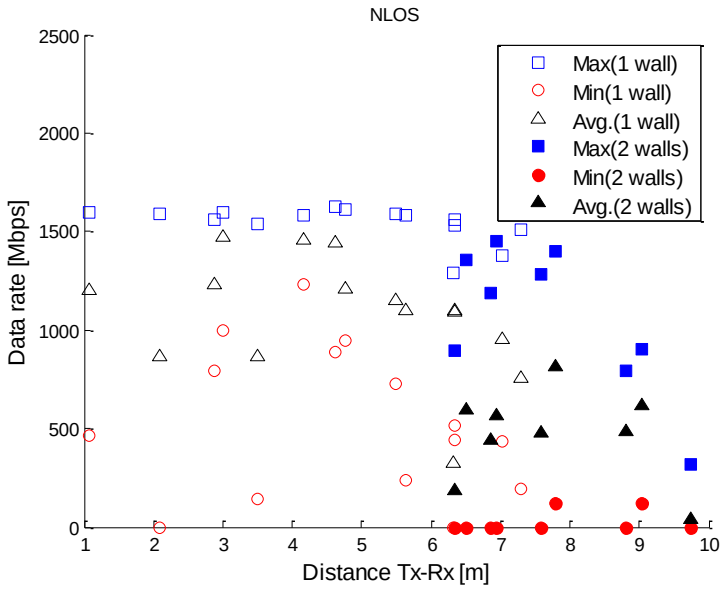

Figure 4.26. 802.11ad TCP throughput in NLOS

The results show that in LOS the data rate is, as expected, very high. In fact, for all Tx-Rx configurations, the maximum achievable data rate is 2.5 Gbps. However, it's almost two times lower than the maximum theoretical throughput which is 4.6 Gbps for the single carrier physical layer. This difference may be explained by the fact the 802.11ad chipset didn't actually use the highest modulation and coding scheme (MCS) available for this standard. This information could not be retrieved from the chipset but it's certain that at least MCS 9 has been used (see Appendix D.2.b for more details). The minimum data rate is globally greater than 1 Gbps and the average of the average data rates is around 1.6 Gbps.

In NLOS, the results show, as expected, lower data rates when compared to the LOS scenarios. The maximum data rate achieved is 1.6 Gbps, the average of the average data rates is around 800 Mbps and in the worst cases the radio link does not last for 40 seconds (0 Mbps). Even if the performance remains inferior to the LOS condition, the data rate in the favorable scenarios remains relatively high when compared to other Wi-Fi versions such as the IEEE 802.11n whose peak throughput is 600 Mbps.

As a conclusion of this study, the results presented in this section showed that the 802.11ad throughput depends on the visibility condition as well as the relative orientation between the AP and the station. The measured throughput is relatively high in the favorable scenarios in both LOS and NLOS conditions. From this observation, one question arises: is it possible to guarantee a certain quality of service at 60 GHz, especially in NLOS? The following sections are meant to answer this interrogation.

4.3.2 RMS delay spread analysis

As explained in Chapter 2 the RMS delay spread is an important parameter of any radio channel because it imposes a limitation to the symbol rate transmission in order to avoid intersymbol interference (ISI).

The study of the RMS delay presented in this section has been conducted by processing the results obtained from the campaign at 60 GHz detailed in Chapter 3. Here, the analysis has been focused on the measured channel impulse responses. For each Tx-Rx configuration, the RMS delay spread has been computed based on the multipath components having:

- an excess delay smaller than 100 ns to filter some measurement defects,
- and a power at most 20 dB lower than the strongest propagation path.

The results displayed in Figure 4.27 show that the RMS delay spread remains globally below 4 ns in LOS versus 15.8 ns in NLOS.

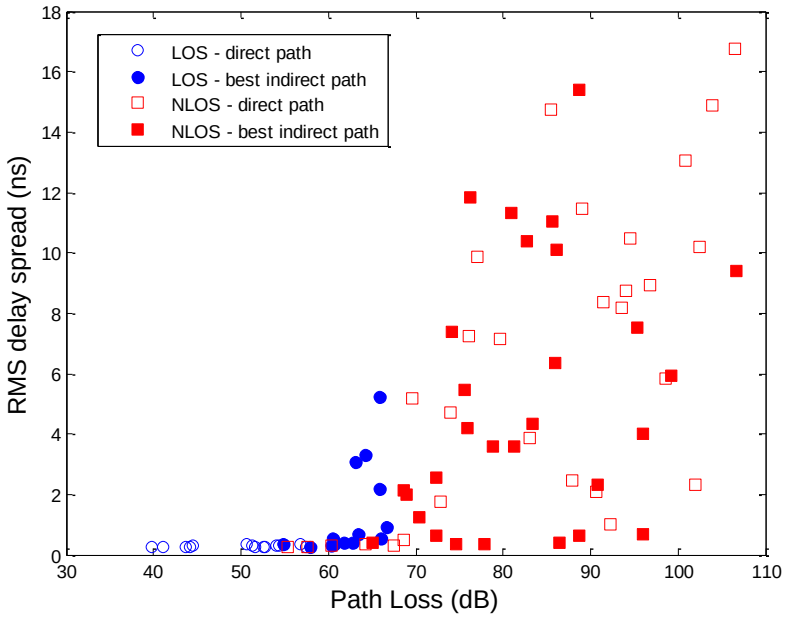

Figure 4.27. Computed RMS delay spread at 60 GHz in LOS and NLOS

The SC-PHY of the IEEE 802.11ad standard uses a modulation rate of 1.76 Gsym/s [51] corresponding to a symbol duration of 0.57 ns. Also, between blocks transmission, there is a guard interval of 64 symbols [52] allowing up to 36 ns of channel equalization. In order to avoid ISI, that latter duration has to be at least 4 times greater than the RMS delay spread [53], [54]. Thus, as a conclusion, in LOS, the ISI probability is very low (since 36 ns > 4*4 ns). However in NLOS, due to greater values of the RMS delay spread, communications may very likely suffer from high ISI. This could be probably reduced with more directional antennas at the expense of a greater vulnerability to obstructions.

4.3.3 Effect of human blockage on the throughput

The throughput measurement campaign described in Section 4.3.1 does not account for the presence of people inside the measurement environment. In order to have an insight of the effect of human blockage on the throughput, 6 Rx positions of the configuration T3 of that campaign have been chosen. These positions have been investigated with up to 4 people simultaneously present in either a static state or randomly walking around (see Figure 4.28).

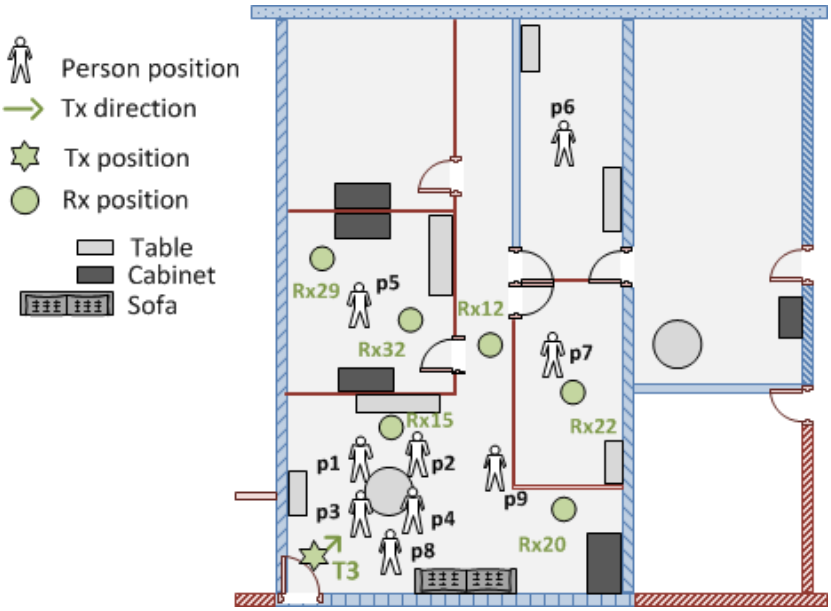

Figure 4.28. Study of the effect of human blockage on the 802.11ad throughput

Among the 6 Rx positions, there are 2 positions in LOS (Rx15 and Rx20) versus 4 in NLOS (Rx12, Rx22, Rx29 and Rx32). The measurement procedure is the same than one described in Section 4.3.1, except that the Rx side is not rotated in azimuth. In fact, the azimuth angle of each Rx position has been set to the azimuth angle which had the greatest angular average throughput (see Section 4.3.1.c) during the throughput measurements with no people inside the measurement environment.

4.3.3.1 Static measurements

The static measurements have consisted in measuring the throughput in 51 scenarios involving up to 4 people. In each case, the persons remain either seated (state A) or standing (state D). The complete list of the scenarios considered at each Rx position is given in Table 4.11. As a reminder, the scenario labeled "*1234D*" means that only the people at locations *p1*, *p2*, *p3* and *p4* are present inside the measurement environment, and are in the *state D*. The same logic is applied to the other notations.

Table 4.11. Configurations tested for each Rx position

Scenarios per Rx position				
	1 person	**2 persons**	**3 persons**	**4 persons**
Rx15 (16)	1A, 1D , 2A, 2D, 3A, 3D, 4A; 4D	13A, 13D, 23A, 23D, 34A, 34D	-	1234A, 1234D
Rx20 (8)	-	23A, 23D, 24A, 24D	234A, 234D	1234A, 1234D
Rx12 (8)	3A, 3D, 4A, 4D, 6A, 6D	34A, 34D	-	-
Rx22 (7)	2D	24A, 24D	246A, 246D, 247A, 247D	-
Rx29 (6)	-	12A, 12D	125A, 125D, 126A, 126D	-
Rx32 (6)				
Total	51 (LOS: 24, NLOS: 27)			

For each scenario the average throughput is computed over 30 seconds as indicated in (4.3). From this mean throughput is determined the relative loss given by:

$$L_D(T_3, R_i, S_{ki})[\%] = 100 * \frac{D_{max}(T_3, R_i, \theta_{max}) - D(T_3, R_i, \theta_{max}, S_{ki})}{D_{max}(T_3, R_i, \theta_{max})} \quad (4.4)$$

where :

- L_D is the relative throughput loss induced by the presence of people,
- R_i is the i-th Rx position,
- S_{ki} is the k-th scenario at R_i,
- D_{max} is the max data rate at R_i when there is no people,
- θ_{max} is the azimuth angle corresponding to D_{max},
- D is the average throughput at R_i for the scenario S_{ki}.

The results for each scenario are shown in Figure 4.29. It's observed that in LOS the relative throughput loss remains globally inferior to 20%. This loss is maximal when there is someone obstructing the direct path, as it is the case for the scenario 1D at Rx15.

However, in NLOS, half of the total numbers of scenarios have at least a relative loss of 50% which in most cases go up to 100 %. This indicates that the radio links are quite sensitive in NLOS to the presence of people, even when they are static. What about the impact of people in motion?

4.3.3.2 Dynamic measurements

Throughput measurements have also been performed when 4 people are randomly walking around during 120 seconds. For each Rx position, the instantaneous TCP throughput is displayed in Figure 4.30. The results show that in LOS, the presence of people randomly walking around induces some downside peaks of the throughput which remains globally greater than 1 Gbps for the whole period of observation. However, in NLOS, the amplitudes of the downside peaks are so important that disruptions of the radio link are observed before one minute in all cases.

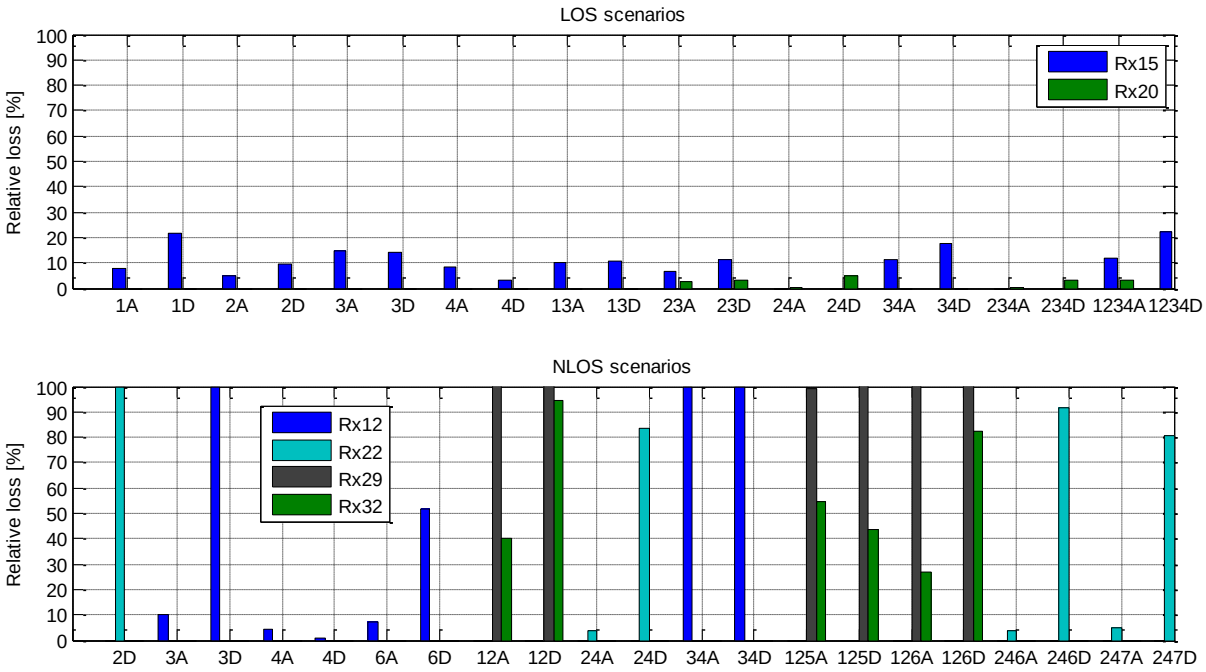

Figure 4.29. Relative throughput loss at 60 GHz in LOS and NLOS

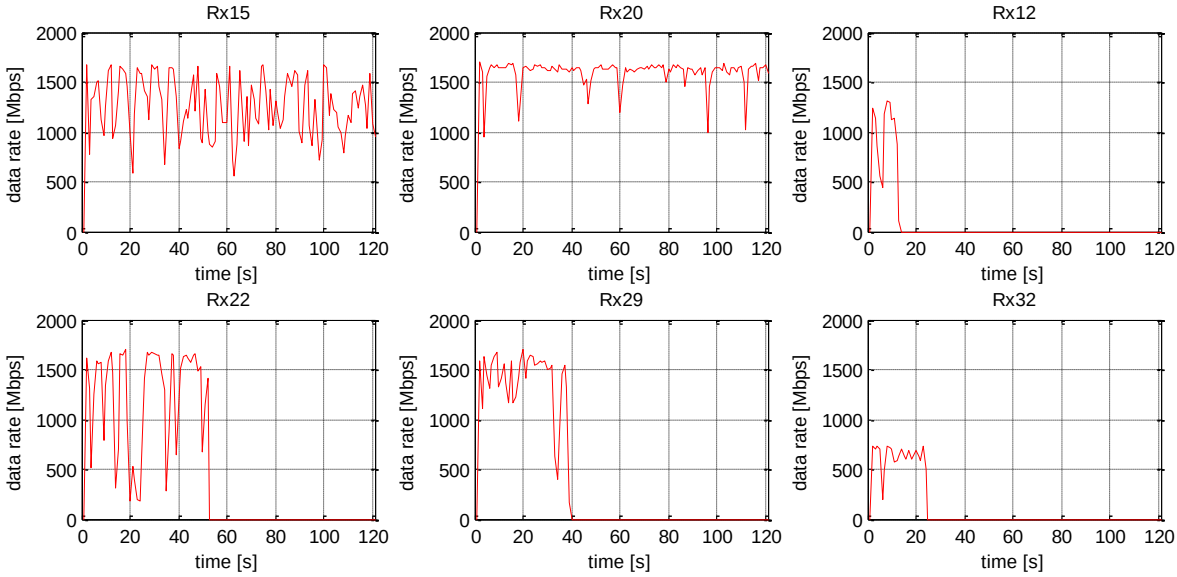

Figure 4.30. Throughput measurements with 4 people randomly walking around

4.3.4 Conclusion

The study accomplished in this section shows that communications at 60 GHz in LOS are quite robust. Based on the measurement results, it is possible to guarantee at least 1 Gbps in visibility conditions. However, in NLOS, the radio link has exhibited a particular sensitivity to the presence of obstacles such as furniture or human body. In this regard, it's not possible to ensure a quality of service at 60 GHz in non-visibility conditions. But high speed communications remain possible in such configurations. For this reason, improving the coverage in NLOS is not irrelevant; this task could be achieved by:

- using antenna arrays of bigger size for a link budget enhancement,

- using metasurfaces [55] to improve indirect paths contribution,
- or making relay operations mandatory features for future wireless technologies (see Appendix D.1.c).

4.4 Chapter summary

In this chapter, the sensitivity of the radio coverage to the transmitter surroundings has been studied in four situations. In the first one, the transmitter is located near a wall edge. The results obtained below 6 GHz exhibit the same behavior on either side of the investigated wall so that the *best* side is the one closest to the most Rx positions. At 60 GHz, the effect of diffraction on a wall edge has been found to be 2 to 18 dB lower than reflection in NLOS. The second situation involved the presence of potentially obstructing doors. The results revealed that below 6 GHz, the choice of the side is important, mostly because of the structure of the wall in which the door is embedded. At 60 GHz, the link budget in NLOS has been subject to up to 9 dB of improvement by simply opening the doors. In the third case, the transmitter is placed in the middle of a room with no obstacles in its surroundings. As a result, a weak sensitivity of the radio coverage has been observed below 6 GHz. The last situation featured a transmitter inside a cabinet. The results displayed an impact of the materials constituting the cabinet, so that the best location has been the only one located outside that piece of furniture.

The nearby environment of the transmitter is not the only factor having an influence on its radio coverage. Indeed, the presence of people in the transmission channel generates supplementary obstacles resulting in additional attenuations of the received signal. This effect called human body shadowing has also been investigated in this chapter. The results show up to 15 dB of extra loss at 60 GHz versus 4 dB below 6 GHz. In both cases, this loss is maximal when there is someone standing near the receiver (below 6 GHz) or obstructing the dominant propagation path (at 60 GHz).

Previous results exhibited a great sensitivity of radio coverage at 60 GHz to obstacles such as doors or people. Their impact on actual data transmission has been studied by the means of 802.11ad equipment. The aim was to determine whether it was possible to ensure a quality of service at this frequency band. The results have shown that communications in LOS have high throughput (peak at 2.5 Gbps) and are quite robust, so that at least 1 Gbps could be ensured, even when some people are obstructing the direct path. In NLOS, the throughputs obtained were also relatively high in favorable configurations (peak at 1.6 Gbps behind a plasterboard wall). However, it’s not possible to guarantee a quality of service because of the sensitivity of the radio link to obstacles such as furniture or people.

Chapter 5

Automatic cell planning enhancement for IEEE 802.11 networks

As implied in the introductive chapter, this thesis has been carried out in two essential parts. The first one, more propagation-measurement oriented, has been addressed in the three previous chapters. The second part, covered by this last chapter, is focused on improving optimization algorithms run by radio network design tools.

Nowadays, most of IEEE 802.11 network design software have a dedicated Automatic Cell Planning (ACP) module. The role of this ACP module is to improve the overall coverage and the throughput by selecting and placing the access points (APs) at different locations in a service area (e.g. a mall, an airport or an office building) based on a user-defined quality of service (QoS) policy. The achievement of this function mostly relies on propagation models (such as the ones established in Chapter 3) and capacity models (e.g. throughput model) whose results are intended to be used by optimization algorithms.

In this chapter, two models meant to enhance ACP modules for IEEE 802.11 networks are presented. The first one is a simplified throughput model which estimates the cell throughput based on the uplink-to-downlink throughput ratio. It allows basing the network design not only on the downlink throughput (mainstream approach), but also on the uplink one. The second one proposes a method of resolution of the multi-objective problem induced by the planning of multi-technology WLANs operating at 5 and 60 GHz.

5.1 Optimization based on uplink to downlink ratio

Historically, the Internet access has been based on an asymmetric paradigm in data usage: the common user, considered as a *spectator*, sends short sized requests (uplink) and receives responses of bigger size (downlink). However, with the advent of cloud computing services, social media or massive online gaming, this pattern is no longer relevant today. Cisco predicts that by 2022, more than 85% of the global IP traffic will be made of gaming, video and multimedia, with Wi-Fi used as access technology for 51 % of Internet traffic [56].

Due to this evolution in usage, taking into account the uplink (UL) traffic tends to be as much important as the downlink (DL) one when designing 802.11 networks. However, since uplink and downlink transmissions are performed over the same 802.11 channel, they can interfere mutually, despite the channel access mechanism: the CSMA/CA (Carrier Sense Multiple Access with Collision Avoidance). The fairness issues resulting from this antagonism have been the subject of several works. [57] and [58] propose dynamic adaptations of some Medium Access Control (MAC) parameters such as the initial backoff contention window, so as to have an optimal uplink to downlink bandwidth ratio. In [59], a

new parameter (utilization ratio) is proposed for the MAC protocol in order to have an efficient control of the uplink and downlink traffic even under saturation condition[10]. [60] suggests an adaptive backoff algorithm that achieves uplink to downlink fairness by computing optimal UL and DL transmission probabilities based on the number of nodes having a packet to transmit (backlog size).

In this section, a simplified throughput model based on the IEEE 802.11 DCF[11] (Distributed Coordination Function) is presented. This analytical model has the particularity to feature a fairness parameter: the desired uplink to downlink throughput ratio.

5.1.1 Review of existing models

Most of throughput models found in the literature use a bi-dimensional Markov chain to model the 802.11 DCF [61]. One of them is Bianchi's model [62] which has received a great attention from the research community. Indeed, this model is quite accurate in estimating 802.11 system throughput *S*, expressed as follows:

$$S = \frac{P_s P_{tr} E[P]}{(1 - P_{tr})\sigma + P_{tr} P_s T_s + P_{tr}(1 - P_s) T_c} \tag{5.1}$$

where:

- $E[P]$ is the average packet payload size, $E[P] = P$ for fixed size packets of length P,
- σ is the duration of a time slot,
- T_s and T_c are the average time the channel is sensed busy respectively because of a successful transmission, or a collision,
- P_s is the probability that a transmission occurring on the channel is successful,
- P_{tr} is the probability that there is at least one transmission during a time slot.

However, its major limitation is its validity only under saturation condition. Other similar models address this issue by representing the non-saturated traffic condition with a non-transmission probability at each node. [2] proposes a modification of the Markov model proposed by Bianchi by adding a new state which corresponds to the absence of packets to transmit at each node. In [63], the transmission probability results from modeling the packets queue of each node with a (Batch Markovian Arrival Process) BMAP/M/1/N queue controlling the (video) traffic load offered to the network. [64] propounds an extension of [2] accounting for channel propagation errors which are not considered in [62].

The throughput model established during this thesis has been inspired by [2]. That latter model is a heterogeneous model which defines various groups of stations (called classes). In the simplistic case of a two-class model, where all stations of a class have identical parameters, the total cell throughput *S* is expressed as follows:

$$S = \frac{\left(P_{s_1} + P_{s_2}\right) L}{(1 - P_{tr})\sigma + \left(P_{s_1} + P_{s_2}\right) T_s + \left(P_{tr} - P_{s_1} - P_{s_2}\right) T_c} = \frac{\left(P_{s_1} + P_{s_2}\right) L}{E_s} \tag{5.2}$$

where L is payload data size, E_s is the mean Markov state time and P_{s_i} is the probability that a station in class *i* successfully transmits a packet:

$$P_{s_i} = \tau_i \, (1 - \tau_i)^{n_i - 1} \prod_{j \neq i} \left(1 - \tau_j\right)^{n_j} \tag{5.3}$$

[10] In saturation condition, all the nodes in the network have always a packet ready to be transmitted.

[11] DCF consists of CSMA/CA and backoff procedure.

where n_k is the number of stations in class k and τ_k the probability that a station in class k attempts a transmission. This probability depends on q_k, the probability that at least one packet is ready to be transmitted. Assuming that the packets arrive to the MAC buffer in a Poisson manner with an arrival rate of λ_k, we have :

$$q_k = 1 - \exp(-\lambda_k E_s) \tag{5.4}$$

The uplink to downlink throughput ratio is defined as follows:

$$\alpha = \frac{Total\ UL\ throughput}{Total\ DL\ throughput} \tag{5.5}$$

The 2-class model detailed earlier can be extended to support this parameter as explained through the following scenario.

Let consider an IEEE 802.11a network consisting of one AP (class 1, n_1 = 1) and N stations at fixed locations (class 2, $n_2 = N$). They exchange packets of size L, arriving to the MAC buffer of each node in a Poisson manner. If the downlink throughput per station is X and the target uplink to downlink ratio is α, then the packet arrival rate of each class is:

$$\lambda_1 = \lambda_{AP} = \frac{NX}{L}, \text{ and } \lambda_2 = \lambda_{STA} = \frac{\alpha X}{L}. \tag{5.6}$$

The system throughput of such parameterized network (see Table 5.1) can then be estimated with the 2-class model by solving the set of nonlinear equations in [2], as detailed in Appendix E. The obtained results have been compared with the simulation of the same scenario by a MATLAB script (developed at Orange Labs) implementing the DCF function of 802.11a (see Appendix F).

Table 5.1. Parameters of the 802.11a network

Parameter	Value	
L	1350 bytes	
$MPDU_{SIZE}$	1378 bytes = 2+2+6+6+6+2+L+4	
W_0	*Initial backoff contention window*	16
m	*Maximum backoff stage*	6
σ	*Time slot duration*	9 µs
δ	*Propagation delay*	1 µs
T_{SIFS}	*SIFS duration*	16 µs
T_{DIFS}	*DIFS duration*	34 µs = $2\sigma + T_{SIFS}$
D_{PHY}	*PHY rate data frames*	54 Mbps
D_{CTRL}	*PHY rate control frames*	6 Mbps
N_{DATA}	52 = 1e6 * (16+6+8*$MPDU_{SIZE}$) / (4*D_{PHY})	
N_{CTRL}	6 = 1e6 * (16+6+8*14)/(4*D_{CTRL})	
T_{ACK}	44 µs = 20µs + 4µs * N_{CTRL}	
T_S	324 µs = 20µs + 4µs*N_{DATA} + T_{SIFS} + 2δ + T_{ACK} + T_{DIFS}	
T_C	324 µs = 20µs + 4µs*N_{DATA} + T_{SIFS} + 2δ + T_{ACK} + T_{DIFS}	

The results, shown in Figure 5.1, exhibit an increase of the system throughput with the number of stations followed by a fall beyond a certain threshold. This decrease indicates that the system progressively reaches the saturation condition as the number of stations increases. This is confirmed by observing the evolution of α_{out}, the uplink to downlink throughput ratio as defined in (5.5), which moves from 0.4 (the desired value) to values greater than 1.

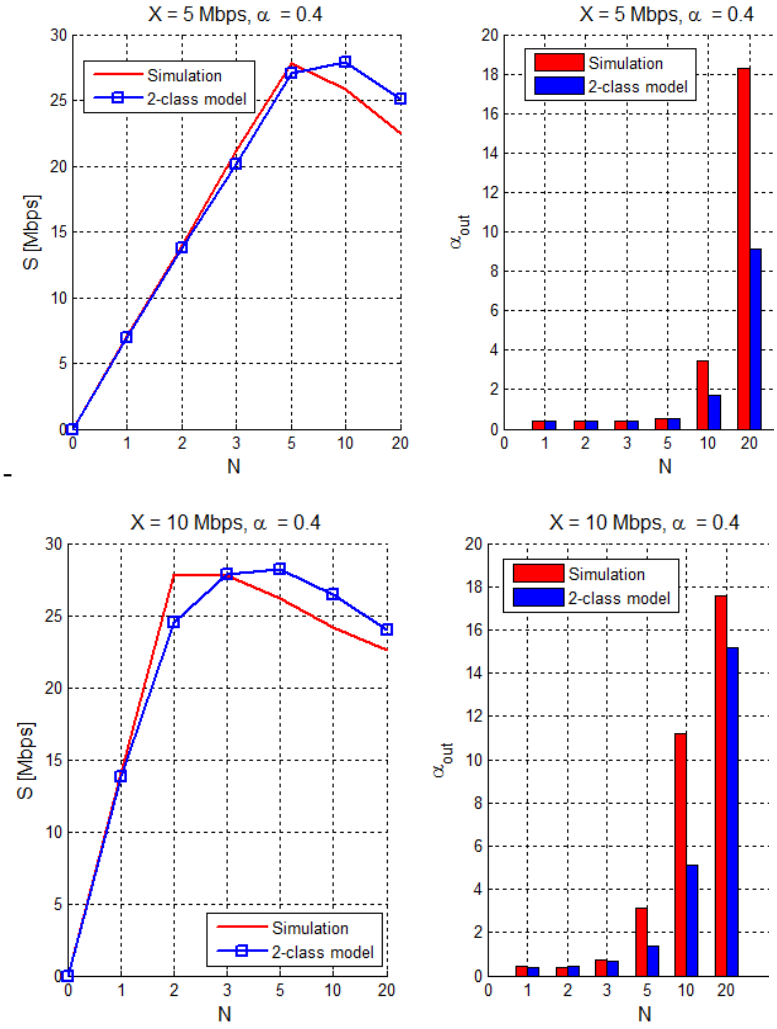

Figure 5.1. Cell throughput and throughput ratio α versus the number of stations

The main issue in using the multi-class model lies in the number of coupled nonlinear equations to solve which increases with the number of classes. In real 802.11 networks, there can be a large number of classes (e.g. grouping them by distance as in [65]). This might lead to additional computational costs being not negligible for ACP modules which run thousands of iterations during optimization phases. This concern led to the simplified throughput model presented in the next section.

5.1.2 Proposed throughput model

The conceptual difference between the model presented in this section and the others aforementioned lies in not considering the channel events from the transmitter perspective but from the receiver instead. In the following, let consider the IEEE 802.11 Basic Service Set (BSS) illustrated in Figure 5.2. It consists of one access point (AP) and *N* stations (STAs) at fixed locations, with:

$$N = N_1 + N_2 + N_3 \tag{5.7}$$

where:

- N_1 is the number of STAs only receiving packets from the AP (DL only),
- N_2 is the number of STAs only sending packets to the AP (UL only),
- N_3 is the number of STAs sending and receiving packet from the AP (DL and UL).

Figure 5.2. IEEE 802.11 BSS with 3 kinds of stations

5.1.2.1 The uplink to downlink throughput ratio

Let consider an arbitrary channel observation duration T_{obs} within the BSS as illustrated in Figure 5.3. For this duration, the uplink to downlink throughput ratio defined in (5.5) is given by:

$$\alpha = \frac{(\sum_{i=1}^{N_2} \lambda_{i,2} + \sum_{j=1}^{N_3} \lambda_{j,3})/T_{obs}}{(\sum_{k=1}^{N_1} L_{k,1} + \sum_{m=1}^{N_3} L_{k,3})/T_{obs}} \tag{5.8}$$

where:

- $\lambda_{i,j}$ is the total payload size received by the AP from STA_i of type j (UL),
- $L_{k,m}$ is the total payload size received by STA_k of type m from the AP (DL).

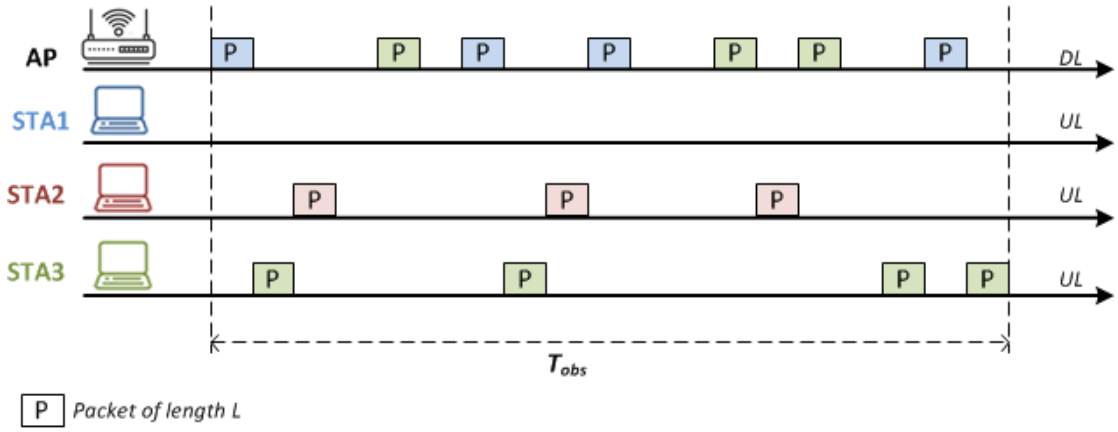

Figure 5.3. Packets exchange during T_{obs}

Assuming that AP and STAs transmit packets of the same fixed length L, then:

$$\lambda_{i,j} = n_{i,j}^{u} L \text{ and } L_{k,m} = n_{k,m}^{d} L \tag{5.9}$$

where:

- $n_{i,j}^{u}$ is the number of packets received by the AP from STA_i of type j (UL),
- $n_{k,m}^{d}$ is the number of packets received by STA_k of type m from the AP (DL).

From (5.8) and (5.9), the uplink to downlink throughput ratio is then deduced as the number of packets received in uplink divided by the number of packet received in downlink during:

$$\alpha = \frac{\sum_{i=1}^{N_2} n_{i,2}^{u} + \sum_{j=1}^{N_3} n_{j,3}^{u}}{\sum_{k=1}^{N_1} n_{k,1}^{d} + \sum_{m=1}^{N_3} n_{m,3}^{d}} \tag{5.10}$$

5.1.2.2 Probability to receive a packet successfully transmitted

From (5.10), is deduced the total number of packets successfully received during T_{obs}:

$$n_P = \sum_{i=1}^{N_2} n_{i,2}^{u} + \sum_{j=1}^{N_3} n_{j,3}^{u} + \sum_{k=1}^{N_1} n_{k,1}^{d} + \sum_{m=1}^{N_3} n_{m,3}^{d} \tag{5.11}$$

The probability P_{DL} that a STA receives a packet successfully transmitted is then:

$$P_{DL} = \sum_{i=1}^{N_1} \sum_{j=1}^{n_{i,1}^{d}} \frac{1}{n_P} + \sum_{k=1}^{N_3} \sum_{l=1}^{n_{k,3}^{d}} \frac{1}{n_P} \tag{5.12}$$

Using (5.11), this probability can be also expressed as:

$$P_{DL} = \frac{\sum_{k=1}^{N_1} n_{k,1}^{d} + \sum_{m=1}^{N_3} n_{m,3}^{d}}{\sum_{i=1}^{N_2} n_{i,2}^{u} + \sum_{j=1}^{N_3} n_{j,3}^{u} + \sum_{k=1}^{N_1} n_{k,1}^{d} + \sum_{m=1}^{N_3} n_{m,3}^{d}} \tag{5.13}$$

A similar reasoning is applied to determine P_{UL}, the probability that the AP receives a packet successfully transmitted:

$$P_{UL} = \frac{\sum_{i=1}^{N_2} n_{i,2}^{u} + \sum_{j=1}^{N_3} n_{j,3}^{u}}{\sum_{i=1}^{N_2} n_{i,2}^{u} + \sum_{j=1}^{N_3} n_{j,3}^{u} + \sum_{k=1}^{N_1} n_{k,1}^{d} + \sum_{m=1}^{N_3} n_{m,3}^{d}} \tag{5.14}$$

By combining (5.10) to (5.13) and (5.14), the final expression of P_{UL} and P_{DL} is then:

$$P_{DL} = \frac{1}{1+\alpha} \text{ and } P_{UL} = \frac{\alpha}{1+\alpha} \tag{5.15}$$

5.1.2.3 System throughput

The system throughput *S*, is estimated by considering the events occurring when one packet is successfully received:

$$S = \frac{L}{\sum_{i=1}^{N_1} P_{STA_{i,1}}^{d} T_{i,1} + \sum_{j=1}^{N_3} P_{STA_{j,3}}^{d} T_{j,3} + \sum_{k=1}^{N_2} P_{STA_{k,2}}^{u} t_{k,2} + \sum_{m=1}^{N_3} P_{STA_{m,3}}^{u} t_{m,3}} \tag{5.16}$$

where:

- L is the size of the received packet,
- $T_{i,j}$ is the duration for a successful transmission to STA_i of type j from the AP (DL),
- $t_{k,m}$ is the duration for a successful transmission to AP from STA_k of type m (UL),
- $P^d_{STA_{i,j}}$ is the probability that STA_i of type j receives a packet from the AP (DL),
- $P^u_{STA_{k,m}}$ is the probability that the AP receives a packet from STA_k of type m (UL).

These probabilities are defined with the following relationships:

$$\sum_{i=1}^{N_1} P^d_{STA_{i,1}} + \sum_{j=1}^{N_3} P^d_{STA_{j,3}} + \sum_{k=1}^{N_2} P^u_{STA_{k,2}} + \sum_{m=1}^{N_3} P^u_{STA_{m,3}} = 1, \quad (5.17)$$

$$\sum_{i=1}^{N_1} P^d_{STA_{i,1}} + \sum_{j=1}^{N_3} P^d_{STA_{j,3}} = P_{DL} \text{ and} \quad (5.18)$$

$$\sum_{k=1}^{N_2} P^u_{STA_{k,2}} + \sum_{m=1}^{N_3} P^u_{STA_{m,3}} = P_{UL} \quad (5.19)$$

Considering that all stations have the same kind of traffic (none of them are greedy), they have the same probability of receiving a packet:

$$P^d_{STA_{i,1}} = P^d_{STA_{j,3}} = P^d, \quad i \in \{1, \dots, N_1\} \text{ and } j \in \{1, \dots, N_3\} \quad (5.20)$$

$$P^u_{STA_{k,2}} = P^u_{STA_{m,3}} = P^u, \quad k \in \{1, \dots, N_2\} \text{ and } m \in \{1, \dots, N_3\} \quad (5.21)$$

where P^d and P^u are respectively the probability that a successfully transmitted packet is received by a STA and by the AP. Combining (5.15), (5.18) and (5.19) leads to :

$$P^d = \frac{1}{(1+\alpha)(N_1+N_3)} \text{ and } P^u = \frac{\alpha}{(1+\alpha)(N_2+N_3)}. \quad (5.22)$$

As a result, the expression of the cell throughput in (5.16) can be expressed as a function of the number of stations and the uplink to downlink throughput ratio:

$$S = \frac{(1+\alpha)L}{\frac{1}{N_1+N_3}\left(\sum_{i=1}^{N_1} T_{i,1} + \sum_{j=1}^{N_3} T_{j,3}\right) + \frac{\alpha}{N_2+N_3}\left(\sum_{k=1}^{N_2} t_{k,2} + \sum_{m=1}^{N_3} t_{m,3}\right)}. \quad (5.23)$$

5.1.2.4 Model validation

This model has been compared to the 2-class model and the DCF simulation within the same scenario described in section 5.1.1. The results, shown in Figure 5.4, indicate the cell throughput computed in each case. Note that Figure 5.4.c uses the same parameters as Figure 5.4.b except that the physical rate of each station is 36 Mbps instead of 54 Mbps.

The comparison between these throughputs exhibits that our model (in green) is an upper bound which estimates the maximum cell throughput meeting the throughput ratio demand (here $\alpha = 0.4$). This feature is interesting because it allows radio design software to perform optimizations based on the maximum capacity resulting from the specified demand as explained in the next section.

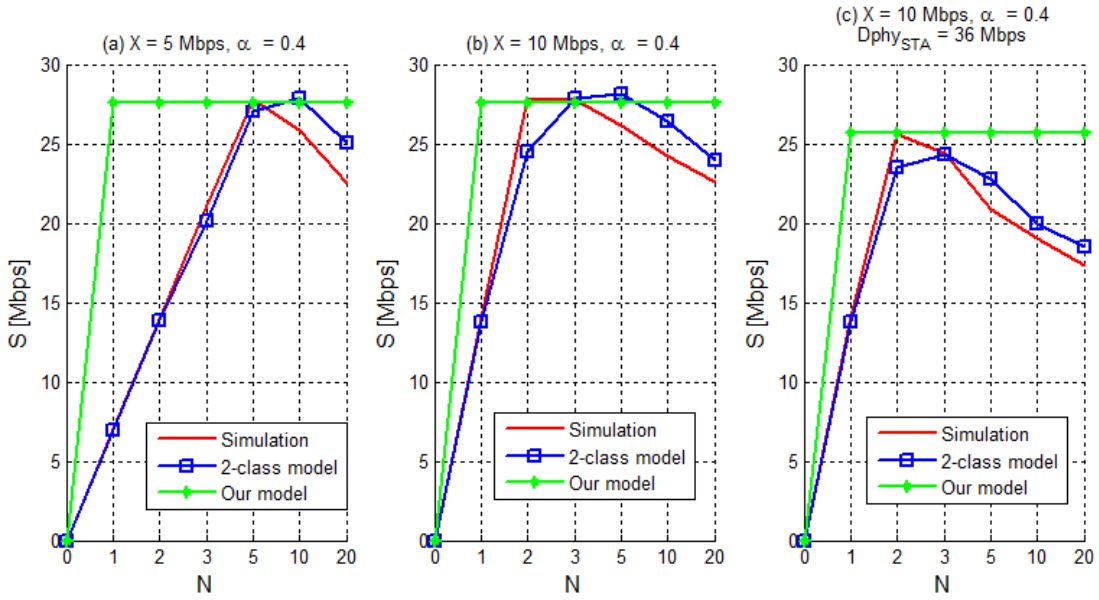

Figure 5.4. Estimated cell throughput versus the number of users

5.1.3 Application of the model

This model has been integrated to XANDA: a radio design software developed at Orange Labs Belfort (see Figure 5.5). More precisely, this model has been implemented inside one of XANDA's ACP modules based on Tabu search [66]. This module has been extended to support the following parameters:

- the number of stations N_1, N_2 and N_3, as defined in section 5.1.2,
- X the demanded load per user in DL,
- α the desired uplink to downlink throughput ratio.

Based on these five parameters, the goal of is to determine the best configuration (set of APs locations operating on selected channels) having its global system throughput S_p meeting the specified demand with a probability p.

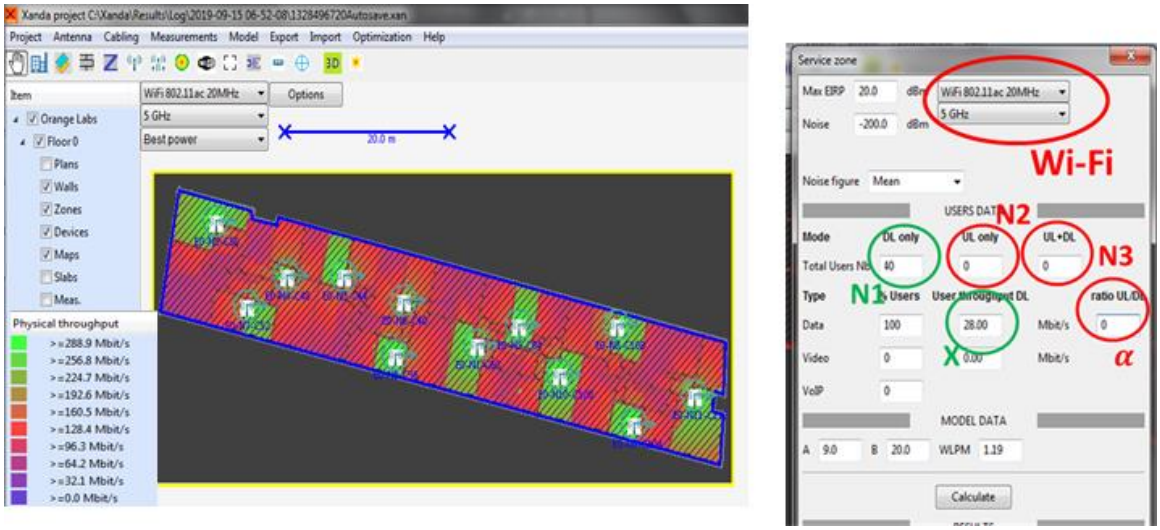

Figure 5.5. XANDA's user interface

The first step has consisted in moving the packet size parameter in (5.23) to the denominator such that the cell throughput expression becomes:

$$S = \frac{1+\alpha}{\frac{1}{N_1+N_3}\left(\sum_{i=1}^{N_1}\frac{1}{D_{i,1}} + \sum_{j=1}^{N_3}\frac{1}{D_{j,3}}\right) + \frac{\alpha}{N_2+N_3}\left(\sum_{k=1}^{N_2}\frac{1}{\delta_{k,2}} + \sum_{m=1}^{N_3}\frac{1}{\delta_{m,3}}\right)}. \quad (5.24)$$

where $D_{i,j}$ is the DL throughput of STA_i of type j and $\delta_{k,m}$ is the UL throughput of STA_k.of type m. Since a given STA can potentially be anywhere in a service area independently of the other STAs location, these throughputs are actually independent random variables. Their value is a function of the STAs locations and the presence of interfering neighbor cells.

5.1.3.1 Interference management in XANDA

At the beginning, XANDA only featured the management of downlink interferences as illustrated in Figure 5.6. The downlink throughput D_i was computed as follows:

$$D_{i,j} = \frac{f_D(SINR_{i,j})}{1+N_{cochannels}} \quad (5.25)$$

where $N_{cochannels}$ is the number of co-channels and f_D is the physical throughput depending on the transmitter MCS and the signal-to-interference-plus-noise-ratio (SINR) at the receiver side as illustrated in Table 5.2.

Table 5.2. Example of achievable throughput in IEEE 802.11ac

MCS index	f_D [Mbps]	Min. SINR [dB]	Receive sensitivity [dBm]	Guard Interval [ns]	Channel bandwidth [MHz]	Spatial Streams
0	21.7	2	-82	400	20	3
1	43.3	5	-79			
2	65	9	-77			
3	86.7	11	-74			
4	130	15	-70			
5	173.3	18	-66			
6	195	20	-65			
7	216.7	25	-64			
8	260	29	-59			
9	288.9	30	-57			

The SINR is computed as follows:

$$SINR\ [dB] = P_{RX}[dBm] - I_{NF}[dBm] - \sum_{j=1}^{N_{icell}} P_{interf_j}[dBm] \quad (5.26)$$

where P_{RX} is the received power, I_{NF} is the noise floor, N_{icell} is the number of interfering cells operating on the same channel, and P_{interf_j} is the interference generated by the j-th interfering cell.

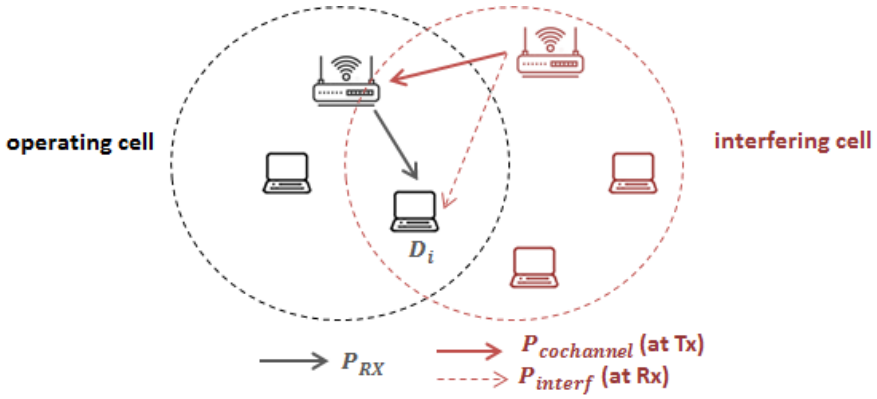

Figure 5.6. Legacy DL interference management in XANDA

In XANDA, an interfering cell reduces the throughput of the operating cell by either decreasing the SINR (through P_{interf}) or increasing the number of co-channels by 1; not both at the same time. The choice of the interfering mode is made as indicated by Algorithm 1.

Algorithm 1 : Legacy choice of the interfering mode in DL

if $P_{cochannel} \geq CCA_{threshold}$ **then**

$N_{cochannels} \leftarrow N_{cochannels} + 1$

else

$SINR \leftarrow SINR - P_{interf}$

end if

If $P_{cochannel}$, the power received by the operating Tx side (AP) when the interfering AP is transmitting, is greater than the clear channel assessment (CCA) threshold, then the number of co-channels is incremented by one. Otherwise, the SINR at the operating Rx side (STA) is diminished by P_{interf}, the power received at the operating Rx side from the interfering AP.

In order to implement our model, this interference management algorithm has firstly been extended to account for the interferences generated by the stations (uplink), as illustrated in Figure 5.7.

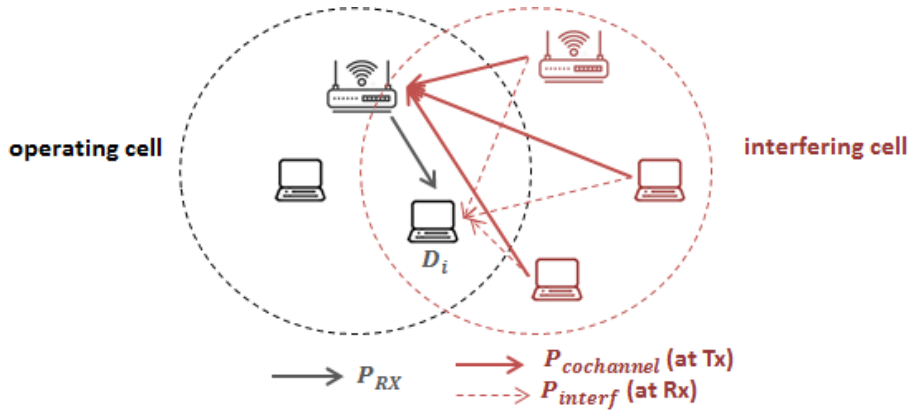

Figure 5.7. Extended DL interference management in XANDA

This improvement led to a modification of Algorithm 1 resulting in Algorithm 2.

Algorithm 2 : Extended choice of the interfering mode in DL

Let RI_{STAs} = *The percentage of STAs in the interfering cell being in co-channel with operating AP.*

Let $P_{interf_{STA}}$ = *The received power at the operating Rx side from the most interfering STA within the interfering cell.*

if $P_{cochannel_{AP}} \leq CCA_{threshold}$ **and** $RI_{STAs} \geq 0.05$ **then**

$N_{cochannels} \leftarrow N_{cochannels} + 1$

else if $P_{cochannel_{AP}} \leq CCA_{threshold}$ **then**

Let $D_{SINR} \leftarrow f_D(SINR - P_{interf_{STA}})/(1 + N_{cochannels})$

Let $D_{COCHAN} \leftarrow f_D(SINR)/(1 + N_{cochannels} + 1)$

if $D_{COCHAN} \leq D_{SINR}$ **then**

$N_{cochannels} \leftarrow N_{cochannels} + 1$

else

$SINR \leftarrow SINR - P_{interf_{STA}}$

end if

else

$SINR \leftarrow SINR - \max(P_{interf_{AP}}, P_{interf_{STA}})$

end if

Three cases have been considered:

1. When the AP and more than 5% of the STAs in the interfering cell are in co-channel with the operating Tx side (AP), the number of co-channels is incremented by one.
2. When the AP and less than 5% of the STAs in the interfering cell are in co-channel with the operating Tx side (AP), a choice is made between increasing the number of co-channels by one and diminishing the SINR at the operating Rx side by $P_{interf_{STA}}$. The priority is given to the case leading to lowest throughput (worst case).
3. In any other case, the SINR at the operating Rx side is diminished from the highest received power from the interfering cell.

This process is repeated for the N_{icell} interfering cells so that the parameters $N_{cochannels}$ and $SINR$, common to all the iterations, are respectively either increased or decreased.

The next step has consisted in implementing within XANDA an interference management for UL transmissions, as illustrated in Figure 5.8. The choice of the interfering cell mode is similar to the one described in Algorithm 2 except that the operating Tx side is the station and the operating Rx side is the AP.

In order to reduce the interferences, the last step has consisted in improving the channel allocation scheme so that the probability of having neighbor cells operating on the same channel is minimized. This allocation scheme has been made flexible in order to perform Wi-Fi channel allocation at 5 GHz with either 8 channels available (UNII-I and UNII-II) or 19 channels available (UNII-I, UNII-II and UNII-II extended), as illustrated in Figure 5.9. The impact of the number of available channels is studied in Section 5.1.3.3.

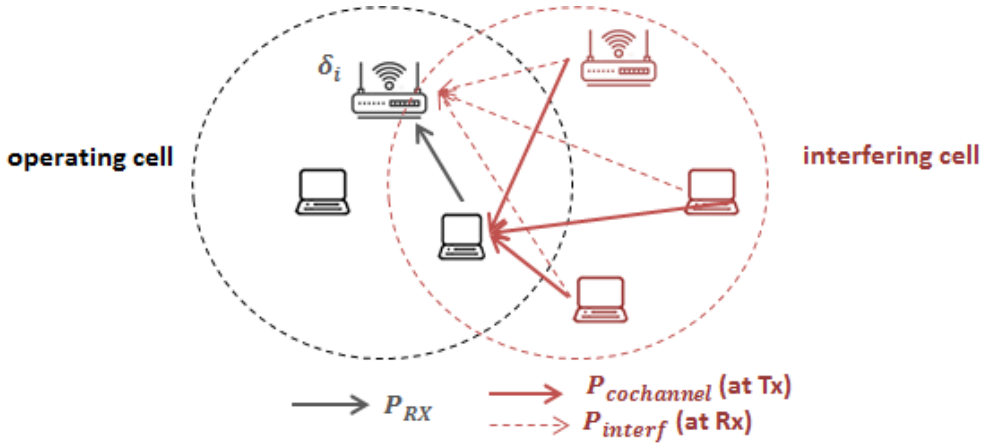

Figure 5.8. UL interference management in XANDA

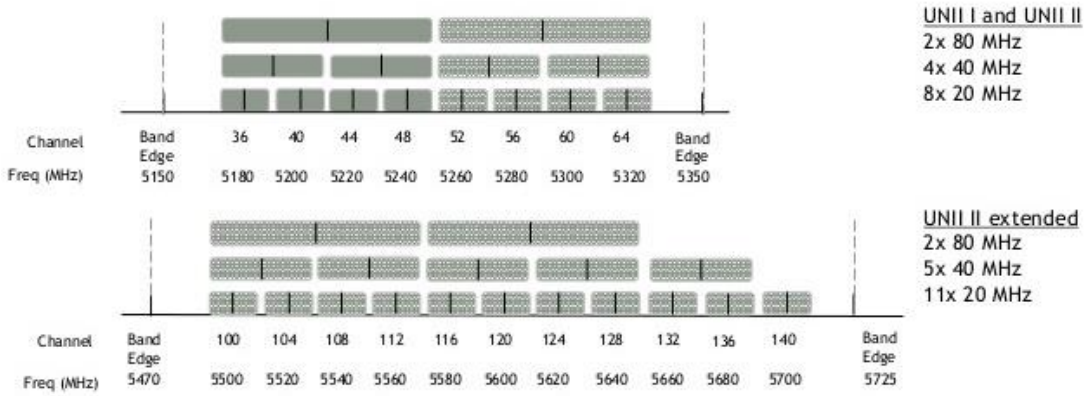

Figure 5.9. Wi-Fi channels available at 5 GHz in Europe

5.1.3.2 System throughput meeting the specified demand

By applying the generalized central limit theorem [67] to (5.24), the sum of the inverse UL and DL throughputs at S denominator can be approximated by a Gaussian random variable G such that $S = (1 + \alpha)/G$ with

$$G = \frac{1}{N_1 + N_3}\left[\mathcal{N}(N_1\mu_{DL},\ N_1{\sigma_{DL}}^2) + \mathcal{N}(N_3\mu_{DL},\ N_3{\sigma_{DL}}^2)\right] + \frac{\alpha}{N_2 + N_3}\left[\mathcal{N}(N_2\mu_{UL},\ N_2{\sigma_{UL}}^2) + \mathcal{N}(N_3\mu_{UL},\ N_3{\sigma_{UL}}^2)\right] \quad (5.27)$$

where μ_{DL} and ${\sigma_{DL}}^2$ are respectively the mean and variance of the sum of the inverse DL throughputs ($\sum 1/D_{i,j}$) , while μ_{UL} and ${\sigma_{UL}}^2$ are respectively the mean and variance of the sum of the inverse UL throughput ($\sum 1/\delta_{k,m}$). G can then be approximated by:

$$G \sim \mathcal{N}\left(\mu_{DL} + \alpha\mu_{UL}, \frac{{\sigma_{DL}}^2}{N_1 + N_3} + \frac{\alpha^2{\sigma_{UL}}^2}{N_2 + N_3}\right) \quad (5.28)$$

The parameters of this random variable are computed by XANDA and depend on the APs configuration. The probability p of having the system throughput greater to a value S_p is then:

$$p = P(S \geq S_p) = P\left(G \leq \frac{1+\alpha}{S_p}\right) = \frac{1}{2}\left(1 + \text{erf}\left[\frac{\frac{1+\alpha}{S_p} - \mu_{DL} - \alpha\mu_{UL}}{\sqrt{2\left(\frac{{\sigma_{DL}}^2}{N_1+N_3} + \frac{\alpha^2{\sigma_{UL}}^2}{N_2+N_3}\right)}}\right]\right) \quad (5.29)$$

where *erf* is the Gauss error function and S_p the system throughput meeting the specified demand with a probability *p*. The expression of S_p is reciprocally derived from (5.29) so that:

$$S_p = \frac{1+\alpha}{\mu_{DL} + \alpha\mu_{UL} + \sqrt{2\left(\frac{{\sigma_{DL}}^2}{N_1+N_3} + \frac{\alpha^2{\sigma_{UL}}^2}{N_2+N_3}\right)}\ .\text{erf}^{-1}[2p-1]} \quad (5.30)$$

In practice, the value of *p* is set to 0.9.

5.1.3.3 Example of application

The implementation of our model has been tested in 3 scenarios involving the deployment of 802.11ac access points (N_{APs}) within a large single floor building of dimension 60 m x 15 m x 2.4 m (see Figure 5.5) containing N_{user} users. The network has been parameterized as indicated in Table 5.3.

Table 5.3. Parameters of the 802.11ac network

Parameter	Value
Number of available channels	19 or 8
Channel bandwidth	20 MHz
Number of spatial streams	3
Max data rate	288.9 Mbps
Demanded load per user (X)	10 Mbps

The first scenario showcases the impact of the APs densification on the DL throughput per user when there are 200 users inside the building and a demanded throughput ratio of 0.2. The results given in Figure 5.9, show that the increase of the number of access points causes a performance improvement up until a certain threshold (here around 60 access points). However, beyond that threshold the densification has a marginal effect and can even deteriorate the performance. It's also observed that the more channels there are, the higher is the throughput. This can be explained by the fact that having more channels available reduces the probability to have interfering neighbor cells; this results in a throughput increase.

The 2 last examples exhibit factors deteriorating the downlink throughput per user. The first one, given in Figure 5.11.a, shows an exponential decay of DL throughput per user when the number of users increases from 1 to 200. The second one, shown in Figure 5.11.b, is an illustration of the antagonism between the uplink and downlink throughput. It's observed that the offered DL throughput per user is almost divided by 2 when the uplink to downlink throughput ratio varies from 0 to 1. The optimal throughput ratio meeting the demand is around 0.36.

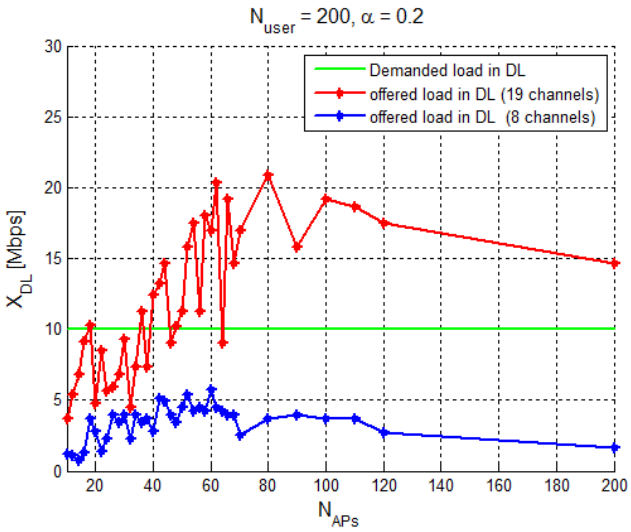

Figure 5.10. Impact of APs densification of the DL throughput per user

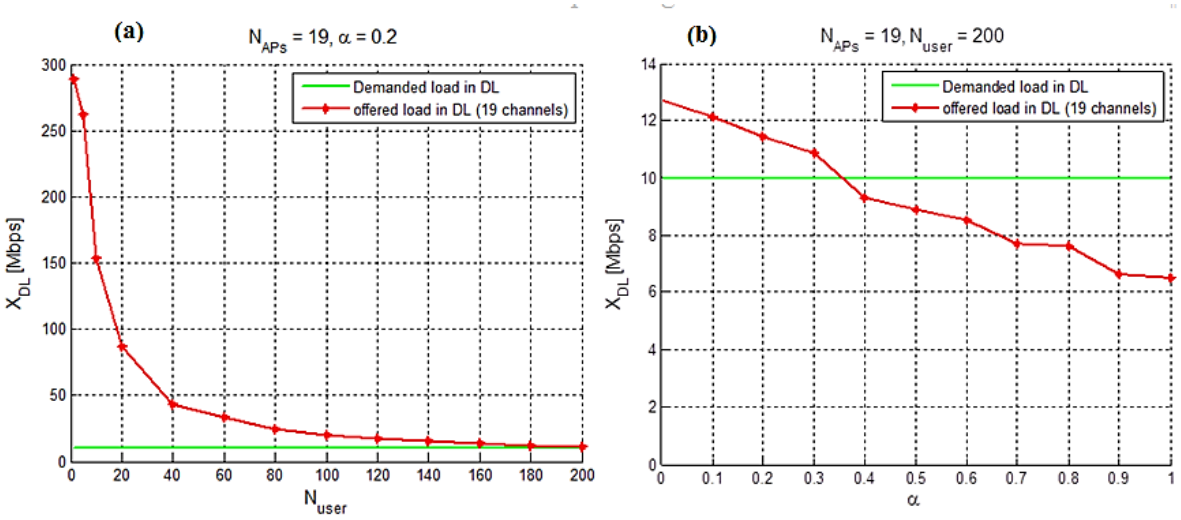

Figure 5.11. DL throughput per user versus number of users (a) and throughput ratio (b)

5.1.4 Conclusion

In this section a simplified throughput model for IEEE 802.11 networks has been presented. It allows estimating the maximum cell throughput based on a desired uplink to downlink throughput ratio. This model is meant to be used by radio design software in order to reduce the computational cost during optimization. However, this easy to use and to implement model has some limitations.

The first limitation is that it overlooks collision effects. This is not a critical issue because, with mechanisms such as RTS/CTS (Request to Send / Clear to Send) and the scheduling mechanism introduced by IEEE 802.11ax, the number of collisions tends to be minimized. The second one is that this model is not valid in saturated conditions. This one is a limitation to the model itself, not its applications. Indeed, as previously mentioned, this model is meant to be applied to radio design software, and the main objective of such planning tools is to prevent saturation.

Finally, as the last limitation, this model does not account for heterogeneous traffic. The future work will consists in extending this model to support packets of different sizes and different transmit and receive probabilities (all stations are at the moment supposed to have the same ones). These future changes will not affect the modeling principle described in this section.

5.2 Planning of multi-technology WLANs

In multi-technology WLANs, the APs feature different wireless technologies operating most of the time at different frequency bands and so with different ranges and throughputs. The OptimiSME wireless extenders introduced in Chapter 1 are an example. A user connected to an OptimiSME network may, depending on its location and capabilities, communicate with the extender at 60 GHz (802.11ad), 5 GHz (80211n/ac) or at 868 MHz (Z-wave, if it's a connected object). The design of such heterogeneous networks is not a trivial task. Some of the main challenges are:

- The optimal positioning of the APs to satisfy the users demand while simultaneously taking into account the coverage area of the different technologies; it allows identifying the best technology to use according to the users location.
- The previous point implies to make sure to avoid the over-dimensioning of the network for one of the technologies. Indeed, it generates additional deployment cost and also creates potentially more interferences resulting in performance degradation (see Section 5.1.3.3).
- Finally, it's important to anticipate the coverage failure of high priority technologies such as 802.11ad (at 60 GHz) which offer a very high throughput at the expense of a great sensitivity of the radio link especially in NLOS (see Chapter 4).

However, since XANDA only designs single-technology WLANs, it has none of the features aforementioned. The purpose of this section is to help radio planning software (such as XANDA) in designing multi-technology WLANs operating at 5 and 60 GHz. Before doing so, it's important to define some key concepts.

5.2.1 Key concepts

Let consider the single floor building in Figure 5.12; it has to be covered by a WLAN. The first step consists in specifying the desired quality of service by the means of **service areas**.

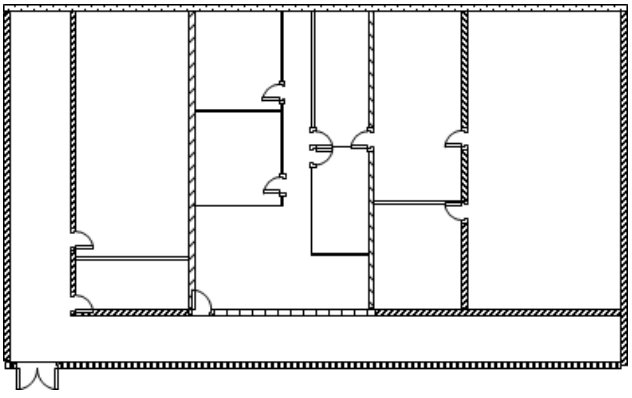

Figure 5.12. Plan of the single-floor building

5.2.1.1 The service area

A service area k is an area within the building which is meant to contain N_k users, at a fixed location, demanding X_k^* Mbps in downlink (each user), and transmitting with an uplink to downlink throughput ratio of α_k. In Figure 5.13, two service areas have been defined to illustrate the concept; the WLAN to design has to support the demand of $N_{user} = N_1 + N_2$ users wherever they may be located in their respective service areas.

5.2.1.2 The users meshing

Since the users may be located anywhere in their respective service area, a statistical approach is necessary. Each service area is sub-divided into small areas called **meshes** of same dimension[12]. The repartition of N_k users in a service area k is supposed to be uniformly distributed over the M_k meshes, i.e. the probability to be located on a given mesh in service area k is $1/M_k$ and the number of users per mesh is on average N_k/M_k. The WLAN to design has to position the APs so that they optimally cover the meshes in received signal strength (coverage) and capacity (throughput demand).

5.2.1.3 The APs meshing

In order to find the optimal APs locations, the first step consists in spreading over the building (regularly or not) a finite set of *virtual* APs called *candidates*. The planning of the WLAN can then be reduced to a combinatorial problem which consists in finding the combination of N_{AP} APs (called *solutions*) between the candidates, which optimally meets the demand per service area k; the value of N_{AP} depends on the site to cover, and represents the minimum number of APs allowing to meet the demand. The candidates' location may be restricted to wall proximity or under the ceiling to optimize computing time.

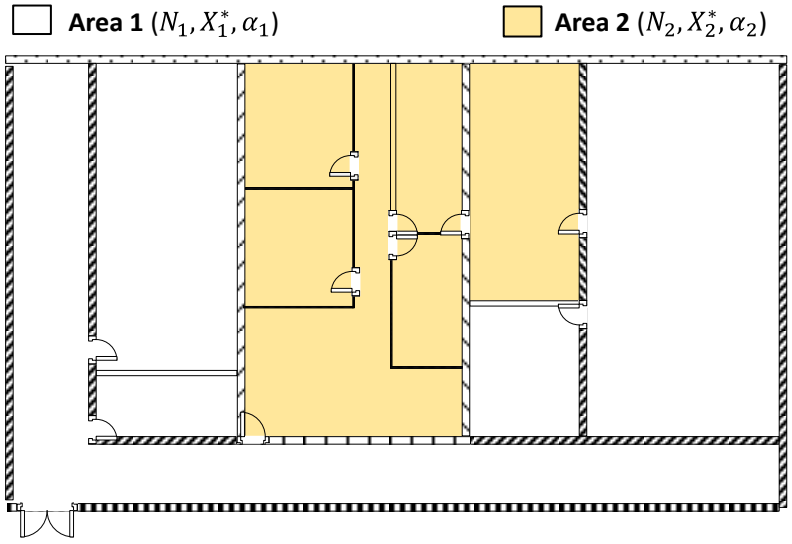

Figure 5.13. Building with 2 service areas

[12] The dimension of a mesh is generally chosen in the range of 0.5 m x 0.5 m to 1 m x 1 m

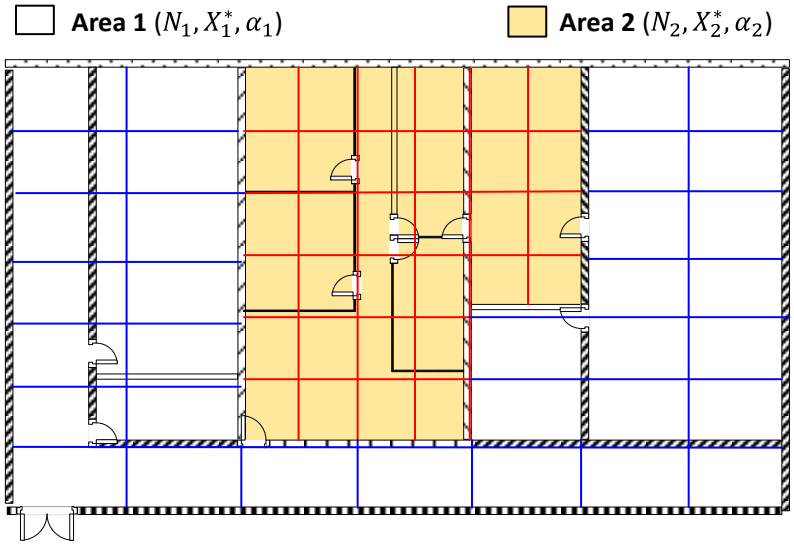

Figure 5.14. Meshed service areas

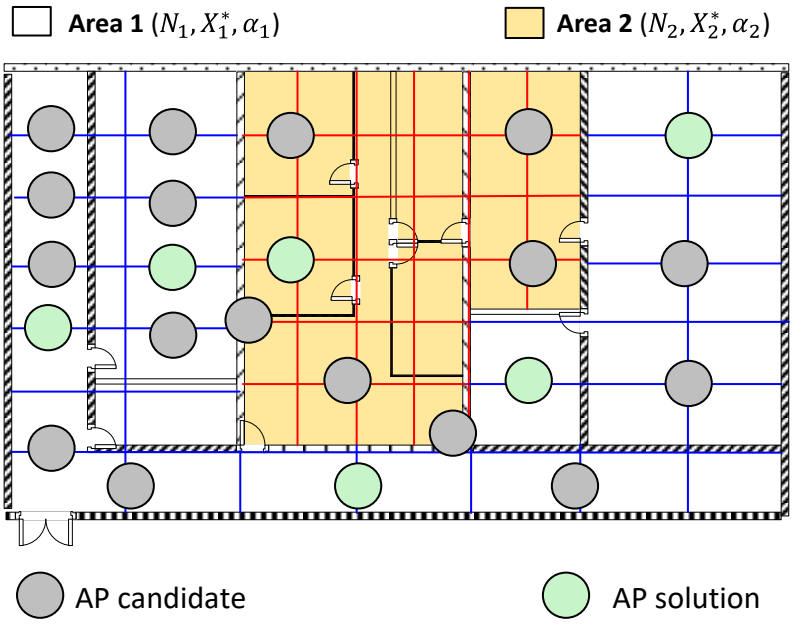

Figure 5.15. APs candidates and solutions

Let P_i $(1 \leq i \leq N_{AP})$, be an arbitrary AP solution. The cell of AP_i is defined as the set of M^i meshes having their downlink throughput being greater than 1 Mbps, and being maximal when they are served by AP_i (in comparison to the other solutions $AP_{j \neq i}$).

When the maximal downlink throughput of a mesh is smaller than 1 Mbps, this mesh is considered to be **out of coverage** for any cell. This threshold of 1 Mbps is an arbitrary choice representing the minimum service requirement.

The previous definition implies that cell i may span over different service areas as follows:

$$M^i = \sum_{k=1}^{N_z} M_k^i \tag{5.31}$$

where:

- N_z is the number of service areas,
- M^i is the number of meshes in cell i,
- M_k^i is the number of meshes in cell i located in service area k.

Also let N_k^i be the number of users connected to AP_i and located in service area k. It is defined as:

$$N_k^i = N_k \frac{M_k^i}{M_k} \tag{5.32}$$

the number of users in cell i is then deduced:

$$N^i = \sum_{k=1}^{N_z} N_k^i \tag{5.33}$$

5.2.2 Generality about the resolution of optimization problems

As previously explained, the design of a (multi-technology or not) WLAN can be reduced to a combinatorial optimization problem. Most of the time, the resolution of such problem is achieved in two great steps: the definition of the problem and the search of the optimal solutions.

5.2.2.1 Definition of the problem

The description of a problem consists in defining:

- what is the set of possible solutions (search space),
- what are the constraints for a solution to be valid,
- how the quality (or fitness) of a solution has to be evaluated.

Let cover these steps through the example given in Section 5.2.1.

a) Definition of the search space

Let Ω be the search space. A possible solution to the problem ω_j $(1 \leq j \leq card(\Omega))$ is a sub-set of N_{AP} APs between the N_{AP}^c candidates: $\omega_j = (AP_1^j, \dots, AP_{N_{AP}}^j)$. Thus, the search space Ω consists of all the N_{AP}-combination of N_{AP}^c candidates. The number of possible solutions is then:

$$N_\Omega = card(\Omega) = \binom{N_{AP}^c}{N_{AP}} = \frac{N_{AP}^c!}{N_{AP}!\,(N_{AP}^c - N_{AP})!} \tag{5.34}$$

If N_{AP} = 8 and the number of candidates is 725, then N_Ω = 1,821,179,025,796,993,050.

b) Definition of the constraints

A constraint is a requirement that has to be met by a solution in order to be valid. In our example, a solution $\omega_j = (AP_1^j, \dots, AP_{N_{AP}}^j)$ is valid if more than 90% of meshes are covered (see Section 5.2.1.3). More constraints will be defined later in Section 5.2.3.4.

The optimal solutions are then deduced by comparing the valid solutions between each other.

c) Evaluation of the solutions

In order to compare two solutions, it's necessary to evaluate their respective quality. This task is achieved by the means of **objective functions**. An objective function f is a function that maps a solution ω_j onto a real value representing its *quality*:

$$f: \quad \Omega \to \mathbb{R}$$
$$\omega_j \longmapsto f(\omega_j), \qquad 1 \leq j \leq N_\Omega$$

Deciding of the *best* solution between two solutions ω_i and ω_j with respect to the objective f depends on whether this function is maximized or minimized. Indeed, if f is **maximized**, the solution ω_i is *better* than the solution ω_j with respect to f when $f(\omega_i) > f(\omega_j)$. Conversely, if f is **minimized**, the solution ω_i is *better* than the solution ω_j with respect to f when $f(\omega_i) < f(\omega_j)$.

Also, depending on the number of objective functions, an optimization problem may either be a single-objective or a multi-objective problem. A **single-objective** problem is a problem having only one objective function f. The set of optimal solutions Ω^* is either $\{\omega_j;\ f(\omega_j) = \max_{\omega_k \in \Omega}(f(\omega_k))\}$ if f is maximized, or $\{\omega_j;\ f(\omega_j) = \min_{\omega_k \in \Omega}(f(\omega_k))\}$ if f is minimized. For such problems, there is generally only one solution: the *best* with respect to the objective.

A **multi-objective** problem is a problem having more than one objective function, $F = (f_1, \dots, f_n)$. This kind of problem can become very challenging when the objectives are in conflict with each other; for instance a solution ω_j may be better than a solution ω_i with respect to an objective f_j and worse with respect to another objective. This ambiguity led to the concept of **dominance**. In a multi-objective problem, a solution ω_i dominates a solution ω_j if ω_i is at least as good as ω_j with respect to all the objectives and strictly better than ω_j for at least one objective. As an example, the dominance for a minimization problem is mathematically defined as:

$$\forall\, k \in [1,n]: f_k(\omega_i) \leq f_k(\omega_j), \qquad \exists m \in [1,n]: f_m(\omega_i) < f_m(\omega_j) \tag{5.35}$$

A solution ω_j^* that is not dominated by any other solution is said to be **Pareto optimal**. The Pareto optimal solutions are the solutions that achieve the best trade-off between the different objectives. The set of all the Pareto optimal solutions is called the **Pareto front**.

In our example, the different solutions may be evaluated based on the offered traffic X_k to each service area k with respect to the initial demand X_k^*. This point is addressed later, in Section 5.2.3.4.

5.2.2.2 Search of the optimal solutions

As explained in the previous section, the optimal solutions are deduced after comparing different valid solutions by the means of one or more objective functions. However, as implied in Section 5.2.2.1.a, the number of possible solutions may be too large to consider an

exhaustive navigation through the entire search space. To address this issue, there exist **metaheuristics**.

A metaheuristic is an optimization algorithm whose objective is to find *optimal*[13] solutions to an optimization problem in an appropriate amount of time by exploring (efficiently) a sample of the search space. A common classification of metaheuristics consists in dividing them between single-point and population based search [68].

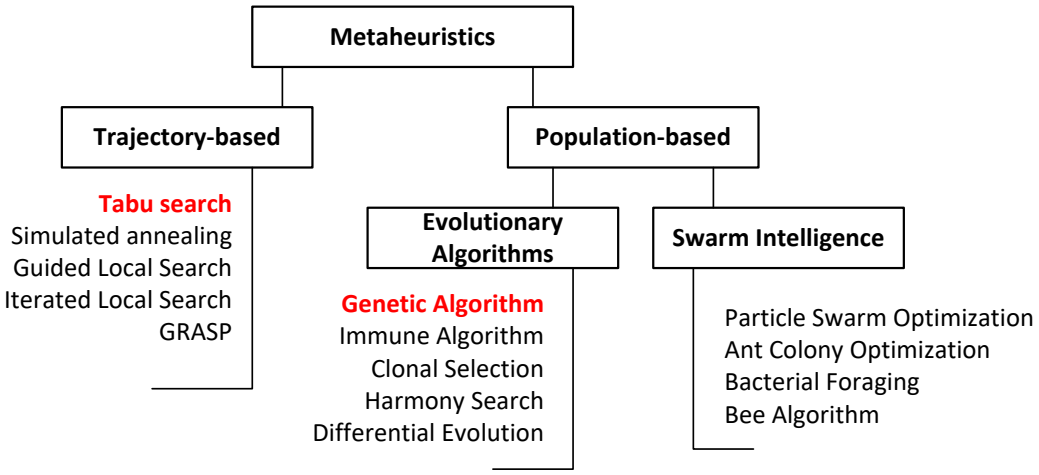

Figure 5.16. Classification of metaheuristics

a) Single-point search

In single-point search (also called trajectory methods) only one solution is evaluated at each iteration. The first solution ω_1 is randomly chosen and the solution at the i-th iteration, ω_i, is chosen in the neighborhood[14] $V(\omega_{i-1})$ of the $i-1$-th solution. A generic description of trajectory methods in single-objective problem is given by Algorithm 3.

Algorithm 3: Generic description of single-point search

Define ω : *the current solution*

Define ω^* : *the best solution encountered*

$\omega \leftarrow$ random choice in Ω

$\omega^* \leftarrow \omega$

while end condition **not** true

  Let $\omega' \in V(\omega)$

  $\omega \longleftarrow \omega'$

  if ω^* **not** better than ω

    $\omega^* \longleftarrow \omega$

  end if

end while

[13] Actually an approached value since the search is not exhaustive.

[14] The neighborhood of a solution ω is a sub-set of the search space: $V(\omega) \subset \Omega$

The logic remains the same for multi-objective problems. One of the most famous trajectory methods is the Tabu search [69] which is implemented by the XANDA's ACP module introduced in Section 5.1.3. This metaheuristic, primarily designed for single-objective problems, has been the subject of several works such as [70] for its extension to multi-objective problems.

b) Population based search

Population based search evaluate at each iteration a set of solutions $(\omega_1, \dots, \omega_n)$ called *population*. As shown in Figure 5.16, there exist different types and categories of population based search. Among them, genetic algorithm [71] is one of the most popular because of its efficiency, ease of implementation and adaptability to any type of problem. In this metaheuristic, *individuals* (the solutions of the population) evolve over *generations* (the iterations) according to 3 rules (operators):

- *Selection*: some individuals called *parents* are selected based on their fitness,
- *Crossover*: two parents are combined to produce new individuals (*children*),
- *Mutation:* a parent is modified to form children.

A generic description of genetic algorithm is given by Algorithm 4.

Algorithm 4 : Generic description of a genetic algorithm

Choose randomly an initial population of size n

Evaluate each individual

while end condition **not** true

  Select the parents based on their fitness

  Perform *crossover* with a probability P_c

  Perform *mutation* with a probability P_m

  Evaluate the new individuals

  Replace the *worst* individuals of the population with the *best* new individuals

end while

One of the well-known multi-objective genetic algorithms is the enhanced Non-dominating Sorting Genetic Algorithm (NSGA-II) [3]. It will be used later on for a multi-objective problem resolution (see Section 5.2.4).

The goal of this thesis is not to propose a novel metaheuristic to resolve the combinatorial problem induced by the design of multi-technology WLANs. Indeed, as their name implies, metaheuristics are designed to be independent of the optimization problem to solve. The purpose of the next section is to formulate a multi-objective problem that can be resolved by metaheuristics in order to design multi-technology WLANs operating at 5 GHz and 60 GHz.

5.2.3 Formulation of the planning problem

Let consider a single floor building divided in N_z service areas having distinct traffic requirements. Let N_{AP} be the minimum number of APs candidates to deploy across the building in order to meet the demand in each service area. The remaining parameters of this problem are listed in Table 5.4.

Table 5.4. Initial parameters of the planning problem

Service areas parameters		
N_k	:	The number of users in service area k
X_k^*	:	The demanded throughput per user in DL in service area k
α_k	:	The demanded uplink to downlink throughput ratio in service area k
M_k	:	The number of meshes in service area k
APs cell parameters		
M^i	:	The number of meshes in cell i
M_k^i	:	The number of meshes in cell i located in service area k, see (5.31)
N_k^i	:	The number of users connected to AP_i and located in service area k, see (5.32)
N^i	:	The number of users connected to AP_i, see (5.33)

This multi-technology design problem is a generalization of a single-technology approach that is now detailed.

5.2.3.1 Single-technology approach

The first step in defining the problem consists in explaining how is computed **the guaranteed throughput per user** in each service area by a solution of N_{AP} candidates. To do that, let AP_i be an arbitrary AP solution and u_k^i the probability that a user exchanging a packet with AP_i is located in service area k:

$$u_k^i = \frac{N_k^i}{N^i} \tag{5.36}$$

The approach to compute the system throughput in cell i is similar to the multi-class model [2], that is to say the stations (or users) are grouped in N_z classes. The class z represents the stations connected to AP_i and located in the service area z.

Based on the throughput model established in the Section 5.1.2, the cell throughput generated by the exchanges between the STAs in class z and AP_i is:

$$S_z^i = \frac{u_z^i L}{\sum_{k=1}^{N_z} u_k^i \left(\sum_{j=1}^{N_k^i} P_{STA_j^k}^d T_j^k + \sum_{m=1}^{N_k^i} P_{STA_m^k}^u t_m^k \right)} \tag{5.37}$$

where:

- L is the size of the received packet,
- T_j^k is the duration for a successful transmission to STA_j in area k by AP_i (DL),
- t_m^k is the duration for a successful transmission from STA_m in area k to AP_i (UL),
- $P_{STA_j^k}^d$ is the probability that STA_j in area k receives a packet from AP_i (DL),
- $P_{STA_m}^u$ is the probability that the AP_i receives a packet from STA_m in area k (UL).

Assuming that all the stations within a service area have the same kind of traffic and using the results in (5.23), S_z^i becomes after moving the packet size parameter to the denominator:

$$S_z^i = \frac{u_z^i}{\sum_{k=1}^{N_z} \frac{u_k^i}{(1+\alpha_k)N_k^i}\left(\sum_{j=1}^{N_k^i}\frac{1}{D_{j_k}^d} + \alpha_k \sum_{m=1}^{N_k^i}\frac{1}{D_{m_k}^u}\right)} \quad (5.38)$$

where:

- $D_{j_k}^d$ is the downlink throughput from AP_i to STA_j in service area k,
- $D_{m_k}^u$ is the uplink throughput from STA_m in service area k to AP_i,
- α_k is the demanded uplink to downlink throughput ratio in service area k.

The total (aggregate) cell throughput S^i in cell i is then deduced as the sum of the cell throughput generated by each service area:

$$S^i = \sum_{z=1}^{N_z} S_z^i \quad (5.39)$$

$$S^i = \frac{1}{\sum_{k=1}^{N_z} \frac{u_k^i}{(1+\alpha_k)N_k^i}\left(\sum_{j=1}^{N_k^i}\frac{1}{D_{j_k}^d} + \alpha_k \sum_{m=1}^{N_k^i}\frac{1}{D_{m_k}^u}\right)} \quad (5.40)$$

By applying the generalized the central limit theorem [67] to (5.40), the sum of the inverse UL and DL throughputs at S^i denominator can be approximated by a Gaussian random variable such that:

$$S^i \sim \frac{1}{\sum_{k=1}^{N_z} \frac{u_k^i}{(1+\alpha_k)N_k^i}\mathcal{N}\left[N_k^i\left(\mu_{k_{DL}}^i + \alpha_k\mu_{k_{UL}}^i\right),\ N_i^k(\sigma_{k_{DL}}^{i^2} + \alpha_k^2\sigma_{k_{UL}}^{i^2})\right]} \quad (5.41)$$

where $\mu_{k_{DL}}^i$ and $\sigma_{k_{DL}}^{i^2}$ are respectively the mean and variance of the $1/D_{j_k}^d$ sum in cell i, while $\mu_{k_{UL}}^i$ and $\sigma_{k_{UL}}^{i^2}$ are respectively the mean and variance of the $1/D_{m_k}^u$ sum. Using the property of linear combination of independent normal random variables on (5.41) lead to:

$$S^i \sim \frac{1}{\mathcal{N}\left(\mu^i,\ \sigma^{i^2}\right)} \quad (5.42)$$

with:

$$\mu^i = \sum_{k=1}^{N_z} \frac{u_k^i}{(1+\alpha_k)}\left(\mu_{k_{DL}}^i + \alpha_k\mu_{k_{UL}}^i\right), \text{ and} \quad (5.43)$$

$$\sigma^{i^2} = \sum_{k=1}^{N_z} \frac{{u_k^i}^2}{(1+\alpha_k)^2 N_k^i}(\sigma_{k_{DL}}^{i^2} + \alpha_k^2\sigma_{k_{UL}}^{i^2}) \quad (5.44)$$

Thus, the cell throughput S_p^i **guaranteed** in cell i with a probability p is defined such that:

$$P(S^i \geq S_p^i) = \frac{1}{2}\left(1 + \text{erf}\left[\frac{\frac{1}{S_p^l} - \mu^i}{\sqrt{2\sigma^{i^2}}}\right]\right) = p \qquad (5.45)$$

Let X_k be the guaranteed DL throughput per user in service area k, with a probability p, by a solution of N_{AP} candidates. X_k is determined as the value satisfying the equation:

$$\sum_{i=1}^{N_{AP}} U_k^i \; P\left(\frac{S^i}{N^i} \geq (1+\alpha_k)X_k\right) = \; p \qquad (5.46)$$

where $U_k^i = \frac{M_k^i}{M_k}$, is the probability that a user in service area k is connected to AP_i.

Finally, the guaranteed DL throughput per user in each service area, by a solution of N_{AP} candidates, is the vector $X = (X_1, \ldots, X_{N_z})$ determined by solving (5.46); in practice $p = 0.9$ for all the service areas.

As an illustration, let consider the solution, represented in Figure 5.17, consisting of 3 APs operating at 5 GHz deployed over 2 service areas such as:

- AP_m covers M_1^m meshes in service area 1,
- AP_l covers M_1^l and M_2^l in respectively service area 1 and service area 2,
- AP_n covers for M_2^n meshes in service area 2,
- M_1^{nc} meshes in service area 1 are not covered with at least 1 Mbps.

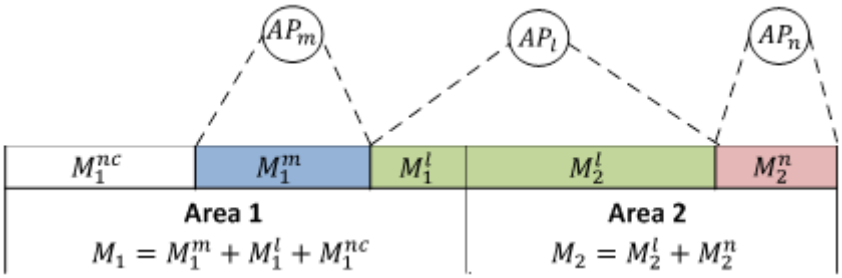

Figure 5.17. Abstract representation of a solution with 3 APs

The value of the model's parameters is given for each AP in Table 5.5. The guaranteed DL throughput per user, in each service area, by this solution with a probability p is the vector $X = (X_1, X_2)$ obtained by solving:

$$\frac{1}{2}\left(\frac{M_1^m}{M_1}\right)\left(1 + \text{erf}\left[\frac{\frac{1}{N^m(1+\alpha_1)X_1} - \mu^m}{\sqrt{2\sigma^{m^2}}}\right]\right) + \frac{1}{2}\left(\frac{M_1^l}{M_1}\right)\left(1 + \text{erf}\left[\frac{\frac{1}{N^l(1+\alpha_1)X_1} - \mu^l}{\sqrt{2\sigma^{l^2}}}\right]\right) = p \qquad (5.47)$$

$$\frac{1}{2}\left(\frac{M_2^n}{M_n}\right)\left(1 + \text{erf}\left[\frac{\frac{1}{N^n(1+\alpha_2)X_2} - \mu^n}{\sqrt{2\sigma^{n^2}}}\right]\right) + \frac{1}{2}\left(\frac{M_2^l}{M_2}\right)\left(1 + \text{erf}\left[\frac{\frac{1}{N^l(1+\alpha_2)X_2} - \mu^l}{\sqrt{2\sigma^{l^2}}}\right]\right) = p \qquad (5.48)$$

Table 5.5. Parameters value per AP solution

Parameters	$AP_m\ (i=m)$	$AP_l\ (i=l)$	$AP_n\ (i=n)$
N_1^i	$N_1(M_1^m/M_1)$	$N_1(M_1^l/M_1)$	0
N_2^i	0	$N_2(M_2^l/M_2)$	$N_2(M_2^n/M_2)$
N^i	$N_1(M_1^m/M_1)$	$N_1(M_1^l/M_1)+N_2(M_2^l/M_2)$	$N_2(M_2^n/M_2)$
u_1^i	1	N_1^l/N^l	0
u_2^i	0	N_2^l/N^l	1
U_1^i	M_1^m/M_1	M_1^l/M_1	0
U_2^i	0	M_2^l/M_2	M_2^n/M_2
μ^i	$\frac{\mu_{1_{DL}}^m+\alpha_1\mu_{1_{UL}}^m}{1+\alpha_1}$	$\sum_{k=1}^{2}\frac{u_k^l\left(\mu_{k_{DL}}^l+\alpha_k\mu_{k_{UL}}^l\right)}{(1+\alpha_k)}$	$\frac{\mu_{2_{DL}}^n+\alpha_2\mu_{2_{UL}}^n}{1+\alpha_2}$
σ^i	$\frac{\sigma_{1_{DL}}^{m^2}+\alpha_1^2\sigma_{1_{UL}}^{m^2}}{(1+\alpha_1)^2N_1^m}$	$\sum_{k=1}^{2}\frac{{u_k^l}^2\left(\sigma_{k_{DL}}^{l^2}+\alpha_k^2\sigma_{k_{UL}}^{l^2}\right)}{(1+\alpha_k)^2N_k^l}$	$\frac{\sigma_{2_{DL}}^{m^2}+\alpha_2^2\sigma_{2_{UL}}^{m^2}}{(1+\alpha_2)^2N_2^m}$

5.2.3.2 Multi-technology approach

In a multi-technology context, when one AP operates at both 5 and 60 GHz, the covered meshes are considered as distinct cells (having the same AP in common). As an illustration, let consider the previous example having, this time, AP_l covering at 60 GHz x_1^l meshes in service area 1 and x_2^l meshes in service area 2.

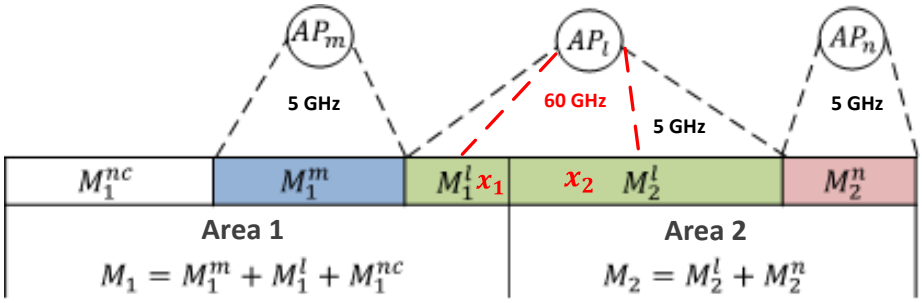

Figure 5.18. Abstract representation of a solution in a multi-technology context

The parameters of the model indicated in Table 5.5 are modified for AP_l as shown by Table 5.6. The computation of the guaranteed throughput per user in each service area is also impacted by this change. For instance, (5.47) has to be extended to account for the additional 60 GHz-cell operated by AP_l (in red below) as follows:

$$\frac{1}{2}\left(\frac{M_1^m}{M_1}\right)\left(1+\operatorname{erf}\left[\frac{\frac{1}{N^m(1+\alpha_1)X_1}-\mu^m}{\sqrt{2\sigma^{m\,2}}}\right]\right) + \frac{1}{2}\left(\frac{M_1^l-x_1^l}{M_1}\right)\left(1+\operatorname{erf}\left[\frac{\frac{1}{N^{l,5G}(1+\alpha_1)X_1}-\mu^{l,5G}}{\sqrt{2\sigma^{l,5G\,2}}}\right]\right) + \frac{1}{2}\left(\frac{x_1^l}{M_1}\right)\left(1+\operatorname{erf}\left[\frac{\frac{1}{N^{l,60G}(1+\alpha_1)X_1}-\mu^{l,60G}}{\sqrt{2\sigma^{l,60G\,2}}}\right]\right)=p \quad (5.49)$$

The same logic is applied to (5.48).

Table 5.6. Parameters value at 5 and 60 GHz

	$\boldsymbol{AP_{l,5G}\ (i=l,\ b=5G)}$	$\boldsymbol{AP_{l,60G}\ (i=l,\ b=60G)}$
$N_1^{i,b}$	$N_1(M_1^l - x_1^l)/M_1$	$N_1(x_1^l/M_1)$
$N_2^{i,b}$	$N_2(M_2^l - x_2^l)/M_2$	$N_2(x_2^l/M_2)$
$N^{i,b}$	$N_1(M_1^l - x_1^l)/M_1 + N_2(M_2^l - x_2^l)/M_2$	$N_1(x_1^l/M_1) + N_2(x_2^l/M_2)$
$u_1^{i,b}$	$N_1^{i,b}/N^{i,b}$	$N_1^{i,b}/N^{i,b}$
$u_2^{i,b}$	$N_2^{i,b}/N^{i,b}$	$N_2^{i,b}/N^{i,b}$
$U_1^{i,b}$	$(M_1^l - x_1^l)/M_1$	x_1^l/M_1
$U_2^{i,b}$	$(M_2^l - x_2^l)/M_2$	x_2^l/M_2
$\mu^{i,b}$	$\sum_{k=1}^{2}\frac{u_k^{l,5G}(\mu_{k_{DL}}^{l,5G}+\alpha_k\mu_{k_{UL}}^{l,5G})}{(1+\alpha_k)}$	$\sum_{k=1}^{2}\frac{u_k^{l,60G}(\mu_{k_{DL}}^{l,60G}+\alpha_k\mu_{k_{UL}}^{l,60G})}{(1+\alpha_k)}$
$\sigma^{i,b}$	$\sum_{k=1}^{2}\frac{u_k^{l,5G\,2}}{(1+\alpha_k)^2N_k^{l,5G}}(\sigma_{k_{DL}}^{l,5G^2}+\alpha_k^2\sigma_{k_{UL}}^{l,5G^2})$	$\sum_{k=1}^{2}\frac{u_k^{l,60G\,2}}{(1+\alpha_k)^2N_k^{l,60G}}(\sigma_{k_{DL}}^{l,60G^2}+\alpha_k^2\sigma_{k_{UL}}^{l,60G^2})$

As a generalization to the multi-technology context, the guaranteed DL throughput per user, in each service area, by a solution of N_{AP} APs is the vector $X=(X_1,\dots,X_{N_z})$. Each component X_k $(1\le k\le N_z)$ is determined by solving:

$$\sum_{i=1}^{N_{AP}}\sum_{b=1}^{N_{technos}^i}U_k^{i,b}P\left(\frac{S^{i,b}}{N^{i,b}}\ge(1+\alpha_k)X_k\right)=p \quad (5.50)$$

where $N_{technos}^i$ is the number of wireless technologies mutualized on AP_i. In this multi-technology context (5 and 60 GHz), a fallback coverage at 5 GHz has also to be considered.

5.2.3.3 Fallback coverage

As demonstrated in Chapter 4, radio links at 60 GHz are quite sensitive especially in NLOS. It's essential to anticipate the possible disruptions of the radio link at that frequency

band. In such cases, the involved users are meant to switch back to a more robust radio link (in the 5 GHz band). Also, some users may not be able to communicate at 60 GHz at all, due to device incompatibility.

To model these situations, the worst scenario is considered: all the radio links at 60 GHz are supposed to be simultaneously down; as a consequence, all the users switch back to the 5 GHz band. In this situation, the guaranteed DL throughput per user in each service area, by a solution of N_{AP} APs, becomes the vector $X' = (X'_1, \dots, X'_{N_z})$. Each component X'_k ($1 \leq k \leq N_z$) is determined by solving:

$$\sum_{i=1}^{N_{AP}} U_k^{i,5G} \; P\left(\frac{S^{i,5G}}{N^{i,5G}} \geq (1+\alpha_k)X'_k\right) = p \qquad (5.51)$$

X' is the guaranteed DL throughput per user by the fallback coverage of the solution.

From what has been previously said, it appears that multi-technology networks operating at 5 and 60 GHz have to deal with 3 types of users:

- The users connected at 60 GHz when the radio link is of good quality;
- The users connected at 5 GHz because the radio link at 60 GHz is of bad quality or disrupted;
- The users who communicate only at 5 GHz due to device restriction.

In order to find solutions which may address efficiently these different situations, a multi-objective approach has been considered.

5.2.3.4 Multi-objective problem

As introduced in the previous sections, let $X = (X_1, \dots, X_{N_z})$ and $X' = (X'_1, \dots, X'_{N_z})$ be the guaranteed DL throughput per user by respectively the initial and the fallback coverage of a solution of N_{AP} candidates deployed over N_z service areas. The demand per user in each service area is represented by the vector $X^* = (X_1^*, \dots, X_{N_z}^*)$ with an uplink to downlink throughput ratio $\alpha = (\alpha_1, \dots, \alpha_{N_z})$. The goal is to find a solution maximizing the guaranteed DL throughputs X and X' with respect to each service area. For this purpose, two objective functions have been defined.

Let f_1 be the objective function defined as:

$$f_1 = \min_{1 \leq k \leq N_z} \frac{X_k}{X_k^*} \qquad (5.52)$$

This function represents the minimum guaranteed normalized throughput per user by the **initial coverage** of the solution. It indicates by how much is at least multiplied the throughput demand of each service area by the initial coverage.

Similarly, let f_2 be the objective function defined as:

$$f_2 = \min_{1 \leq k \leq N_z} \frac{X'_k}{X_k^*} \qquad (5.53)$$

This function corresponds to the minimum guaranteed normalized throughput per user by the **fallback coverage (at 5 GHz)** of the solution. It indicates by how much is at least multiplied the throughput demand of each service area by the fallback coverage. An optimal solution to the problem is a solution **maximizing** the objectives f_1 and f_2.

However, in order to be valid, the solutions have to satisfy the 2 following constraints:

1. The initial coverage has to cover more than 90% of the global area

$$g_1 = \frac{\sum_{i=1}^{N_{AP}} M_k^i}{\sum_{k=1}^{N_z} M_k} \geq 0.9 \quad (5.54)$$

If this condition is satisfied for the initial coverage, it's also satisfied for the fallback coverage because 5 GHz radio links have a better range than 60 GHz links. Thus, an area covered at 60 GHz is implicitly covered at 5 GHz, but the reciprocal is not true.

2. The demand per service area has to be fulfilled by the initial coverage:

$$g_2 = \min_{1 \leq k \leq N_z} \frac{X_k}{X_k^*} \geq 1 \quad (5.55)$$

As a reminder, X and X' are determined by solving respectively (5.50) and (5.51) for each service area.

5.2.4 Problem resolution

To test the resolution of the multi-objective problem previously defined, let consider the single floor office building represented in Figure 5.19. It consists of four service areas:

- The service area 1 is a video conference room containing up to $N_1 = 10$ users. The demanded minimum DL throughput per user is 6 Mbps with an uplink to downlink throughput ratio of 1.
- The service area 2 is a small screening room containing a connected 4k TV ($N_2 = 1$) which streams Ultra HD videos requiring at least 25 Mbps. The uplink to downlink throughput ratio is 0.
- The service area 3 is also a video conference room bigger than service area 1 and containing up to $N_3 = 20$ users.
- The service area 4 mostly consists of the different office rooms. It contains up to 40 users browsing on the internet, sending e-mails or downloading files. The demanded throughput per user is 10 Mbps with an uplink to downlink throughput ratio of 0.4.

The objective is to deploy inside this building a multi-technology WLAN consisting of N_{AP} APs operating at 5 GHz (802.11ac) and 60 GHz (802.11ad) using the approach formulated in the previous section.

5.2.4.1 Implementation procedure

The implementation of the problem has been achieved through the following steps.

a) Meshing with XANDA

The first step has consisted in describing the environment and the service areas within XANDA, as illustrated in Figure 5.20. XANDA has been responsible for performing the meshing process described in section 5.2.1. In this problem, a total of 725 candidates have been positioned alongside the walls with a spacing of 1 m on average; and the services areas have been divided into meshes of dimension 0.5 m x 0.5 m. The meshing result is summarized in Table 5.7.

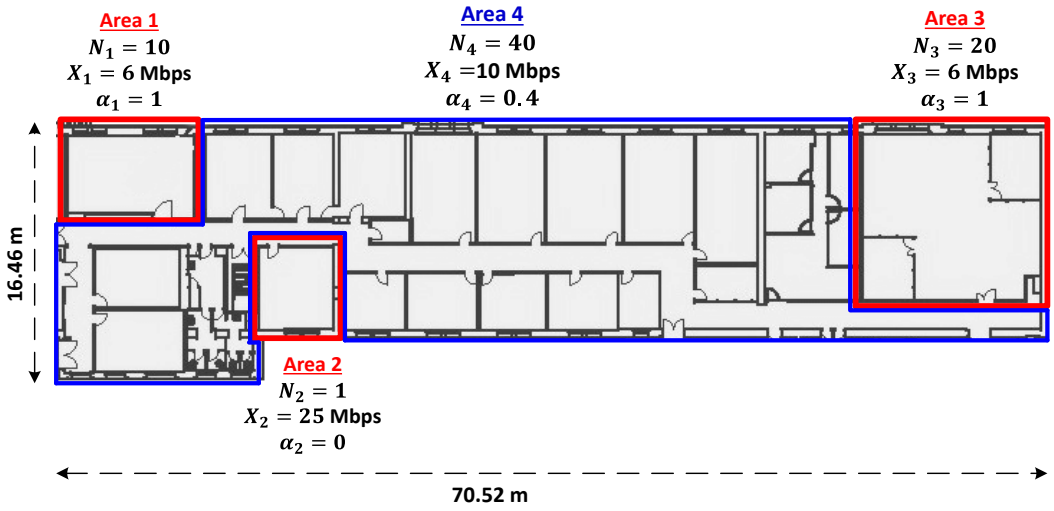

Figure 5.19. Single floor building with 4 service areas

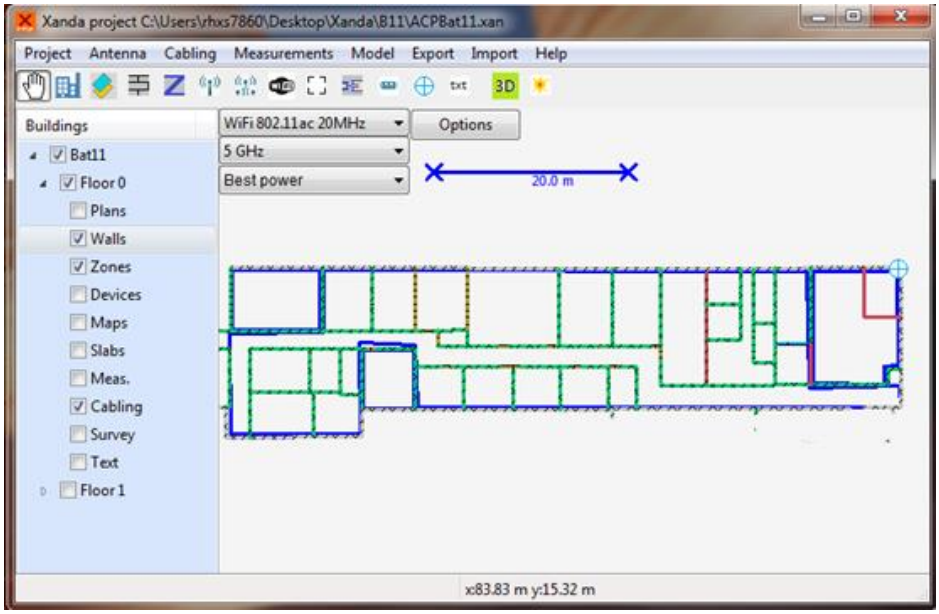

Figure 5.20. Single floor building with 4 service areas in XANDA

Table 5.7. Meshing of the building with XANDA

Users meshing					
	Service area 1	**Service area 2**	**Service area 3**	**Service area 4**	**Total**
M_k	216	132	405	3201	3954
N_k	10	1	20	40	71
X_k^*	6 Mbps	25 Mbps	6 Mbps	10 Mbps	-
α_k	1	0	1	0.4	-
APs meshing					
APs candidates		725			

The next step has consisted in computing, for each AP candidate, the throughput offered to each of the 3954 meshes based on the Signal-to-Noise-Ratio (SNR) at the receiver side[15]. Since XANDA only features the planning of single technology WLANs, this process has been carried out 2 times:

- The first iteration computed the coverage related to an IEEE 802.11ac network (5 GHz), where APs and STAs exchange packets over 20 MHz-channels with 2 spatial streams. The highest achievable data rate is 173.3 Mbps.
- The second iteration determined the coverage related to an IEEE 802.11ad network (60 GHz), where APs and STAs exchange packets over 2 GHz-channels in the single carrier PHY mode. The highest achievable MCS is 7, corresponding to a data rate of 1.925 Gbps (see Appendix D.2).

At the end of each iteration, the results have been exported to a csv file (Comma-Separated Value). Each file, having a size of about 89 MBytes, contains 2,866,650 entries (725 candidates x 3954 meshes) formatted as illustrated in Table 5.8. The exported files are then used as inputs for a PYTHON script which defines and solves the problem.

Table 5.8. Example of 3 entries at 5 GHz for the same mesh in service area 1[16]

id AP	id service area	id mesh	SNR	Data rate
0	1	1	50.2 dB	173.3 Mbps
…				
163	1	1	40.1 dB	123.3 Mbps
…				
330	1	1	18.5 dB	9.5 Mbps

b) Problem implementation with pymoo

The problem has been solved with **pymoo**[17], a PYTHON framework for research allowing the definition and the resolution of single and multi-objective problems. A simplified architecture of the framework adapted to the resolution of our problem is illustrated in Figure 5.21.

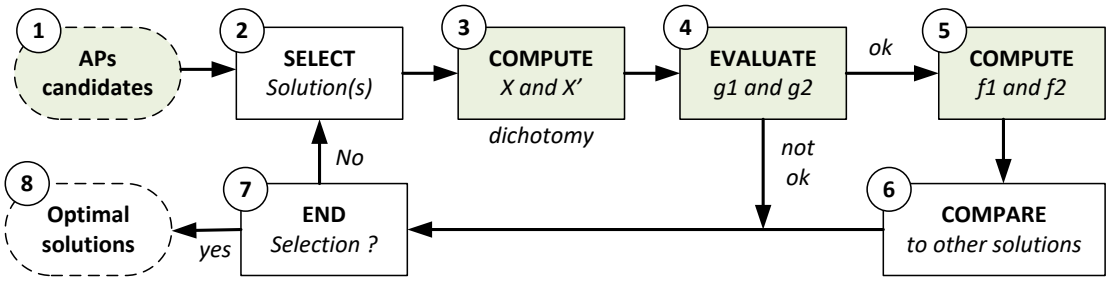

Figure 5.21. Pymoo simplified architecture

Two kinds of blocks can be identified on the diagram. The blocks in green have been implemented during this thesis and correspond to the definition of the problem (see Appendix G for more details). The blocks in white, implemented by the framework, depend on the

[15] The interferences have been overlooked.

[16] A mesh is firstly identified by its Cartesian coordinates (x, y, z) which are associated to an index (id).

[17] Available at https://pymoo.org/index.html, the version used in this thesis is ver. 0.3.0.

metaheuristic chosen to solve the problem. Among the eight metaheuristics featured by the pymoo framework, NSGA-II [3] has been selected for the resolution of the multi-objective problem because it's recognized as one of the leading algorithms in the field. Its parameterization is detailed in Table 5.9.

Table 5.9. NSGA-II parameterization

Parameter	Value
Population size	20
Number of generations	100
Crossover operator	Simulated Binary Crossover (SBX) [72]
Crossover distribution index	3
Crossover probability	0.9
Mutation operator	Polynomial mutation [73]
Mutation distribution index	3
Mutation probability	0.5

Three instances of the problem have been considered:

- The first one is the **full multi-technology (F-MT)** instance where all the AP candidates operate at both 5 and 60 GHz;
- The second one is the **single-technology (ST)** instance, where all the candidates operate at 5 GHz. In this case, which is actually a single-objective problem since $f_1 = f_2$, the constraint g_2 has been overlooked for the sake of comparison;
- The last one is the **partial multi-technology (P-MT)** instance which features a random mix between AP candidates operating solely at 5 GHz and AP candidates operating at both 5 and 60 GHz.

For each instance of the problem, a population of 20 solutions has been evaluated over 100 generations by the NSGA-II algorithm. In order to keep track of the population evolution over the generations, the number of iterations had to be restrained (to 100), due to limited RAM memory capacity (64 GB). Each solution is a N_{AP}-combination of AP candidates. The value of N_{AP} has been incrementally determined by performing some tests prior to the resolution of the problems. Its value corresponds to the minimum number of APs allowing finding at least one solution to the F-MT problem from the first generation to the last one. In this example, N_{AP} has been found to be equal to 11 for the F-MT instance (this value has then be used for the other instances).

5.2.4.2 Results

Figure 5.22 displays the evolution of the population for each of the three instances of the problem over 100 generations. The solutions of the single-technology (ST) problem are represented by the green stars. As expected, it's observed that the initial and the fallback coverages have the same fitness ($f_1 = f_2$). Also, since this multi-objective problem is actually a single-objective one, there is only one optimal solution after 100 generations. That solution does not meet the demand of at least one service area because $f_1 = f_2$ = 0.92 (as a remainder, the g_2 constraint on the initial coverage have been overlooked for this problem instance).

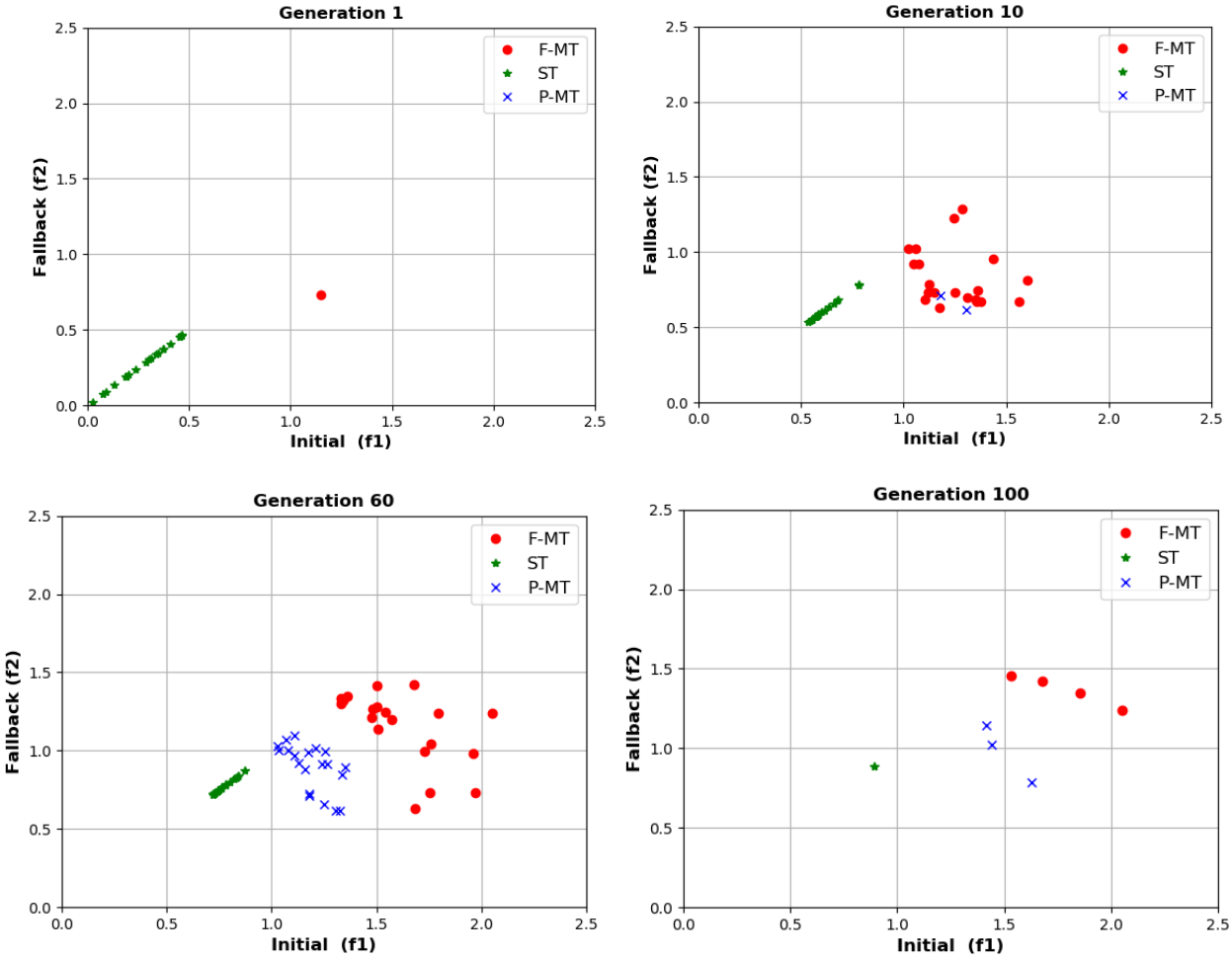

Figure 5.22. Solutions of the 3 instances of the problem over 100 generations

The solutions of the full multi-technology (F-MT) problem are represented by the red dots. The results show significant improvements of the population quality over the generations. Indeed, after 10 generations, around 25% of the population had the fallback coverage meeting the demand in each service area ($f_2 \geq 1$). At the 60-th generation, 75% of the population had both the initial and fallback coverages meeting the demand in each service area. After 100 generations, the estimated Pareto front consists of finally 4 (non-dominated) solutions. The best solution with respect to f_1 has its initial and fallback coverages multiplying the demand by respectively at least 2.05 and 1.25, and the best solution with respect to f_2 multiplies the demand by respectively at least 1.54 and 1.46. The purpose of solving multi-objective problems is to provide a set of compromise solutions. The choice of the final solution depends on the preferences (A posteriori) of the decision maker since the proposed solutions are optimal with respect to the defined objectives.

It clearly appears that the F-MT instance provide better solutions to the problem than the ST instance. In between, the P-MT instance, as its name implies, provides intermediates solutions represented by the blue crosses. After 10 generations, only 10% of the population satisfied the g_2 constraint. After 60 generations, around 50% of the population had both initial and fallback coverages meeting the demand in each service area. After 100 generations, the estimated Pareto front consists of 3 solutions whose fallback coverage barely meets the demand of all service areas. Thus, with an emphasis put on the objective f_2, the P-MT instance is slightly better than the ST instance.

5.2.5 Conclusion and future works

In this section has been formulated a multi-objective problem for the planning of multi-technology WLANs operating at 5 and 60 GHz. The implementation and resolution of the problem proved its compliancy with network design tools such as XANDA and the benefit of multi-technology WLANs when compared to single technology WLANs.

However, some aspects in the definition of the problem can be improved. The first one is to provide a better method, other than the incremental approach, to determine the minimum number of APs solutions (N_{AP}). An alternative may be to do an estimation based on the building dimensions and the average effective coverage radius of the wireless technologies. It would be a first step in reducing the computing time which is a challenge in itself.

The second improvement could be the definition of a third objective function adding new aspects to the problem resolution, other than simply maximizing the minimum throughputs. A solution could be to consider the airtime utilization during the problem resolution. Indeed, the airtime utilization (AT) of a cell i is defined as:

$$AT^i = \sum_{j=1}^{N^i} \frac{user\ j\ throughput\ demand}{user\ j\ transmission\ capability} \tag{5.56}$$

This metric defines what percentage of a channel is used and indicates how burdened is the corresponding AP. Minimizing the airtime utilization would help to achieve a load balancing between the different APs in the solution. As a consequence, a new user joining the network would theoretically have more chances to be associated with any AP.

Moreover, the applicability of the throughput model, established in Section 5.1.2, to the multi-technology WLAN planning problem has been assumed, because 802.11ad networks have contention-based access periods (CBAP) based on the 802.11 DCF (see Appendix D.1). However, since the MAC layer features other access periods for data exchange (Service Periods), further investigations will be necessary to make sure that this approximation still holds and, if necessary, make some adjustments.

Finally, in order to make the resolution of the problem fully independent of the chosen metaheuristic, additional parameters have to be defined. One of them is the neighborhood operator used by trajectory-based methods such as the Tabu search. It's also not excluded to redefine crossover and mutation operators adapted to the problem. These operators have a proven impact on the quality and the diversity of the optimal solutions.

5.3 Chapter summary

The planning of WLANs is a challenging task which is addressed by radio network design software. These planning tools feature most of the time dedicated Automatic Cell Planning (ACP) modules consisting of optimization algorithms whose purpose is, *inter alia*, to find the best sites (APs) location. In order to provide optimal locations, these algorithms rely on models to estimate coverage (propagation models) and capacity (throughput models). In this chapter, two models have been proposed to enhance ACP modules for IEEE 802.11 networks.

With the evolution in the Internet usage over the past few decades, the uplink traffic has become as much important as the downlink one for the common user. In this regard, the first main section of this chapter proposed a throughput model introducing a fairness parameter between the uplink and downlink throughputs. Results show that this model allows estimating the maximum achievable aggregate throughput of a 802.11 cell based on a desired

uplink to downlink throughput ratio. This simplified model has found an application to an actual ACP module, developed at Orange Labs Belfort, by estimating the minimum cell throughput that can be guaranteed with a certain probability. However, this model still needs improvements, especially for the management of heterogeneous traffic.

Since the planning of multi-technology WLANs can be reduced to a multi-objective combinatorial optimization problem, the second main section of this chapter focused on the definition of a model of resolution in the case of WLANs operating at 5 and 60 GHz. The method has consisted in computing and maximizing the minimum guaranteed throughput per user by the initial and fallback coverages of the Pareto optimal solutions. An implementation of this model proved its applicability to ACP modules and also the benefits of multi-technology WLANs when compared to single-technology WLANs. This model will require further improvements particularly to find the solution approaching the Pareto front in a moderate amount of time.

Chapter 6

Conclusion and perspectives

6.1 Conclusion

One the main benefits of multi-technology wireless networks lies in the variety of services, proposed at a reduced cost by the network operators, and seamlessly accessed by the end-users for various applications such as data, voice, videos, domotics, etc. However this type of heterogeneous networks has structural drawbacks. This thesis has focused on one of them which revolves around the initial deployment of wireless technologies having different coverage radius and pooled over the same devices. In practice, this task is achieved by the Automatic Cell Planning (ACP) modules of radio network design software. These modules rely on complementary models such as propagation models (for coverage) and throughput model (for capacity) in order to find optimal design solutions. The main results of this thesis have been oriented towards the production of such model.

In Chapter 2 a brief review of some (co)existing wireless technologies in indoor environments has been given. These wireless systems rely on a time varying propagation channel which is characterized by various types of model. Among them, there exist path loss models which estimate the mean signal level at the receiver side for a given distance with the transmitter. Based on a state of the art of existing indoor path loss models, log-distance and Motleey-Keenan [1] path loss models have been selected for our studies because of their simplicity. These models have then been calibrated by performing channel sounding measurements.

Chapter 3 has presented two measurement campaigns performed with a vector network analyzer in a typical residential environment. The first one has been carried out over 7 frequency bands between 800 MHz and 6 GHz. From the measurements results, two multi-frequency path loss models have been calibrated. The first one is a log-distance model and the second one is the generalized multi-wall model (G-MWM), based on the Motley-Keenan model, which takes into account two types of obstacles when predicting the path loss: *dividing walls* having a thickness smaller than 10 cm and *load-bearing* walls having a thickness greater than 10 cm. A comparative study has proven the G-MWM to achieve the best tradeoff between accuracy and simplicity of the building's representation. In the second measurement campaign, directional and omnidirectional path loss models have been established at 60 GHz. The directional path loss model has exhibited that in LOS, the difference in terms of received power between the strongest path (direct path) and the second strongest (best indirect path) decreases significantly over distance (of about 20 dB over 6 m); in NLOS, the received signal level is higher on the best indirect path. On the other hand, the omnidirectional model has shown that LOS communications benefits from multipath propagations while NLOS transmissions are strongly hindered by obstacles and surrounding objects.

In Chapter 4 has been conducted a study of the sensitivity of the transmitter's radio coverage to its surroundings. When the transmitter has been placed on either side of a wall

edge, no significant changes have been observed below 6 GHz at the tested receive positions. However at 60 GHz, the diffraction effects on the wall edge have been found to be 2 to 18 dB lower than the reflections as the receiver moved away from the edge. Moreover, the presence of potentially obstructing doors between the transmitter and the receiver has been of great importance at 60 GHz with up to 9 dB of link budget improvement by simply opening the doors. The additional losses due to the presence of people in the transmission channel have also been investigated. The results have shown up to 15 dB of extra loss at 60 GHz versus 4 dB below 6 GHz. This supplementary loss has been maximal with people standing near the receiver (below 6 GHz) or obstructing the dominant propagation path (at 60 GHz). Finally, the possibility of guaranteeing a quality of service for communications at 60 GHz has been inquired by performing throughput measurements with IEEE 802.11ad equipment. The measurement results revealed that at least 1 Gbps could have been guaranteed in LOS even in case of obstruction of the direct path. However in NLOS, the radio link was too sensible to the presence of obstacles such as furniture or people to ensure any quality of service.

At last, in Chapter 5 , two analytical models for radio network planning tools have been established. The first one is a throughput model, for IEEE 802.11 networks, introducing a fairness parameter between the uplink and downlink traffic. Results have shown that this model estimates the maximum achievable cell throughput based on a desired uplink to downlink throughput ratio. An application of this model to an existing ACP module has permitted to estimate the minimum guaranteed cell throughput with a probability of 0.9. The second model has proposed a multi-objective resolution of the combinatorial optimization problem inherent to the planning of multi-technology WLANs. The design solutions evaluation has consisted in computing and maximizing the minimum normalized guaranteed throughput by the initial coverage (5 and 60 GHz) and also the fallback coverage (only 5 GHz). This model applicability to ACP module has been proven through an implementation illustrating the benefits in terms of capacity of multi-technology WLANs when compared to single-technology WLANs.

6.2 Future work

Heterogeneous wireless networks are the future of wireless communication. A perfect illustration is the next generation of mobile network, 5G, which will provide numerous services by the means of multiple Radio Access Technologies (multi-RAT). Wi-Fi, the most popular wireless technology in indoor environment, will most certainly follow this trend, with multi-band access points operating at 2.4, 5, 6 and 60 GHz fully supporting the incoming IEEE 802.11ax (recently rebranded as Wi-Fi 6) and 802.11ay standards having distinct applications. In this regard, radio network design software will require suitable models to keep track of this (r)evolution.

Even though our throughput model requires some improvements like the management of heterogeneous traffic flows, it’s still adapted to popular existing Wi-Fi version such as Wi-Fi 4 (802.11n) or Wi-Fi 5(802.11ac). However, the next generation of Wi-Fi introduces a completely different modeling of the MAC layer. Therefore our model would necessarily have to be extended to:

- Account for multi-user transmissions in both uplink and downlink. In fact at the moment only single-user transmissions are considered. This change will probably have an impact on the definition of the uplink to downlink throughput ratio parameter.
- Account for heterogeneous stations (using different Wi-Fi version) sharing the same channel. Indeed, stations using Wi-Fi 6 would certainly have to share the same channel than “old” stations preventing a very efficient use of the spectrum.

Despite all these changes, our approach of the planning of multi-technology WLANs as a combinatorial optimization problem remains the same. As a consequence some aspects of the multi-objective model proposed in this thesis have, as well, to be improved:

- *Reduced optimization time*: the first step could be to identify the fastest way possible to determine the minimum number of required APs to satisfy the demand.
- *A more meaningful design*: by providing additional objective functions to evaluate solutions in a qualitative manner. For instance load balancing is a great asset of multi-technology networks that is not yet considered when evaluating solutions.
- *More qualitative solutions*: by "specializing" metaheuristics in the resolution of the problem. This step will require the re-definition of some search operators such as the neighborhood operator or the crossover operator. These operators have a proven impact on the quality and the diversity of the optimal solutions.

Bibliograpyhy

[1] J. Keenan and A. Motley, “Radio coverage in buildings,” *British Telecom Technology Journal*, vol. 8, no. 1, pp. 19–24, 1999.

[2] D. Malone, K. Duffy, and D. Leith, “Modeling the 802.11 Distributed Coordination Function in Nonsaturated Heterogeneous Conditions,” *IEEE/ACM Transactions on Networking*, vol. 15, no. 1, pp. 159–172, Feb. 2007.

[3] K. Deb, A. Pratap, S. Agarwal, and T. Meyarivan, “A fast and elitist multiobjective genetic algorithm: NSGA-II,” *IEEE Transactions on Evolutionary Computation*, vol. 6, no. 2, pp. 182–197, Apr. 2002.

[4] “IEEE Standard for Wireless LAN Medium Access Control (MAC) and Physical Layer (PHY) Specifications,” *IEEE Std 802.11-1997*, pp. 1–445, Nov. 1997.

[5] “IEEE Standard for Information technology– Local and metropolitan area networks– Specific requirements– Part 11: Wireless LAN Medium Access Control (MAC)and Physical Layer (PHY) Specifications Amendment 5: Enhancements for Higher Throughput,” *IEEE Std 802.11n-2009 (Amendment to IEEE Std 802.11-2007 as amended by IEEE Std 802.11k-2008, IEEE Std 802.11r-2008, IEEE Std 802.11y-2008, and IEEE Std 802.11w-2009)*, pp. 1–565, Oct. 2009.

[6] “IEEE Standard for Information technology–Telecommunications and information exchange between systems—Local and metropolitan area networks–Specific requirements–Part 11: Wireless LAN Medium Access Control (MAC) and Physical Layer (PHY) Specifications–Amendment 4: Enhancements for Very High Throughput for Operation in Bands below 6 GHz.,” *IEEE Std 802.11ac(TM)-2013 (Amendment to IEEE Std 802.11-2012, as amended by IEEE Std 802.11ae-2012, IEEE Std 802.11aa-2012, and IEEE Std 802.11ad-2012)*, pp. 1–425, Dec. 2013.

[7] “IEEE Standard for Information technology–Telecommunications and information exchange between systems–Local and metropolitan area networks–Specific requirements-Part 11: Wireless LAN Medium Access Control (MAC) and Physical Layer (PHY) Specifications Amendment 3: Enhancements for Very High Throughput in the 60 GHz Band,” *IEEE Std 802.11ad-2012 (Amendment to IEEE Std 802.11-2012, as amended by IEEE Std 802.11ae-2012 and IEEE Std 802.11aa-2012)*, pp. 1–628, Dec. 2012.

[8] T. S. Rappaport, *Wireless communications: principles and practice*, 2. ed., 18 printing. Upper Saddle River, NJ: Prentice Hall PTR, 2009.

[9] G. Tesserault, “Modélisation multi-fréquences du canal de propagation,” PhD Thesis, Université de Poitiers, Poitiers, France, 2006.

[10] H. Sizun, *La propagation des ondes radioélectriques*. Paris; Berlin; Heidelberg; New York; Hong Kong; London; Milan; Tokyo: Springer, 2003.

[11] A. Goldsmith, *Wireless communications*, Reprinted. Cambridge: Cambridge Univ. Press, 2009.

[12] K. Issiali, “Study of smart antennas and MU-MIMO techniques for indoor radio engineering and planning tools,” PhD Thesis, Université européenne de Bretagne, Rennes, France, 2015.

[13] T. K. Sarkar, Zhong Ji, Kyungjung Kim, A. Medouri, and M. Salazar-Palma, "A survey of various propagation models for mobile communication," *IEEE Antennas and Propagation Magazine*, vol. 45, no. 3, pp. 51–82, Jun. 2003.

[14] ITU-R, "Propagation data and prediction methods for the planning of indoor radiocommunication systems and radio local area networks in the frequency range 900 MHz to 100 GHz,." Rec. ITU-R P.1238-4, 1997.

[15] D. M. J. Devasirvatham, C. Banerjee, M. J. Krain, and D. A. Rappaport, "Multi-frequency radiowave propagation measurements in the portable radio environment," in *IEEE International Conference on Communications, Including Supercomm Technical Sessions*, 1990, pp. 1334–1340 vol.4.

[16] S. Y. Seidel and T. S. Rappaport, "914 MHz path loss prediction models for indoor wireless communications in multifloored buildings," *IEEE Transactions on Antennas and Propagation*, vol. 40, no. 2, pp. 207–217, Feb. 1992.

[17] "Digital mobile radio towards future generation systems." COST 231 Final Report, 1999.

[18] A. G. M. Lima and L. F. Menezes, "Motley-Keenan model adjusted to the thickness of the wall," in *SBMO/IEEE MTT-S International Conference on Microwave and Optoelectronics*, 2005, pp. 180–182.

[19] G. Wolfle and F. M. Landstorfer, "Dominant paths for the field strength prediction," in *VTC '98. 48th IEEE Vehicular Technology Conference. Pathway to Global Wireless Revolution (Cat. No.98CH36151)*, 1998, vol. 1, pp. 552–556 vol.1.

[20] L. Zhang, "Channel Measurement and Modeling in Complex Environments," PhD Thesis, Technical University of Madrid, Madrid, Spain, 2016.

[21] W. G. Newhall, T. S. Rappaport, and D. G. Sweeney, "A spread spectrum sliding correlator system for propagation measurements," *RF Design Magazine*, no. 4, pp. 40–54, 1996.

[22] V. Erceg *et al.*, "TGn Channel Models," *IEEE 802.11-03/940r4*, 10-May-2004. [Online]. Available: https://mentor.ieee.org/802.11/dcn/03/11-03-0940-04-000n-tgn-channel-models.doc. [Accessed: 29-Jul-2019].

[23] G. Breit *et al.*, "TGac Channel Model Addendum," *IEEE 802.11-09/0308r1212*. [Online]. Available: https://mentor.ieee.org/802.11/dcn/09/11-09-0308-12-00ac-tgac-channel-model-addendum-document.doc. [Accessed: 29-Jul-2019].

[24] W. C. Y. Lee, "Estimate of local average power of a mobile radio signal," *IEEE Transactions on Vehicular Technology*, vol. 34, no. 1, pp. 22–27, Feb. 1985.

[25] Kang Jianfeng, Zhao Zhuyan, Guan Hao, B. Vejlgaard, and Liu Guangyi, "TD-LTE network indoor performance with Micro and Femto deployment in a realistic metropolitan scenario," in *2013 IEEE Wireless Communications and Networking Conference (WCNC)*, 2013, pp. 3948–3952.

[26] C. Li *et al.*, "Height gain modeling of outdoor-to-indoor path loss in metropolitan small cell based on measurements at 3.5 GHz," in *2014 International Symposium on Wireless Personal Multimedia Communications (WPMC)*, 2014, pp. 552–556.

[27] Alexander Maltsev *et al.*, "Channel Models for 60 GHz WLAN Systems," *IEEE doc. 802.11-9/0334r8*, May-2010. [Online]. Available: http://www.ieee802.org/11/Reports/tgad_update.htm. [Accessed: 07-Aug-2019].

[28] S. Deng, M. K. Samimi, and T. S. Rappaport, "28 GHz and 73 GHz millimeter-wave indoor propagation measurements and path loss models," in *2015 IEEE International Conference on Communication Workshop (ICCW)*, 2015, pp. 1244–1250.

[29] J. Järveläinen, K. Haneda, and A. Karttunen, “Indoor Propagation Channel Simulations at 60 GHz Using Point Cloud Data,” *IEEE Transactions on Antennas and Propagation*, vol. 64, no. 10, pp. 4457–4467, Oct. 2016.

[30] I. A. Hemadeh, K. Satyanarayana, M. El-Hajjar, and L. Hanzo, “Millimeter-Wave Communications: Physical Channel Models, Design Considerations, Antenna Constructions, and Link-Budget,” *IEEE Communications Surveys Tutorials*, vol. 20, no. 2, pp. 870–913, Secondquarter 2018.

[31] D. Dupleich *et al.*, “Multi-band Indoor Propagation Characterization by Measurements from 6 to 60 GHz,” in *2019 13th European Conference on Antennas and Propagation (EuCAP)*, 2019, pp. 1–5.

[32] Hirokazu Sawada, Kaoru Yaginuma, Masahiro Umehira, Katsuyoshi Sato, Shuzo Kato, and Hiroshi Harada, “Non-line-of-sight propagation measurements at 60GHz for millimeter-waves WPAN,” in *2008 Asia-Pacific Microwave Conference*, 2008, pp. 1–4.

[33] L. Chaigneaud, V. Guillet, and R. Vauzelle, “A 3D ray-tracing tool for broadband wireless systems,” in *IEEE 54th Vehicular Technology Conference. VTC Fall 2001. Proceedings (Cat. No.01CH37211)*, 2001, vol. 4, pp. 2043–2047 vol.4.

[34] A. A. AlAbdullah, N. Ali, H. Obeidat, R. A. Abd-Alhmeed, and S. Jones, “Indoor millimetre-wave propagation channel simulations at 28, 39, 60 and 73 GHz for 5G wireless networks,” in *2017 Internet Technologies and Applications (ITA)*, 2017, pp. 235–239.

[35] Z. Genc, U. H. Rizvi, E. Onur, and I. Niemegeers, “Robust 60 GHz Indoor Connectivity: Is It Possible with Reflections?,” in *2010 IEEE 71st Vehicular Technology Conference*, 2010, pp. 1–5.

[36] S. Li, Y. Liu, L. Lin, D. Sun, S. Yang, and X. Sun, “Simulation and Modeling of Millimeter-Wave Channel at 60 GHz in Indoor Environment for 5G Wireless Communication System,” in *2018 IEEE International Conference on Computational Electromagnetics (ICCEM)*, 2018, pp. 1–3.

[37] Suiyan Geng, S. Ranvier, Xiongwen Zhao, J. Kivinen, and P. Vainikainen, “Multipath propagation characterization of ultra-wide band indoor radio channels,” in *2005 IEEE International Conference on Ultra-Wideband*, 2005, pp. 11–15.

[38] T. Nitsche, C. Cordeiro, A. B. Flores, E. W. Knightly, E. Perahia, and J. C. Widmer, “IEEE 802.11ad: directional 60 GHz communication for multi-Gigabit-per-second Wi-Fi [Invited Paper],” *IEEE Communications Magazine*, vol. 52, no. 12, pp. 132–141, Dec. 2014.

[39] V. Guillet, “Narrowband and wideband characteristics of 60 GHz radio propagation in residential environment,” *Electronics Letters*, vol. 37, no. 21, pp. 1310–1311, Oct. 2001.

[40] Ł. Januszkiewicz, “Analysis of Human Body Shadowing Effect on Wireless Sensor Networks Operating in the 2.4 GHz Band,” *Sensors (Basel)*, vol. 18, no. 10, Oct. 2018.

[41] G. R. MacCartney, T. S. Rappaport, and S. Rangan, “Rapid Fading Due to Human Blockage in Pedestrian Crowds at 5G Millimeter-Wave Frequencies,” in *GLOBECOM 2017 - 2017 IEEE Global Communications Conference*, 2017, pp. 1–7.

[42] M. Jacob, C. Mbianke, and T. Kürner, “A dynamic 60 GHz radio channel model for system level simulations with MAC protocols for IEEE 802.11ad,” in *IEEE International Symposium on Consumer Electronics (ISCE 2010)*, 2010, pp. 1–5.

[43] C. Slezak, V. Semkin, S. Andreev, Y. Koucheryavy, and S. Rangan, “Empirical Effects of Dynamic Human-Body Blockage in 60 GHz Communications,” *IEEE Communications Magazine*, vol. 56, no. 12, pp. 60–66, Dec. 2018.

[44] M. Yamagishi, T. Hikage, M. Sasaki, M. Nakamura, and Y. Takatori, "FDTD-Based Numerical Estimation of Human Body Blockage Characteristics in 26GHz Band Indoor Propagation," in *2018 48th European Microwave Conference (EuMC)*, 2018, pp. 878–881.

[45] S. Collonge, G. Zaharia, and G. E. Zein, "Influence of the human activity on wide-band characteristics of the 60 GHz indoor radio channel," *IEEE Transactions on Wireless Communications*, vol. 3, no. 6, pp. 2396–2406, Nov. 2004.

[46] M. Fakharzadeh, J. Ahmadi-Shokouh, B. Biglarbegian, M. R. Nezhad-Ahmadi, and S. Safavi-Naeini, "The effect of human body on indoor radio wave propagation at 57–64 GHz," in *2009 IEEE Antennas and Propagation Society International Symposium*, 2009, pp. 1–4.

[47] R. J. Weiler, M. Peter, W. Keusgen, and M. Wisotzki, "Measuring the busy urban 60 GHz outdoor access radio channel," in *2014 IEEE International Conference on Ultra-WideBand (ICUWB)*, 2014, pp. 166–170.

[48] W. Qi, J. Huang, J. Sun, Y. Tan, C. Wang, and X. Ge, "Measurements and modeling of human blockage effects for multiple millimeter Wave bands," in *2017 13th International Wireless Communications and Mobile Computing Conference (IWCMC)*, 2017, pp. 1604–1609.

[49] C. J. Gibbins, "Radiowave propagation in the 30-60 GHz band," in *IEE Colloquium on Radiocommunications in the Range 30-60 GHz*, 1991, pp. 1/1-1/4.

[50] X. Wang *et al.*, "Millimeter Wave Communication: A Comprehensive Survey," *IEEE Communications Surveys Tutorials*, vol. 20, no. 3, pp. 1616–1653, thirdquarter 2018.

[51] D. Grieve, B. Cutler, and J. Harmon, "Understanding IEEE 802.11ad Physical Layer and Measurement Challenges," p. 68, 2014.

[52] D. Grieve, "IEEE 802.11ad PHY Layer Testing," *Wireless Communications*, p. 40, 2012.

[53] R. van Nee and R. Prasad, *OFDM for wireless multimedia communications*. Boston: Artech House, 2000.

[54] Cetin KURNAZ and Hulya GOKALP, "Investigating the relation between optimum guard interval and channel delay spread for a MC-CDMA system," *Turkısh Journal Of Electrıcal Engıneerıng Computer Scıences*, vol. 20, no. 3, 2012.

[55] C. Liaskos, S. Nie, A. Tsioliaridou, A. Pitsillides, S. Ioannidis, and I. Akyildiz, "A New Wireless Communication Paradigm through Software-Controlled Metasurfaces," *IEEE Communications Magazine*, vol. 56, no. 9, pp. 162–169, Sep. 2018.

[56] "Cisco Visual Networking Index: Global Mobile Data Traffic Forecast Update, 2017–2022 White Paper," *Cisco*. [Online]. Available: https://www.cisco.com/c/en/us/solutions/collateral/service-provider/visual-networking-index-vni/white-paper-c11-738429.html. [Accessed: 29-Mar-2019].

[57] Y. Gao and L. Dai, "Optimal Downlink/Uplink Throughput Allocation for IEEE 802.11 DCF Networks," *IEEE Wireless Communications Letters*, vol. 2, no. 6, pp. 627–630, Dec. 2013.

[58] H. Feng, T. Wang, and B. Hu, "An optimized DCF schema with Downlink and Uplink bandwidth control in 802.11 WLAN," in *TENCON 2005 - 2005 IEEE Region 10 Conference*, 2005, pp. 1–5.

[59] K. Sung Won, K. Byung-Seo, and F. Yuguang, "Downlink and uplink resource allocation in IEEE 802.11 wireless LANs," *IEEE Transactions on Vehicular Technology*, vol. 54, no. 1, pp. 320–327, Jan. 2005.

[60] J. Y. Kim, H. Jin, J. Seo, S. H. Kim, and D. K. Sung, "Adaptive Transmission Control for Uplink/Downlink Fairness in Unsaturated CSMA Networks," *IEEE Communications Letters*, pp. 1–1, 2019.

[61] F. Wang, S. Li, Z. Dou, and D. Peng, "Markov Modeling Methods for Performance Analysis of IEEE 802.11 Protocol," in *2018 IEEE 3rd Advanced Information Technology, Electronic and Automation Control Conference (IAEAC)*, 2018, pp. 2071–2075.

[62] G. Bianchi, "Performance analysis of the IEEE 802.11 distributed coordination function," *IEEE Journal on Selected Areas in Communications*, vol. 18, no. 3, pp. 535–547, Mar. 2000.

[63] N. Najjari, G. Min, J. Hu, and W. Miao, "Performance Analysis of WLANs under Bursty and Correlated Video Traffic," in *2017 14th International Symposium on Pervasive Systems, Algorithms and Networks 2017 11th International Conference on Frontier of Computer Science and Technology 2017 Third International Symposium of Creative Computing (ISPAN-FCST-ISCC)*, 2017, pp. 250–256.

[64] F. Daneshgaran, M. Laddomada, F. Mesiti, and M. Mondin, "Unsaturated Throughput Analysis of IEEE 802.11 in Presence of Non Ideal Transmission Channel and Capture Effects," *IEEE Transactions on Wireless Communications*, vol. 7, no. 4, pp. 1276–1286, Apr. 2008.

[65] E. W. D. García, "Admission Capacity estimations in IEEE 802 . 11 Access Points Technical Report," 2008.

[66] A. Chariete, V. Guillet, and J. Thiriet, "Optimization of Wi-Fi access point placement in an indoor environment," in *2016 13th International Conference on New Technologies for Distributed Systems (NOTERE)*, 2016, pp. 1–6.

[67] E. W. Weisstein, "Lindeberg-Feller Central Limit Theorem." [Online]. Available: http://mathworld.wolfram.com/Lindeberg-FellerCentralLimitTheorem.html. [Accessed: 09-Oct-2019].

[68] M. Birattari, L. Paquete, T. Stützle, and K. Varrentrapp, "Classification of metaheuristics and design of experiments for the analysis of components," 2001.

[69] F. Glover, "Future paths for integer programming and links to artificial intelligence," *Computers & Operations Research*, vol. 13, no. 5, pp. 533–549, Jan. 1986.

[70] S. Kulturel-Konak, A. E. Smith, and B. A. Norman, "Multi-objective tabu search using a multinomial probability mass function," *European Journal of Operational Research*, vol. 169, no. 3, pp. 918–931, Mar. 2006.

[71] D. E. Goldberg, *Genetic algorithms in search, optimization, and machine learning*. Reading, Mass: Addison-Wesley Pub. Co, 1989.

[72] K. Deb, K. Sindhya, and T. Okabe, "Self-adaptive simulated binary crossover for real-parameter optimization," in *Proceedings of the 9th annual conference on Genetic and evolutionary computation - GECCO '07*, London, England, 2007, p. 1187.

[73] M. Hamdan, "The Distribution Index in Polynomial Mutation for Evolutionary Multiobjective Optimisation Algorithms: An Experimental Study," in *Proceedings of the 4th International Conference on Electronics Computer Technology*, Kanyakumari, India, 2012.

Appendix

Appendix A Measurement environment

Plan

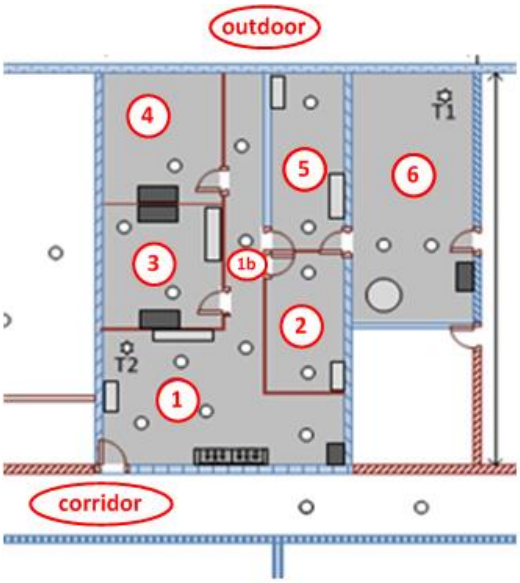

Room 1

Room 1b

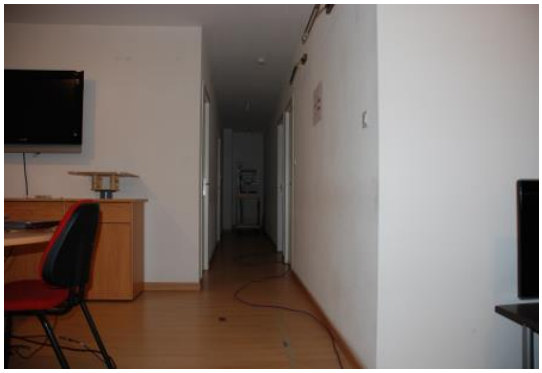

Room 2

Room 3

Room 4

Room 5

Room 6

Corridor

Outdoor

Figure A.1. Pictures of the measurement environment

Appendix B Antennas pattern

Appendix B.1. Omnidirectional Tx and Rx antennas (0.8 – 6 GHz)

a) Characteristics

XPO2V-0.8-6.0/1485

COBHAM

Wideband Omni Antenna

The most important thing we build is trust

Designed for Security Application

Suitable for Unmanned Systems Applications

High Power

Lightweight

Rugged

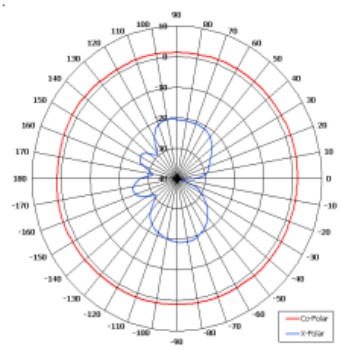

Azimuth Pattern

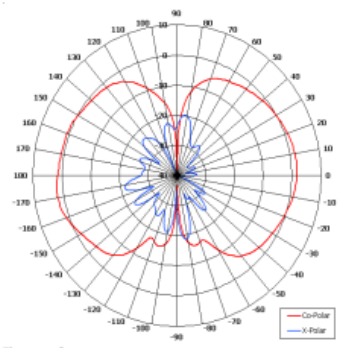

Elevation Pattern

ELECTRICAL	
Frequency	0.80 - 6.00 GHz
Gain	2.0 dBi Nom
Polarisation	Linear (Vertical)
Beamwidth	360° (Az) x 75° (El) Approx
Cross Polar	25 dB Typ
VSWR	2.7:1 Max, 1.7:1 Typ
Power Rating	100 W
Front to Back	N/A

MECHANICAL	
Standard Finish	Black
Mass	220g (0.49 lbs Approx)
Temperature	-20° to +50°C
Wind Loading	1.94 Kg (4.27lbs) @ 100mph

MOUNTING OPTIONS	
Kits Available	N/A
See separate data sheets	

ADDITIONAL NOTES

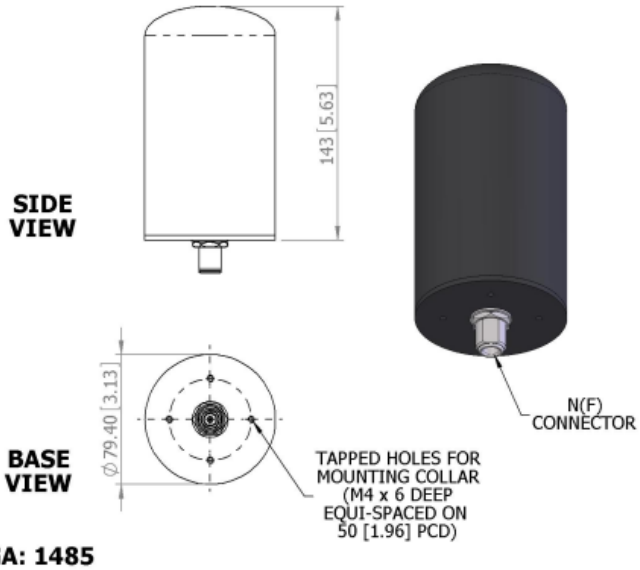

GA: 1485

Issued 030810

For further information please contact:
Cobham Antenna Systems, Microwave Antennas
Lambda House, Cheveley,
Newmarket, Suffolk CB8 9RG, UK.
Tel +44 (0)1638 732 177
Fax +44 (0) 1638 731999
Email newmarket.sales@cobham.com

b) Antenna gain approximation

The antenna gain has been measured at different frequency bands:

Table B.1. Antenna gain at different frequency

Frequency (GHz)	0.8	0.9	1.8	2.2	2.5	3.5	5.5
Gain (dBi)	0.2	0.2	1.2	1.5	2.1	2.6	3.1

From this result is deduced an approximation of the antenna gain as a function of the frequency *f* (in GHz):

$$G(f)\ [\text{dBi}] = 0.43 + 3.69\log_{10}(f) \tag{7.1}$$

Appendix B.2. Directional Tx antenna (60 GHz)

This antenna has been developed at Orange Labs Belfort. Its radiation pattern is displayed in Figure B.1.

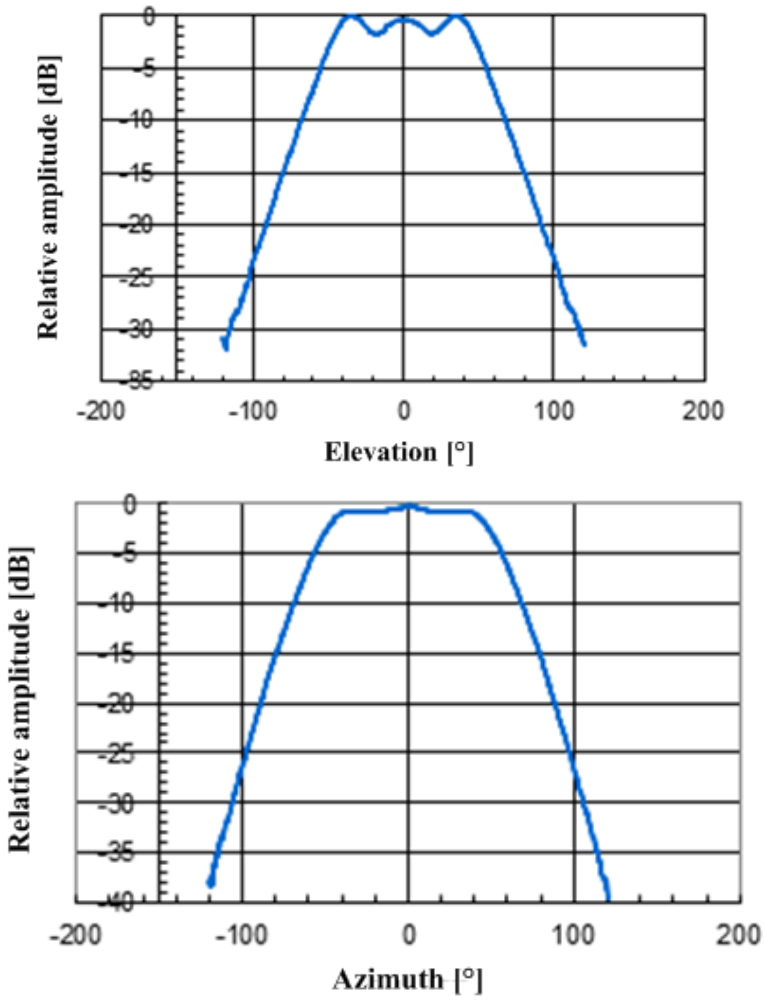

Figure B.1. Radiation pattern of 120°-Tx antenna in E and H-planes

Appendix B.3. Directional Rx antenna (60 GHz)

Standard Gain Horn

Model 25240-20

Waveguide Size:	WG25 (WR15, R620)
Nominal Gain:	20 dBi
Operating Frequencies:	49.9 - 75.8 GHz
Overall Length (A):	48.0 mm (1.890 inch)
Aperture Width (B):	18.50 mm (0.728 inch)
Aperture Height (C):	12.80 mm (0.504 inch)
Waveguide Width (D):	3.759 mm (0.148 inch)
Waveguide Height (E):	1.880 mm (0.074 inch)
Flare Length (F):	38.00 mm (1.496 inch)

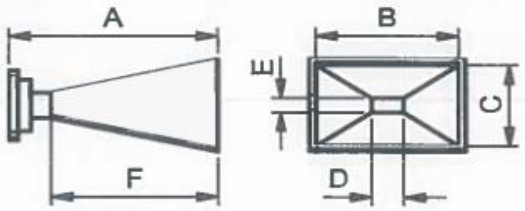

Typical Performance Data

Frequency (GHz)	Gain (dBi)	Beamwidth E-Plane	Beamwidth H-Plane	Frequency (GHz)	Gain (dBi)	Beamwidth E-Plane	Beamwidth H-Plane	Frequency (GHz)	Gain (dBi)	Beamwidth E-Plane	Beamwidth H-Plane
49.9	17.99	23.8°	22.1°	60	19.48	19.8°	18.4°	70.5	20.74	16.9°	15.6°
50	18.01	23.8°	22.1°	60.5	19.55	19.7°	18.2°	71	20.79	16.8°	15.5°
50.5	18.09	23.6°	21.8°	61	19.61	19.5°	18.1°	71.5	20.85	16.6°	15.4°
51	18.17	23.3°	21.6°	61.5	19.68	19.3°	17.9°	72	20.90	16.5°	15.3°
51.5	18.25	23.1°	21.4°	62	19.74	19.2°	17.8°	72.5	20.95	16.4°	15.2°
52	18.33	22.9°	21.2°	62.5	19.80	19.0°	17.7°	73	21.01	16.3°	15.1°
52.5	18.41	22.7°	21.0°	63	19.87	18.9°	17.5°	73.5	21.06	16.2°	15.0°
53	18.49	22.4°	20.8°	63.5	19.93	18.7°	17.4°	74	21.11	16.1°	14.9°
53.5	18.56	22.2°	20.6°	64	19.99	18.6°	17.2°	74.5	21.16	16.0°	14.8°
54	18.64	22.0°	20.4°	64.5	20.05	18.4°	17.1°	75	21.21	15.9°	14.7°
54.5	18.71	21.8°	20.2°	65	20.11	18.3°	17.0°	75.5	21.26	15.8°	14.6°
55	18.78	21.6°	20.1°	65.5	20.17	18.2°	16.8°	75.8	21.29	15.7°	14.6°
55.5	18.86	21.4°	19.9°	66	20.23	18.0°	16.7°				
56	18.93	21.2°	19.7°	66.5	20.29	17.9°	16.6°				
56.5	19.00	21.1°	19.5°	67	20.35	17.8°	16.5°				
57	19.07	20.9°	19.4°	67.5	20.41	17.6°	16.3°				
57.5	19.14	20.7°	19.2°	68	20.46	17.5°	16.2°				
58	19.21	20.5°	19.0°	68.5	20.52	17.4°	16.1°				
58.5	19.28	20.3°	18.9°	69	20.58	17.2°	16.0°				
59	19.35	20.2°	18.7°	69.5	20.63	17.1°	15.9°				
59.5	19.41	20.0°	18.5°	70	20.69	17.0°	15.8°				

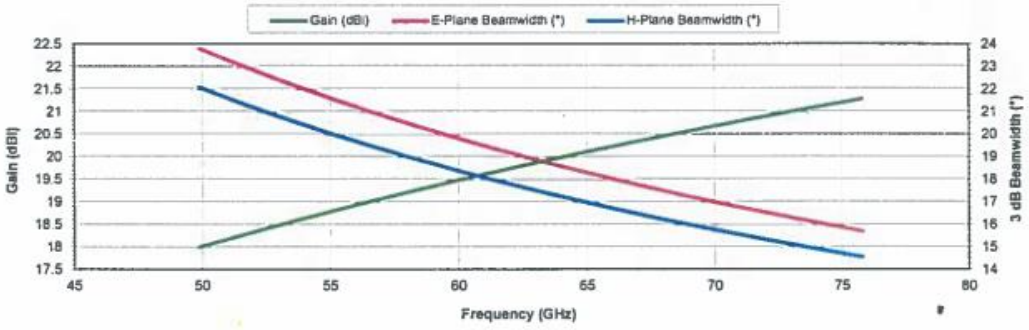

Notes:
Gain calculations based on NRL Report 4433 - accuracy to approx ± 0.3dBi
Half-power (3dB) beamwidth estimates calculated using 50.8 λ / C (E-Plane) and 68.1 λ / B (H-Plane). This is a 'large aperture' approximation that breaks down at gain values smaller than around 12 dBi. For 10dBi Standard Gain Horns, beamwidths are approximately 63° at the lowest frequency and 48° at the highest frequency.

FLANN MICROWAVE LTD
Dunmere Road
Bodmin, Cornwall
PL31 2QL
United Kingdom
Tel: +44 (0)1208 77777
Fax: +44 (0)1208 76426

FLANN MICROWAVE INC
One Boston Place
Suite 2600
Boston
Massachusetts, MA 02108-4407
Tel: 617 621 7034
Fax: 617 577 8234

sales@flann.com www.flann.com

15/1/2015 Form 305 Iss 23

Appendix B.4. Omnidirectional Rx antenna (60 GHz)

O-5836230230-15-S1

Rev. 1.0

and Omnidirectional Antenna, 360 Degree

ription:

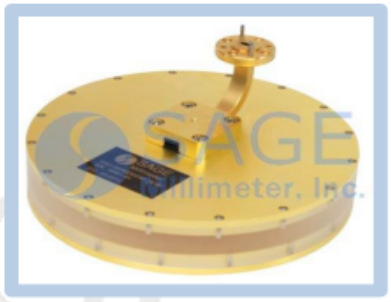

l SAO-5836230230-15-S1 is a WR-15 omnidirectional na that operates between 58 and 62 GHz. This vertically zed antenna offers 360 degrees azimuth coverage with ±3 gular gain flatness. The antenna features a half power width of 30 degrees in the vertical direction and 2 dB gain the entire frequency range.

ures:

- 360˚ Azimuth Coverage
- 30˚ Vertical 3 dB Beamwidth
- Vertically Polarized

Applications:

- Communication Links
- EW Systems
- Indoor Local Area Networks

rical Specifications:

Parameter	Minimum	Typical	Maximum
uency Range	58 GHz		62 GHz
		2 dB	
Variation	-3 dB		3 dB
uth		360˚	
Beamwidth, Vertical		30˚	
R		2:1	
er Handling	1 W		
ification Temperature		+25°C	
ating Temperature	-40°C		+85°C

hanical Specifications:

Parameter	Connector
t	WR-15 Waveguide with UG-385/U Flange
	1.78" (H) x 4.00" (Ø)
Material	Aluminum
h	Gold Plated
ght	12.0 Oz
ne	AO-V2

www.sagemillimeter.com | 3043 Kashiwa Street, Torrance, CA 90505
Phone: 424-757-0168 | Fax: 424-757-0188 | Email: sales@sagemillimeter.com

Appendix C Sensitivity measurements results

Appendix C.1. Wall edge scenario below 6 GHz

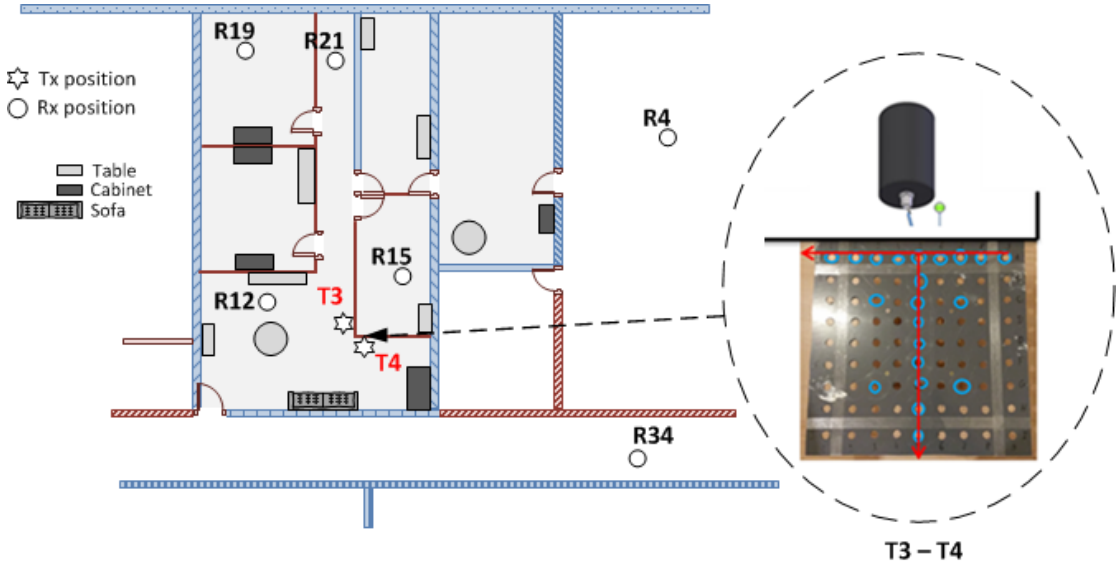

R4 – Parallel movement	R4 – Perpendicular movement
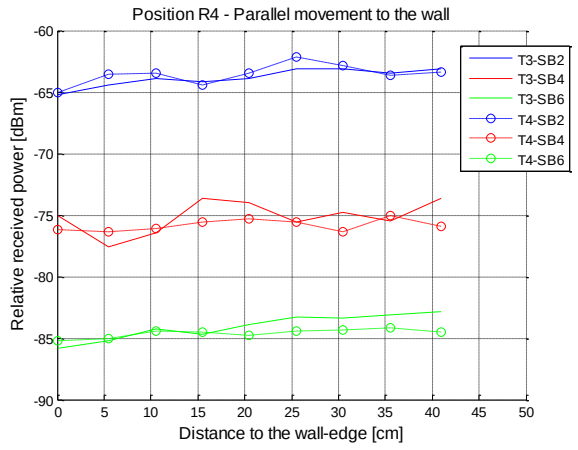	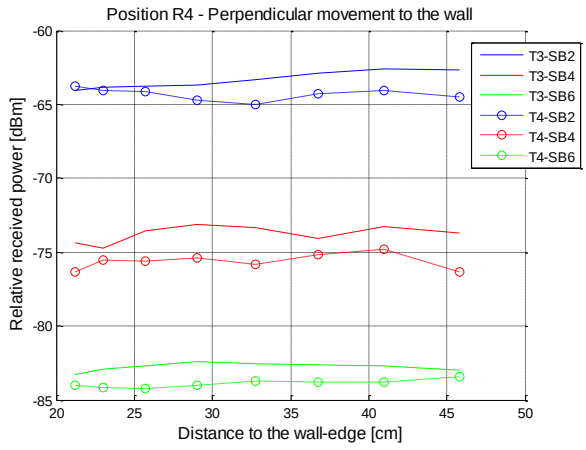
R12 – Parallel movement	**R12 – Perpendicular movement**
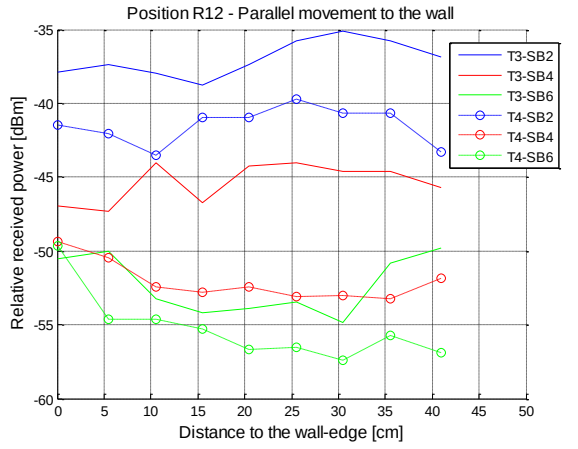	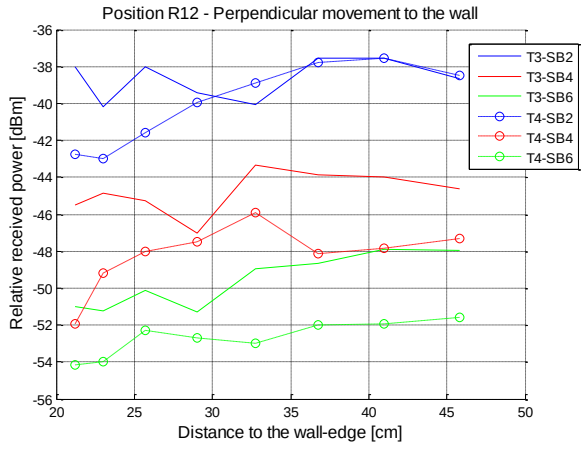

R15 – Parallel movement

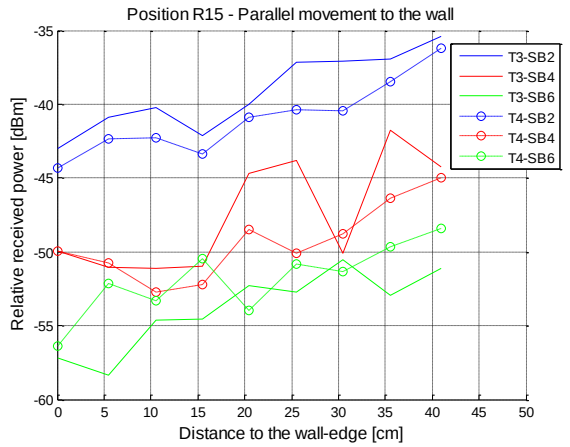

R15 – Perpendicular movement

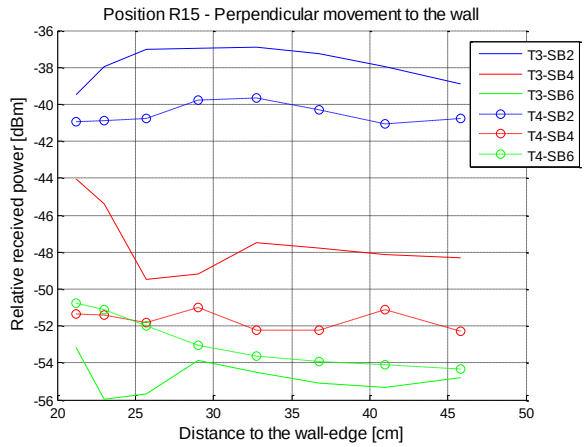

R19 – Parallel movement

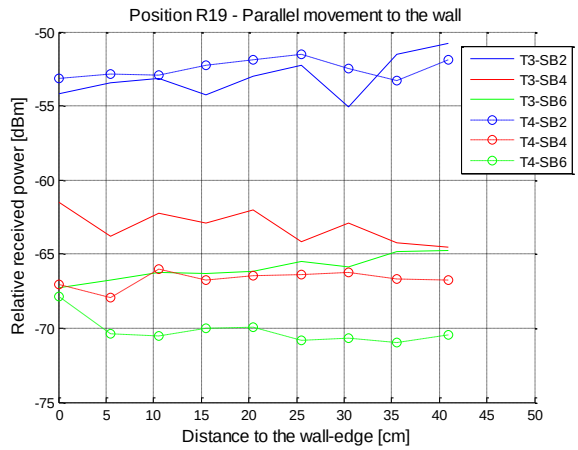

R19 – Perpendicular movement

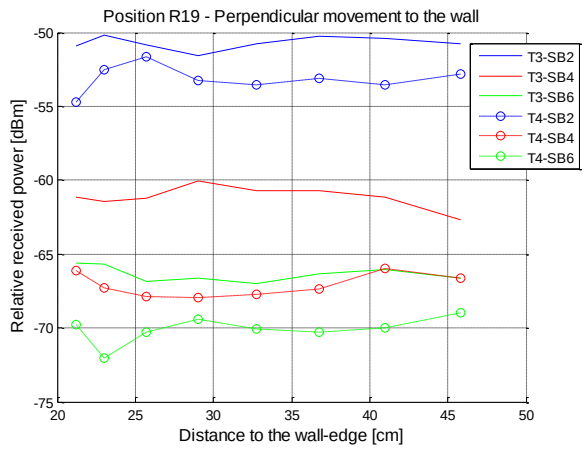

R21 – Parallel movement

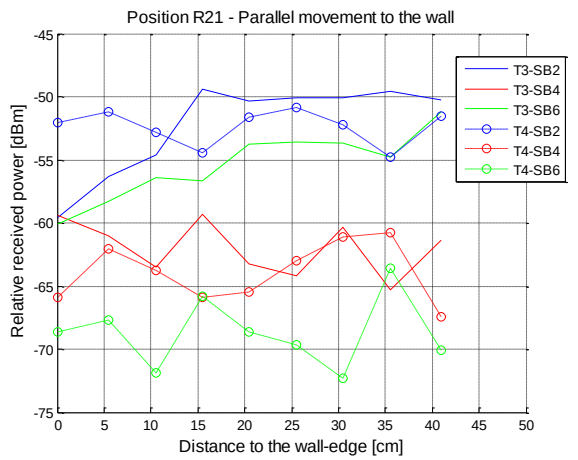

R21 – Perpendicular movement

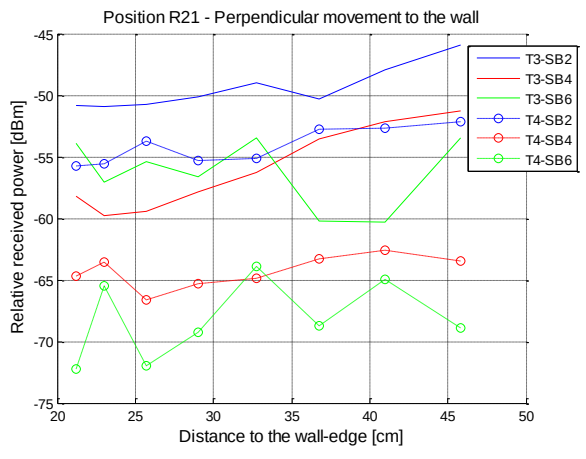

R34 – Parallel movement	R34 – Perpendicular movement
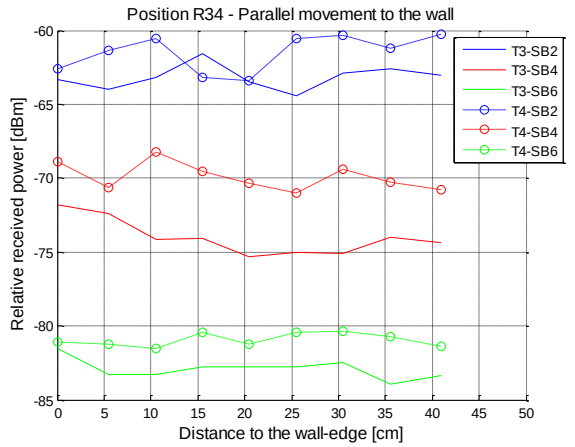	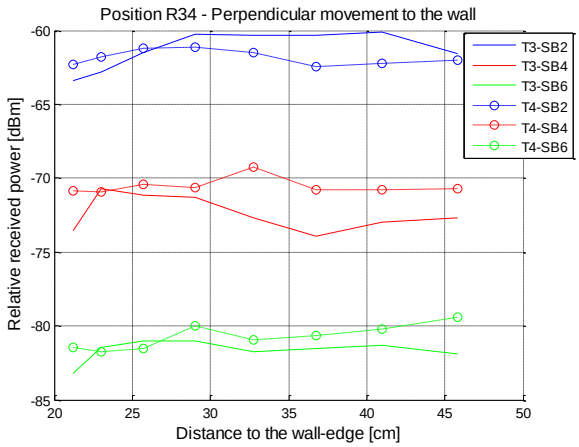

Appendix C.2. Transmitter near a door below 6 GHz

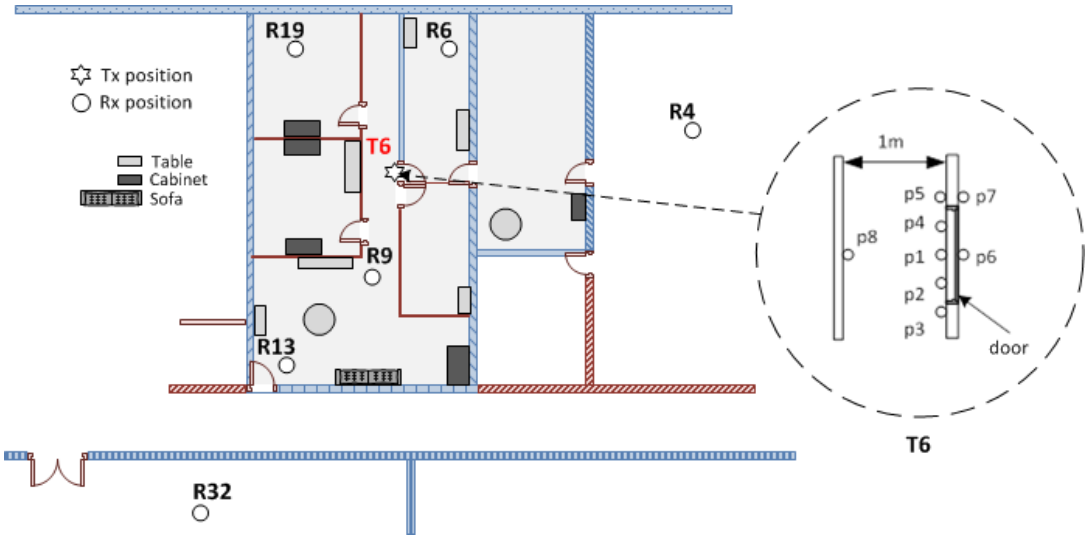

Tx above the door – SB2
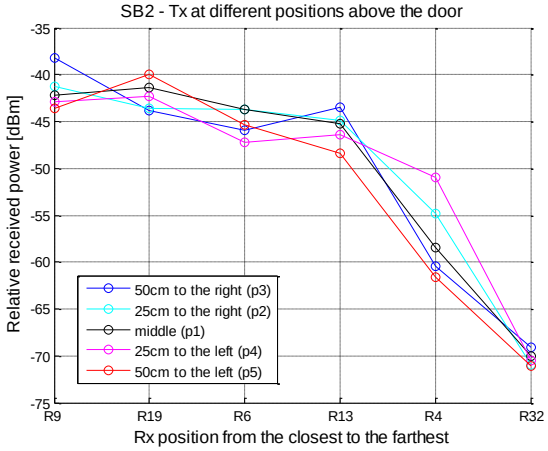

- SB4 -	- SB6 -
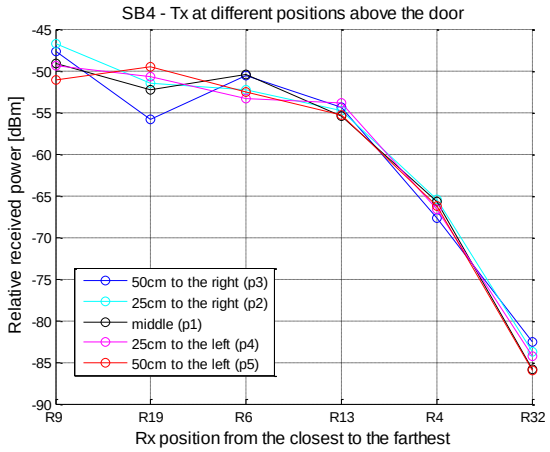	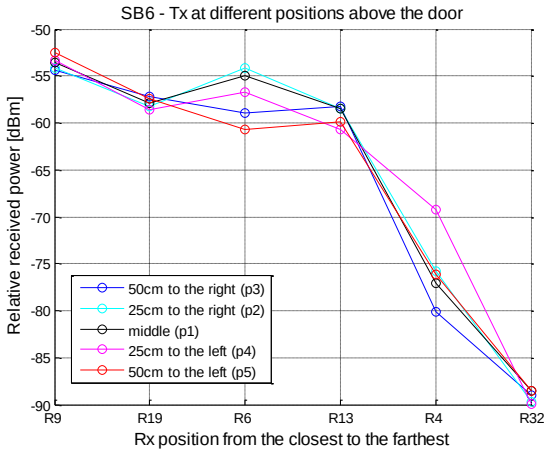

Tx above or in front of the door – SB2

- SB4 -	- SB6 -
	

Tx above or behind the door – SB2	
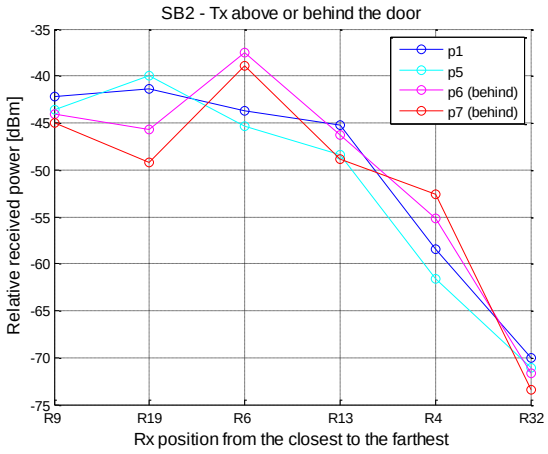	
- SB4 -	**- SB6 -**
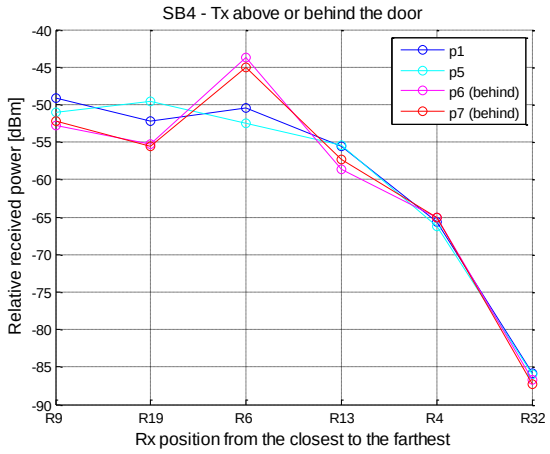	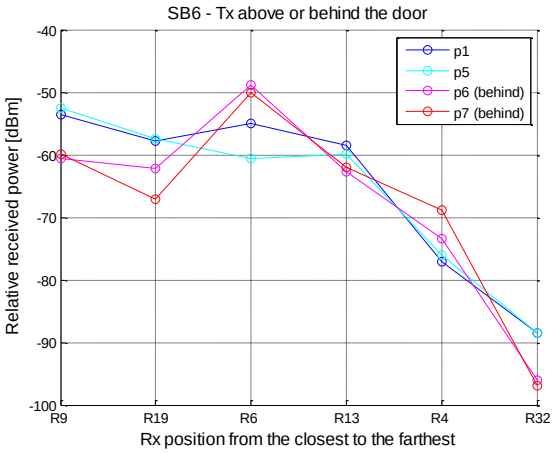

Appendix C.3. Transmitter in the middle of a room

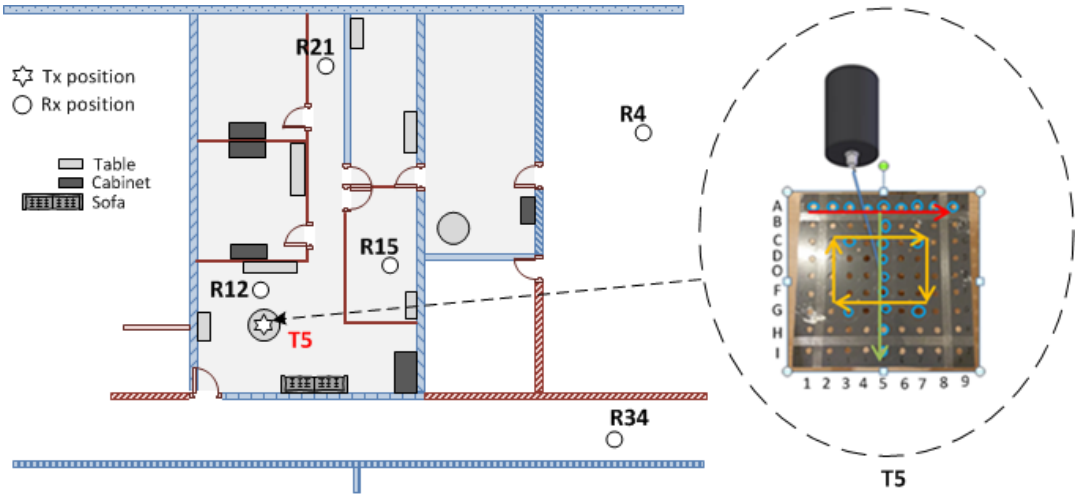

Horizontal movement – SB2

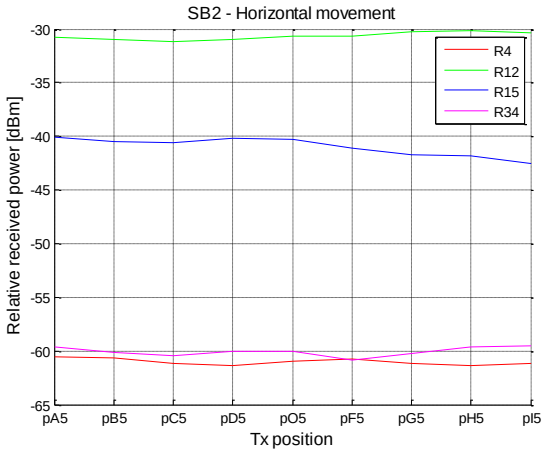

- SB4 -

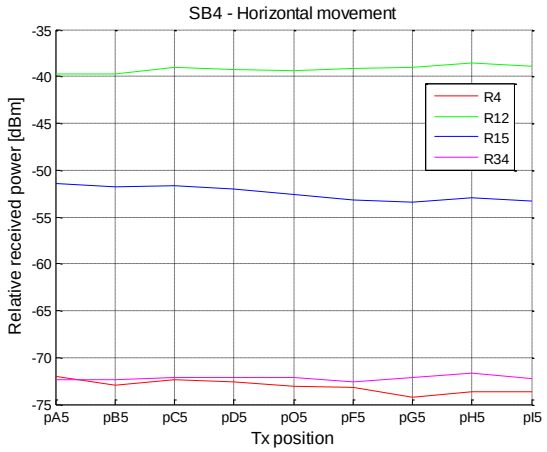

- SB6 -

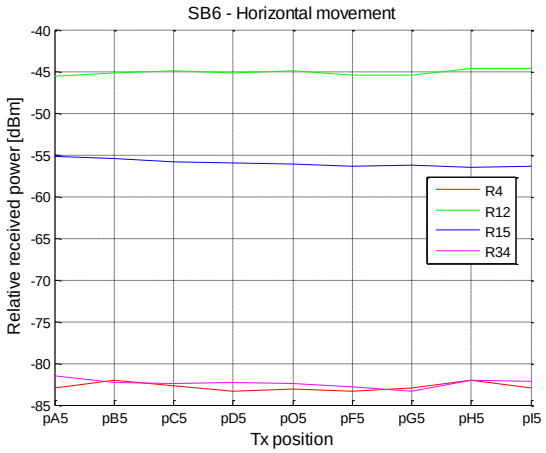

Vertical movement – SB2

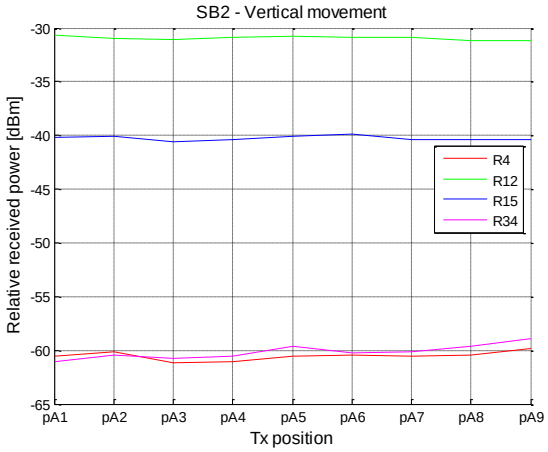

- SB4 -	- SB6 -
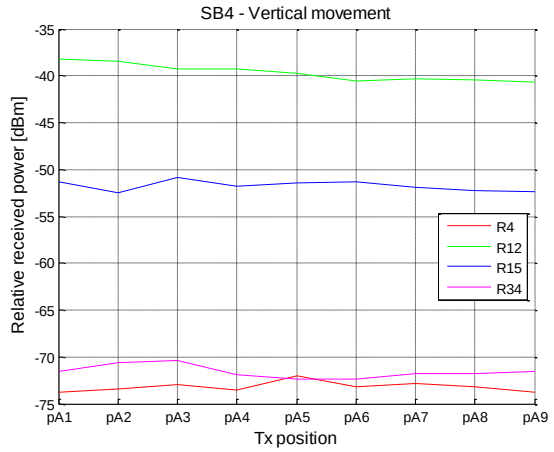	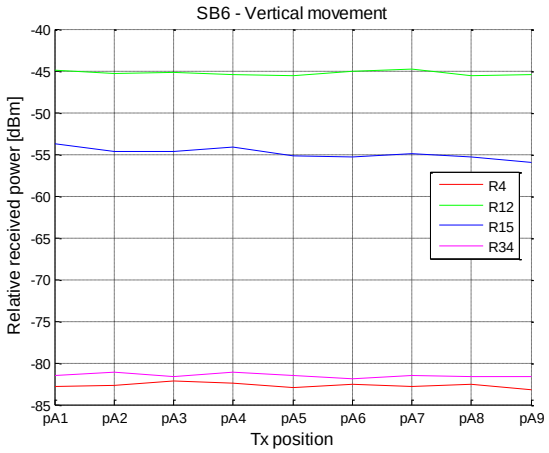

Square movement – SB2

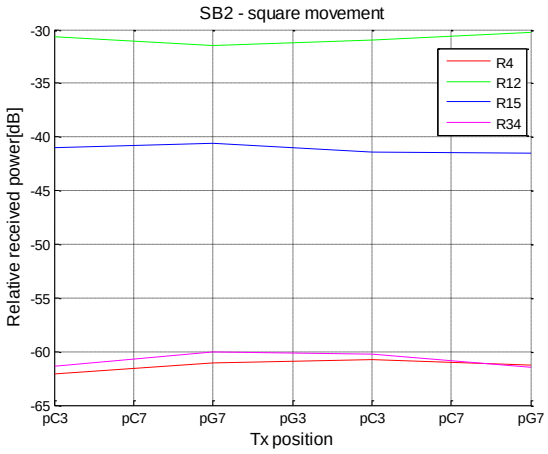

- SB4 -	- SB6 -
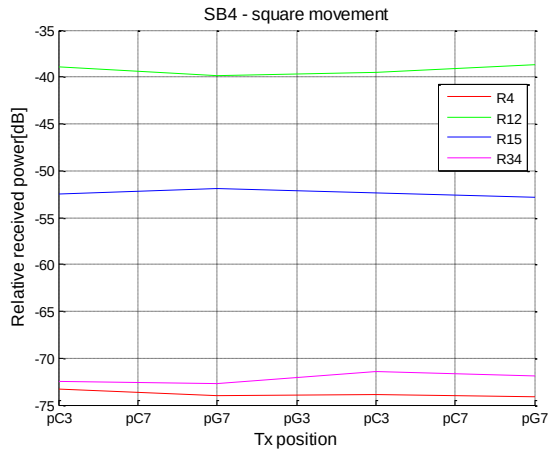	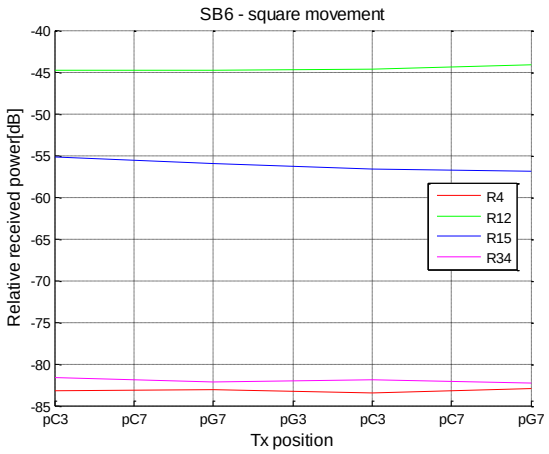

Appendix C.4. Transmitter inside a cabinet

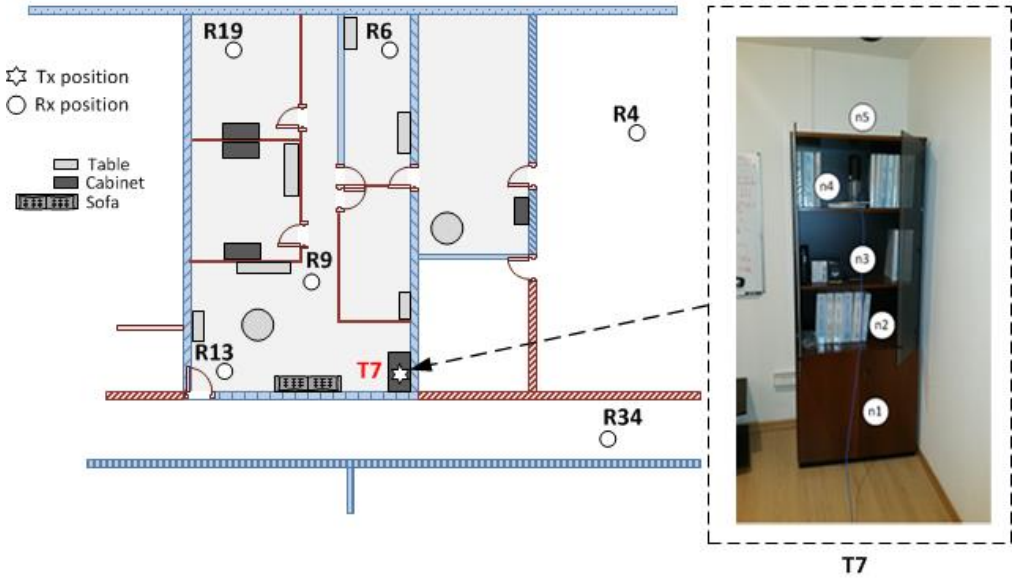

- SB2 -

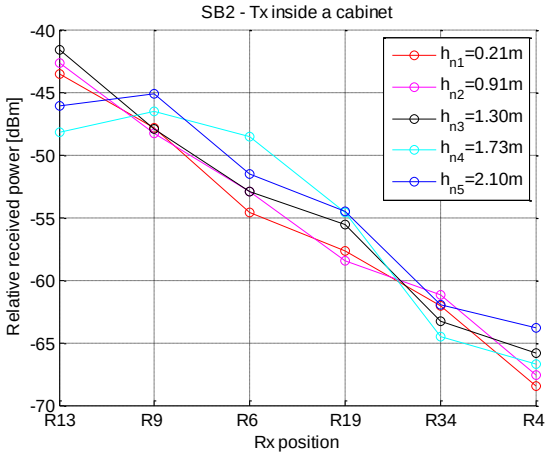

- SB4 -

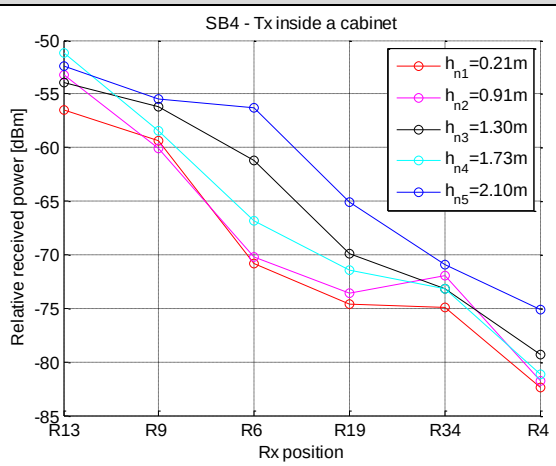

- SB6 -

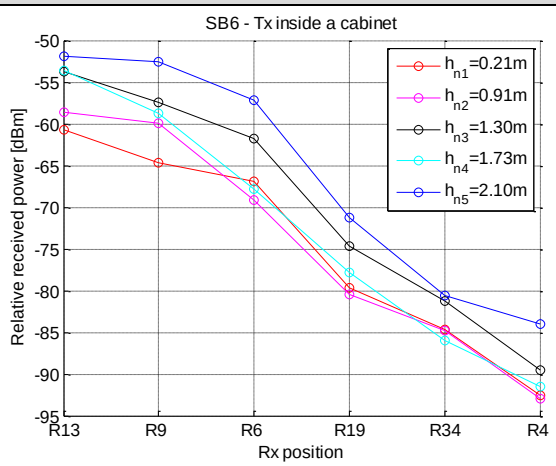

Appendix C.5. Human body shadowing below 6 GHz

In LOS scenarios

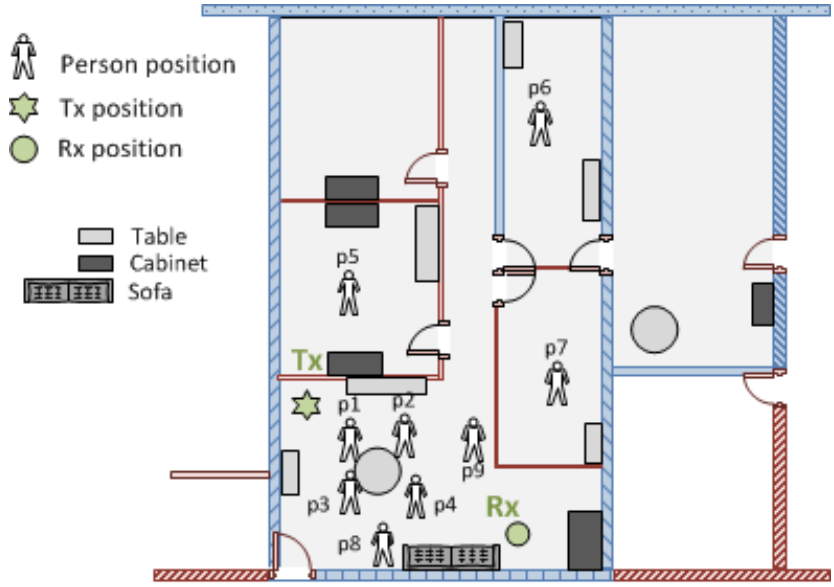

As a reminder, the scenario labeled "*1234D*" means that only the people at locations *p1*, *p2*, *p3* and *p4* are present inside the measurement environment, and are in the *state D*. The same logic is applied to the other notations.

- LOS, h_{Tx} = 0.23 m -

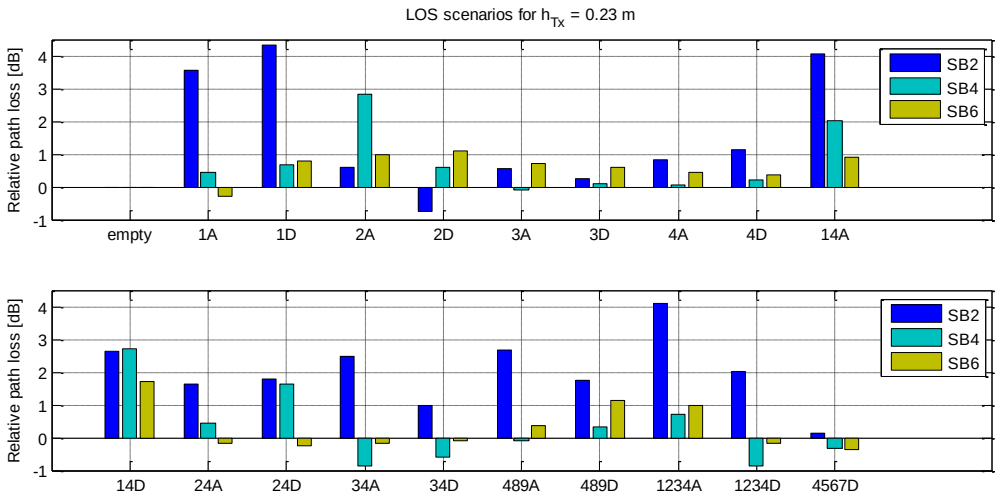

- LOS, $h_{Tx} = 1.05$ m -

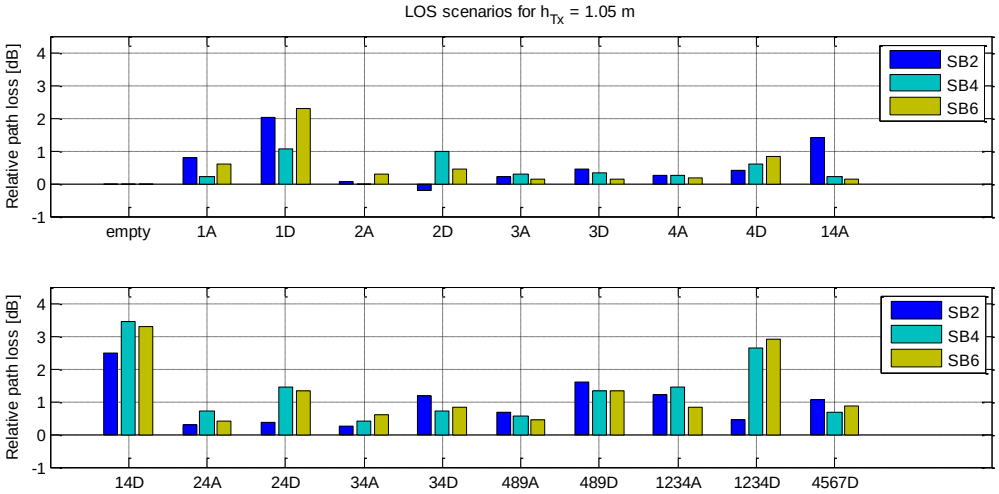

- LOS, $h_{Tx} = 1.67$ m -

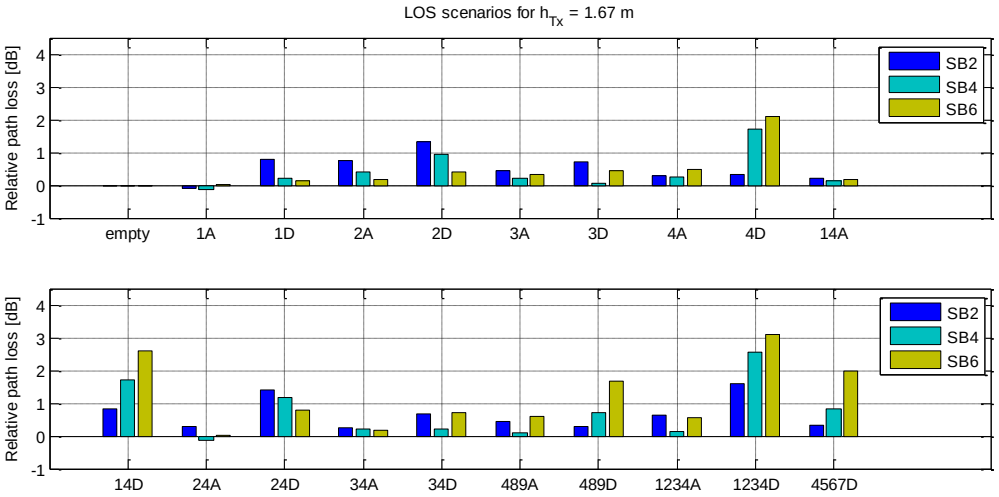

- LOS, $h_{Tx} = 2.30$ m -

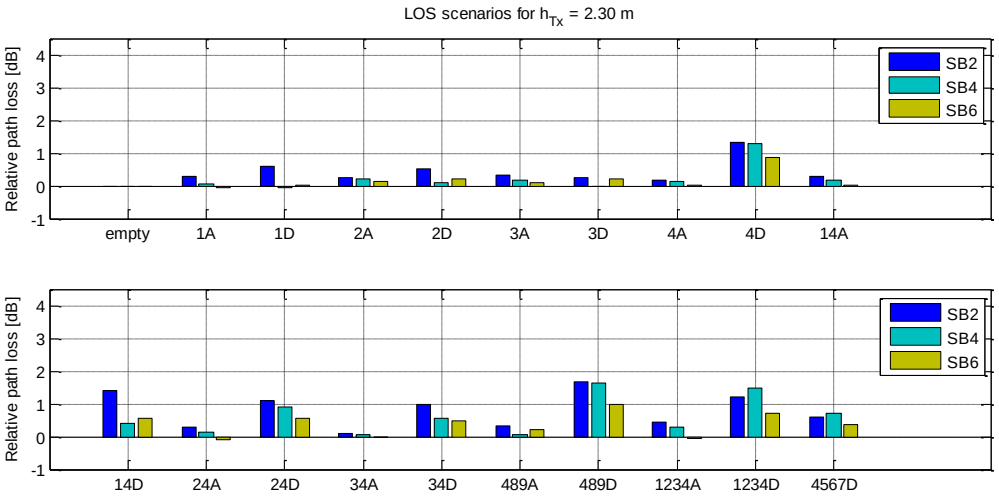

In NLOS scenarios

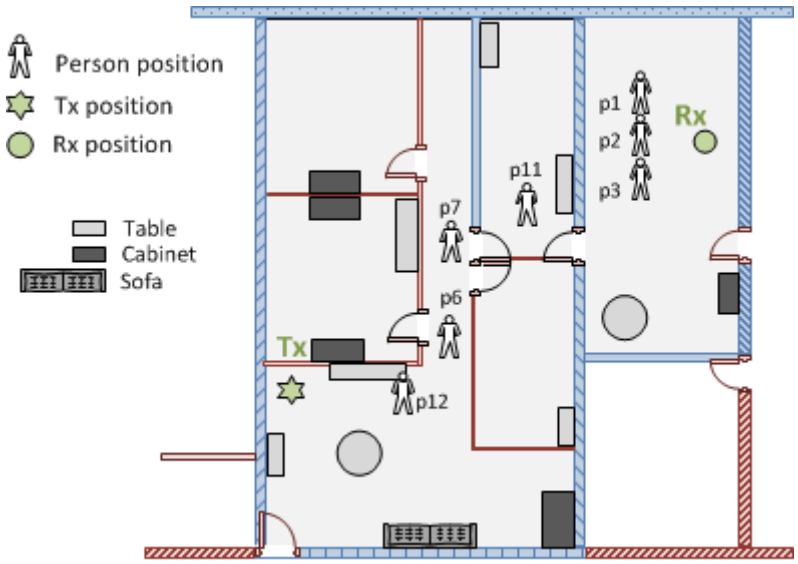

As a reminder, the scenario labeled "*6_7_11_12D*" means that only the people at locations *p6*, *p7*, *p11* and *p12* are present inside the measurement environment, and are in the *state D*. The same logic is applied to the other notations.

- NLOS, $h_{Tx} = 0.23$ m -

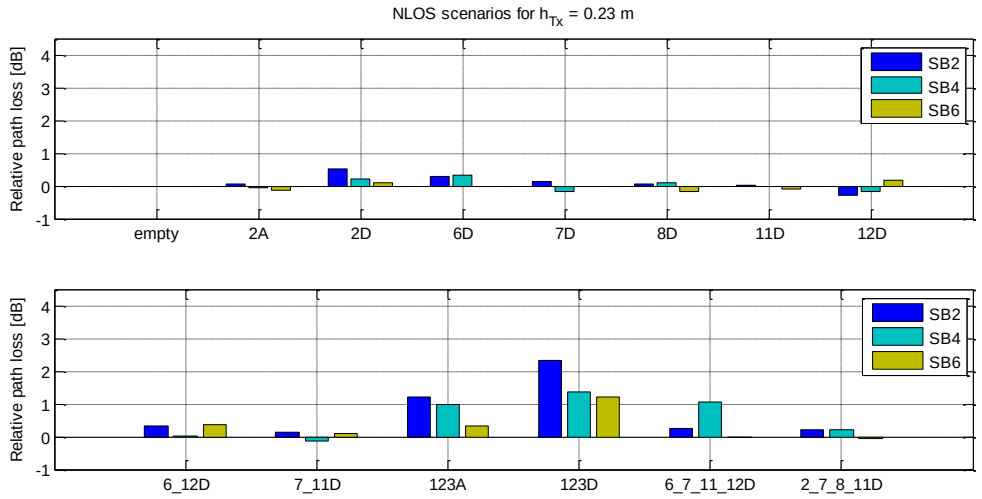

- NLOS, $h_{Tx} = 1.05$ m -

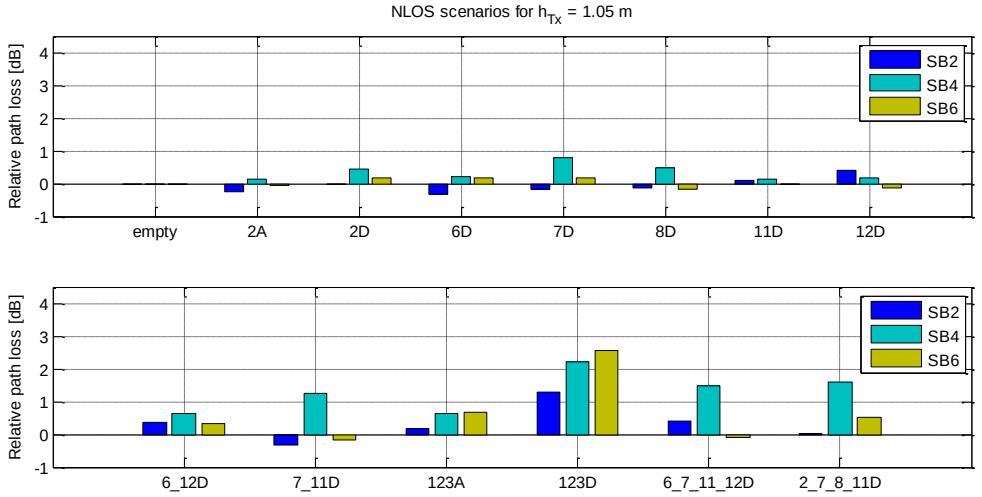

- NLOS, $h_{Tx} = 1.67$ m -

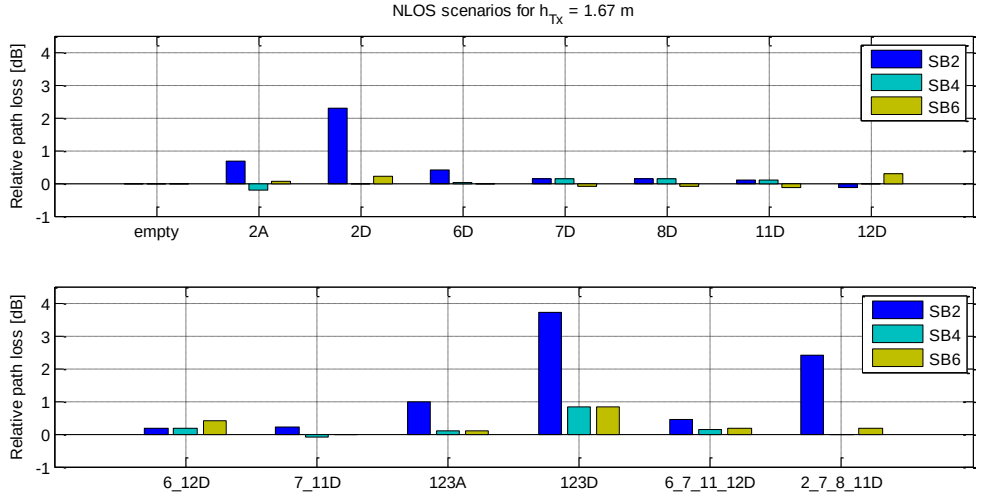

- NLOS, $h_{Tx} = 2.30$ m -

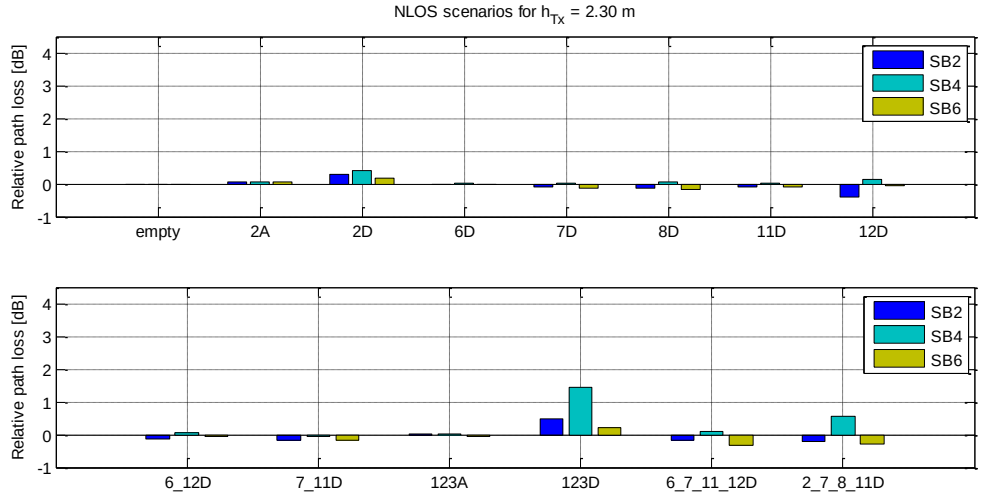

Appendix D Overview of IEEE 802.11ad

The IEEE 802.11ad Standard is also referred to as Directional Multi-Gigabit (DMG). Its general architecture is the same as others IEEE 802.11 standards: it's composed of a set of DMG STAs operating in a DMG BSS. There exist 3 types of DMG BSS:

1. **Infrastructure BSS**: similar to other IEEE 802.11 standards with one access point (AP) acting as a hub;
2. **Independent BSS** (IBSS) : for peer to peer communications between STAs;
3. **Personal BSS** (PBSS): this is basically an IBSS with one station assuming the role of PBSS control point (PCP). The PCP generates the beacon frames and schedules the access periods.

Appendix D.1. Overview of MAC features

a) Channel access periods

The medium time, within a DMG BSS, is divided into beacon intervals. Each beacon interval is subdivided into access periods that are of 4 kinds:

4. **Beacon Transmission Interval** (BTI): a period for the transmission of DMG beacons;
5. **Association Beamforming Training** (A-BFT): a period for achieving beamforming training with the STA sending the beacons;
6. **Announcement Transmission Interval** (ATI): a period for request-responses exchanges between PCP/AP and member STAs;
7. **Data Transfer Interval** (DTI): a period for frame exchanges between STAs by either competing for the channel (CBAP) or by having it reserved by the PCP/AP (SP).

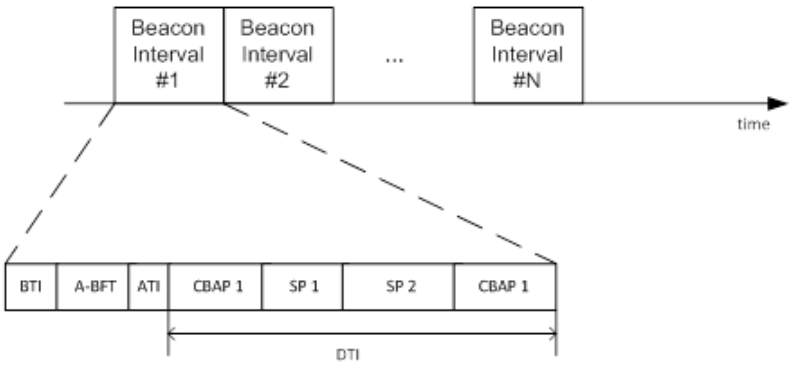

Figure D.1. DMG channel access periods

b) DMG Beamforming

The beamforming training is triggered by a DMG STA (the initiator) towards another DMG STA (the responder). This training is divided into 2 phases: the **Sector Level Sweep (**SLS) phase and the **Beam Refinement Protocol** (BRP) phase.

The purpose of the SLS phase is to determine the best Tx sector at the initiator when the responder uses a quasi-omnidirectional antenna pattern (Initiator Sector Sweep), and the best Tx sector at the responder when the initiator uses a quasi-omnidirectional antenna pattern (Responder Sector Sweep). Thus, only Tx beamforming is performed during the SLS phase.

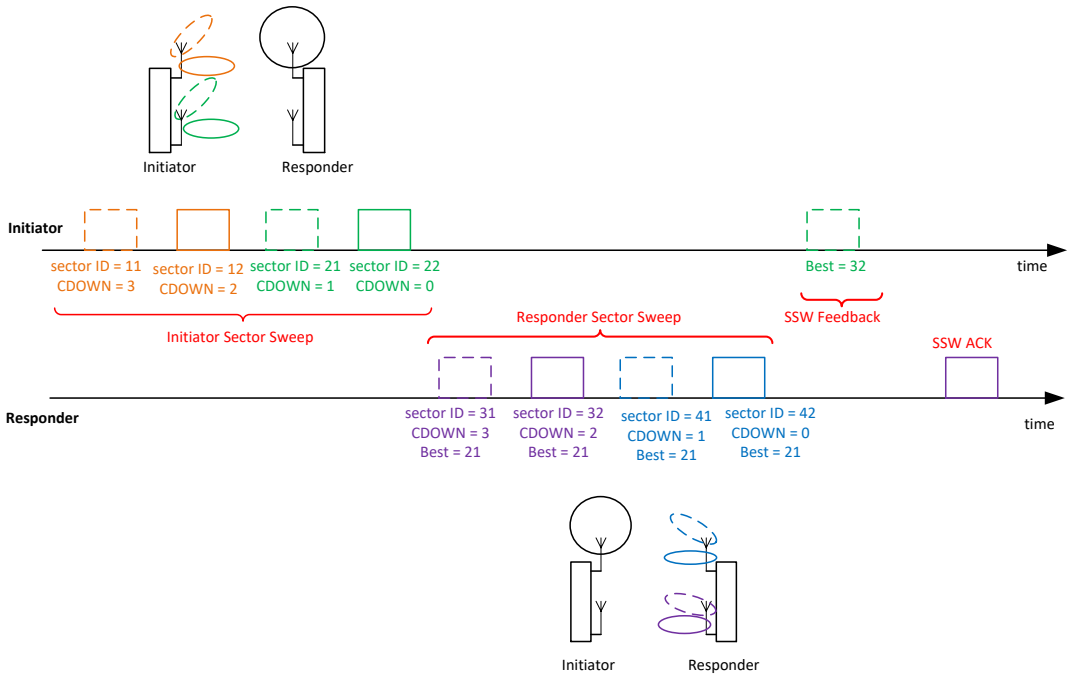

Figure D.2. Example of SLS phase

The BRP phase is an optional feature which allows both initiator and responder to perform more accurate Tx and Rx beamforming trainings.

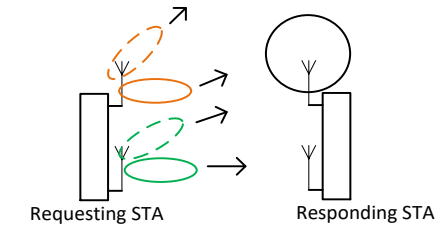

(a) Selection of the best TX sectors with a quasi-omni RX antenna

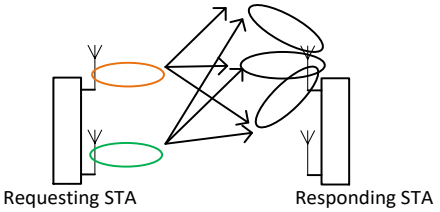

(b) Selection of the best TX and RX sector pair (MID)

Figure D.3. Example of BRP phase

c) *DMG relay*

The DMG Relay function allows a DMG STA (called S-REDS) to transmit frames to another DMG STA (called D-REDS) via a relay DMG STA (RDS) playing the role of frame repeater.

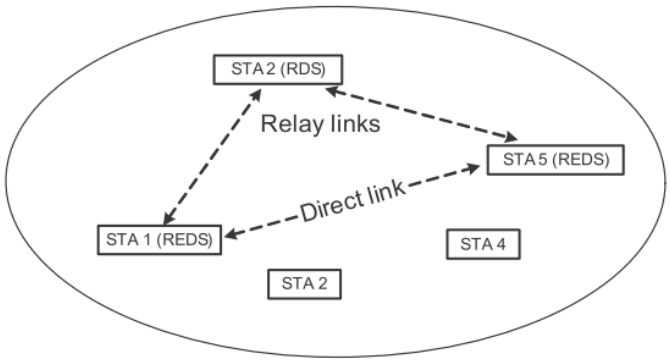

Figure D.4. DMG Relay function

This function is useful when there is a poor link quality between the S-REDS and the D-REDS. There are two types of relay:

- **Link Switching**: The RDS is used only for the time of disruption of the link between the S-REDS and the D-REDS.
- **Link Cooperating**: The RDS is used for all exchanges between the S-REDS and the D-REDS.

Appendix D.2. Overview of PHY features

a) Channelization

Four channels having a bandwidth of 2.16 GHz are available for DMG BSSs.

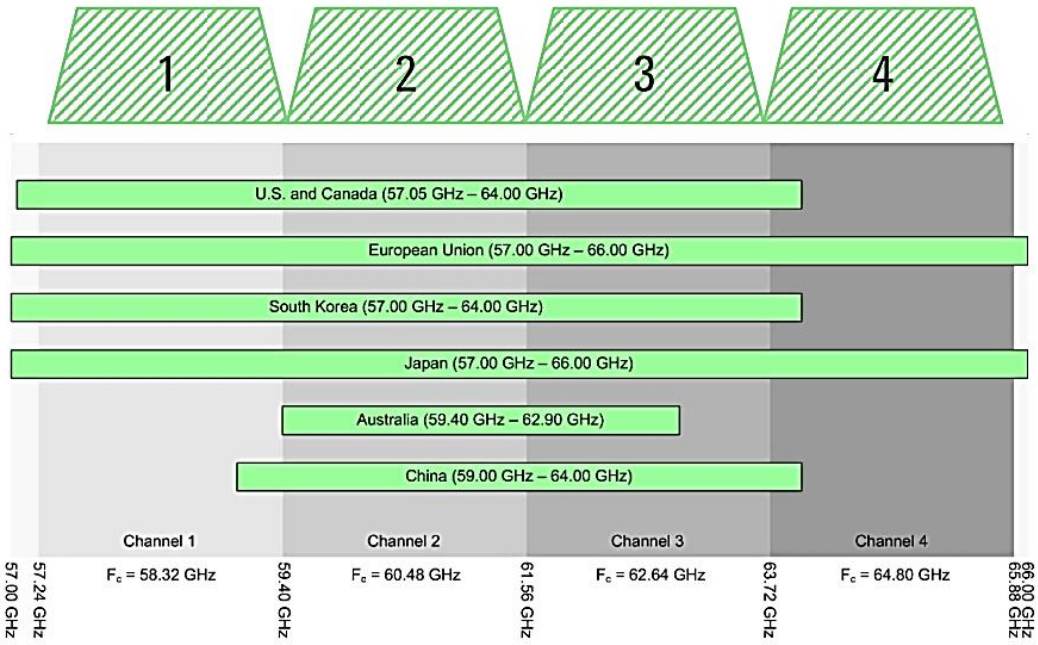

Figure D.5. DMG Channels

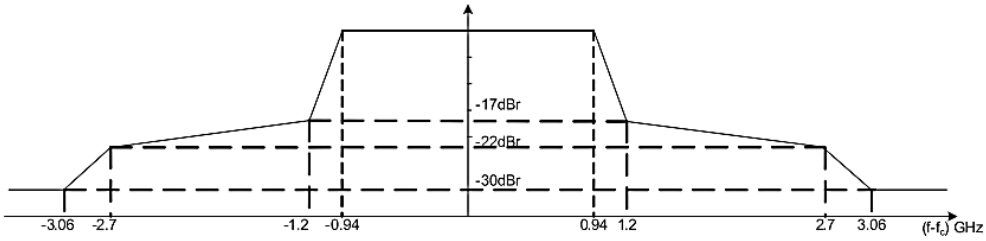

Figure D.6. Transmit mask over one DMG channel

b) Modulation and Coding Scheme

DMG PHY supports three modulations:

Control Modulation : MCS 0 (DMG Control PHY)
Single Carrier Modulation : MCS 1 to MCS 12 (DMG SC PHY)
MCS 25 to MCS 31 (DMG Low-power SC PHY)
OFDM Modulation : MCS 13 to MCS 24 (DMG OFDM PHY)

The support of **DMG Control PHY** is mandatory and is transmitted using MCS 0

Table D.1. DMG Control PHY MCS

MCS index	Modulation	Receive Sensitivity	Data rate (Mbps)	Mandatory
0	DBPSK	-78 dBm	27.5	yes

The support of **DMG SC PHY** is mandatory and has the following MCSs:

Table D.2. DMG SC PHY MCSs

MCS index	Modulation	Receive Sensitivity	Data rate (Mbps)	Mandatory
1	$\pi/2$-BPSK	-68 dBm	385	yes
2	$\pi/2$-BPSK	-66 dBm	770	yes
3	$\pi/2$-BPSK	-65 dBm	962.5	yes
4	$\pi/2$-BPSK	-64 dBm	1155	yes
5	$\pi/2$-BPSK	-62 dBm	1251.25	
6	$\pi/2$-QPSK	-63 dBm	1540	
7	$\pi/2$-QPSK	-62 dBm	1925	
8	$\pi/2$-QPSK	-61 dBm	2310	
9	$\pi/2$-QPSK	-59 dBm	2502.5	
10	$\pi/2$-16QAM	-55 dBm	3080	
11	$\pi/2$-16QAM	-54 dBm	3850	
12	$\pi/2$-16QAM	-53 dBm	4620	

The support of **DMG OFDM PHY** is optional. and has the following MCSs:

Table D.3. DMG OFDM PHY MCSs

MCS index	Modulation	Receive Sensitivity	Data rate (Mbps)	Mandatory
13	SQPSK	-66 dBm	693	yes
14	SQPSK	-64 dBm	866.25	yes
15	QPSK	-63 dBm	1386	yes
16	QPSK	-62 dBm	1732.50	yes
17	QPSK	-60 dBm	2079	yes
18	16-QAM	-58 dBm	2772	
19	16-QAM	-56 dBm	3465	
20	16-QAM	-54 dBm	4158	
21	16-QAM	-53 dBm	4504.50	
22	64-QAM	-51 dBm	5197.50	
23	64-QAM	-49 dBm	6237	
24	64-QAM	-47 dBm	6756.75	

The **DMG low-power SC PHY** is an optional mode that can provide lower processing power requirements for DMG transceivers. The DMG low-power SC PHY has the following MCSs:

Table D.4. DMG low-power SC PHY MCSs

MCS index	Modulation	Receive Sensitivity	Data rate (Mbps)	Mandatory
25	$\pi/2$-BPSK	-64 dBm	626	yes
26	$\pi/2$-BPSK	-60 dBm	834	yes
27	$\pi/2$-BPSK	-57 dBm	1112	yes
28	$\pi/2$-BPSKQ	-57 dBm	1251	yes
29	$\pi/2$-BPSKQ	-57 dBm	1668	yes
30	$\pi/2$-BPSKQ	-57 dBm	2224	yes
31	$\pi/2$-BPSKQ	-57 dBm	2503	yes

Table D.5. Timing parameters of the DMG PHY

Parameter	Value
N_{SD}: Number of data subcarriers	336
N_{SP}: Number of pilot subcarriers	16
N_{DC}: Number of DC subcarriers	3
N_{ST}: Total Number of subcarriers	355
N_{SR}: Number of subcarriers occupying half of the overall BW	177
Δ_F : subcarrier frequency spacing	5.15625 MHz(2640 MHz/512)
F_s: OFDM sample rate	2640 MHz
F_c: SC chip rate	1760 MHz = ⅔ F_s
T_s: OFDM Sample Time	0.38 ns=1/F_s
T_c: SC Chip Time	0.57 ns=1/F_c
T_{DFT}: OFDM IDFT/DFT period	0.194 μs
T_{GI}: Guard Interval duration	48.4 ns= T_{DFT}/4
T_{seq}	72.7 ns=128×T_c
T_{STF}: Detection sequence duration	1236 ns=17× T_{seq}
T_{CE}: Channel Estimation sequence duration	655 ns=9×T_{seq}
T_{SYM}: Symbol Interval	0.242 μs= T_{DFT}+T_{GI}
T_{HEADER}: Header Duration	0.242 μs=T_{SYM} (OFDM) 0.582 μs =2×512× T_c (SC)
F_{CCP}: control PHY chip rate	1760 MHz
T_{CCP}: control PHY chip time	0.57 ns = $1/F_{CCP}$
T_{STF-CP}: control PHY short training field duration	3.636 μs =50× T_{seq}
T_{CE-CP}: control PHY channel estimation field duration	655 ns=9× T_{seq}
T_{Data}	N_{SYM}×T_{SYM} (OFDM) (N_{BLKS}×512+64)×T_c (SC) NOTE—N_{SYM} is defined in 21.5.3.2.3.3 and N_{BLKS} is defined in 21.6.3.2.3.3.

Appendix E Resolution of the 2-class model

The system throughput of the 2-class model in the scenario described in section 5.1.1 has been determined by solving a set of nonlinear coupled equations. This task has been achieved by a script written in PYTHON language and using the function ***fsolve():***

```
Data        = (n1, n2, X, alpha, L)
z           = fsolve(fn_2class_model, np.array(
              [0, 0, 0, 0, 0, 0, 0.1, 0.1, 0, 0, 5e-5, 0]), data)
Es          = np.round(z[10],7)
Ps1, Ps2    = np.round(z[8],7), np.round(z[9],7)
S1          = np.round(Ps1*L*8/(Es*1e6),7)
S2          = np.round(Ps2*L*8/(Es*1e6),7)
S           = np.round(S1+S2, 7) # -- System Throughput -- #
alpha       = np.round(S2/S1, 7)
print "S, alpha : ", S, ",", alpha
```

The system of equations to solve is defined in the function ***fn_2class_model()*** which is implemented as follows:

```
def fn_2class_model(z, *data):

    n1, n2, X, alpha, L = data

    """ ---  Parameters 802.11a ---  """
    Wo      = 16
    m       = 6
    dphy     = 56e6
    dctr    = 6e6
    Ndps    = dphy * 4e-6
    Ncps    = dctr * 4e-6
    Smac    = 24
    Scryp   = 8
    Sack    = 14
    Scrc    = 4

    """ Arrival rate lambda1,2 """
    l1      = n2 * X / (8*L)
    l2      = alpha * X / (8*L)

    """ Durations """
    T_phyH  = 20e-6
    Tprop   = 1e-6

    Tslot   = 9e-6
    Tsifs   = 16e-6
    Tdifs   = 2*Tslot + Tsifs

    Ldata   = 4e-6 * np.ceil(L*8/Ndps)
    Tdata   = T_phyH + 4e-6 * np.ceil((16+6+8*(L+Scryp+Smac+Scrc))/Ndps)
    Tack    =  T_phyH + 4e-6 * np.ceil((16+6+8*Sack)/Ncps)
    Ts      = Tdata + Tsifs + Tack + Tdifs + 2*Tprop
    Tc      = Ts

    """ The 12 unknows value to determine """
    t1      = z[0]
    t2      = z[1]
    p1      = z[2]
    p2      = z[3]
    Idle1   = z[4]
    Idle2   = z[5]
    q1      = z[6]
    q2      = z[7]
```

```
    Ps1     = z[8]
    Ps2     = z[9]
    Es      = z[10]
    Ptr     = z[11]

""" The 12 equations are stored in variable F """
F = np.empty((12))
```

In [2], the equation (7) given by:

$$1 - p_l = \prod_{j \neq l}(1 - \tau_j) \quad \text{for } l = 1, \ldots, n$$

is coded for each class as:

```
F[0] = 1 - p1 - pow(1 - t1, n1 - 1) * pow(1 - t2, n2)
F[1] = 1 - p2 - pow(1 - t1, n1) * pow(1 - t2, n2 - 1)
```

The only equation in section C of [2] given by:

$$P_{idle_l} = 1 - p_l$$

is coded for each class as:

```
F[2] = Idle1 - (1 - p1)
F[3] = Idle2 - (1 - p2)
```

The equations (5) and (6) in [2] respectively given by

$$\begin{aligned}\frac{1}{b_{(0,0)_e}} = (1-q) + \frac{q^2 W_0 (W_0+1)}{2(1-(1-q)^{W_0})} \\ + \frac{q(W_0+1)}{2(1-q)}\left(\frac{q^2 W_0}{1-(1-q)^{W_0}} + (1-P_{idle})(1-q) - qP_{idle}(1-p)\right) \\ + \frac{pq^2}{2(1-q)(1-p)}\left(\frac{W_0}{1-(1-q)^{W_0}}\right. \\ \left. - (1-p)P_{idle}\right)\left(2W_0\frac{1-p-p(2p)^{m-1}}{1-2p} + 1\right)\end{aligned}$$

and,

$$\tau = b_{(0,0)_e}\left(\frac{q^2 W_0}{(1-p)(1-q)(1-(1-q)^{W_0})} - \frac{q^2 P_{idle}}{1-q}\right)$$

are coded for each class as:

```
F[4] = t1 \
       - 1 / ((1 - q1)
              + (pow(q1, 2) * Wo * (Wo + 1)) / (2 * (1 - pow(1 - q1, Wo)))
              + ((q1 * (Wo + 1)) / (2 * (1 - q1))) * (
                  (1 - q1) * (1 - Idle1) - q1 * Idle1 * (1 - p1) + pow(q1, 2) * Wo
/ (1 - pow(1 - q1, Wo)))
              + (p1 * pow(q1, 2) / (2 * (1 - q1) * (1 - p1))) * ((Wo / (1 - pow(1 -
q1, Wo))) - (1 - p1) * Idle1) * (
                  (2 * Wo * (1 - p1 - p1 * pow(2 * p1, m - 1)) / (1 - 2 * p1)) + 1)
              ) \
         * (pow(q1, 2) / (1 - q1)) * ((Wo / ((1 - p1) * (1 - pow(1 - q1, Wo)))) -
Idle1)

F[5] = t2 \
       - 1 / ((1 - q2)
              + (pow(q2, 2) * Wo * (Wo + 1)) / (2 * (1 - pow(1 - q2, Wo)))
              + ((q2 * (Wo + 1)) / (2 * (1 - q2))) * (
                  (1 - q2) * (1 - Idle2) - q2 * Idle2 * (1 - p2) + pow(q2, 2) * Wo
/ (1 - pow(1 - q2, Wo)))
```

```
            + (p2 * pow(q2, 2) / (2 * (1 - q2) * (1 - p2))) * (
            (Wo / (1 - pow(1 - q2, Wo))) - (1 - p2) * Idle2) * (
                (2 * Wo * (1 - p2 - p2 * pow(2 * p2, m - 1)) / (1 - 2 * p2)) + 1)
            ) \
        * (pow(q2, 2) / (1 - q2)) * ((Wo / ((1 - p2) * (1 - pow(1 - q2, Wo)))) -
Idle2)
```

The Poisson approximation in section D of [2] given by:

$$q_l = 1 - \exp(-\lambda_l E_s)$$

is coded for each class as:

```
F[6] = q1 - (1 - math.exp(-l1 * Es))
F[7] = q2 - (1 - math.exp(-l2 * Es))
```

The equations (7) and (8) in [2] lead to:

$$P_{S_l} = \sum_{i=1}^{n_l} \tau_i (1 - p_l)$$

which is coded for each class as:

```
F[8] = Ps1 - n1 * t1 * (1-p1)
F[9] = Ps2 - n2 * t2 * (1-p2)
```

The equations in section F and C respectively given by :

$$E_s = (P_{s1} + P_{s2})T_s + (1 - P_{s1} - P_{s2})T_c + (1 - P_{tr})\sigma$$

and

$$P_{tr} = 1 - \prod_{i=1}^{n} (1 - \tau_i)$$

which finally end the ***fn_2class_model()*** function as follows:

```
F[10] = Es - Tslot * (1-Ptr) - Ts * (Ps1 + Ps2) - Tc * (Ptr - Ps1 - Ps2)
F[11] = Ptr - (1- pow(1-t1, n1)*pow(1-t2,n2))

return F
```

Appendix F MATLAB script for 802.11a DCF

The script simulates the packets exchange between N nodes (1 AP and $N-1$ stations) within an IEEE 802.11a BSS. The simulation ends when $N\_packets$ (=100,000 in practice) have been transmitted without collision. The system throughput and the ratio α are then deduced:

```
% k is the number of packets sent by each node
% -->k(1) is the number of packets sent by the AP
% -->k(i>1) is the number of packets sent by STA_i
% t is the duration needed to transmit the N_packets
S           = 1e-6.*8*sum(k).*L./t;
alpha       = sum(k(2:N)/k(1));
```

Before reaching this step, the script first fills the buffer of each node with a sufficient number of packets arriving in a Poisson manner:

```
% Fill the buffer of each of the N nodes
for j=1:N

    lambda  = lambdaSTA;               % lambda = arrival rate
    q       = ceil(2*N_packets/(N+1)); % q = queue_size

    % if the node is the AP j == 1
    if j==1
        lambda  = lambdaAP;
        q       = q*C;       % More packets in AP buffer
    end

    % The arrival times follow an exponential distribution
    % --> The number of packets in the buffer has the Poisson distribution
    arrtime=Tslot*floor(-log(rand)/lambda/Tslot);
    i=1;
    while (i<q)
        arrtime = [arrtime; arrtime(i, :)+Tslot*floor(-log(rand)/lambda/Tslot)];
        i=i+1;
    end
    n=length(arrtime);           % arrival times t_1,...,t_n

    node(j).arr_queue=arrtime;
    node(j).longueur_queue=n;
    clear arrtime
end
```

Then, while the termination condition is not met:

```
t  = 0;
i  = 0;
while i < N_packets
```

The backoff is randomly chosen in order to determine at which instant t_x each node will attempt transmission:

```
% Initial backoff (only when i = 0)
x0 = ceil(w .* rand(1,N)) - 1 ;

% Transmission instant for each node
for i=1:N
    x(i)  =x0(i)*Tslot+ node(i).arr_queue(1);
    % --- additional code -------- %
End

% Order the node (index) by instant of transmission
[tx,index] = sort(x);
```

The node having the smallest t_x value transmits its packet during T1

```
t = tx(1)+ T1;
```

A collision happens when two or more nodes have the same t_x than the transmitting one:

```
for ii = 2:N
    if tx(1) == tx(ii)
        % -- collision detected ! -- %
    end
end
```

If there is no collision, the transmitting station receives the acknowledgment after T2:

```
% Duration increased
t = t + T2;
%One packet successfly transmitted
i           = i + 1;
k(index(1)) = k(index(1)) + 1;
% The backoff is randomly chosen for the next transmission
w(index(1))  = w0;
x0(index(1)) = ceil(w(index(1)) * rand) - 1;
```

If a collision happens, for each node *ii* involved:

```
% The congestion window is doubled
w(index(ii)) = 2 * w(index(ii));
% a new backoff is randomly chosen for the next transmission
x0(index(ii)) = ceil(w(index(ii)) * rand) - 1;
```

This process is repeated until the $N\_packets$ are transmitted without collision.

Note that this appendix does not depict the whole script. For the sake of simplicity, some parts have been overlooked, such as:

- The initialization of some parameters like the T1 and T2 durations;
- The management of the number of retransmissions after a collision;
- Etc.

Appendix G Implementation of the ACP problem

The multi-technology WLAN planning problem has been implemented with pymoo, a PYTHON framework, whose simplified architecture adapted to the resolution of the problem is illustrated in Figure G.1.

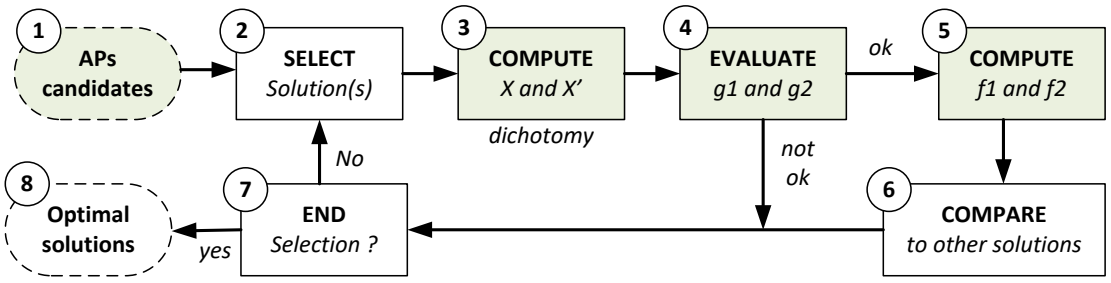

Figure G.1. Pymoo simplified architecture

The blocks in green, representing the definition of the problem, have been implemented during this thesis as follows:

Appendix G.1. Block 1 implementation

The purpose of this block has been to help in defining the search space. It has mainly consisted in specifying the number of candidates (725) and their identifiers (0 to 724) so that a solution consists of N_{AP} APs chosen between the candidates in the range [0, 724].

This block has also helped in creating the three instances of the problem by indicating the technologies featured by the selected candidates. As an example, the **full multi-technology** instance, in which all the candidates operate at 5 and 60 GHz, is created as follows:

```
if self.technos == TECHNOS_560G_ONLY:
    self.TechnoCurrentSol = np.ones(self.NbApSol) * RADIO_5G60G
```

Similarly, the **single-technology** instance corresponds to the following parameterization:

```
if self.technos == TECHNOS_5G_ONLY:
    self.TechnoCurrentSol = np.ones(self.NbApSol) * RADIO_5G
```

Finally, in the **partial multi-technology** instance, the random selection is based on the candidates identifier. If the selected candidate identifier is even, that candidate is considered operating at 5 and 60 GHz. However, if the selected candidate identifier is odd, that candidate is considered operating only at 5 GHz. This choice is implemented as follows:

```
if self.technos == TECHNOS_MIX:
    self.TechnoCurrentSol = self.CurrentSolution % 2
```

Appendix G.2. Block 3 implementation

The first step in block 3 has consisted in computing the initial parameters of the problem, listed in Table 5.6. This task has been performed by a joint processing of the two csv files (exported by XANDA) with the **Pandas** library. This (long) step won't be further detailed for the sake of simplicity.

Based on these parameters, X and X', the guaranteed DL throughput per user in each service area by respectively the initial and fallback coverages, are determined via the following binary search[18]:

```
X           = np.zeros(self.NbAreas)  # X  = [0, 0, 0, 0]
X_backup    = np.zeros(self.NbAreas)  # X' = [0, 0, 0, 0]
x_min       = 0
x_max       = 288
precision   = 0.001

for k in range (self.NbAreas):

    """ -- Guaranteed Xk  for initial coverage """
        X[k] = self.dichotomy(k, x_min, x_max, precision, mu_cell, sigma_cell)

    """ Guaranteed X'k for fallback coverage in area k """
        X_backup[k] = self.dichotomy(k, x_min, x_max, precision,
                                     mu_cell_backup,  sigma_cell_backup)


self.X          = X             # X  = [X1, X2, X3, X4]
self.X_backup   = X_backup      # X' = [X'1, X'2, X'3, X'4]
```

where the ***dichotomy()*** function is recursively defined as:

```
def dichotomy(self, k, x_min, x_max, precision, mu, sigma):

    "p = 0.9"
    proba   = 0.9
    proba_x = 0

    x_k     = (x_max + x_min)/2
    if x_max - x_min  == 0 :  return x_k

    "---  Equation (5.50)  -- "
    for type_techno in range(NB_TYPE_TECHNO):

        " b = type_techno and i = l "
        for l in range(self.NbApSol):

            Mk      = self.NbMeshesArea[k]
            Mk_l    = self.NbMeshesCell[l, k, type_techno]
            N_l     = np.sum(self.NbUser_cell[l,:,type_techno])

            " demand in the cell for area k "
            dmd     = N_l*(1+alpha[k])*x_k
            num     = (1/dmd) - mu[l, type_techno]
            den     = math.sqrt(2 * sigma[l, type_techno])

            proba_x += (Mk_l/Mk) * 0.5 * (1+ special.erf(num/den))

    " Result of the dichotomy "
    error  = math.fabs(proba - proba_x)
    if  error <= precision:
        return x_k

     " Recursivity "
    if proba_x < proba :
        return self.dichotomy(k, x_min, x_k, precision, mu, sigma)

    return self.dichotomy(k, x_k, x_max, precision, mu, sigma)
```

[18] The nonlinear equations (5.50) and (5.51) provide respectively a single solution because the *erf* function is an increasing function.

Appendix G.3. Blocks 4 and 5 implementation

Based on X and X' determined in Block 3, the objective functions f_1 in (5.52) and f_2 in (5.53) (as well as the constraints g_1 and g_2) can finally be implemented as:

```
"---------- Objective function f1 ----------"
def fn_max_min_throughput(self):

    ratio_x = self.X / self.ThroughputDemandArea
    fx      = np.min(ratio_x)
    gx = -1

    if self.pCouv.sum() < 0.9 :
        "Constraint #1 : Less than 90% of the global area covered "
        return 0, 1

    if   fx  < 1 :
        "Constraint #2 : The demand per area is not fulfilled "
        return 0, 1

    "-fx means in pymoo maximize fx"
    return -fx, gx



"---------- Objective function f2  ----------"
def fn_max_fallback_throughput(self):

    ratio_x_backup  = self.X_backup/self.ThroughputDemandArea
    fx              = np.min(ratio_x_backup)
    gx      = -1
    return -fx, gx
```

Finally, the resolution of the chosen scenario is carried out in pymoo with the ***minimize()*** function:

```
" CSV files exported by XANDA "
csv_5g          = 'Export5_GHz.csv'
csv_60g         = 'Export60_GHz.csv'

type_problem                = MULTI_OBJECTIVE_PROBLEM

" Choice of the scenario : 560G_ONLY, 5G_ONLY or MIX "
technos                     = TECHNOS_560G_ONLY

" Inputs problem "
NbApSol                     = 11
ThroughputDemandPerArea     = np.array([6, 25, 6, 10])
DensityUserPerArea          = np.array([10 / 216, 1 / 132, 20 / 405, 40 / 3201])
alpha                       = np.array([1.0, 0.0, 1.0, 0.4])

" Problem definition  "
problem     = MyProblem(NbApSol, ThroughputDemandPerArea, DensityUserPerArea,
                        alpha, type_problem, technos, csv_5g, csv_60g)

" Algorithm parameterization "
pop_size        = 20
ngen            = 100
method          = get_algorithm("nsga2", pop_size=pop_size,
                            sampling=get_sampling("int_random"),
                            crossover=get_crossover("int_sbx", prob=0.9, eta=3.0),
                            mutation=get_mutation("int_pm", prob=0.5 ,  eta=3.0),
                            elimate_duplicates=True)

" Resolution "
res = minimize(problem, method, termination=('n_gen', ngen), seed=1, save_history=True)
```

INSA de RENNES
Service des Formations

AVIS DU JURY SUR LA REPRODUCTION DE LA THESE SOUTENUE

Titre de la thèse:
Design of Models for the Planning of Indoor Multi-technology Wireless Networks

Nom Prénom de l'auteur : KACOU MARC EMMANUEL VIVIEN-MARIE WOZ

Membres du jury :
- Monsieur LOUZIR Ali
- Monsieur LAGRANGE Xavier
- Monsieur GUILLET Valéry
- Monsieur EL ZEIN Ghais
- Monsieur ZAHARIA Gheorghe
- Monsieur GORCE Jean-Marie
- Madame LIENARD Martine
- Madame SAGNARD Florence

Président du jury :
X. LAGRANGE

Date de la soutenance : 12 Décembre 2019

Reproduction de la these soutenue

☒ Thèse pouvant être reproduite en l'état
☐ Thèse pouvant être reproduite après corrections suggérées

Fait à Rennes, le 12 Décembre 2019

Signature du président de jury

Le Directeur,

M'hamed DRISSI

Titre : Conception de modèles pour la planification de réseaux sans fil multi-technologies en indoor

Mots clés : Propagation indoor ; mesures de canal ; modèle de path loss ; ondes millimétriques ; réseaux sans fil hétérogènes ; planification de réseaux sans fil

Résumé : L'évolution constante des technologies sans fil telles que le Wi-Fi, les normes de réseaux mobiles ou d'objets connectés, a donné naissance à de nouvelles applications et usages. Les possibilités offertes par cette multitude d'alternatives sont exploitées par les réseaux sans fil hétérogènes qui, en combinant au sein d'un réseau unique plusieurs technologies, permettent aux utilisateurs d'accéder à des services complémentaires de façon transparente. Cependant, pour bénéficier pleinement de ces avantages, plusieurs défis techniques sont à relever. L'un d'eux est relatif au déploiement de ces réseaux multi-technologies. En pratique, cette tâche s'appuie sur des règles et outils d'ingénierie afin de réaliser une planification optimale.
Dans ce contexte, un objectif de la thèse a été d'établir des modèles sur lesquels peuvent se baser les outils d'ingénierie radio afin d'optimiser le déploiement de réseau locaux sans fil multi-technologies.Il s'agit principalement de calibrer des modèles de propagation pour l'estimation de couverture radio en environnement indoor résidentiel entre 800 MHz et 60 GHz; d'établir un modèle de débit pour l'estimation de capacité Wi-Fi en fonction du trafic montant et descendant; et de concevoir un modèle de résolution multi-objectif pour optimiser le positionnement de points d'accès opérant à 5 et 60 GHz.
En complément, cette thèse a également proposé des recommandations pratiques visant à placer au mieux les points d'accès en phase de déploiement. Cela s'est fait par le biais d'études de sensibilité de couverture à divers facteurs, tels que l'environnement immédiat de l'émetteur ou encore la présence de personnes faisant obstruction.

Title : Design of Models for the Planning of Indoor Multi-technology Wireless Networks

Keywords : Indoor propagation; channel measurements; path loss models; millimeter-waves; heterogeneous wireless networks; automatic cell planning

Abstract : The constant evolution of wireless technologies such as Wi-Fi, mobile networks standards or IoT, has given rise to new applications and usages. The possibilities offered by this multitude of alternatives are exploited by heterogeneous wireless networks which, by combining within a single network several technologies, provide the users with a seamless access to complementary services. However, to take full advantage of these benefits, there are several technical issues to address. One of them is related to the deployment of these multi-technology networks. In practice, this task relies, most of the time, on radio network design software to achieve optimal planning.
In such context, the main objective of this thesis is to establish models which can be used by radio network planning tools in order to the deployment of multi-technology wireless local area networks. This task has involved calibrating propagation models for radio coverage estimation, in residential indoor environments from 800 MHz to 60 GHz; developing a throughput model for Wi-Fi capacity estimation based on uplink and downlink traffic; and establishing a multi-objective resolution model to optimize the positioning of access points operating at 5 and 60 GHz.
Moreover, this thesis also proposes practical recommendations for a better positioning of access points during deployment phases. This task has been achieved through coverage sensitivity studies to various factors, such as the transmitter surroundings or the presence of obstructing people.